

Thermal Treatment of Fuel Residues and Problematic Nuclear Wastes

Sean Thomas Barlow *BSc(Hons) MInstP MINCOSE*

Supervisors:

Professor Neil C. Hyatt

Professor Russell J. Hand

Dr. Claire L. Corkhill

Dr. Martin C. Stennett

A thesis submitted in fulfilment of the requirements for the degree of
Doctor of Philosophy

Alternative Format Thesis



Immobilisation Science Laboratory

Department of Materials Science and Engineering

The University of Sheffield

May 2019

Abstract

Problematic nuclear wastes and fuel residues plague the nuclear industry worldwide. In this Thesis thermal treatment is demonstrated through the development of various simulated nuclear wasteforms and surrogate materials from a variety of nuclear waste topics.

Development of vitreous wasteforms for the treatment of intermediate level Magnox sludge from the Storage Ponds at Sellafield is discussed in this Thesis with both low activity uranium and surrogate materials. Magnesium borosilicate glasses were found to have comparable durability with current UK high level waste (HLW) glass whilst incorporating the whole spectrum of waste anticipated into a single composition. Highly metallic feeds could be incorporated into the wasteform with no adverse effects on the dissolution of such samples. If implemented, this composition could result in a 25% volume reduction in waste to be disposed saving approximately £82 million compared to the current baseline plan.

Ascertaining the long-term integrity and safety of fuel residues arising from nuclear meltdowns, such as the Chernobyl and Fukushima accidents, through thermal synthesis of low activity simulants is explored in this Thesis. Two simulant Chernobyl ‘lava-like’ fuel containing materials (LFCM) were developed recreating the typical morphology and microstructure found in real samples, including a World first to successfully document formation of Chernobylite from a glass melt whilst aqueous durability was analogous to that of UK borosilicate HLW glass.

Investigating how thermal treatment of americium waste built-up in stockpiles of civil plutonium is outlined in this Thesis. A novel cerium niobite, a simulant for americium, was synthesised with the crystal structure and suitability as a wasteform assessed. One potential use for an americium ceramic could be as a power source in a radioisotope thermoelectric generator (RTG); however it was determined an Am structured niobite for this application would be unsuitable, due to the phase transformation this material exhibited at elevated temperatures. This work opens avenues for further research on other potential materials.

Acknowledgements

Reflecting on the past four or so years of my research at Sheffield, I am reminded of what a great learning environment this has been, academically, socially and professionally. Completion of this Thesis has been a journey that has taken me across the globe, meeting many new friends and finding me a career I enjoy. Getting to the completion of this Thesis has not been a solo exercise however, a significant number of people have assisted in varying ways along the journey and whom which I would like to give thanks.

To my supervisor Professor Neil Hyatt, without whom this research would not have been realised, I give my sincerest thanks for your determination and belief in me, to aid in my development as a scientist and now engineer. Thank you for providing both the independence and support required in my research and for being such a committed and dedicated supervisor.

To Professor Russell Hand, Dr Claire Corkhill and Dr Martin Stennett, thank you for all your imparted knowledge and project support. The contributions you've made to both my development as a scientist and this work are profound. Thank you for all discussions on glass science Russell, dissolution science Claire and all things-laboratory based Martin.

Thanks must also be given to the staff at the University of Sheffield's Department of Materials Science and Engineering in general; be it administrative, financial or technical support they have been on hand to help. I am reminded of the support given by Dr. Lisa Holland for glass melting advice and support as well as Dr Nik Reeves for XRD and crystallographic refinement support. An acknowledgement is also given to Dr Heath Bagshaw at the University of Manchester and Dr Emma McCabe from the University of Kent for support in data collection and analysis.

Importantly I would like to thank EPSRC for their financial support to this research through the Nuclear FiRST DTC programme at both the University of Manchester and University of Sheffield. Additional funding support was provided by the MRS2017 Student Scholarship Award, Margaret Elizabeth Lee Fellowship and Institute of Physics Student Conference Fund for which considerable thanks is given.

My time at Sheffield has been invigorated and made one of the most enjoyable times of my life by fellow course-mates and friends from both the Nuclear FiRST DTC and ISL groups, with our weekly pub trips, meals out, walks in the peaks and giving me an international outlook on life. In no particular order, I would like to thank Colleen, Daniel C, Sebastian, Seddon and Michael from my DTC cohort, along with Michal, Shishir, Adam, Dilwar, James, Daniel B, Tannagorn, Joe, Marco and Xinyuan for being such awesome office buddies and providing important breaks from studying through activities such as climbing, swimming, squash, hiking, eating and drinking. Wetherspoons anyone?

To Natcha, thank you for being by my side this past year. Your kindness and joyous spirit have been a constant source of energy to draw upon in time of need. Your contribution to this Thesis is through your loving support for me.

To my parents Stuart and Christine, thank you for making me the person I am today. You have been my bedrock; loving and supporting me in all my ambitions, your contribution is more than can be expressed in words. To my siblings Daniel, James and Sarah-Jane, you have shared with me your joy, laughter and fun times supporting me to see this work through to completion for which I am eternally grateful.

Conferences, Papers, Presentations, Outreach & Professional Training

Publications

- Sean Barlow and Michael Kirkham, *The building blocks of education*. Nuclear Future, Vol. 11 (1), 2015, pp. 61–63.
- S. T. Barlow, M. C. Stennett, R. J. Hand, S. P. Morgan, and N. C. Hyatt, *Thermal Treatment of UK Magnox Sludge*. Proceedings of the 2nd Petrus-OPERA PhD and Early Stage Researcher Conference, 2016, pp. 19–22.
- S. T. Barlow, D. J. Bailey, A. J. Fisher, M. C. Stennett, C. L. Corkhill and N. C. Hyatt, *Synthesis of simulant ‘lava-like’ fuel containing materials (LFCM) from the Chernobyl reactor Unit 4 meltdown*. MRS Advances, Vol. 2 (11), 2016, pp. 609-614. doi:10.1557/adv.2016.642
- Sean T. Barlow, Daniel J. Bailey, Adam J. Fisher, Martin C. Stennett, Clemence Gausse, Claire L. Corkhill, Viktor A. Krasnov, Sergey Yu. Sayenko and Neil C. Hyatt, *Synthesis, characterisation and corrosion behaviour of simulant Chernobyl nuclear meltdown materials*. npj Materials Degradation, submitted on 02/04/19.

Conferences Attended

- Nuclear FiRST DTC Winter School, Buxton Palace Hotel, UK, 08/01/2014-10/01/2014.
- Joint Nuclear CDTs Winter School, Birmingham Crown Plaza Hotel, UK, 06/01/2015-08/01/2015.
- Thermal Treatment Symposium 2015, Warrington, UK, 15/01/2015.
- Farewell to Magnox, Wylfa, UK, 28/10/2015.
- EPSRC Fission & Fusion Symposium, Manchester, UK, 14/12/2015.
- Joint Nuclear CDTs Winter School, Birmingham Royal Angus Hotel, UK, 06/01/2016-08/01/2016.
- ESRC Nuclear Futures Seminar, Sheffield Halifax Hall, UK, 27/01/2016-28/01/2016.
- ESRC Nuclear Futures Seminar, Sheffield Leopold Hotel, UK, 06/04/2016-07/04/2016.
- 2nd Petrus-OPERA PhD and Early Stage Researcher Conference 2016, Delft University of Technology, Netherlands, 27/06/2016-01/07/2016.
- Society of Glass Technology Centenary Conference, Sheffield, UK, 04/09/16-08/09/16 (**Chaired session on Waste Vitrification**).
- MRS Fall 2016 Meeting and Exhibit, Boston, Massachusetts, USA, 27/11/2016-02/12/2016
- Joint Nuclear CDTs Winter School, St Johns Hotel Solihull, UK, 04/01/2017-06/01/2017
- Institute of Physics Nuclear Industry Group, The Centre at Birchwood Park, Warrington, UK, 28/09/2017

- Scientific Basis for Nuclear Waste Management XLI, Sydney, Australia, 29/10/2017-03/11/2017

Presentations

- Thermal Treatment of Magnox Sludge by Immobilisation in Borosilicate Glass (poster) – Joint Nuclear CDTs Winter School, 08/01/2015.
- Glass formulations for thermal treatment of Magnox sludges (poster) – Thermal Treatment Symposium, 15/01/2015.
- Thermal Treatment of Magnox Sludge ILW (poster) – EPSRC Fission & Fusion Symposium, 14/12/2015.
- Thermal Treatment of Magnox Sludge Intermediate Level Waste (oral) – Joint Nuclear CDTs Winter School, 07/01/2016.
- Thermal Treatment of UK Magnox Sludge (oral) – 2nd Petrus-OPERA PhD and Early Stage Researcher Conference 2016, 27/06/2016.
- Glass formulations for Magnox Sludge Immobilisation (oral) – Society of Glass Technology Centenary Conference, 06/09/2016.
- Glass formulations for Thermal Treatment of UK Magnox Sludge Waste (oral) – MRS Fall 2016 Meeting and Exhibit, 30/11/2016
- Synthesis of Simulant Lava-Like Fuel Containing Materials from the Chernobyl Nuclear Disaster (oral) – MRS Fall 2016 Meeting and Exhibit, 30/11/2016
- Simulant Lava-Like Fuel Containing Materials from the Chernobyl Disaster (oral) – Joint Nuclear CDTs Winter School, 04/01/2017
- From Magnox to Chernobyl: A report on clearing-up problematic nuclear waste (**Invited Speaker**) – Institute of Physics Nuclear Industry Group, 28/09/2017
- Thermal Treatment of Magnox Sludge Intermediate Level Nuclear Waste through Vitrification (oral) – Scientific Basis for Nuclear Waste Management XLI, 31/10/2017
- Synthesis and characterisation of rare Ce₃NbO₇ compounds for use as nuclear space batteries by neutron powder diffraction and X-ray absorption spectroscopy (oral) – Scientific Basis for Nuclear Waste Management XLI, 01/11/17

Outreach

- Meet the Scientist, Museum of Science and Industry, Manchester, 02/08/2014.
- Science Spectacular 2014, University of Manchester, Manchester, 25/10/2014.
- Discovery Night 2015, University of Sheffield, Sheffield, 13/03/2015.
- Sheffield Festival of Science and Engineering 2015, Sheffield, 17/03/2015-18/03/2015.
- Science Spectacular 2015, University of Manchester, 31/10/2015.

Professional Training

- EAL Level 1 Award in Introductory Welding Skills – 600/1903/7 (Wilkinson Welding Academy 18/03/2015).
- Compressed [Cylinder] Gas Safety Workshop (The Gas Safety Co. 19/03/2015).
- Radiation Protection Supervisor Training (Radman Associates 21/05/2015-22/05/2015).
- Project Management – Industrial Placement (DavyMarkham Ltd. 04/05/2017-27/02/2018).

Awards

- MRS2017 Student Scholarship – 2017.
- Margaret Elizabeth Lee Fellowship – 2017.
- Institute of Physics Student Conference Fund – 2017.
- EPSRC Nuclear FiRST PhD studentship – 2013-2018.

Table of Contents

Abstract.....	II
Acknowledgements	III
Conferences, Papers, Presentations, Outreach & Professional Training	V
Table of Contents	VIII
List of Abbreviations	XII
List of Figures.....	XIV
List of Tables	XVIII
1. Introduction – Research Impetus	19
2. Background.....	22
2.1. Historic & Current Use of Atomic Energy	22
2.2. Current Commercial Nuclear Power Reactors & Future Designs	24
2.3. The Nuclear Fuel Cycle	27
2.3.1. Mining	28
2.3.2. Conversion	28
2.3.3. Enrichment	29
2.3.4. Fuel Fabrication.....	29
2.3.5. Reactor Use	30
2.3.6. Interim Storage & Reprocessing	30
2.4. Nuclear Waste Management.....	32
2.4.1. Waste Classification and Volume	32
2.4.2. Long Term Waste Management	35
2.4.3. Wasteform Alteration	38
2.5. First Generation Magnox Storage Ponds & Silos.....	40
2.6. Chernobyl Lava-like Fuel Residues	42
2.7. Plutonium Product and Residues	45
2.7.1. Americium Extraction & Use in RTG.....	46
2.7.2. Weberite-type ceramics	48
2.8. Processing Routes for Problematic Nuclear Wastes and Fuel Residues	49
2.8.1. Vitrification	49

2.8.2.	Ceramication & Glass Composite Materials	53
2.8.3.	Hot Isostatic Pressing	54
3.	Materials and Experimental Techniques	55
3.1.	Magnox Sludge Glass Processing.....	55
3.1.1.	Batch Preparation - Glass	57
3.1.2.	High temperature processing - Glass	59
3.1.3.	Powdering & sectioning glass samples	60
3.2.	Magnox Sludge HIP Processing	61
3.2.1.	Batch Preparation – HIP.....	61
3.2.2.	Thermal Synthesis – HIP.....	61
3.3.	Chernobyl Lava-Like Fuel Containing Material Processing.....	62
3.3.1.	Batch Preparation – LFCM	62
3.3.2.	Thermal Synthesis – LFCM	64
3.3.3.	Powdering and sectioning LFCM samples	64
3.4.	Cerium Niobate Ceramics Processing	66
3.4.1.	Batch Preparation – Ce ₃ NbO ₇	66
3.4.2.	Thermal Synthesis – Ce ₃ NbO ₇	67
3.4.3.	Powdering Ce ₃ NbO ₇ samples.....	67
3.5.	Characterisation techniques	68
3.5.1.	X-Ray Diffraction	68
3.5.2.	Neutron Diffraction	70
3.5.3.	Electron Diffraction.....	71
3.5.4.	Scanning Electron Microscopy & Energy Dispersive X-Ray Spectroscopy .	73
3.5.5.	Simultaneous Thermal Analysis.....	75
3.5.6.	Helium Pycnometry.....	76
3.5.7.	X-ray Absorption Spectroscopy	77
3.5.8.	Bulk Chemical Analysis.....	78
3.5.9.	Aqueous Dissolution	79
4.	Thermal Treatment of Simulated Magnox Sludge.....	81
4.1.	Draft paper: A Comparative Study between Non-Radioactive Surrogates Neodymium and Mischmetal in Magnesium Borosilicate and Aluminosilicate Glasses	81
4.1.1.	Introduction	82

4.1.2.	Methodology	83
4.1.3.	Results	85
4.1.4.	Discussion	103
4.1.5.	Conclusions	107
4.1.6.	Acknowledgments	108
4.2.	Draft Paper: Thermal Treatment of Magnox Sludge Intermediate Level Nuclear Waste through Vitrification	109
4.2.1.	Introduction	110
4.2.2.	Experimental procedures	111
4.2.3.	Results	113
4.2.4.	Discussion	129
4.2.5.	Conclusions	133
4.2.6.	Acknowledgments	134
4.3.	Further Work – Hot Isostatic Pressing of Sludge Waste	135
4.3.1.	Introduction	135
4.3.2.	Results	135
4.3.3.	Discussion	141
4.3.4.	Conclusions	142
5.	Thermal Treatment of Simulated Chernobyl Lava-Like Fuel Containing Materials	144
5.1.	Initial Development - Published Paper: Synthesis of simulant ‘lava-like’ fuel containing materials (LFCM) from the Chernobyl reactor Unit 4 meltdown.....	144
5.1.1.	Introduction	145
5.1.2.	Review of LFCM and Compositions as Synthetic Targets	146
5.1.3.	Experimental Procedure	146
5.1.4.	Results & Discussion	147
5.1.5.	Conclusions	150
5.1.6.	Acknowledgements	150
5.2.	Development of Representative Samples – Submitted Paper: Synthesis, characterisation and corrosion behaviour of simulant Chernobyl nuclear meltdown materials	151
5.2.1.	Introduction	152
5.2.2.	Experimental Procedure	153

5.2.3. Results	156
5.2.4. Discussion	165
5.2.5. Acknowledgments	168
6. Thermal Treatment of Americium Residues	169
6.1. Draft Paper: Synthesis and characterisation of rare Ce_3NbO_7 weberite-type compounds by neutron powder diffraction and X-ray absorption spectroscopy	169
6.1.1. Introduction	170
6.1.2. Experimental	172
6.1.3. Results	174
6.1.4. Discussion	183
6.1.5. Conclusions	187
6.1.6. Acknowledgements	187
7. Conclusions and Recommended Future Work.....	188
7.1. Overall Conclusions	188
7.2. Recommended and Ongoing Future Work	192
Appendix A	194
Appendix B	199
References.....	201

List of Abbreviations

AGR	Advanced Gas Cooled Reactor
BWR	Boiling Water Reactor
BVS	Bond Valance Sum
CEA	Atomic Energy and Alternative Energies Commission (France)
TGA	Thermogravimetric Analysis
DoE	Department of Energy (United States)
DTA	Differential Thermal Analysis
EDX	Energy Dispersive X-rays
EDS	Energy Dispersive Spectroscopy
ESA	European Space Agency
FGMSP	First Generation Magnox Storage Ponds
GCR	Gas Cooled Reactors
GDF	Geological Disposal Facility
HIP	Hot Isostatic Press
HLW	High Level Waste
ICDD	International Centre for Diffraction Data
ICP-ES	Inductively Coupled Plasma Emission Spectrometry
ILW	Intermediate Level Waste
LFCM	Lava-like Fuel Containing Materials
LLW	Low Level Waste
MAS	Magnesium Aluminosilicate
MBS	Magnesium Borosilicate
MSSS	Magnox Swarf Storage Silos
NASA	National Aeronautics and Space Administration

NBO	Non-bridging Oxygen
NDA	Nuclear Decommissioning Authority
NNL	National Nuclear Laboratory
NPD	Neutron Powder Diffraction
PCT-B	Product Consistency Test B
PHWR	Pressurised Heavy Water Reactor
PWR	Pressurised Water Reactor
RTG	Radioisotope Thermoelectric Generator
SEM	Scanning Electron Microscopy
SNF	Spent Nuclear Fuel
TEM	Transmission Electron Microscope
VHT	Vapour Hydration Test
XAS	X-ray Absorption Spectroscopy
XANES	X-Ray Absorption Near-Edge Spectroscopy
XRD	X-ray Diffraction

List of Figures

Figure 2-1. Fission of uranium-235 demonstrating splitting of the atom [15]	22
Figure 2-2. World's first commercial scale nuclear power station, Calder Hall, UK [24].....	23
Figure 2-3. First generation Magnox type nuclear power station, Wylfa, Anglesey [28].....	24
Figure 2-4. Second generation AGR type nuclear power station, Heysham [29]	25
Figure 2-5. Third generation PWR type nuclear power station, Sizewell, Suffolk [30]	25
Figure 2-6. The nuclear fuel cycle [36]	27
Figure 2-7. LLW waste storage containers [56]	32
Figure 2-8. (A) Cross-section of cemented Magnox swarf [64] (B) Cemented wasteform canister [65].....	33
Figure 2-9. Stainless steel HLW canister & Figure 2-10. HLW interim storage facility [66]	34
Figure 2-11. Relative radiotoxicity of SNF as a function of time, adapted from [70]	35
Figure 2-12. Illustration of a GDF design for nuclear wastes [74].....	36
Figure 2-13. Example of the multi-barrier safety system for a GDF [67].....	37
Figure 2-14. Aqueous dissolution mechanisms against time for a glass product.....	39
Figure 2-15. Temperature & pH dependence on glass dissolution (illustrative purposes) derived from [82].....	39
Figure 2-16. First Generation Magnox Storage Ponds, Sellafield [83]	40
Figure 2-17. Chernobyl Unit 4 as of July 2016, taken during site visit.....	42
Figure 2-18. New Safe Confinement for Chernobyl Unit 4 as of July 2016, taken during site visit.	44
Figure 2-19. THORP Product Store for separated plutonium [104].....	45
Figure 2-20. NASA's Curiosity Rover on Mars powered by a ^{238}Pu RTG (Courtesy NASA/JPL-Caltech) [112]	47
Figure 2-21. Enthalpy vs temperature for a glass and crystal; highlighting T_g and T_m	50
Figure 2-22. Alkali-borosilicate glass pseudo-ternary liquidus phase diagram where A_2O is any alkali oxide, adapted from [143].....	52
Figure 2-23. AVH-like glass melter used at the UK vitrification plant	53
Figure 3-1. Magnesium aluminosilicate (left) & magnesium borosilicate (right) pseudo-ternary liquidus phase diagrams [155], [156]	55
Figure 3-2. Heating profile for LFCM samples.....	64
Figure 3-3. Heating profile for Ce_3NbO_7	67
Figure 3-4. Bruker D2 Phaser XRD internals.....	69
Figure 3-5. X-Ray diffraction by a crystal	69
Figure 3-6. Schematic of ISIS HRPD diffractometer	71
Figure 3-7. Selected Area Electron Diffraction TEM	72
Figure 3-8. Usable signals from electron-surface interactions	73
Figure 3-9. Interaction volume from where usable signals are detected	74
Figure 3-10. STA 449 F3 Jupiter schematic from Netzsch [183]	75

Figure 3-11. Gas expansion pycnometer schematic	76
Figure 3-12. XAS experimental set-up schematic (X05LA beamline)	77
Figure 3-13. Schematic of a typical ICP-ES set-up.....	79
Figure 4-1. Dichromatic neodymium doped glass.....	86
Figure 4-2. Powder X-ray diffraction data for Nd corroded waste samples.....	87
Figure 4-3. Powder X-ray diffraction data for Mm corroded waste samples.....	87
Figure 4-4. Backscattered SEM of inhomogeneous MBS-C (Mm) and EDS spectra for the marked points of interest.	88
Figure 4-5. Backscattered SEM image of MAS-C (Nd) showing sample consistency. The small (50 μ m) bubble in the bottom left corner is a relic from the casting process.	88
Figure 4-6. Powder X-ray diffraction data for metallic waste loaded Mm glass samples.....	89
Figure 4-7. Backscattered SEM of MAS-M (Mm) showing $Ce_{1-x}Nd_xO_{2-x/2}$ crystallites and corresponding EDS Spectra.....	90
Figure 4-8. Ce-Nd-B crystals within SEM image of MAS-M (Mm) and corresponding EDS element maps.	90
Figure 4-9. Mg-Al-O crystals within SEM image of MAS-M (Mm) and corresponding EDS element maps.	91
Figure 4-10. SEM image of MBS-M (Mm) and EDS spectra of regions of interest.....	91
Figure 4-11. Powder X-ray diffraction data for metallic waste loaded Nd glass samples.	92
Figure 4-12. BSE micrographs highlighting various morphologies present within MAS-M (Nd). A – BSE image of crystalline phase. B – BSE micrograph of homogenous phase. C – High magnification BSE image of crystalline phase with light and dark phases labelled. D - Associated EDS spectra for the light and dark phases shown in C.....	93
Figure 4-13. BSE images of MBS-M (Nd), exhibiting NdB_6 crystallisation and associated EDS spectra.....	94
Figure 4-14. Collected DTA for samples created in the study, with glass transition (T_g), crystallisation (T_c) and liquidus points (T_l) labelled.....	95
Figure 4-15. Average pH of Nd (left) and Mm (right) samples during PCT-B experiments.....	98
Figure 4-16. Normalised mass loss of B from Nd (left) and Mm (right) samples as a function of time.	98
Figure 4-17. Normalised mass loss of Si from Nd (left) and Mm (right) samples as a function of time.	99
Figure 4-18. Normalised mass loss of Mg from Nd (left) and Mm (right) samples as a function of time.	100
Figure 4-19. BSE micrographs of alteration layers on MAS-C (Nd) glass after 28 days and corresponding EDS maps.	101
Figure 4-20. BSE image of alteration layers on MBS-C (Mm) after 28 days.....	101
Figure 4-21. XRD pattern for Nd doped metallic waste glasses after 28 day alteration.	102
Figure 4-22. XRD pattern for Nd doped corroded waste glasses after 28 day alteration.....	102
Figure 4-23. XRD pattern for Mm doped metallic waste glasses after 28 day alteration.	103
Figure 4-24. XRD pattern for Mm doped corroded waste glasses after 28 day alteration.	103
Figure 4-25. First Generation Magnox Storage Ponds, Sellafield, Cumbria UK [83]	111

Figure 4-26. Powder X-ray diffraction data of MAS and MBS base glasses.....	114
Figure 4-27. Powder X-ray diffraction data of MAS and MBS base glasses loaded with corroded waste simulant.	115
Figure 4-28. Low magnification back-scattered SEM image and close-up EDX spectra showing microstructure and composition within MBS-C; Top EDX spectra for light phase; Bottom EDX spectra for dark phase.	116
Figure 4-29. Back-scattered SEM image showing homogenous MAS-C glass & corresponding EDX spectra; similar results were obtained for both base glass samples.....	116
Figure 4-30. EDX maps for key components of MBS base glass.	117
Figure 4-31. EDX maps for key components of MAS base glass.....	117
Figure 4-32. Powder X-ray diffraction data of samples loaded with metallic wastes.....	118
Figure 4-33. Back-scattered SEM micrographs of MBS-M (left) and MAS-M (right).	118
Figure 4-34. Back-scattered SEM image and EDX spectra showing dendritic crystals within MBS-M; Top EDX spectra for bright crystalline inclusion (A); Bottom EDX spectra for dark glass phase (B).	119
Figure 4-35. Back-scattered SEM image and EDX spectra showing fused crystals within MAS-M; Top EDX spectra for bright crystalline phase; Bottom EDX spectra for dark glass phase. .	119
Figure 4-36. Thermal analysis of samples created in this study showing T_g , T_c and T_1	120
Figure 4-37. XANES plots for each sample (left) and oxidation state versus E_0 energy shift, Error bars +/-0.1 (right).....	121
Figure 4-38. First derivative of XANES data highlighting uranyl.	122
Figure 4-39. pH of all sample solutions over the experimental period.	125
Figure 4-40. Normalised mass loss of boron, silicon, magnesium and uranium ($g\ m^{-2}$) versus time for all waste glass samples.....	126
Figure 4-41. SEM micrographs of MAS-C glass showing alteration layers after 28 day dissolution (top) and EDS spectra of from points A, B and B (bottom).	127
Figure 4-42. EDX maps of MAS-C glass alteration layer.....	127
Figure 4-43. SEM micrograph of MBS-C showing 28 day alteration layer.....	128
Figure 4-44. XRD trace of MBS-M and MAS-M after 28 day alteration experiment.	128
Figure 4-45. XRD trace of MBS-C and MAS-C after 28 day alteration experiment.....	129
Figure 4-46. Post-HIP MBS-1000 sample; surface deformation and discolouration (A) and highlighted glossy black spots (B).....	136
Figure 4-47. Sectioned can from MBS-1000 sample; Blue glass surrounding white powdery material (A) and heavily corroded internal HIP can (B)	137
Figure 4-48. XRD data of calcined simulant Magnox sludge at 600 °C (A) and 1000 °C (B) ..	138
Figure 4-49. XRD data for MBS-600 after HIP synthesis	138
Figure 4-50. XRD for MBS-1000 after HIP synthesis	139
Figure 4-51. SEM micrographs showing SiO_2 phase present in MBS-600 (A) and a Si-Al rich region within MBS-1000 (B). Note the bright spots corresponded to a Fe-Cr-Mo spinel like phase.	139
Figure 4-52. STA of Simulant Magnox Sludge.....	140
Figure 4-53. DTA-TG data from MBS-600	141

Figure 5-1. XRD plot of simulant brown (left) and black (right) LFCM.....	148
Figure 5-2. Back-scattered SEM micrograph of simulant brown LFCM labeling the crystalline phases present.	149
Figure 5-3. EDS maps of key elements in brown LFCM.....	150
Figure 5-4. Powder x-ray diffraction data obtained for simulant Brown and Black LFCM compositions.	157
Figure 5-5. Labelled back-scattered electron images of simulant (a) Brown; and (b) Black LFCM compositions, highlighting phases identified with the aid of EDX and XRD.....	158
Figure 5-6. Back Scattered Electron micrographs of high uranium zircon (chernobylite, (Zr _{0.90} U _{0.10})SiO ₄) within simulant Brown LFCM; (a) agglomerated crystals; (b) EDS data showing incorporation of uranium in the zircon phase; and (c) evidence of zoning within zircon and presence of Zr-rich particles in the centre of the zircon.	160
Figure 5-7. Uranium L _{III} edge XANES data for simulant Brown and Black LFCMs, with reference to uranium standards of known oxidation state, (a) showing full XANES spectra; and (b) linear regression of the extracted normalised edge position of standards and samples.....	162
Figure 5-8. Graphs of N _{Li} for (a) Si; (b) Al; (c) U; (d) Ca; (e) Na; and (f) Mg for Black (■) and Brown (●) LFCM leached in UHQ water at 50 °C.....	163
Figure 5-9. SEM-EDS analysis of Black LFCM after 28 days of corrosion using the VHT method, showing the formation of a spherical alteration phase.	165
Figure 5-10. SEM-EDS analysis of Black LFCM particles samples after 28 days of leaching at 50°C in water.	165
Figure 6-1. XRD pattern acquired from the surface of a pellet of composition Ce ₃ NbO ₇ , post reaction in 5% H ₂ -95% N ₂ for 24h, showing enrichment in CeNbO ₄	175
Figure 6-2. XRD pattern acquired from the surface of a pellet of composition Ce ₃ NbO ₇ , post reaction in 5% H ₂ -95% N ₂ , showing enrichment in CeNbO ₄ , and after 148 h with the surface layer removed.	176
Figure 6-3. Schematic crystal Structure for Ce ₃ NbO ₇ in <i>Cmcm</i> spacegroup (left) and <i>Pmcn</i> (right). Ce(1)O ₈ units are revealed as blue cubes, Ce(2) ions shown by orange spheres and NbO ₆ octahedra represented by green octahedra.	176
Figure 6-4. Electron diffraction pattern obtained in the 0 2 1 plane.	177
Figure 6-5. Final fit of refined structural model for Ce ₃ NbO ₇ in space group <i>Pmcn</i> to neutron diffraction data, showing observed, fitted and difference profiles; tick marks show allowed reflections for Ce ₃ NbO ₇ and CeNbO ₄	178
Figure 6-6. XAS spectra for Ce ₃ NbO ₇ and two reference samples	181
Figure 6-7. Reciprocal magnetic susceptibility for Ce ₃ NbO ₇ over the range 2 K ≤ T ≤ 300 K.	182
Figure 6-8. DTA data (400 – 1670 K) and TGA (400 – 900 K) data for Ce ₃ NbO ₇	183
Figure 6-9. Powder XRD of sample after thermal analysis showing transformation into other indexed phases.	183
Figure 6-10. Structure field map for Ln ³⁺ B ⁵⁺ O ₇ compounds, Grey = Defect fluorite type, Green = Y ₃ TaO ₇ type, Blue = La ₃ NbO ₇ type	186

List of Tables

Table 2-1. Various elemental compositions of LFCM in literature.....	43
Table 3-1. Bounding simulant Magnox wastes	56
Table 3-2. Compositions of batched glass samples	57
Table 3-3. Reagents used in glass research	58
Table 3-4. Synthesis conditions for glass samples	59
Table 3-5. Reagents used for LFCM research	63
Table 3-6. Compositions of batched LFCM samples	63
Table 3-7. Reagents used in preparation of Ce ₃ NbO ₇ sample	66
Table 4-1. Bounding extremes waste composition from FGMSP and MSSS.....	83
Table 4-2. Analysed and batched glass compositions studied.....	84
Table 4-3. Extracted thermal event temperatures for all samples.	94
Table 4-4. Measured density of glass compositions.....	96
Table 4-5. Forward and residual dissolution rates with average pH.	97
Table 4-6. Summary of phases observed in all samples by XRD analysis.....	105
Table 4-7. Bounding waste compositions for FGMSP.....	112
Table 4-8. Analysed glass compositions from ICP-OES and batched compositions in mol%. .	114
Table 4-9. Extracted values for glass transition (T _g), crystallisation points (T _c) and liquidus temperature (T _l).	120
Table 4-10. Extracted E ₀ values and corresponding oxidation state from XANES.	122
Table 4-11. Calculated density of synthesised glass compositions.....	123
Table 4-12. Normalised forward dissolution rates for boron and uranium in g m ⁻² d ⁻¹ with average pH of solution.	124
Table 4-13. Saturation indexes (SI) calculated during the dissolution of waste glass compositions at 90°C in UHQ water.	124
Table 5-1. Synthesized LFCM compositions	146
Table 5-2. Composition of simulant Lava-like Fuel Containing Material compositions (mol %), as batched and as determined by ICP-OES after aqua regia digest of thermally treated samples.	154
Table 5-3. Temperatures of key thermal events within simulant Brown and Black LFCM.	161
Table 5-4. Normalised corrosion rates for elements observed to increase in concentration over 28 day corrosion period.	162
Table 6-1. Rietveld refined structural parameters output for <i>Pmcn</i> (#62) Ce ₃ NbO ₇ from room temperature NPD data; R _{wp} = 5.80%, R _p = 5.37%, χ^2 = 2.995.	179
Table 6-2. Select interatomic bond lengths in Ce ₃ NbO ₇ calculated from refined NPD data; Average Ce BVS: 2.96, Average Nb BVS: 4.84.	180
Table 6-3. Extracted E ₀ values and corresponding oxidation state.	181

1. Introduction – Research Impetus

Since the dawn of the atomic age, radioactive fuel residues arising from civil and military use of nuclear power have, and continue to be, a major issue for the nuclear industry worldwide. The high levels of radioactivity, coupled with the biological toxicity of the fuel residues create hazards that are deemed intolerable in today's society and need urgent attention to clear up and make safe. Fuel residues are often associated with all types of radiation from alpha and beta due to long lived radionuclides such as uranium plus gamma radiation from the many elements present in spent fuel.

A significant number of first generation storage facilities built in the 1950s and 1960s are now decaying due to their age and are in urgent need of attention [1], [2]. There are several such sites around the world that are of concern including the United States Department of Energy (DoE) Hanford site, the French Atomic Energy and Alternative Energies Commission (CEA) Marcoule site and the United Kingdom's Nuclear Decommissioning Authority (NDA) Sellafield site [3]. Each has their own unique problems specific to the types of materials that were handled at the respective facilities, but contain fuel residues ranging from radioactive sludges to separated plutonium. Fuel residues can also be found at sites of nuclear accidents such as at Chernobyl in Ukraine where residues of the destroyed reactor core and fuel can be found in various rooms and shafts [4]. High levels of radioactivity are frequently recorded at all these sites and subsequently they are the highest priority in terms of clean-up operations [5]. This thesis aims to address these issues through thermal treatment with representative simulant materials.

The general background to the nuclear industry in the UK, including how such a varied and diverse amount of radioactive waste came to exist will be explored in the background section, Chapter 2, along with the science behind how nuclear energy is harnessed and utilised. A particular focus will be on the management of problematic spent nuclear fuel residues including how nuclear waste is dealt with in the UK past, future and present. This review of the literature will explore the nature of the sludge wastes and fuel residues, specific to the UK, arising from the First Generation Magnox Storage Ponds (FGMSP) and Magnox Swarf Storage Silos (MSSS) and charts their origin since the early 1950s. These wastes are high in magnesium content, in both metallic and hydroxide form as well as uranium in both its metallic and oxide forms and present a unique challenge to the industry today [5].

Fuel residues from the Chernobyl nuclear disaster are also introduced in Chapter 2 in the form of lava-like fuel containing materials (LFCM) which are crystallised glassy materials made from melted nuclear fuel and reactor structural material [6]. These materials are highly radioactive and present a significant hazard to the decommissioning and clean-up of the Chernobyl site, especially now the New Safe Confinement structure is in place (as of late 2016) [7].

Not all nuclear material is designated as waste however; in the UK plutonium stockpiles are currently considered an asset rather than a liability with potential uses as fuel in advanced reactors such as breeder and fast reactors [8]. Civil plutonium stockpiles, themselves a fuel product and/or residue, decay to produce americium-241 which has many potential uses, from smoke alarms to space batteries [9]. ^{241}Am based space batteries are the planned power source for European Space Agency (ESA) missions beyond the orbit of Jupiter in the form of a radioisotope thermoelectric generator (RTG) [9]. Immobilising the americium in a stable advanced ceramic would be desirable for these applications or for disposal and is also explained in Chapter 2.

Materials used during this research are listed in Chapter 3 alongside the processing conditions required for the synthesis of the glass, glass-ceramic, full-ceramic and dried sludge samples. Techniques for the characterisation of the samples are also detailed and explained from 1st principles in Chapter 3.

Sludge wastes can be very diverse within a single storage pond or silo due to settling of heavier constituents and a combination of intact and partially intact fuel elements [10]. In Chapter 4 immobilisation of non-radioactive and low activity uranium doped simulant sludge waste arising from the FGMSF and MSSS are investigated. Durable glass wastefoms are intended as an alternative to the current cementation plan. The main aims of these projects are to ascertain the effectiveness of vitrifying high magnesium content Magnox sludge wastes at the Sellafield site, whilst analytically comparing the properties of the surrogate materials neodymium, mischmetal (mixed lanthanide metal) and low-activity uranium vitreous products. This chapter will also briefly look into the consolidation of the wet sludge wastes via calcination and immobilisation by hot isostatic pressing (HIPing) with the intention to create a product suitable for disposal. A hot isostatic press (HIP) was used to heat and apply high pressure to the calcined sludge wastes combined with glass formers to create glassy materials containing the radioactive waste components that would then be suitable for disposal.

The synthesis of simulant lava-like fuel containing materials formed during the Chernobyl nuclear disaster is important to allow for assessment of the durability and longevity of real material formed during the nuclear disaster. Results from the synthesis of LFCM are detailed in Chapter 5 with comparison made between the samples produced in this study and those extracted from the analysis of actual samples from the 1990's. The evolution of these materials with time was investigated via alteration experiments under wet and high humidity environments.

Substituting americium for cerium, a novel cerium niobate ceramic was created for potential use as a wastefom or an ^{241}Am space battery and the full characterisation of the new material is detailed in Chapter 6. High temperature solid state synthesis using cold-uniaxial pressing was used to create the ceramic phase with detailed characterisation, including neutron diffraction, performed to determine the single phase nature of the material and to define the lattice parameters and space group of the new material.

Overall conclusions will be collated in Chapter 7 with the key findings of the projects discussed. Chapter 7 will also present recommendations for future work that can be done in this area that will be of potential use to researchers and will hopefully inform the nuclear industries of the United Kingdom and Ukraine of prospective methods to assess and eventually clear hazardous wastes currently residing at Sellafield and in the Chernobyl Unit 4 reactor using simulant materials.

2. Background

2.1. Historic & Current Use of Atomic Energy

The atom is one of the most powerful, and destructive, sources of energy mankind has ever harnessed. German radiochemists Otto Hahn and Fritz Strassmann first discovered the phenomenon of nuclear fission by accident in 1938. Whilst searching for new transuranic elements produced when uranium was bombarded with neutrons, they discovered short lived substances lighter than expected. Instead of producing heavier elements, they had in fact split the heavy uranium atom into the lighter elements barium and krypton something previously thought not possible, see Figure 2-1 [11]. The result was later interpreted by Lise Meitner and Otto Frisch in their 1939 paper naming the process fission and definitively identifying these products as barium and krypton by subtracting the atomic number of barium from uranium [12]. Another paper by Otto Frisch in 1939 showed that the energy liberated from nuclear fission is in the region of 200 MeV and that the element thorium shows similar properties when bombarded with neutrons; this signified the potential of uranium and thorium as an energy source [13]. The realisation of a nuclear chain reaction was first identified by Frédéric Joliot-Curie, Hans von Halban and Lew Kowarski after identifying that the number of neutrons emitted in a fission of uranium is greater than one and hence uncontrolled chain reactions, such as nuclear bombs, or controlled chain reactions, in nuclear reactors, is possible [14].

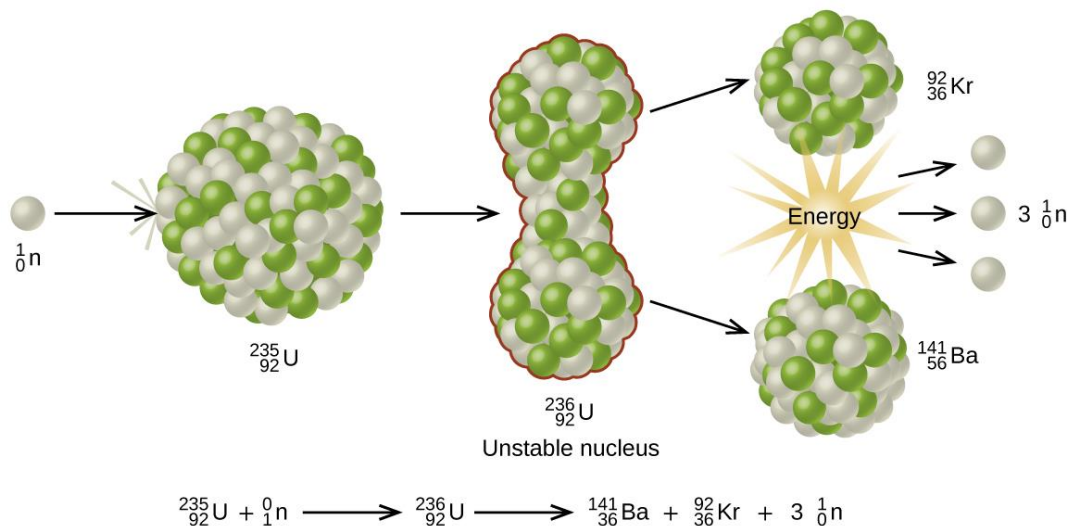


Figure 2-1. Fission of uranium-235 demonstrating splitting of the atom [15]

Only 6 years after the discovery of nuclear fission, the Manhattan Project between the allied powers of Canada, the United Kingdom and the United States of America had succeeded in creating a large scale nuclear chain reaction of plutonium-239; the first atomic explosion at the

Trinity test site [16]. From 1947 the USA, UK, France and Soviet Union were testing nuclear devices and resulting in the arms race of the Cold War which would last until 1991. In July 1941 the UK's MAUD Committee produced two summary reports, titled "Use of Uranium for a bomb" and "Use of Uranium as a Source of Power" [17]. The latter document concluded that controlled fission of uranium could be used to provide energy and that the idea of a 'uranium boiler', or nuclear reactor, was within reach [18]. Heat generated in such a nuclear reactor could be used to boil water and create steam to power a steam turbine generator and the reaction controlled by use of a moderator material such as water or graphite to slow neutrons allowing further fission events and sustaining a chain reaction. This new peaceful civil use nuclear energy was made famous in the "Atoms for Peace" speech by US President Eisenhower before the United Nations General Assembly in 1953 [19]. Nuclear propelled naval vessels such as the submarine *USS Nautilus* or the aircraft carrier *USS Enterprise* were among the first to show nuclear power harnessed for peaceful purposes and opened the door for the civil use of this energy. The icebreaker *Lenin* was the first civil nuclear powered ship to be launched closely followed by the cargo ship *NS Savannah*. Nuclear powered icebreakers continue to be used to this day due to the advantages of not needing to refuel the reactors for long periods of time and the long range that can be achieved, vital in extreme environments such as the Arctic and Antarctic regions [20]. The first nuclear reactor to generate electricity was the Experimental Breeder Reactor 1 (EBR-1) built by the Argonne National Laboratory in Idaho USA which created enough electricity to power four 200 W bulbs in December 1951, later increased to 100 kW [21]. In 1954 the Obninsk reactor Atom Mirny (Peaceful Atom) AM-1 in Russia became the first to supply electricity to a grid with a generating capacity of 5 MWe which was later superseded by the Magnox type Calder Hall Reactors in Cumbria UK in October 1956, the first commercial nuclear power station, with a capacity of 50 MWe, later increased to 200 MWe (Figure 2-2) [22], [23].



Figure 2-2. World's first commercial scale nuclear power station, Calder Hall, UK [24]

2.2. Current Commercial Nuclear Power Reactors & Future Designs

From the late 1950s and early 1960s significant investment into civil nuclear energy programs were underway worldwide, with power stations being constructed in Canada, France, Germany, Italy, Japan, Netherlands, UK, USA and the former USSR states [25]. Four major designs for reactors were researched and built, two using light water as a moderator and coolant, the pressurised water reactor (PWR) and the boiling water reactor (BWR), one utilising heavy water, the pressurised heavy water reactor (PHWR) and one using CO₂ gas as a coolant and graphite as a moderator (GCR) [25]. There is also the USSR designed light water graphite moderated reactors (LWGR). The USA pioneered the use of the PWR and BWR designs with the UK leading GCR projects and Canada pursuing the PHWR. In the UK carbon dioxide cooled reactors moderated with graphite blocks were first implemented in the form of the Magnox fleet of power stations built from 1953 and of which one still remains operational (as of 2015) in Wylfa, North Wales UK, see Figure 2-3. The second generation of the GCR designs was the advanced gas-cooled reactors (AGR) which still operate in the UK today, generating approximately 20% of the nation's electricity (Figure 2-4) [26]. The UK has 7 AGR power stations with two reactors each, situated along the coastline, becoming operational from 1976 with electricity generation planned to continue until the late 2020's [27]. The UK also has a third generation nuclear power station sited at Sizewell and is of the most common design worldwide, the PWR, which became operational from 1996, the last nuclear power station built in the UK to date (Figure 2-5) [20].



Figure 2-3. First generation Magnox type nuclear power station, Wylfa, Anglesey [28]



Figure 2-4. Second generation AGR type nuclear power station, Heysham [29]



Figure 2-5. Third generation PWR type nuclear power station, Sizewell, Suffolk [30]

Recent demand in low carbon electricity and policies curbing the use of fossil fuels has pushed the world into a “nuclear renaissance”. The UK government now has plans for new reactors at several sites across England and Wales (Scotland has decided against future nuclear power) in order to meet the gap from closing down coal power fire stations due to environmental policies such as the European Union’s Large Combustion Plant Directive [31]. An EDF Energy led consortium plan to build new power stations with each consisting of two Areva European Pressurised Reactor (EPR) light water reactors at Hinkley Point in Somerset and Sizewell in Suffolk. A Hitachi led program called Horizon Nuclear Power plan to build two Hitachi Advanced Boiling Water Reactor (ABWR) at sites in Wylfa Newydd in Wales and Oldbury, Gloucestershire, and a Toshiba lead company NuGen plan to build three Westinghouse AP1000 PWRs at Moorside in Cumbria, close to the Sellafield site [32].

The next cohort of civil nuclear power stations to be built from 2030 onwards will likely be of a fourth generation reactor design, promised to bring enhanced safety and reliability, low cost electricity, proliferation resistance and reduced waste or even waste utilisation [20]. Six designs have been chosen as worthy of further potential:

Gas cooled fast reactors (GFR)

- Lead cooled fast reactors (LFR)
- Sodium cooled fast reactors (SFR)
- Molten salt reactors (MSR)
- Very high temperature gas cooled reactors (VHTR)
- Super-critical water cooled reactors (SCWR) [20], [33]

Fast reactors are capable of using fast neutrons to fission uranium, plutonium and trans-uranic elements without the use of a moderator to convert fast neutrons to thermal neutrons. The use of ^{239}Pu or highly enriched uranium, ^{235}U , is preferred due to the larger neutron capture cross section to fast neutrons compared to thermal neutrons. The ability of fast neutrons to fission trans-uranic elements and transmute them to shorter lived elements has meant a resurgence in interest into gas, lead and sodium cooled fast reactors as a means of reducing the amounts of long lived radioactive waste produced supporting the safety case for disposal [34].

MSRs have been proposed as a Generation IV reactor type due to the theoretically enhanced passive safety by utilising molten liquid salt as both the fuel and coolant. Moderating is performed by the graphite core and extraction of fission products is achieved at a processing plant attached to the reactor. Refuelling can be done on load since fission products are removed and new fuel added simultaneously which adds to the cost effectiveness of this reactor type. Passive safety is implemented in the form of a drain plug which is melted at elevated temperatures such that in the event of accident, the fuel is drained from the reactor killing the chain reaction [33].

VHTRs are an improvement upon the UK's current Generation II AGR reactors by using graphite moderated core with helium gas as a coolant. Fuel particles are coated in graphite shells allowing for higher operating temperatures than conventional reactors offering greater electricity generating efficiency. The excess heat generation could also be used for heat intensive applications such as hydrogen gas generation, useful as a future energy source in the automotive industry.

SCWRs enhance upon the current generation of PWRs but with the water heated to supercritical temperature and pressure providing greater thermodynamic efficiency and enabling the use of electrical turbines commonly used in fossil-fuelled power stations.

2.3. The Nuclear Fuel Cycle

The almost closed cycle in which uranium is used as a fuel is termed the nuclear fuel cycle. The process is one of the most advanced and technically demanding industrial cycles involving various stages of mining, conversion, enrichment and fabrication before the fuel can be used. These first processes are termed the front-end of the cycle with the steps to remove the fuel, reprocess and dispose of the material termed the back-end. The possibility of reusing the spent fuel material after reprocessing makes this industrial process a true cycle in which nuclear material can be used repeatedly, see Figure 2-6. As a large proportion of the uranium remains unused after discharge from the reactor, typically 95% and residually enriched, it can be recycled to produce more fresh fuel. This has the added bonus of reducing the quantities of highly active material to dispose of reducing disposal costs but does require complex and challenging industrial processes [35].

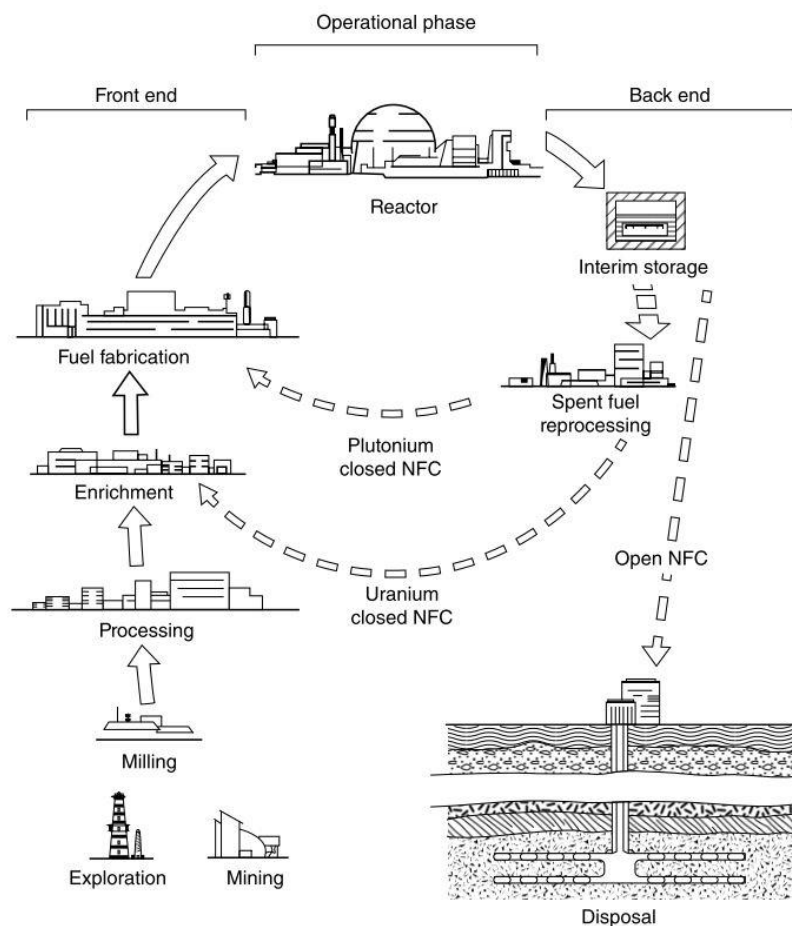


Figure 2-6. The nuclear fuel cycle [36]

2.3.1. Mining

Uranium, first discovered by Klaproth in 1789 [37], is the 48th most abundant element in the Earth's crust at approximately 2 ppm making it 10 times more abundant than silver and mercury put together [38]. Up to 435 Bq/kg of ²³⁸U can be found in coal, up to 10% of which may be released into the local atmosphere and found within soils near fossil fuelled power stations or fertiliser plants due to emissions containing soot or ash [35], [36], [38], [39]. The majority of uranium ore is in the form of the mineral uraninite, or pitchblend, in the form of UO₂ however it is also found in many other minerals such as coffinite, brannerite, uranothorianite, tobernite and autunite [25]. Over 88% of the world's identified resources of uranium reside in only 10 countries, with the majority (24.1%) in Australia, Kazakhstan (17.2%) and Canada (9.2%) [25]. There are three main ways of extracting the uranium ores from the ground, open-pit mining, underground mining and in-situ leaching [40]. If the ores are located near to the surface then traditional open-pits are dug into the ground, such as those used for copper mining. After the extraction and the pits are closed, the topsoil and waste is used to fill the pit, but still has a significant impact on the surface environment [41]. More akin to coal mining, deep uranium deposits can be extracted by creating roadways and shafts into the overlying material which has less of a surface impact than open-pit mining, but at a much higher cost so only used when high grade ore is present [41]. The third mining type, in-situ leaching, requires the injection of an acidic leaching solution into the ground at the depth of the uranium deposit and pumping the solution back up from surrounding wells [42]. The surrounding rock must be permeable to the leaching solution such that it can reach the ore and leach out the uranium. This technique is only of use in arid conditions where no drinking water is extracted from the ground due to the impact this method has on the subterranean environment. With any of these mining methods, the ore or leachate must be milled upon extraction and the uranium containing material separated from its surrounding host or leachate [25]. The output of the milling process is concentrates consisting of usually uranates such as Mg₂U₂O₇ or oxides such as UO₂, UO₃ or U₃O₈ which is referred to as "yellowcake" [25].

2.3.2. Conversion

Conversion of the uranium concentrates is required to create metallic uranium, used for Magnox fuel, or into a gaseous form for isotopic enrichment (See Section 2.3.3). In the gaseous conversion process, the "yellowcake" or other uranium concentrates are converted into the gaseous UF₆ which is transported to the enrichment site [18], [20], [25].

2.3.3. Enrichment

Natural uranium consists of two main isotopes of uranium, ~99.3 % ^{238}U and 0.7 % ^{235}U [43]. A sustained chain reaction with natural uranium is difficult due to the very small amount of fissile isotope ^{235}U but can be achieved with graphite or heavy water reactors such as the Magnox GCRs or Canadian PHWRs [44]. To reduce the costs of acquiring heavy water or the use of graphite the nuclear fuel can be enriched; whereby the ^{235}U content is increased whilst the fertile ^{238}U content is reduced. The ^{238}U isotopes capture many of the neutrons created in the chain reaction, whilst ^{235}U isotopes will fission after a neutron is absorbed, and hence are preferred in greater quantities in order to extract more energy. Two main methods for the isotopic enrichment of natural uranium exist, gaseous diffusion or ultracentrifugation [45].

Gaseous diffusion relies on the mass of the $^{235}\text{UF}_6$ being slightly lighter than that of $^{238}\text{UF}_6$ such that under high pressure in a semi-permeable vessel the lighter constituents of the gas will preferentially move towards the outside of the vessel and pass through the semi-porous membrane more so than the heavier constituents resulting in a content of UF_6 fractionally more enriched in ^{235}U than before. To increase the fraction of the fissile component the process is repeated with the slightly enriched component in a cascade and each time the quantity of ^{235}U is increased until it reaches the desired enrichment, typically between 2 and 5 % [45].

Ultracentrifugation also relies on the difference in mass between the isotopes of uranium. The gaseous UF_6 is introduced to a centrifuge where the gas is rotated; this creates a gravitational pressure/force gradient from the centre of the vessel towards the periphery where the force is greatest. Centrifugal forces cause the heavier isotopes to collect on the edge whilst the lighter ^{235}U slowly migrates towards the centre where it can be extracted. Again, the amount of the fissile isotope separated is very low, so large numbers of centrifuges are required to achieve the enrichment needed [45].

2.3.4. Fuel Fabrication

Once the enrichment level required has been reached, the UF_6 is converted into UO_2 as a ceramic for use as the nuclear fuel, or reduced to U metal for use in Magnox reactors. Ceramic based UO_2 type fuel is used in PWR, BWR and AGR designs where the UO_2 is pressed into pellets, the exact shape and size of which depends on the type of reactor. Pellets of fuel are loaded into long thin fuel pins which are sealed to prevent the release of radionuclides created during burnup in the reactor, this fuel cladding also serves to prevent corrosion of the fuel and provide a heat exchange surface. These fuel pins are assembled together in groups to form a fuel assembly which can then be loaded into the reactor core for use over several years. The choice of cladding material varies between reactor types with the most dissimilar being the Magnox (magnesium non-oxidising) alloy used in the UK's first generation nuclear power

stations, composed of 99% Magnesium and 1% Aluminium. PWR fuel cladding is often an alloy called zircaloy-4, a zirconium alloy including tin or niobium due to the improved corrosion resistance in water compared to magnesium alloys whilst BWRs use zircaloy-2 cladding [25], [39].

2.3.5. Reactor Use

A fresh fuel assembly can remain in a nuclear reactor for several years before the concentration of ^{235}U becomes too low to sustain chain reactions efficiently. Typically, over 90% of ^{238}U remains in the fuel when it is removed due to the build-up of neutron absorbing components and the reducing amount of fissile material rendering further use uneconomical. This fuel is now spent, and termed spent nuclear fuel (SNF), which needs to be handled with care due to the high activity caused by irradiation and the build-up of new elements such as plutonium and short-lived minor actinides.

2.3.6. Interim Storage & Reprocessing

Interim storage and/or reprocessing are the back end of the nuclear fuel cycle where choices are made as to the future of the SNF. The fuel is first stored underwater to allow for cooling and the short lived isotopes to undergo nuclear transmutation, before it is transported to either the reprocessing site or disposal facility. Current UK practice, along with France, Japan and Russia, is to reprocess all spent nuclear fuel at the Sellafield site, such that SNF from reactors across the country is sent to the Thermal Oxide Reprocessing Plant (ThORP) facility for further processing and recycling [46]. Magnox SNF is reprocessed in the Magnox Reprocessing Separation Plant, with operations due to conclude with the reprocessing of all Magnox fuel by circa 2020 [47]. ThORP operations are expected to conclude in late 2018 with the completion of all reprocessing contracts [48] after which SNF will be used in an open fuel cycle where the material will be placed into interim storage after discharge from the reactor. Long-term/final disposal of SNF will involve the placement into geologically deep; engineered facilities (see section 2.4.2).

In a closed nuclear fuel cycle, or one in which SNF is reprocessed, the plutonium, uranium extraction (PUREX) process is the predominant industrial process by which the plutonium content built up in SNF is separated from the reusable uranium [25], [49]. In this process transport flasks containing SNF are opened under water and the fuel elements removed. These are then reduced in size fraction by cutting into small chunks and dissolved in nitric acid to separate the components and where the oxidation states are controlled to U (VI) and the plutonium to Pu (IV) [39]. This is extracted leaving behind a waste stream of fission products

which is scrubbed and disposed of separately as radioactive liquor. The plutonium is reduced to the Pu (III) oxidation state which is extracted leaving behind a pure uranium stream [35]. The plutonium is transferred to a secure storage facility and the uranium made available for re-enrichment and reuse as nuclear fuel. The radioactive liquor contains the remaining ~3% of the SNF consisting of fission products which contribute to the majority of radioactivity and heat generating ability. Separated plutonium is stored securely due to the proliferation risk posed whilst the uranium can be re-enriched and used to form new fuel. The main advantage of reprocessing is the significant volume reduction in waste to be disposed, since over 90% of the ^{238}U remains in SNF, resulting in fewer costs for final disposal and the separation of the potentially useful plutonium (See section 2.7.1) [50]. Separated plutonium can be combined with uranium and utilised in a mixed U-Pu oxide fuel (MOX) for use in a nuclear reactor, as is the case in France [51]. The low content of plutonium (up to 30%) is used as the fissile component and can be combined with natural uranium and allow the reactor to run efficiently without enrichment of the uranium. This step allows for nuclear material to be recycled reducing the amount of waste that is generated which needs to be sent for final disposal.

An open fuel cycle involves the ‘once through’ use of material in that no reprocessing takes place (see Figure 2-6). This is the preferred choice in several nations such as Canada, Finland, Germany, Spain, Sweden and the USA [46]; including the UK from 2018. The UK Government have specified that SNF from any new UK nuclear power station would not be reprocessed and instead proceed for direct disposal, citing availability and low cost of uranium on the world market [52]. Multi-barrier principles are often employed in reducing the risk from nuclear waste, with transport containers or casks often being the last level of protection forming a highly durable engineered barrier to the movement of material outside the containment.

2.4. Nuclear Waste Management

The phrase “*With great power comes great responsibility*” is often used in the nuclear industry as although the power created from atomic energy can be massive, the duty of handling the long lived radiotoxic waste it produces is also a great responsibility that must be appropriately dealt with. In the UK, nuclear waste is divided into different categories depending on activity and heat generating ability and is managed very differently, as highlighted in the sections below.

2.4.1. Waste Classification and Volume

Low Level Waste (LLW)

LLW is defined as nuclear material having a radioactive content less than 4 GBq/te from alpha radiation or 12 GBq/te from beta or gamma radiation [53]. This waste is generated from various activities such as medical, research, industry and military and although it represents more than 90% of the UKs inventory by volume, it only accounts for less than 0.1% of the radioactivity [54]. Currently this waste is compacted and encapsulated in cement before disposal in steel containers at the LLW repository near the village of Drigg, Cumbria, a shallow subsurface disposal facility (Figure 2-7) [55]. Very low level waste (VLLW) can often be disposed via standard, civil landfill sites. The waste management plan for LLW is not expected to change in the interim since this is a well-established process however longer lived LLW would require storage in a deep geological disposal facility (see section 2.4.2).



Figure 2-7. LLW waste storage containers [56]

Intermediate Level Waste (ILW)

Waste that exceeds the limits set on LLW, but not excessively heat generating and not requiring heat to be factored into design of storage/disposal facility, is termed ILW [57]. This type of nuclear waste is predominantly generated from the decommissioning of legacy nuclear facilities but also from the reprocessing of nuclear fuel and from general operations of nuclear facilities [36], [58]. A significant volume of this type of waste exists from legacy operations at the Sellafield and Dounreay sites such as sludges and spent fuel cladding as well as a small amount from hospitals, research labs and the defence industry [59]. ILW is typically encapsulated in cement within stainless steel drums or boxes (Figure 2-8) and kept at interim storage facilities [55], [60]. As of the 2013 & 2016 UK waste inventory, ILW constitutes 6.4% of all radioactive waste volume at 290,000 m³, although this value is expected to rise due to further decommissioning of defunct facilities and continued reprocessing of SNF [61], [62]. No final disposal route for this waste category exists although plans are for transfer to a geological disposal facility (GDF) once the capability exists [58]. Current interim storage methods for sludges and other hazardous wastes include removal from current ponds and silos for transfer to new engineered storage facilities (See section 2.5) [63].



Figure 2-8. (A) Cross-section of cemented Magnox swarf [64] (B) Cemented wasteform canister [65]

High Level Waste (HLW)

HLW is the most hazardous category into which nuclear waste can be placed due to the temperature creating problems for disposal. HLW consists of the main fission products from uranium and plutonium burn-up. This waste is often in the form of radioactive liquor from the reprocessing of SNF and represents around 95% of the radioactivity of nuclear waste in the UK but is less than 0.1% of the total volume [61]. As of 1st April 2016, 1,150 m³ of this waste was

packaged into 7,650 containers [62]. These wastes emit intense radioactivity for tens of thousands of years and are a key focus of Sellafield and the NDA. UK HLW, as with most countries, is stored as a highly active liquor which is evaporated, or calcined, and vitrified into a solid, dense glass wasteform which is both chemically and physically durable. The molten vitrified waste is cast into 150 L stainless steel canisters (Figure 2-9) and sealed by remote welding. The design is such to allow for remote handling and manipulation to reduce the worker hazard. The sealed vitrified HLW canisters are currently stored at the Sellafield site in engineered, convection cooled vaults (Figure 2-10) where they will remain for up to 50 years before disposal. As with ILW, no final disposal option exists for HLW and hence the waste will remain in interim storage until a suitable disposal option is decided upon and implemented [60].

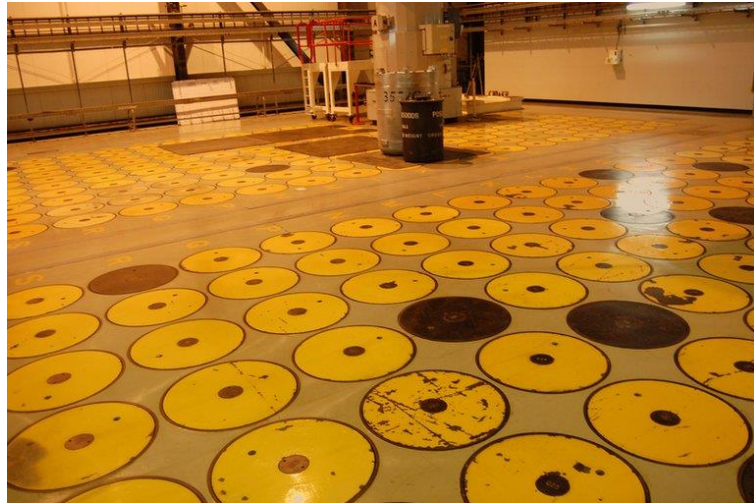


Figure 2-9. Stainless steel HLW canister & Figure 2-10. HLW interim storage facility [66]

Spent Nuclear Fuel (SNF) & Exotic Materials

This class of material is not currently deemed as waste as there is potential future use, however, if it was determined that it would have no realistic application, it would become waste and hence be assigned a waste management scheme [67].

SNF still contains approximately 93% ^{238}U , 1% ^{235}U and 1% ^{239}Pu by weight, all of which are currently considered an asset [68]. The uranium and plutonium can be extracted via reprocessing and the uranium used to create more nuclear fuel whilst the plutonium can be used to form MOX, or as a potential source of ^{241}Am for the European Space Agency (ESA) radioisotope thermoelectric generators (RTG) programme (See section 2.7.1). UK separated plutonium is currently stored on the Sellafield site whilst awaiting an application [69]. Currently SNF can be either reprocessed or stored for direct disposal.

Exotic materials includes items such as MOX fuel elements and associated material, highly

enriched uranium as well as wastes from the decommissioning of nuclear submarines. Material created during nuclear accidents can also be classed as ‘exotic’ such as damaged spent fuel and lava-like fuel containing materials from Chernobyl, see section 2.6. These materials are non-standard and often require specialist waste management schemes which differ to those for LLW, ILW and HLW.

2.4.2. Long Term Waste Management

To date, reprocessing and long term disposal remain the exclusive solutions to managing the volume of nuclear waste. With reprocessing, highly active liquors are produced that require vitrification and storage, therefore long term disposal is the key focus of many national nuclear agencies around the world. As seen from Figure 2-11, circa 10^6 years are required for SNF (actinide content) to reduce in activity to that of background, natural uranium ore. These radioactive materials must remain safe and isolated from the environment for at least this length of time.

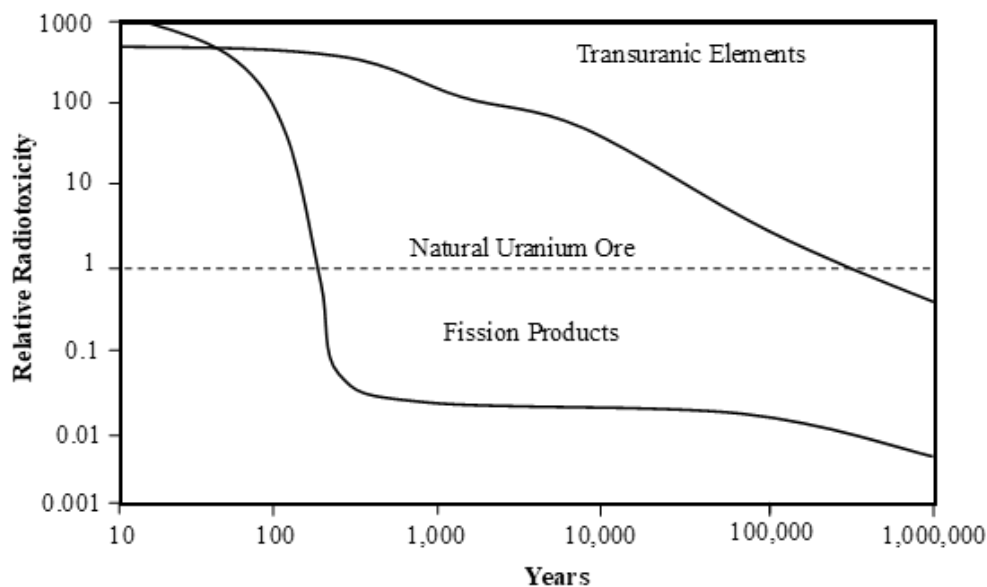


Figure 2-11. Relative radiotoxicity of SNF as a function of time, adapted from [70]

Many alternative solutions to long term disposal have been touted, and discounted in the past, including placement of waste canisters at subduction zones beneath the Earth’s crust, space disposal and placement in the deepest oceanic trenches [71]–[73]. Each of these concepts has advantages and disadvantages, for instance placement within a subduction zone has the advantage of waste packages eventually becoming absorbed into the Earth’s mantle and removed from the biosphere. Unfortunately, the fate of the waste would largely be unknown and there is possibility of re-release of the material back into the biosphere through geological events such as volcanism. Placement on the deep sea floor has the advantage of placing the

waste where there is little to no animal or plant life and away from human interference however this has already been made illegal by international treaties. When the containment barriers eventually breakdown, waste would enter the water and, although diluted, potentially be transported to the biosphere and through various food chains. Space disposal, either in near earth orbit, placement on the moon or destruction within the sun has been proposed several times, having the advantage of removing the hazardous material from Earth completely and, in the case of sending waste to the Sun, removing it forever. Space travel and rocket launches are inherently dangerous however and there is significant risk of a launch failure or accidental re-entry in which the waste material would be spread over a wide area causing significant widespread contamination rendering this means of disposal impossible. The risks associated are still a concern for the launching of ^{238}Pu radioisotope generators on NASA missions and results in the advanced design of packages containing radioactive material to mitigate these risks (See Section 2.7.1).

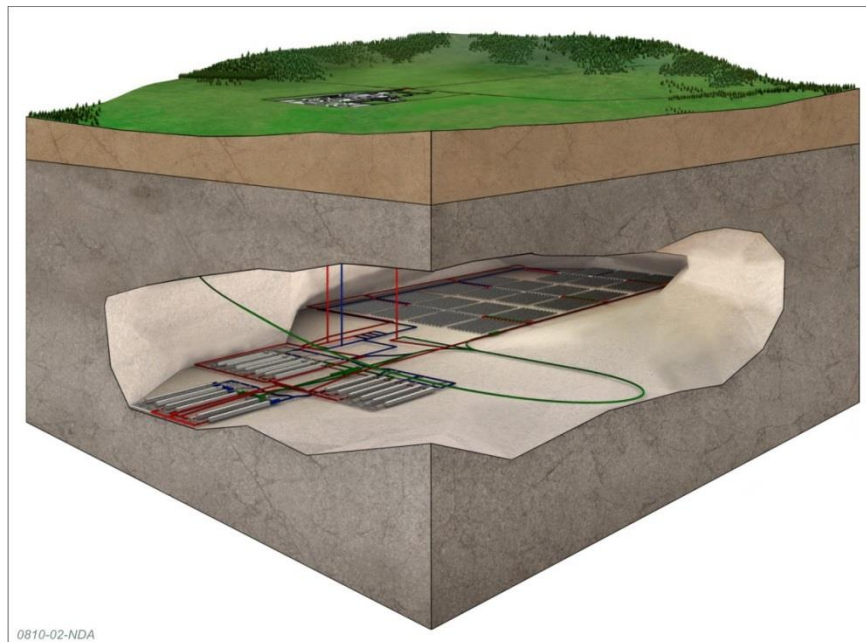


Figure 2-12. Illustration of a GDF design for nuclear wastes [74]

Long term disposal of nuclear waste is a management practice that involves the isolation of nuclear waste from the biosphere for circa 10^6 years. One way to ensure the waste remains isolated for this duration is the use of a multi-barrier concept deep below the Earth's surface within a geological disposal facility (GDF), see Figure 2-12 [67]. The multi-barrier approach is the key to the GDF design, as highlighted in Figure 2-13. With this approach, the waste will be isolated from the environment via multiple layers of protection. Initially the waste will be immobilised or encapsulated in the wastefrom itself, anticipated to contain the waste for the period of time in which it is deemed hazardous [75]. Surrounding this is the waste package in which the wastefrom is placed, normally a stainless steel canister or drum which is used for transport. The waste package is placed in a vault which is surrounded by the first of 2 engineered barriers, a buffer material that protects the waste packages from ground movement

and limits the mobility of radionuclides if they escape the first 2 barriers. The second engineered barrier is the structure of the GDF itself which is built within the last barrier, the ground or lithosphere itself. A GDF is designed to be built hundreds of meters below the ground in a stable geological rock formation which will act as the final barrier where ground water flow is expected to be very low such that any escape of radionuclides from the waste will take hundreds of thousands of years to reach the biosphere, by which time, radioactivity will have reduced to that of background levels [67].

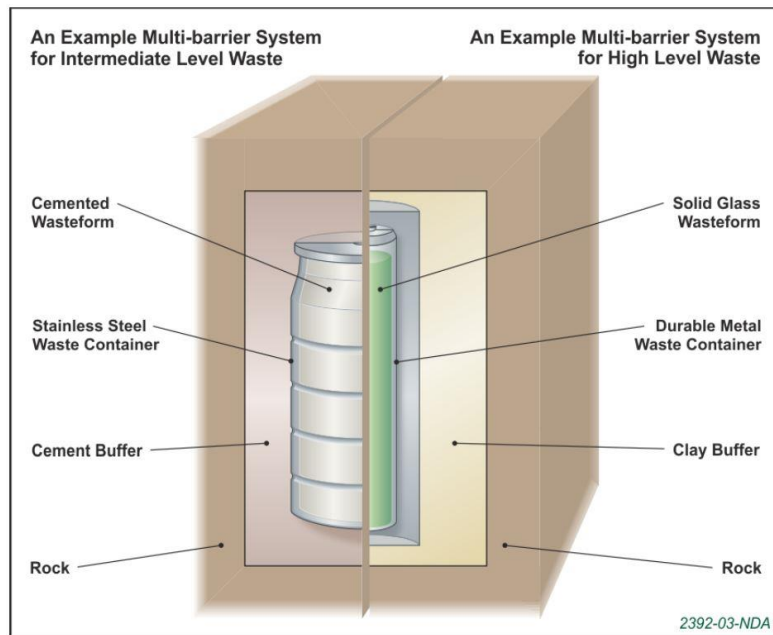


Figure 2-13. Example of the multi-barrier safety system for a GDF [67]

LLW, ILW and HLW packages will be handled and disposed of via different means [75]. UK LLW is currently stored on the Drigg site in Cumbria in near surface disposal as cemented products, however, some specific longer lived LLW will be consigned to a GDF once completed. Cemented ILW packages will be packed in close proximity within a GDF and once the ILW vault is at capacity, will be covered and sealed with a cement buffer or back-fill material as seen on the left side of Figure 2-13. Vitrified HLW and possibly SNF will be separated from ILW and LLW, due to the heat created, and surrounded in a clay buffer or back-fill material, most likely bentonite (see right hand side of Figure 2-13). Cement cannot be used with HLW as the heat generated will drive off the water used in cement hydration causing severe dehydration and cracking, providing a pathway out of the engineered barrier. A collocation GDF design for HLW and ILW is the UK's preferred option for long term disposal as it avoids the cost of building two separate expensive facilities and has a lower environmental impact. A second GDF has not been ruled out however [67].

2.4.3. Wasteform Alteration

Once emplaced within a GDF, or other waste disposal concept, there is concern that alkaline cement leachate from the construction of such disposal systems could increase the corrosion and dissolution of vitrified materials [76]. Over extended time periods, vitreous wasteforms in the presence of water will undergo alteration and potentially release radioactive material from the disposal facility into the wider the environment. Therefore, the durability of such wasteforms to alteration and dissolution is of great significance to the planning of a nuclear waste disposal facility [77].

Several processes are responsible for the alteration and dissolution of glass in the presence of water, including hydration, ion exchange, or inter-diffusion, hydrolysis and precipitation [77]. These factors are dependent on the properties of the glass and the alteration solution. Five distinct regions of dissolution of a glass can be determined, although 4 of which are a short term and relatively fast acting; these distinct regions are shown in Figure 2-14. Stage I of dissolution is dominated by inter-diffusion of water into the glass via ion-exchange with any alkali glass modifiers such as sodium, resulting in a silica rich region, and an increase in the local pH of the solution due to the presence of the alkali material.

Stage II follows due to the increased pH causing hydrolysis of the glass network, breaking Si-O bonds, and the co-precipitation of the hydrated phases on the glass surface forming a gel-like layer of silicon and other glass components. The hydrated gel layer is amorphous and can act as a passivation layer to prevent further alteration of the glass.

The glass enters Stage III with a transition from high rates of dissolution to a residual rate (Stage IV). Two main reasons for the slowing of the alteration have been proposed, the gel layer forming a passivation layer for further alteration, and solution saturation (assuming static conditions) [78]–[80]. A potential alteration rate resumption is postulated (Stage V) due to the precipitation of secondary phases out of solution causing a deviation in solution saturation and/or due to the precipitated phases destabilising the gel layer [81].

Alteration of glass is dependent on the test conditions such as pH of the alteration solution and the temperature in which the test occurs; however, the effect of these conditions varies according to glass composition. Figure 2-15 shows the effect of temperature and pH on the initial glass dissolution rate such that increased temperatures lead to increased rates of dissolution. It can also be observed from Figure 2-15 that high or low pH causes an increase in glass dissolution; these effects can be used to accelerate the alteration of nuclear waste glasses such that long length scales can be simulated in the laboratory using pH and temperature alone.

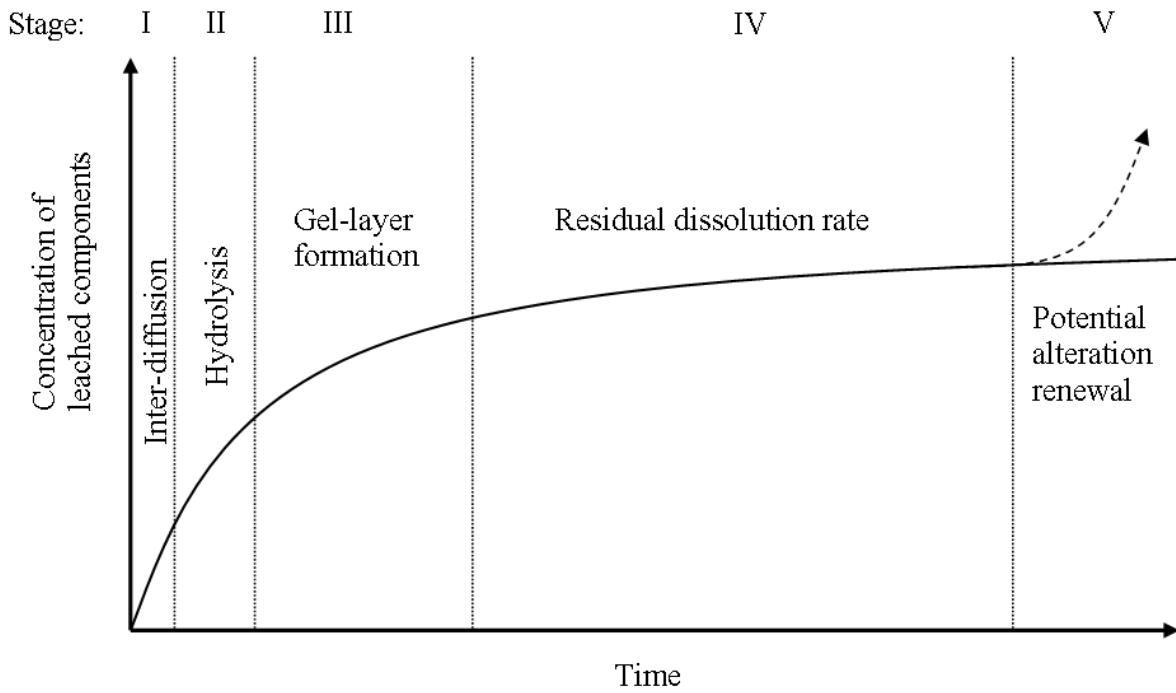


Figure 2-14. Aqueous dissolution mechanisms against time for a glass product

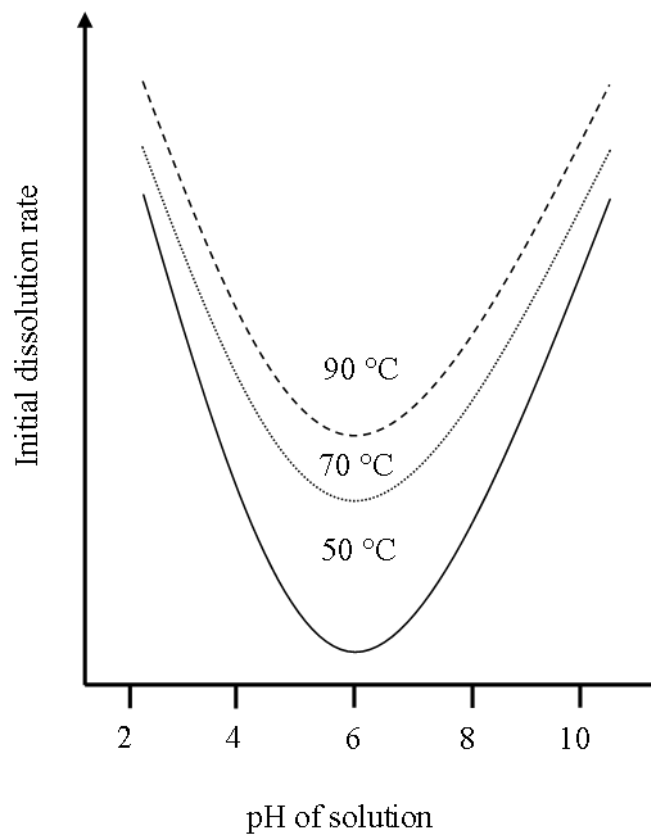


Figure 2-15. Temperature & pH dependence on glass dissolution (illustrative purposes) derived from [82]

2.5. First Generation Magnox Storage Ponds & Silos

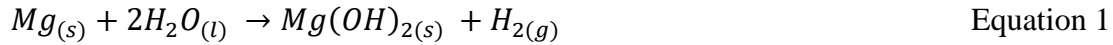
The UK operated first generation Magnox nuclear reactors for electricity and plutonium production with the opening of Calder hall, the world's first commercial nuclear power plant, in 1953 [23]. The last of the Magnox reactors to shutdown was Wylfa in 2015. These first generation graphite moderated, carbon dioxide cooled reactors used natural, unenriched uranium metal fuel clad in a **magnesium non-oxidising** (Magnox) alloy [25], [39]. Although all Magnox reactors are now in the process of being decommissioned, wastes generated during their operation continue to pose a significant radiological risk, particularly the sludges and swarf material found in the First Generation Magnox Storage Ponds (FGMSP), see Figure 2-16, and Magnox Swarf Storage Silos (MSSS).



Figure 2-16. First Generation Magnox Storage Ponds, Sellafield [83]

Magnox SNF is currently reprocessed, in a similar procedure to the ThORP plant, to recover uranium and plutonium at the Magnox Reprocessing Plant located at Sellafield. These operations are expected to continue until 2020 by which point all Magnox SNF should have been reprocessed [61], [63]. Magnox SNF arriving at Sellafield was initially stored in the FGMSP, open air water-filled cooling ponds, prior to reprocessing as seen in Figure 2-16. Sheared cladding created during the reprocessing stage was also stored underwater in the MSSS. SNF was intended to remain underwater for short periods of time whilst waiting for reprocessing, the water acting as radiation shielding and to reduce the risk of fire from the combustible Magnox cladding. Due to industrial action by coal miners during the 1970s and 1980s, electricity production, and hence throughput of nuclear fuel, at Magnox stations was increased to in order to 'keep-on-the-lights'. This increased throughput led to a build-up of SNF arriving for reprocessing at the FGMSP. Lengthy shutdowns caused by downtime at the reprocessing facility also led to a build-up of SNF resulting in storage for periods longer than

originally anticipated [39], [63], [84]. The increased storage time led to considerable corrosion of the reactive Magnox cladding and uranium fuel forming a radiologically hazardous layer of magnesium hydroxide sludge on the bottom of the cooling pond [85]. Since Magnox is composed of 99% magnesium, it can be assumed the corrosion proceeds as per Equation 1 producing magnesium hydroxide sludge and hydrogen gas.



Magnesium hydroxide $Mg(OH)_2$ is a white coloured inorganic compound with a low solubility in water and a decomposition temperature of 350 °C, yielding the oxide MgO [86]. This material forms a contaminated sludge layer that settles on the bottom of the FGMSP and MSSS which likely has the inclusion of corroded uranium phases from the corrosion of metallic uranium fuel. Reaction of uranium metal with water has shown to produce UO_2 and hydrogen gas, via the process shown in Equation 2 below [87].



X-ray diffraction analysis of similar sludges formed from corrosion of metallic uranium at the Hanford site in the USA identify various uranium phases including UO_2 , U_4O_9 , U_3O_7 , U_3O_8 and hydrated uranium oxide phases [87]. Higher uranium oxidation indicates a greater degree of corrosion of the metallic fuel.

The NDA UK Radioactive Waste Inventory datasheets indicate around 3,148 m³ of ILW sludge is present in the storage ponds and silos at Sellafield, requiring extensive decommissioning to reduce the hazard posed [88]–[90]. Due to poor state of repair, Magnox sludge in the FGMSP will be retrieved and placed into interim storage within new engineered facilities, the Sellafield Sludge Plant 1. No final treatment route has been decided for this waste. MSSS waste remediation involves retrieval and encapsulation in a cementitious wasteforms, consistent with treatment of other ILW streams [63]. A Silos Direct Encapsulation plant has been constructed at Sellafield to this effect [63].

Research into a safe treatment route for the ILW Magnox sludge has been explored in Chapter 4 along with an alternative method to cementation for the MSSS wastes which could effectively combine both waste streams with one processing solution.

2.6. Chernobyl Lava-like Fuel Residues

April 1986 saw the explosive meltdown of the Chernobyl Unit 4 reactor in Ukraine (see Figure 2-17), causing 31 deaths and potentially many more due to widespread contamination, spread a large part of Europe and the former USSR [39]. The incident was caused by a loss of control of the reactor during an experimental power failure test, due to human operator error and reactor design [91]. The power failure test was intended to determine if, during a power outage, the slowing turbines could power emergency cooling pumps long enough for back-up systems to enable and take over the operation of pumps and other back-up systems. The speed of the turbines had to be increased to maximum before the test could begin and hence control rods were removed from the reactor core to enable more power to be created [92]. This was carried out without the knowledge of the reactor operation and safety team and subsequently more control rods were removed from the core than was considered safe and the reactor's power began to surge. During this time it was apparent the slowing down turbines were not sufficient to power the emergency cooling pumps causing the temperature in the water cooled graphite moderated reactor to increase rapidly. The Chernobyl reactor was a RBMK-1000 design which had a positive void coefficient which allowed the reactivity of the core to increase with any voids in the coolant [92]. The rapid increase in temperature of the coolant caused the water to quickly flash to steam creating voids which accelerated further the number of fission events in the core and splitting open fuel pins before causing an explosion of the core [91]. A second, more powerful explosion occurred soon after resulting in the destruction of the reactor building, lifting a circa 1000 ton steel cover plate in the process, and exposing the core to the environment and atmosphere [93]. Upon reacting with the oxygen in the air, the hot graphite moderators set alight acting to pump various radionuclides such as ^{137}Cs and ^{131}I into the atmosphere [91].



Figure 2-17. Chernobyl Unit 4 as of July 2016, taken during site visit.

In the preceding explosion, the temperature was such to cause melting of the uranium dioxide and zirconium fuel cladding with temperatures in excess of 2600 °C [7]. The melted fuel and cladding breached the reactor containment vessel and interacted with structural materials from the building such as steel and concrete, forming a corium or lava-like fuel containing materials (LFCM) [7]. The LFCM combined with the silicate minerals in the concrete and formed a heavily crystalline silicate melt that subsequently flowed through various pipes into the sub-reactor rooms in the lower levels before cooling enough to vitrify [94]. It is estimated around 1200 tonnes of LFCM was produced containing circa 90 tonnes of SNF [95]. These nuclear wastes and fuel residues are a major issue requiring international support to remediate. The glassy, crystalline LFCM is observed in three distinct variants, brown lava, black lava and polychromatic lava [7]. Brown LFCM was found to contain significant quantities of uranium (~10 mass %) [94]–[98] and polychromatic samples had blue veins in a glossy surface [99]. LFCM is found to contain a majority glassy phase with crystalline inclusions of UO_x relics of the original UO_2 fuel, UO_x with Zr substitution and a high uranium zircon $(Zr,U)SiO_4$, termed Chernobylite [6]. The exact composition of the LFCM has been found to vary and therefore a survey of the literature identifies many differing compositions for Chernobyl lavas. A list of the various elemental compositions stated in the literature for brown and black type LFCM is shown in Table 2-1.

Table 2-1. Various elemental compositions of LFCM in literature

LFCM Type	Ref.	Elemental Composition (mass %)														
		Si	Ca	Zr	Na	Ba	Al	Mn	Fe	Cr	Mg	Ni	B	Ti	Cu	U
Brown	[6]	36.6	7.2	4.0	0.6	-	4.0	-	0.2	-	4.4	-	-	-	-	2.0
Black		37.2	8.2	2.9	0.4	-	3.8	-	0.3	-	1.3	-	-	-	-	3.2
Brown	[96]	37.2	8.2	2.9	0.4	-	3.8	-	0.3	-	1.3	-	-	-	-	3.2
Black		29.8	5.5	3.2	4.2	0.1	4.8	0.3	1.4	0.2	2.4	0.1	-	0.1	0.5	4.7
Brown	[99]	30.0	4.9	4.0	4.0	-	4.2	0.9	-	0.4	3.6	-	0.1	-	-	10.9
Black		28.0	4.5	4.0	3.9	-	4.0	0.3	-	0.3	3.0	-	-	-	-	6.4
Brown	[95]	27.4	4.4	4.4	3.6	0.2	3.3	0.4	0.8	-	3.9	-	-	-	-	8.8
Black		29.5	4.7	4.2	4.1	0.2	4.3	0.3	-	-	3.2	-	-	-	-	4.4
Brown	[98]	24.7	3.9	4.0	3.3	-	2.9	-	0.7	-	3.3	-	0.1	-	-	8.8
Black		29.8	5.5	3.2	4.2	-	4.8	-	1.4	-	2.4	-	0.1	-	-	4.5

Plans to remediate the site and ensure the long term safety of Chernobyl Unit 4 include now in place, hermetically sealed, New Safe Confinement (see Figure 2-18) to cover the old sarcophagus; built hastily in the aftermath of the disaster to prevent the spreading of contamination). This new, 100 m high, 270 wide and 144 m long structure [91] will allow for dismantling of the destroyed core and recovery of the damaged SNF and LFCM for disposal, both of which require non-standard handling. Removal of the material from the site is the key priority to allow for further decommissioning activities to take place. The material will be placed into a specially designed and built facility for the storage of the abnormal waste from the Chernobyl reactor. LLW and ILW have been buried in a surface level trench type repository lined with clay for waterproofing and a system of ducts for drainage. HLW has been stored in a grouted form within the walls of the destroyed reactor, however these will eventually need to be moved [100]. SNF has yet to be moved from the site, with the current sarcophagus acting as the interim storage medium; however LFCM, SNF and other materials will eventually be disposed [101].



Figure 2-18. New Safe Confinement for Chernobyl Unit 4 as of July 2016, taken during site visit.

To allow for the safe disposal of LFCM, research has been carried out on creating low radioactivity simulant samples using natural uranium, intended to be of use for characterising the long term durability of Chernobyl LFCM. The results of this can be found in Chapter 5.

2.7. Plutonium Product and Residues

Another important nuclear fuel product and residue that needs addressing is the large stockpile of separated civil plutonium currently residing in secure vaults at Sellafield (see Figure 2-19). As of 2017, the UK has the world's largest stockpile of separated plutonium and is seen by the UK government as an 'zero value asset' which has potential for future use, therefore it isn't classified as HLW or any other type of waste [8], [31]. Storage currently costs the UK at least £40 million/year so reducing the inventory or removing it all together is a priority. As described earlier, the separated plutonium can be used to create MOX fuel for fission within a conventional reactor, as in France, reducing the demand for uranium. Another possibility is the targeted transmutation of the plutonium via a fast reactor into stable isotopes or those with much shorter half-lives which can be stored in dedicated facilities; reducing the long term radioactivity of the material [102]. Stored civil plutonium consists of different isotopic amounts including ^{238}Pu , ^{239}Pu , ^{240}Pu , ^{241}Pu and ^{242}Pu depending on where the plutonium was produced, the type of reactor and the burnup [103]. One of the major difficulties with storing plutonium is the unintended decay into shorter lived and hence more active radioisotopes for which additional radiation shielding is required. One such example is the successive neutron capture of ^{239}Pu to ^{241}Pu within a reactor and then beta decay to ^{241}Am whilst in stores over 14 years as shown in Equation 3. This requires additional shielding of Pu containers and monitoring for build-up of ^{241}Am , placing affected packages into over-packs or repackaging altogether [75]. One potential solution to repackaging would be to remove the ^{241}Am from the civil plutonium altogether.

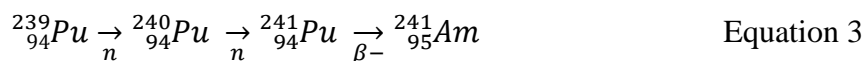


Figure 2-19. THORP Product Store for separated plutonium [104]

2.7.1. Americium Extraction & Use in RTG

Extraction of ^{241}Am from civil plutonium stockpiles is possible and has been demonstrated by the UK's National Nuclear Laboratory (NNL) [105]. Using a complex americium extraction process, americium can be separated from aged civil plutonium, reducing the overall activity of the plutonium stockpiles and enabling reprocessing of MOX fuel. An advantage of this route is the product, ^{241}Am has many potential uses, chiefly in a European radioisotope thermoelectric generator (RTG), muted for use on European Space Agency (ESA) missions to the outer solar system where conventional solar powered craft would not function [9], [106].

RTGs utilise the thermoelectric, or Seebeck, effect, to generate electricity from the temperature gradient between the natural decay heat of radioisotopes and cold of space. Decaying radioisotopes emit radiation in the form of an alpha or beta particle or gamma ray. Some radioisotopes emit more than one type of radiation. Within an RTG the emitted radiation is stopped, or slowed, and the subsequent heat generated deposited into a solid transducer thermally attached to the hot side of the semiconductor, such as silicon germanium (SiGe) [107]. A flow of heated electrons flowing from the hot side to the cool side, or heat sink, of the semiconductor produces a direct current and electric potential that can be used to power a device. Efficiency is low in such devices with typically between 5 and 7% of the thermal energy converted into electrical power, as such, isotopic heating is also utilised to warm components and to achieve the maximum benefit from the device [106].

The choice of radioisotope to use was studied by the National Aeronautics and Space Administration (NASA) in 1968 [108], with the key requirements for a RTG radioisotope being the type of radiation emitted due to natural decay, the half-life of the isotope, power density and availability of the material [107]. Type of radiation is important as the energy needs to be deposited into the transducer material to ensure maximum efficiency. Alpha and beta radiation can be deposit their energy into a small area however gamma rays will require significantly sized transducers, rendering their use as an RTG inadequate. Alpha radiation would require the smallest size and hence mass of transducer therefore being more favourable. High energy gamma radiation can cause radiation effects in surrounding material such as sensitive electronics, and worker dose uptake, and are to be avoided. The half-life of the radioisotope is important as it defines the lifespan of the RTG and ability to generate electricity as well as how much can be generated. The power density, or amount of thermal output per gram of material, is often linked to the half-life and activity of the isotope with higher power density favoured. However, the higher the power density, the higher the resultant radiation damage on the semiconductor [107].

^{238}Pu has been selected by NASA as the primary source of heat and electrical power used on spacecraft that travel beyond the orbits of Jupiter, or require an energy dense, reliable power source, as is the case for the Curiosity rover on Mars Figure 2-20. ^{238}Pu is the preferred radioisotope of choice for these applications due to being a pure alpha emitter, resulting in less shielding required for when handled on the ground, for the launch mass into space and to reduce any interference with any sensitive scientific. The isotope also has a useful half-life (~88 years),

enough for long duration missions required for an outer solar system journey and ^{238}Pu has a high power density ($557 \text{ W}_T/\text{kg}$), dependant on form [109].

Unfortunately this particular isotope is in short supply due to limited production, from irradiation of ^{237}Np , and in order to power future missions such as that taken by the Voyager probes or the New Horizons craft, an alternative heat generating radioisotope is needed by nations without the capability of producing ^{238}Pu . The ESA has identified ^{241}Am , as an ideal candidate and can be obtained economically from stocks of civil plutonium [105], [110], [111].

^{241}Am is a moderately long lived isotope with a half-life of 432 years and, like ^{238}Pu , decays only via alpha emissions making it ideal as a surrogate for plutonium in an RTG [107]. As a consequence of the longer half-life, the theoretical power density is reduced to $111 \text{ W}_T/\text{kg}$, over 5 times less than ^{238}Pu , meaning a significant increase in mass would be required to achieve the same electrical or thermal output.

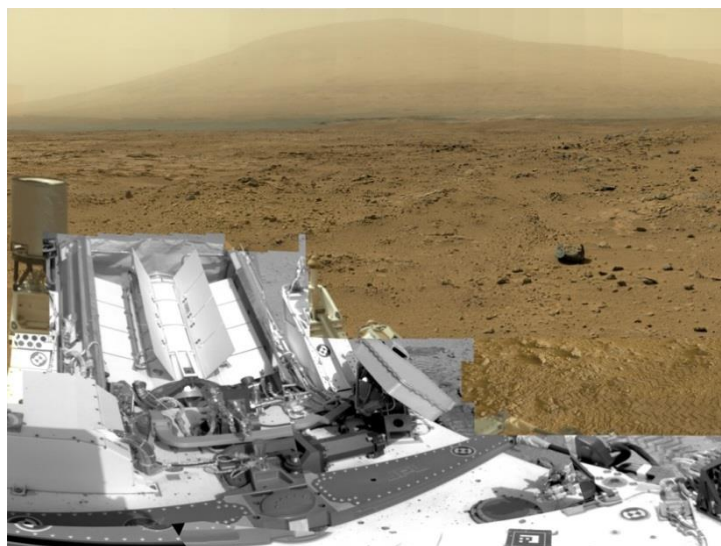


Figure 2-20. NASA's Curiosity Rover on Mars powered by a ^{238}Pu RTG (Courtesy NASA/JPL-Caltech) [112]

Developing durable ceramic phases for the immobilisation of americium has been explored in recent work including ceramic-metallic (cermet) encapsulation [109], [110], [113]. Research on finding the optimum form for americium, oxide or otherwise, is still ongoing. Americium compounds are often observed in the +III oxidation state, although the IV, V and VI oxidation states are also possible [114].

The use of americium in the laboratory is problematic due to the intensity of the radiation emitted and therefore the use of surrogate materials is needed. The most commonly used surrogates are neodymium and cerium due to comparable important properties, such as similar cationic radii, reduction and oxidation behaviour, crystal symmetry and space group [110],

[115], [116]. Due to auto-oxidation, Ce^{4+} is difficult to reduce to the trivalent +III state, hence Ce^{3+} was targeted as a surrogate of interest to cover a gap identified in the research, with few reports of cerium niobates recorded in the literature.

2.7.2. Weberite-type ceramics

One potential candidate form for americium immobilisation could be in durable weberite-type niobate ceramics, with a composition of Ln_3NbO_7 , where Ln is all lanthanides except cerium, which have been extensively studied [117]–[119]. Hitherto, Ce_3NbO_7 had not been frequently reported in literature due to the difficulty in obtaining single phase material with the Ce cation in the +III oxidation state. The crystallographic space grouping of the larger ionic radii lanthanide in this ceramic has long been difficult to assign due to subtle differences in symmetry of the frequently postulated space groups. Larger ionic radii lanthanide in these compounds are generally assigned the Cmcm or D_{2h}^{17} (No. 63) space group [120], [121], however, recent research has shown the crystallographic symmetry to vary as a function of the ionic radius with La-Nd lanthanide aligning well with the Pmnc or D_{2h}^{16} (No.62) space group [117]. Only two publications on Ce_3NbO_7 exist in the literature, a publication focusing on impure Ce_3NbO_7 fitted X-ray data to the $\text{Fm}\bar{3}m$ space group [122] and a recent study by Inabayashi et al. [123] fitting X-ray data to the Pnma space group, an alternative setting of Pmnc .

A phase transition from lower symmetry Pmnc to higher symmetry Cmcm has been reported in Ln_3NbO_7 ceramics which occurs as a function of temperature and lanthanide ionic radii, which also confuses the correct space group to assign these compounds [124]. It was reported that the phase transition temperature reduces with increasing lanthanide ionic radii and also with the pentavalent cation radii. This phase transition is reportedly due to a distortion in ‘A’ site and ‘B’ site polyhedral [125], where the ‘A’ site and ‘B’ site are two cations, the ‘A’ site cation being the larger of the two. For cerium niobate samples, this phase transition is expected to occur around room temperature.

2.8. Processing Routes for Problematic Nuclear Wastes and Fuel Residues

Treatment of all nuclear wastes involves creating durable solid wasteforms that can be packaged and stored effectively. Methods include drying and compaction, grouting/cementation and thermal treatments including ceramic synthesis and vitrification [36]. To date, most LLW is compacted and/or grouted in cement (see Section 2.4.1) and ILW is often grouted however novel processing techniques including vitrification are becoming more popular due to the increased passive safety and potential volume reduction [126]–[128]. An important challenge for the nuclear industry is consideration of appropriate waste treatments for the wide array of nuclear wastes present, ensuring a suitable wasteform is produced. This problem is compounded by the varying properties, characteristics and classification of some problematic nuclear wastes and fuel residues. A processing route that is cost effective and durable in the long term is required.

Whilst an inexpensive and proven method of encapsulating nuclear wastes into a durable solid material, cementation is a concern for particular wastes of high volume and high content of reactive components, such as Magnox wastes from the FGMSP and MSSS. Modifications to ordinary Portland cement (OPC) such as the addition of pulverised fly ash (PFA) or blast furnace slag (BFS) are made to allow for a wasteform acceptable for nuclear waste purposes [129] however these do not account for the reactivity of metallic waste, such as Magnox, which will cause reaction with the pore water present in cement materials according to Equation 1 [85]. Hydrogen released during the reaction causes swelling and dimensional changes in waste packages which reduces the expected life of cemented waste packages to ~350 years, but with a possible range of between 30 and 5800 years depending on conditions [85]. Gas generation from reaction with the reactive metals and from radiolysis of pore water combined with carbonation of the outer surfaces can cause instability in the cemented wasteforms [10]. Other more durable, less reactive and long-lived wasteforms, such as vitrified products, would be required for more hazardous material such as HLW and specific ILW.

2.8.1. Vitrification

Vitrification is the process of converting a substance to a non-crystalline amorphous solid, also known as a glass, where no long-range ordering of the structure exists. This process is exploited in nature through lightning strikes on sand and from molten lava interacting with water, forming obsidian, the oldest naturally occurring glass material dating to the cretaceous period, up to 100 million years ago with very low corrosion rates in the presence of groundwater [130]. These materials were used by pre-historic man for hunting and cutting by forming sharp blades and arrow heads. Humans have been creating glass glazes from around 12,000 BC and man-made pure glass beads created over 9000 years ago before industrial production by the Ancient Egyptians 3500 years ago [36], [131].

With the longevity of natural analogues, glass wastefoms, and hence vitrification, are seen as a means of ensuring nuclear waste is isolated and immobilised for the lengths of time the waste remains hazardous [131].Vitrification is widely accepted for the safe treatment of hazardous radioactive materials, with HLW currently immobilised as glass in the UK, France and the USA [44]. Interest in thermal treatment such as vitrification for ILW wastes has grown in recent years due to the key technological drivers including considerably higher waste loading, significant volume reduction and superior durability as well as enhanced passive safety [127]. This is possible by chemically bonding waste into the structure of a glass through oxidation of the waste components combined with evaporation of any waters of crystallisation and removal of any organic phases. The desired vitreous nuclear wasteform would be resistant to crystallisation, have low melting/processing temperatures, high physical and chemical durability, no phase separation and consistency in future melts [131]. A number of glass compositions have been developed since the introduction of nuclear waste vitrification in order to ascertain and improve the chemical durability, lower the melting temperature and improve the processing of glasses [44], [76], [126], [128], [132], [133].

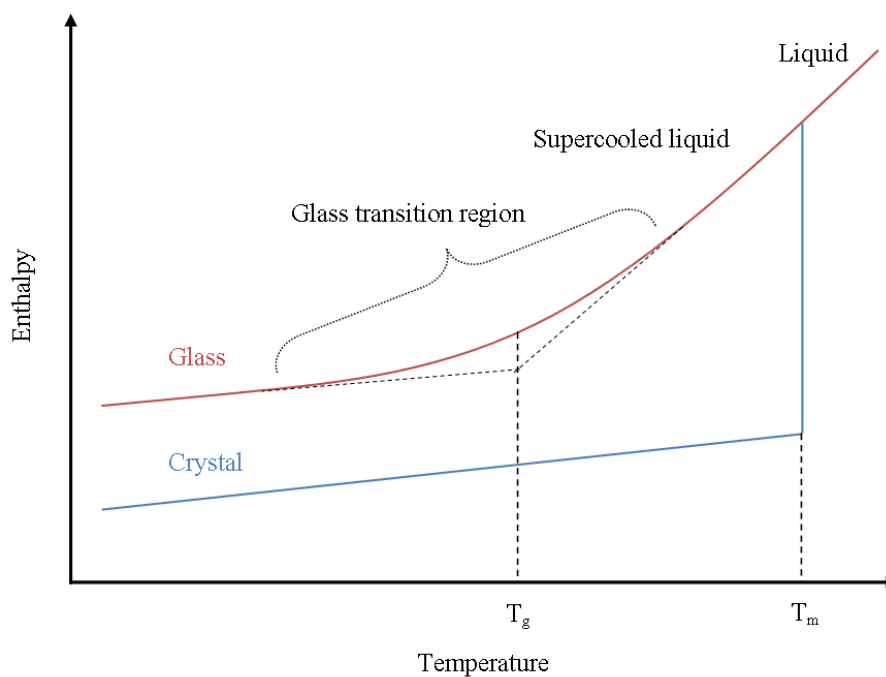


Figure 2-21. Enthalpy vs temperature for a glass and crystal; highlighting T_g and T_m

Any material that undergoes a glass transition, or transformation, is defined as a glass, including non-traditional materials such as metals, polymers and even water in the form of amorphous ice. The glass transition is the phenomenon observed when a material is converted from a liquid state to a supercooled liquid whereby crystallisation of the structure does not occur below the materials melting point (T_m). Viscosity in the supercooled liquid rises as the

temperature falls such that atoms cannot rearrange back to a liquid state and the material is essentially fixed as a frozen liquid in a solid form. The conversion from a liquid state to a solid form does not occur at a specific temperature but over a range of temperatures depending on the cooling rate; the temperature at which this region begins is referred to as the glass transition temperature (T_g), an approximation of when the supercooled liquid transforms to a solid upon cooling [36]. In terms of enthalpy of the system, it can be observed that the linear dependence between enthalpy and temperature of a liquid and supercooled liquid upon cooling is discontinuous upon reaching the glass transition temperature whereby the enthalpy deviates from the norm and is no longer dependent on temperature [134], as can be observed in the enthalpy vs temperature plot in Figure 2-21. In contrast, a crystalline melt undergoes a discontinuous change in enthalpy upon melting.

Formation of an oxide based glass can readily be achieved with particular compounds, namely network forming oxides SiO_2 , B_2O_3 , P_2O_5 and GeO_2 [134], however many other potential glass formers, termed intermediates, include Al_2O_3 , Sb_2O_3 , PbO and ZrO_2 which only form glass in the presence of a network former [135], [136]. Compounds which modify the properties of glass, termed network modifiers, act as charge balancers and often include Na_2O , CaO , MgO and Li_2O . These compounds have the effect of changing the melting temperature but reduce the structural connectivity in glass by reducing the number of oxygen atoms that can be bonded to [135], [136]. The commonly agreed structural model for glass follows that by the Zachariasen-Warren Network Theory [137]–[139] whereby polyhedral of the network formers are created, SiO_4 tetrahedra and BO_3 triangles, that edge share bridging oxygen atoms. The theory also explains how large, low charge cations such as Na^+ , Li^+ and Ca^{2+} charge balance non-bridging oxygens (NBO), discontinuities formed between separated polyhedral groups, and modify the glass network, whilst small and highly charged cations such as Mg^{2+} and Zr^{4+} act as intermediates due to their relative field strength [139]. Nuclear waste can be chemically bonded to this glass network, incorporating the waste into the microstructure, with elements not capable of forming part of the glass network being encapsulated within the glass structure.

The most commonly used glass type used by the UK nuclear industry is based on the borosilicate glass network, with SiO_2 being the main glass forming oxide involving SiO_4 tetrahedra along with B_2O_3 forming BO_4 tetrahedra and BO_3 triangles which interlink via bridging oxygens [36]. NBOs are charge balanced by ionic bonding to large positive charged cations, which can include some waste constituents such as caesium, sodium or strontium. Uranium can be chemically bonded into glass as a network modifier or as an intermediate oxide depending on composition and synthesis conditions, with oxidising atmospheres during melting forming higher oxidation state uranium (V) and (VI) behaving as network modifiers. Under reducing conditions U (IV) can be produced which can act as an intermediate oxide and form part of the glass network [135], [140]. Inhomogeneity can be present in borosilicate glasses caused by the separation of the two distinct glass forming regions of boron and silica [134], [141]; this glass-in-glass phase separation can potentially reduce the corrosion resistance of the glass system in certain compositions [142]. Figure 2-22 shows the pseudo-ternary

liquidus phase diagram of an alkali-borosilicate glass highlighting the region in which nuclear waste glasses are formed and common commercial glasses [143].

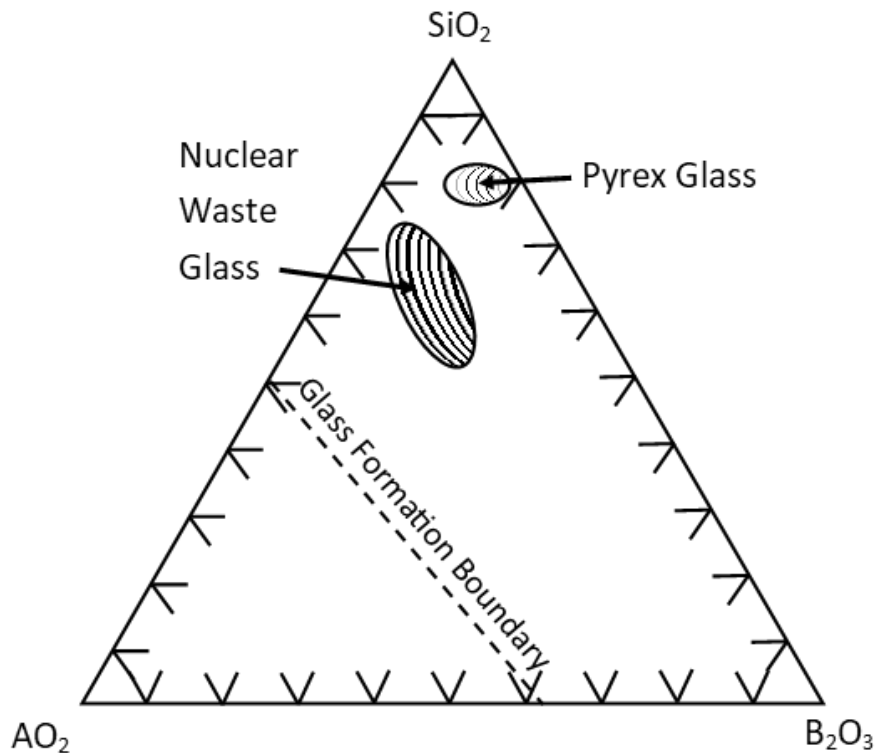


Figure 2-22. Alkali-borosilicate glass pseudo-ternary liquidus phase diagram where A_2O is any alkali oxide, adapted from [143]

Glass production in the UK is by the Atelier de Vitrification de la Hague (Vitrification Workshop of the Hague) or AVH process, a two-step vitrification process where liquid waste, typically the radioactive liquor from the PUREX reprocessing (see section 2.3.6), is dried in a rotary calciner before vitrification in an induction-heated hot crucible melter [36], [144]. The molten product is cast into stainless steel canisters as seen in Figure 2-9 and sealed remotely by welding. An overview of the melter is shown in Figure 2-23. These melters could also be used for immobilising ILW [144], particularly for ‘wet’ or hydrated wastes from the FGMSP and MSSS.

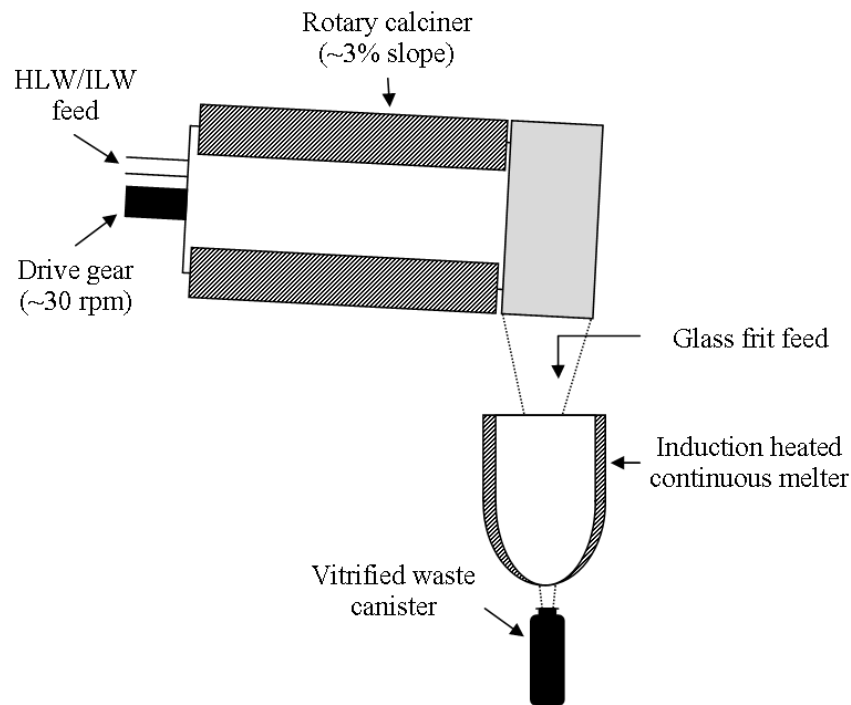


Figure 2-23. AVH-like glass melter used at the UK vitrification plant

2.8.2. Ceramics & Glass Composite Materials

Creating full crystalline ceramic materials could be employed for various problematic nuclear wastes such as plutonium products and residues [144], [145]. Ceramics could include the immobilising of waste into a single phase ceramic, such as quartz first demonstrated at Pennsylvania State University in 1973 [143], [145] or into multiphase ceramics such as the often mentioned synthetic rock, Synroc, range of wastefoms [44], [143], [146], [147]. Single phase ceramics such as perovskite and pyrochlore are often researched and can be created with suitably high waste loading and density [44], however due to the difficulty in creating pure ceramics, the synroc multiphase ceramics and glass composite materials such as glass-ceramics are proposed for many problematic nuclear wastes. Within the typical conditions expected of a GDF, many crystalline materials are known have superior chemical durability to conventional nuclear waste glasses [44]. Glass-ceramics combine the beneficial properties of both ceramics and glasses with particular, targeted, radionuclides immobilised in the crystalline phases whilst other radionuclides are immobilised in the glass phase which is more flexible to chemical changes. These so-called advanced wastefoms can be produced by a variety of methods including devitrification of a host glass and hot isostatic pressing (See Section 2.8.3) to grow a crystalline phase within a bulk glass [148].

2.8.3. Hot Isostatic Pressing

Hot isostatic pressing (HIP) has been around since the 1950's, with its first applications on manufacture of nuclear fuel, so the relevance to the HIP process on the nuclear industry is profound. Initially termed as gas pressure bonding due to the process requiring high pressure, HIPing has become a recognised industrial process for processing of metals and ceramics [149].

This novel process for nuclear waste produces wastefoms that are created at lower temperatures than traditional production methods and using less time. The method involves pre-calcining batch material and then baking out whilst under vacuum and sealing into a HIP can before applying isostatic high pressure whilst simultaneous heating such that the initial batch becomes a liquidus body and is densified by the high pressure forming a material of almost theoretical density by bringing particles close together via the process of diffusion bonding along with creep and plastic deformation of particles [150]. Before the HIP run, the canister containing the sample is baked-out under vacuum to allow for volatilisation of any low temperature organics and impurities then sealed by tungsten inert gas (TIG) arc welding. The canister also acts as an initial over pack for the waste, much in the same way as nuclear waste glass is cast into steel canisters and cement into drums, but also has the advantage of containing all volatile fission products within. Care needs to be taken to ensure that no interaction will take place between the batch materials and the cans used; eutectics have the potential to alter the composition from the anticipated composition, melt temperature and pressure, hindering the formation of a stable and durable wastefom. The structure of the wastefom created by this method is often that of a glass ceramic, providing the beneficial properties of both. A glass or glass-ceramic could be created to immobilise various wastes under the HIP however pre-treatment such as calcination of the waste would be required to remove any volatiles which, if present, would reduce the effectiveness of the HIP process and result in poor densification [151]. A two-step processing method, as with the UK HLW vitrification, could be employed to calcine waste and combine the required reagents. Whilst HIP'ing has the potential to produce high quality wastefoms, size restrictions limit its current full scale use and the capital investments required are high [22].

Thermal treatment of ILW using the HIP process has already been demonstrated with ion-exchange media such as that used in the clean-up operations at the Fukushima Daiichi nuclear power station [152]. If applied to current ILW stocks in the UK, similar HIP wastefoms have the potential for significant volume reduction, calculated between 4 and 5 times compared to the non-processed ILW [153], [154].

Magnox sludge from the FGMSP and MSSS varies in consistency significantly; to represent this in the research two separate waste compositions were considered at the extremes of what is expected to encompass all possible scenarios. One extreme of the waste, representing Magnox fuel that has suffered severe corrosion, contains mostly hydroxides and oxides of uranium as a result of corrosion of the metallic uranium fuel. The other enveloping waste composition represents material that has suffered little corrosion and is mostly in the metallic form, including the uranium. The two bounding extremes of the waste are shown in Table 3-1 below. The simulants were defined in consultation with Dr Sean Morgan of Sellafield Ltd. No fission products, such as Sr or Cs were added as, although their presence is likely in real samples, the anticipated concentration of such components is low compared to Mg and U.

Table 3-1. Bounding simulant Magnox wastes

Component	Corroded Waste (wt%)	Metallic Waste (wt%)
Mg (metal):	5	12
Mg(OH)₂:	80	20
U (metal):	5	68
U₃O₈:	10	0

The simulant wastes were added to MAS and MBS glass compositions forming a suit of 6 samples to take forward for advanced characterisation, including the base glass compositions. Use of simulants for uranium, including neodymium and a rare earth alloy mischmetal (Mm), composed of approximately 50% Ce, 25% La and 25% Nd, were also explored such that the Nd or Mm replaced all U in samples on a molar level. This created an additional 8 samples. The major glass compositions created in this research are shown in Table 3-2, where ‘-C’ samples correspond to doping with corroded waste and ‘-M’ corresponds to doping with metallic waste.

Table 3-2. Compositions of batched glass samples

Sample designation		Oxide composition as batched (mol%)								
		SiO ₂	B ₂ O ₃	MgO	Na ₂ O	Al ₂ O ₃	UO ₃	Nd ₂ O ₃	Ce ₂ O ₃	La ₂ O ₃
MBS test samples		21-35	19-27	46-55	-	-	-	-	-	-
MAS test samples		40-59	0-20	20-30	0-20	10-12	-	-	-	-
Base Glass	MBS	25.4	25.0	49.6	-	-	-	-	-	-
	MAS	48.0	2.0	20.0	20.0	10.0	-	-	-	-
Waste loaded Glass	MBS-C (U)	25.1	24.7	49.1	-	-	1.0	-	-	-
	MBS-M (U)	21.7	21.3	42.4	-	-	14.5	-	-	-
	MAS-C (U)	45.5	1.6	28.3	18.4	5.6	0.6	-	-	-
	MAS-M (U)	40.8	3.7	25.4	16.5	5.0	8.7	-	-	-
	MBS-C (Nd)	25.2	24.7	49.2	-	-	-	0.9	-	-
	MBS-M (Nd)	24.1	23.7	47.0	-	-	-	5.2	-	-
	MAS-C (Nd)	45.6	1.6	28.3	18.4	5.6	-	0.5	-	-
	MAS-M (Nd)	43.2	1.6	26.8	17.5	5.3	-	5.6	-	-
	MBS-C (Mm)	25.3	24.8	49.4	-	-	-	0.1	0.3	0.1
	MBS-M (Mm)	23.4	23.0	45.8	-	-	-	1.9	3.9	2.0
	MAS-C (Mm)	45.7	1.6	28.4	18.4	5.6	-	0.1	0.1	0.1
	MAS-M (Mm)	43.9	1.6	27.3	17.7	5.4	-	1.0	2.1	1.0

3.1.1. Batch Preparation - Glass

Standard laboratory reagents used in the research are shown in Table 3-3. The reagents for specific glass samples were weighed into stoichiometric amounts using a calibrated balance with an accuracy of ± 0.01 g and transferred to polyethylene sample bags. Intimate mixing of the batches whilst in the sample bag was performed for over 1 minute to ensure the batch contents are evenly distributed and any conglomerates or lumps of material are broken down. Sample bags of batch were stored sealed in a dry location prior to thermal synthesis. Nd metal was sectioned to less than 3 mm³ before adding to the batch.

Radioactive materials, U and U_3O_8 , were batched and weighed in stoichiometric amounts separately from the non-radioactive reagents with a balance within a dedicated U/Th glovebox. U metal monoliths were sectioned to less than 3 mm^3 . The radioactive components were added to the premixed non-radioactive reagents before further in-bag mixing. The U and U_3O_8 were added immediately before melting to avoid the risks of storing and unnecessary transport of hazardous material. Adding the batch to the alumina crucible was also performed within the dedicated U/Th glovebox for radioactive samples.

Table 3-3. Reagents used in glass research

Reagent	Supplier	Purity (%)
SiO₂	Sigma-Aldrich	99.5
H₃BO₃	Sigma-Aldrich	99.5
Na₂CO₃	Alfa Aesar	98
Al(OH)₃	Acros Organics	95
Mg(OH)₂	Sigma-Aldrich	95
Mg (metal)	Acros Organics	99.9
U₃O₈	British Drug Houses	99
U (metal)	British Drug Houses	99
Nd₂O₃	Sigma Aldrich	99.9
Nd (metal)	Alfa Aesar	99.1
Mischmetal	Contact Left Ltd.	99

Initial test samples for scoping the eutectic on the MBS pseudo-ternary liquidus phase diagram consisted of 10 g batches which were scaled up to 200 g to produce sufficient material for testing purposes. The final optimised, waste loaded samples with U, Nd and Mm were produced in 80 g batches, sufficient for the detailed characterisation whilst minimising the use of expensive or hazardous reagents and radioactive waste produced. Table 3-4 shows the synthesis conditions, crucible and furnace type used for each set of samples.

Table 3-4. Synthesis conditions for glass samples

	Sample designation					
	MBS test samples	MAS test samples	MBS	MAS	MBS waste loaded	MAS waste loaded
Crucible	Mullite	Alumina	Alumina	Alumina	Alumina	Alumina
Furnace	Electric	Electric	Gas	Electric	Electric	Electric
Synthesis conditions	1200-1250 °C 3 hrs	1200-1500 °C 5hrs	1250 °C 3 hrs	1500 °C 5 hrs	1250 °C 3 hrs	1500 °C 5 hrs
Annealing conditions	500-610 °C 1 hr	560 °C 1 hr	610 °C 1 hr	560 °C 1 hr	620 °C 1 hr	560 °C 1 hr

3.1.2. High temperature processing - Glass

The prepared batch was added to alumina and mullite crucibles filling approximately 80% maximum volume to avoid any foaming-over of the melt and compacting down the powders to ensure a maximum yield of glass is produced from each crucible. Test samples used for scoping out the pseudo-ternary liquidus phase diagrams for optimum compositions were created in gas furnaces and electric muffle furnaces whilst the final optimised compositions loaded with waste were melted in alumina crucibles, supplied by Almath, in electric muffle furnaces only. The temperature and length of time required for synthesis are shown in Table 3-4. Test samples were synthesised and annealed at varying temperatures to determine the optimum processing method, which was then applied for the waste loaded samples. Residual stress built-up in the cast samples was removed by annealing, when the temperature was not correct cracking of the glass ensued. All samples were annealed and cooled to room temperature at 1 °C/minute.

Test scale samples were produced in an Elite Thermal Systems BRF15/5-2416 Muffle Furnace for 3 hours in mullite crucibles. Visual inspection of the melts at temperature was made to assess the fluidity and ability to cast. Upon reaching the desired synthesis time, the crucible was removed from the furnace using long steel tongs and placed into an annealing furnace for 1 hour. These samples were not cast as only visual inspection was required.

MBS base glass sample was produced in a gas furnace dedicated for glass melting with stirring the melt using an automated alumina paddle to ensure a homogenous melt was produced. The alumina crucible with batch was preheated to 1100 °C overnight and added to the pre-set 1250 °C gas furnace for 3 hours with the stirring at ~60 rpm commencing after 1 hour. Upon completion of the melting regime, the molten glass was cast into preheated steel

moulds arranged to form a rectangular bar sample. After cooling sufficiently enough to solidify, the mould was removed, and the glass bar placed into an annealing oven for 1 hour at 610 °C before cooling to room temperature.

MAS and waste loaded samples were synthesised in an Elite Thermal Systems BRF15/5-2416 Muffle Furnace as with the test samples but using alumina crucibles. The furnace was sited in a fume hood to extract any potentially contaminated fumes from the radioactive uranium melts. Due to concerns of the potential for radioactive contaminated fumes, mechanical stirring in an open furnace was not an option for the active waste loaded samples, and hence subsequent samples were created in the same electric muffle furnace for consistency. Upon completing the melting regime the molten glass was cast into bars and annealed for 1 hour before cooling to room temperature in a controlled manor.

3.1.3. Powdering & sectioning glass samples

To create powdered samples for testing and analysis, a stainless steel percussion mortar was used to crush glass into smaller size fragments which were then sieved between two stainless steel sieves to provide material with three distinct size fractions, glass greater than 150 µm, in between 75µm and 150 µm and powdered glass less than 75 µm. Small scale test samples were crushed in the percussion mortar and ground to a powder using a pestle and mortar with a small amount of isopropyl alcohol. All crushed glass was checked with a magnet to remove any iron contamination from the steel mortar. Glass with a size fraction of between 75µm and 150 µm were used for glass dissolution studies, see 3.5.9. Powdered radioactive samples were created by the same method but in a dedicated laboratory for active materials whilst sealed within polyethylene bags to contain any hazardous dusts produced.

To section and polish samples into representative monoliths for use in the scanning electron microscope, a Buehler IsoMet slow saw with cutting fluid and Kemet 300 polishing wheel were used. The process of grinding and polishing sectioned samples starts with P400 followed by P800 and P1200 grade silicon carbide grit papers. This is followed by polishing using 3 µm diamond suspension (Buehler) and a Planocloth pad before final polishing with 1 µm diamond suspension (Buehler) and a cashmere pad to create an optically blemish free surface. Sectioning and polishing of radioactive samples was performed in a dedicated laboratory for handling low quantities of active material; all radioactive liquors created were collected and stored securely in the laboratory.

3.2. Magnox Sludge HIP Processing

Glass compositions developed from Magnox sludge glass processing mentioned in Section 3.1 were synthesised in an alternative method using HIP equipment. This method, outlined below, required additional processing steps to ensure volume reduction in the final sample. A simulant Magnox sludge was provided by the UK National Nuclear Laboratory produced by hydrothermal alteration of fresh Magnox AL80 fuel elements composed of approximately 99.2 wt% Mg and 0.8 wt% Al.

3.2.1. Batch Preparation – HIP

Preparing the simulant Magnox sludge provided by NNL required calcination to remove free water and bound waters of hydration from the hydroxide material, both of which would reduce the effectiveness of the HIP and not provide the necessary densification and pose a risk of internal pressurisation of the HIP can. Developing from the base borosilicate glass samples from previous work (Section 4.1 and Section 4.2), the MgO content was replaced with that of the simulant waste, using 87% Mg(OH)₂ & 13% Mg for total MgO content; in order to preserve stoichiometry of corroded waste stream described in Section 3.1. Batched material was calcined at 600 °C & 1000 °C in two samples before packing into a pre-prepared HIP can.

3.2.2. Thermal Synthesis – HIP

HIP cans are created from 1.5 inch outer diameter 316 seamless stainless steel piping with the lid and base components fabricated from stainless steel bar; the evacuation tube is also seamless stainless steel piping. All parts are welded using TIG welding technique with the lid attached after the can has been packed. Prepared batch is packaged into HIP cans using a hydraulic press to ensure maximum amount of material is produced and densification is effective. A 5 mm space is left between top of the compacted batch and top of the can to allow for the countersunk lid and so as not to interfere with the welding process. Once sealed the dimensions, mass and volume displacement of the can are made to determine the degree of volume reduction after the synthesis process.

3.3. Chernobyl Lava-Like Fuel Containing Material Processing

To recreate the microstructure and morphology of Chernobyl LFCM samples with a low radioactive simulant, a survey of the literature was required to determine the composition of the solidified lavas and the conditions in which they formed, see Table 2-1. A composition based on the literature was created and further refinement, via increasing the Zr content, was performed to obtain a representative sample. For the thermal synthesis, consideration of the conditions in the remains of the reactor core in which the real material was made was considered. It was found from the presence of zircon in LFCM, that the temperature of the melt could not have exceeded 1500 °C, since zircon cannot form above this temperature [6], for this reason the thermal synthesis was conducted at 1500 °C. Due to the long and slow cooling of the reactor over many days and weeks, a long cooldown of the sample to room temperature at 1 °C/minute was selected. To further simulate the conditions expected a reducing atmosphere was selected for the thermal synthesis due to the absence of Zircaloy cladding, the melting of which is thought to have caused reducing conditions by removing oxygen from the local atmosphere [4].

3.3.1. Batch Preparation – LFCM

Chernobyl LFCM was produced in a similar method to Magnox sludge glass, using the reagents listed in Table 3-5. 316 grade stainless steel powders were used to represent the steel LFCM would have interacted with during its creation. Non-radioactive batch components were weighed into stoichiometric amounts using a calibrated balance with an accuracy of ± 0.01 g and transferred to polyethylene sample bags. The radioactive components, uranium, were batched separately in a dedicated glovebox and added to the non-radioactive batch before in-bag mixing. The batching of uranium components was performed directly before the thermal synthesis step to reduce the risk of storing the radioactive powder for longer than necessary. A table of the compositions batched in this work are shown in Table 3-6. Batch sizes were circa 20 g, depending on crucible availability, with the final representative samples produced in 23 g batches. Samples Brown_1 and Black_1 were developed for the initial results paper as described in Section 5.1 whilst Brown_2 and Black_2 were developed for the second results paper as outlined in Section 5.2.

Table 3-5. Reagents used for LFCM research

Reagent	Supplier	Purity (%)
SiO₂	Lochaline Quartz Sand	99.6
CaCO₃	Fisher	98
ZrO₂	Aldrich	99
Na₂CO₃	Alfa Aesar	98
BaCO₃	Alfa Aesar	99
Al(OH)₃	Acros Organics	95
Mn₂O₃	Aldrich	99
Fe/Cr₁₈/Ni₁₀/Mo₃	Goodfellow	99
Mg(OH)₂	Sigma-Aldrich	95
UO₂	British Drug Houses	99

Table 3-6. Compositions of batched LFCM samples

Sample designation	Oxide composition as batched (mol%)									
	SiO ₂	CaO	ZrO ₂	Na ₂ O	BaO	Al ₂ O ₃	MnO	Fe ₂ O ₃	MgO	UO ₂
Brown LFCM	65.6	7.3	3.3	5.3	0.1	4.2	0.5	0.5	10.7	2.5
Black LFCM	67.9	8.2	3.0	5.8	0.1	5.1	0.4	-	8.4	1.2
Brown LFCM ₁	65.5	7.3	3.9	5.3	0.1	4.1	0.5	0.5	10.6	2.2
Black LFCM ₁	64.0	7.9	7.7	7.1	-	4.3	-	-	7.8	1.2
Brown LFCM ₂	65.2	7.3	7.6	7.9	-	1.9	-	0.6	10.1	2.4
Black LFCM ₂	65.2	6.9	7.8	5.2	0.1	4.4	0.5	0.4	8.0	1.6

3.3.2. Thermal Synthesis – LFCM

The prepared batch was added to rectangular alumina ‘boat’ crucibles to approximately 90% of the volume, to avoid any spill over from a bubbling or foaming of the batch during melting. The crucible was filled in the dedicated active area for U samples and transferred to the furnace laboratory with transport containment.

The filled crucible was placed in an Elite Thermal Systems TSH 15/50/450 tube furnace where the ends were sealed with silicone oil bubblers. Flowing H₂/N₂ gas was passed over the sample and into the furnace for 3 hours prior to starting the heat cycle to ensure oxygen is displaced and a reducing atmosphere is present. To ensure the atmosphere remains reducing, a positive pressure of H₂/N₂ was maintained at 1 bar throughout the thermal synthesis. A heating profile for the thermal synthesis is shown in Figure 3-2.

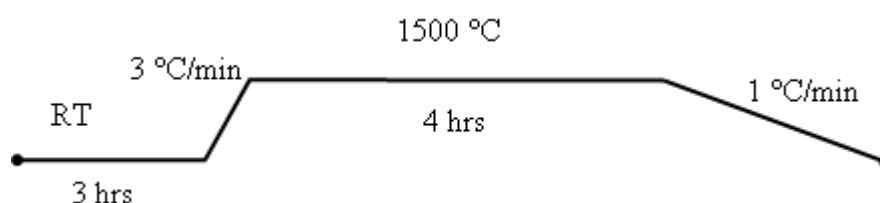


Figure 3-2. Heating profile for LFCM samples

An annealing step at 690 °C for 70 hrs with cooling to room temperature at 5 °C/min was performed using an Elite Thermal Systems BRF15/5-2416 Muffle Furnace to reduce cracking and stresses within the sample, but also to grow the crystalline phases present with the samples to aid detection and characterisation. For the development of representative samples (Section 5.2), samples were heat treated at 720 °C for 72 hrs in an electric muffle furnace with cooling to room temperature at 5 °C/min. No reducing atmosphere was needed for these experiments.

3.3.3. Powdering and sectioning LFCM samples

Sections of the synthesised LFCM samples were cut using a Buehler IsoMet slow saw with cutting fluid as for Magnox sludge glass. Since these samples all contain uranium, the sectioning was performed in the dedicated radioactive materials laboratory. Grinding of the LFCM sections was performed by hand using successive grades of silicon carbide grit paper P400, P800 and P1200 followed by polishing to an optical finish using 3 µm diamond suspension (Buehler) on a Planocloth polishing pad and 1 µm diamond suspension (Buehler).

on a cashmere polishing pad. Monolithic sample sized 10 mm by 5 mm by 1 mm were sectioned for use in vapour hydration testing (VHT) durability studies [157].

Small, previously sectioned, representative samples were ground into powders using a Fritz Pulverisette 23 micro mill with zirconium oxide pot and milling media. Milling was performed for 3 minutes at 40 Hz with isopropyl alcohol whilst the mill pot was double sealed with polyethylene bags, before air drying within a fume cupboard. Milled powders were stored dry in polypropylene sample pots prior to use.

3.4. Cerium Niobate Ceramics Processing

Conventional solid state ceramic synthesis methodology was employed to create Ce_3NbO_7 samples from oxides of cerium and niobium. This method involves calcining the batch components before batching them, creating green-body pellets and then reacting at high temperature. The last two steps were repeated with regrinding until a single phase material was achieved. Sintering of these pellets was not performed in this research. To create cerium in the +III oxidation state, when batching as Ce (IV), a reducing atmosphere was required when performing thermal synthesis. The production method and reaction temperature selected was adapted from that most frequently used in the literature for similar weberite-type ceramics [125], [158]–[161].

3.4.1. Batch Preparation – Ce_3NbO_7

Reagents used for batching cerium niobate ceramics, shown in Table 3-7, were calcined at 600 °C for 12 hours before stoichiometric amounts were batched using a calibrated balance with an accuracy of ± 0.01 g into polystyrene weighing dishes. The batched material was transferred to a zirconium oxide mill pot with zirconium oxide milling media and isopropyl alcohol for wet mixing to ensure homogeneity. This was performed in a Fritz Pulverisette 6 mill at 550 rpm for 6-8 minutes, after the wet mix was dried at 110 °C for 3 hours. The dried batch was pressed into 10 mm by 6 mm ‘green body’ pellets by applying 41 MPa (3 ton-force/inch²) of uniaxial pressure for 1 minute. Some dried batch material was not pressed. Typical batch size was 10 g, with extra material initially weighed out to account for any potential losses incurred during calcination.

Table 3-7. Reagents used in preparation of Ce_3NbO_7 sample

Reagent	Supplier	Purity (%)
CeO_2	Acros Organics	99.9
Nb_2O_5	British Drug Houses	99.5

3.4.2. Thermal Synthesis – Ce_3NbO_7

Green-body pellets were placed into rectangular alumina boat crucibles and covered with the powdered batch material to act as an oxygen-getter and prevent surface oxidation. The crucible was placed in an Elite Thermal Systems TSH 15/50/450 tube furnace with the ends sealed with silicone oil airlocks. Flowing H_2/N_2 gas was passed through the furnace for 3 hours prior to starting the heat cycle to create a reducing environment and ensure oxygen is displaced. To ensure the atmosphere remains reducing, a positive pressure of H_2/N_2 was maintained at 1 bar throughout thermal synthesis. A heating profile for the thermal synthesis of Ce_3NbO_7 is shown in Figure 3-3.

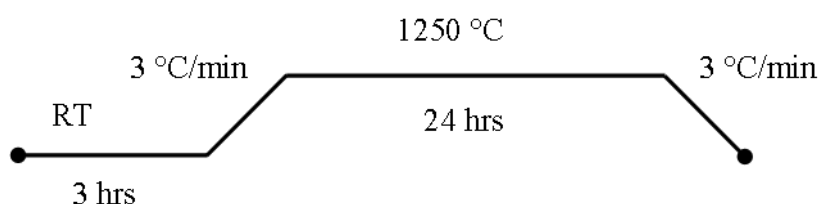


Figure 3-3. Heating profile for Ce_3NbO_7

After reaction it was observed the outer layer (<1 mm) of each pellet was visibly darker from the interior and was therefore abraded off using P800 silicon carbide grit paper. In some cases, multiple reactions were required to form phase pure samples, this involved grinding the pellets to a powder and pressing into a ‘green-body’ and reacting for a further 24 hours.

3.4.3. Powdering Ce_3NbO_7 samples

To create powdered samples from which to characterise the novel material, the reacted pellets of Ce_3NbO_7 were crushed in a pestle and mortar before wet milling with isopropyl alcohol in the Fritz Pulverisette 6 mill at 500 rpm for 8 minutes. The milled powder was dried at 110 °C for 3 hours to form fine dry powdered Ce_3NbO_7 . This process was also used to grind reacted pellets for a second or third reaction, if required. Powdered samples were stored dry in sealable polypropylene storage containers until use.

3.5. Characterisation techniques

3.5.1. X-Ray Diffraction

To determine the crystalline phase assemblage or to confirm the amorphous nature of materials, powder X-Ray Diffraction (XRD) analysis was conducted with corresponding phase analysis. A Bruker D2 Phaser in reflectance mode (30 kV, 10 mA) and a STOE STADIA P (PSD) in transmission mode (40 kV, 35 mA), both with Cu $K\alpha_1$ radiation sources, were the main diffractometers used in this research. Data in reflectance mode was collected over the range $10^\circ < 2\theta < 70^\circ$ whilst data from transmission mode XRD was collected over $10^\circ < 2\theta < 120^\circ$. $K\beta$ radiation was removed from the Bruker D2 Phaser using a Ni foil filter ensuring monochromatic Cu $K\alpha_1$ (1.5406 Å), however the STOE STADIA P did not have filtering.

Collected XRD data was processed using the Bruker DiffractEva 3.0 software with indexing of any crystalline peaks using the built in database and/or the International Centre for Diffraction Data (ICDD) database [162].

Powder samples were prepared for XRD depending on the equipment being used and the sample in question. For the Bruker D2 Phaser, standard non-radioactive samples were placed onto a dedicated sample holder and made flush with the surface of the holder with glass slides. Radioactive samples for the D2 required preparing in the radioactive laboratory where the powder was be mixed with white Elmer's (PVA) glue and spread in an even layer across a thin acetate disk. This disk would then be placed onto a dedicated zero background sample holder and secured into place using a spray on fixative. Sample preparation for the STOE STADIA P was similar to the radioactive D2 preparation with the sample glued onto an acetate disk which is fixed to an iron specimen holder for placing into the instrument. Figure 3-4 shows the internals of the Bruker D2 phaser used for XRD analysis, the X-ray source is located on the left of the image and the detector on the right; the rotating sample holder is situated in the middle.

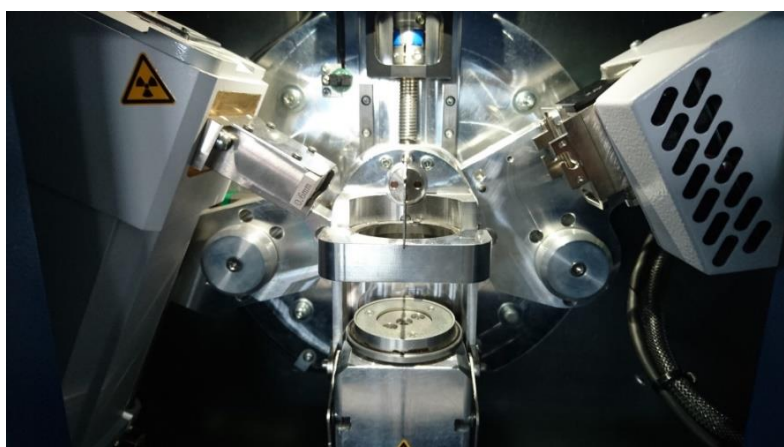


Figure 3-4. Bruker D2 Phaser XRD internals

Diffraction by X-rays has been known since 1912 with the experiments by Max von Laue and explained by the Bragg's [163], [164]. The determination of crystal structure by XRD due to diffraction of incident beams of X-rays by lattice planes of the crystal is described by Bragg's law, see Equation 4 [165].

$$\lambda = 2d \sin \theta$$

Equation 4

Where λ = wavelength of incident radiation, d is interplanar spacing and θ = angle of incident beam. When constructive interference of diffracted radiation occurs, peaks are formed in a diffraction pattern that correlate with the lattice planes of the crystalline structure. In amorphous glass materials, there is no long range ordering of lattice planes and hence the diffraction pattern for glass is that of diffuse scattering centred at the d -spacing associated with long range Si-Si next nearest neighbour and Si-O bonds [165], [166]. This peak broadening is increased with decreasing crystallinity.

A sketch of the diffraction of X-rays off a crystal lattice in the reflectance geometry is shown in Figure 3-5. The incident X-rays are diffracted off the lattice and reflected from the surface. In transmission mode, the detected X-rays scatter off the lattice and are detected on the opposite side of the incident beam, as opposed to in reflection mode, which requires thin samples.

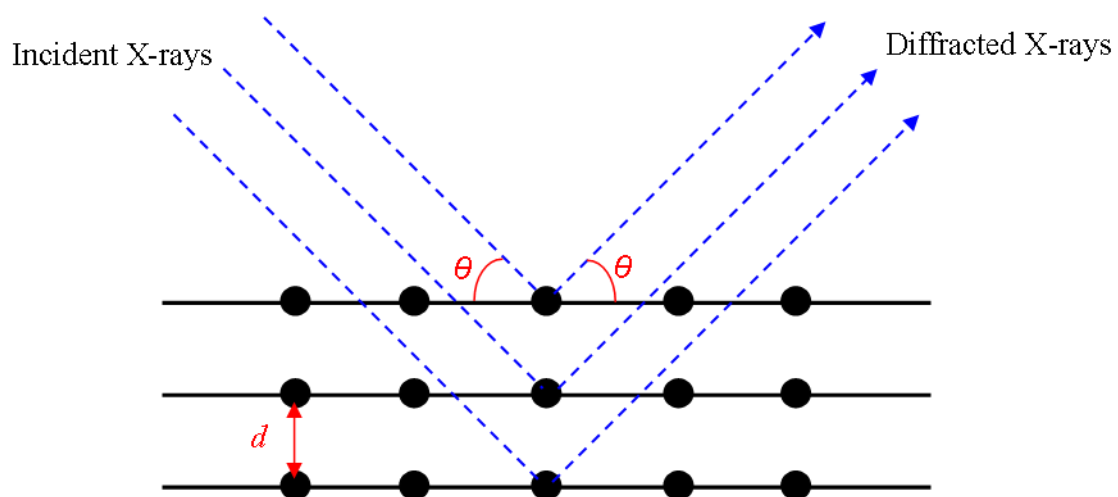


Figure 3-5. X-Ray diffraction by a crystal

3.5.2. Neutron Diffraction

Using the same principles as X-ray diffraction, neutron diffraction utilises neutrons which due to wave-particle duality, have a comparable de Broglie wavelength to X-rays, but interact with an incident atom differently. Whereas X-rays interact with orbital electrons, neutrons, being neutral in charge, interact with the atoms comparatively small nucleus via the strong nuclear force, resulting in sharper, more defined diffraction peaks [167], [168]. Being weakly interacting, neutrons have a large penetration (low absorption) depth into a sample and can interact well with atoms of any atomic number, unlike X-rays which are absorbed by many heavier elements and have a smaller scattering length for lighter elements. A consequence of the weak interaction is that incident neutrons are poorly scattered, resulting in a necessity to have larger samples available for analysis than would be required by X-ray diffraction, therefore this is a bulk analysis technique.

A pulsed neutron source, or spallation source will produce neutrons in pulses which are incident onto a sample, resulting in a wide range of neutron energies. The time at which each scattered neutron arrives at a detector after irradiation is recorded producing a diffraction pattern from various scattering angles where the independent variable is the time of flight (TOF) of neutrons instead of the usual 2θ scattering angle from XRD. Combining the de Broglie and Bragg equation, seen earlier, results in Equation 5, where h = Planck's constant, m = mass of neutron, v = velocity of neutron, t = time of flight of neutron and l = length of the flight path. From this equation the interplanar d-spacing can be determined.

$$\lambda = \frac{h}{mv} = \frac{ht}{ml} = 2d \sin \theta$$

Equation 5

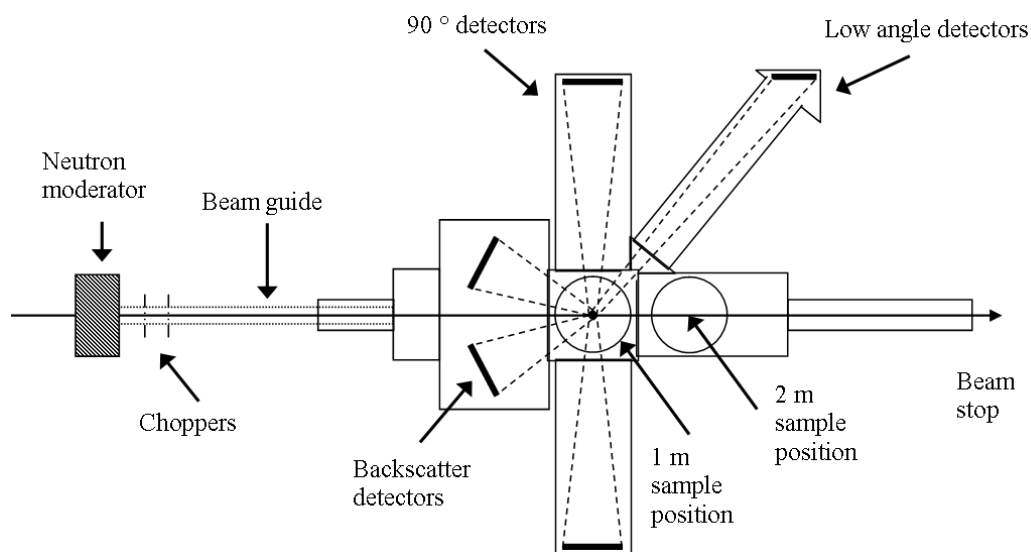


Figure 3-6. Schematic of ISIS HRPD diffractometer

Neutron diffraction was only used for the structural analysis of cerium niobate samples. Powdered material was analysed at the high resolution neutron diffraction at the ISIS spallation source, part of the Rutherford Appleton Laboratory in the UK, using the High Resolution Powder Diffractometer (HRPD) instrument with TOF neutrons. This diffractometer, with the highest resolution of its kind in the world, performed a two hour scan at 80 μA beam current on powdered sample from 30 ms to 130 ms using a NBS solid state silicon backscattering detector bank [169]. A schematic of the diffractometer used is shown in Figure 3-6 where the incident beam enters from the left and interacts with a sample in the 1 m position with detection of diffracted neutrons in the rear backscatter detectors, 90° detectors and forward low angle detectors.

Rietveld refinement, developed by Hugo Rietveld, is a method for fitting the peaks of a crystalline diffraction pattern, obtained from either neutron or X-ray analysis. This function uses the crystal structure limitations, atomic coordinates, site occupancy and thermal parameters with the experimental parameters such as the unit cell size and analysis conditions to effectively refine a hypothetical model to observed data [170]. This method was used to determine the crystal structure of the cerium niobate compound using the EXPGUI GSAS software (version 1251) [171], [172].

3.5.3. Electron Diffraction

Comparable to principles of X-ray and neutron diffraction, electron diffraction relies on the elastic scattering or diffraction of electrons by planes of atoms within a thin section of a crystalline material and is achieved using a transmission electron microscope (TEM). In this technique, the negatively charged electrons interact with the positively charged core of an atom and unlike X-rays, electrons negative charge allows for accurate focusing meaning diffraction from a single crystal of a sample can be obtained [173]. Whilst XRD and neutron diffraction have a beam size greater than that of a single crystal, thereby sampling many crystallites and forming many Debye-Scherrer rings, an electron diffraction beam is smaller than a single crystal and hence can interact with a single crystallite more easily resulting in a sharp single crystal Bragg peak or Debye-Scherrer ring, that correspond to a scattering angle twice the atomic plane Bragg angle [174].

By using a second, or intermediate, aperture within the TEM, a selected area for electron diffraction can be defined and through use of a double-tilt specimen holder, a sample can be manipulated and orientated within the electron beam to provide a diffraction pattern on the back focal plane aligned along a known crystal axis informing as to the composition or structure of the crystallite under investigation. This is shown in Figure 3-7 below.

Compared to X-ray and neutron diffraction, electron diffraction is less quantitative due to probing smaller regions, however this can therefore be used to distinguish features that would

be missed in both X-ray and neutron diffraction such as the correct space group for a crystalline system as will be discussed in Chapter 6. Selected area electron diffraction patterns were obtained at the University of Manchester on a FEI Techni F30 TEM with an accelerating voltage of 300 keV. An accompanying Gatan Orius CCD camera was used to collect diffraction patterns. Data collection was performed by Dr Heath Bagshaw with my assistance. A finely ground powder sample was placed onto a holey type carbon TEM grid which was placed within a double tilt sample holder for manipulation within the sample beam. Comparison of the obtained diffraction pattern to those simulated using the SingleCrystal v3.1.1 software allowed for identification of the crystal zone axis and any forbidden reflections which would determine the correct space group for the sample.

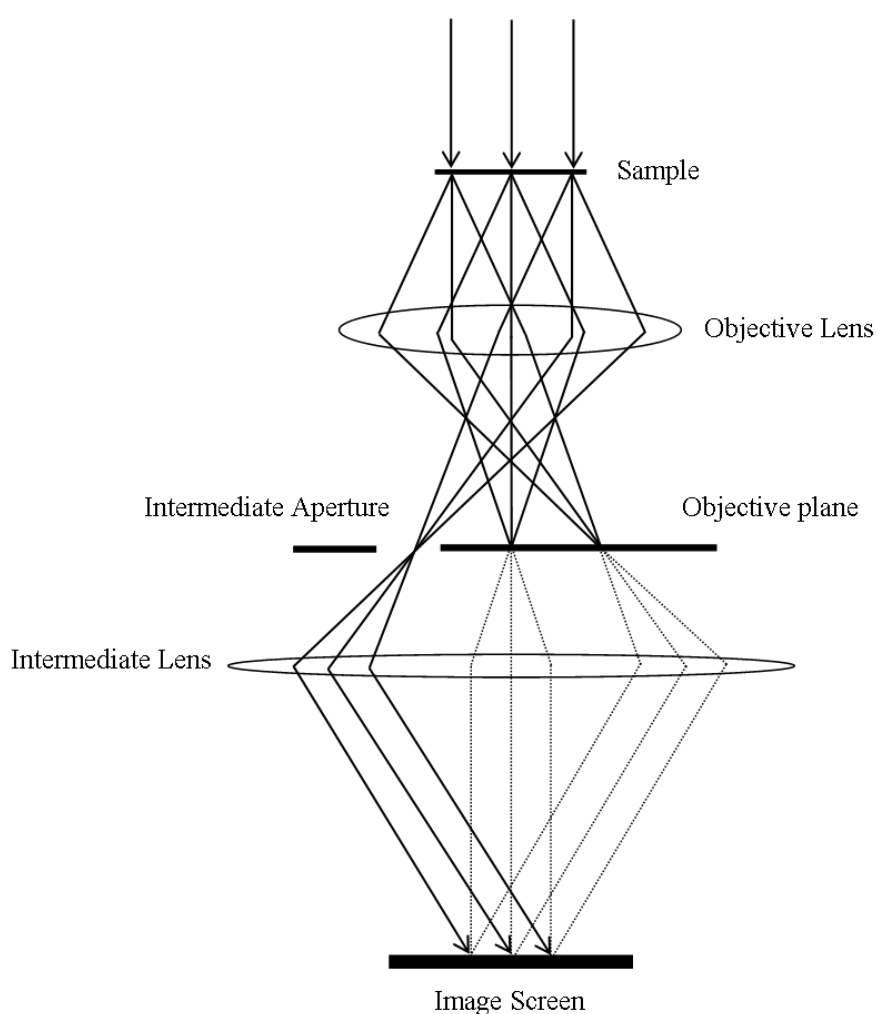


Figure 3-7. Selected Area Electron Diffraction TEM

3.5.4. Scanning Electron Microscopy & Energy Dispersive X-Ray Spectroscopy

Scanning electron microscopy (SEM) is a powerful tool for determining the morphology of a sample as well as its microstructure, especially when coupled with energy dispersive X-ray spectroscopy (EDX) for elemental data. Electron microscopy is superior to traditional optical microscopy due to the smaller wavelength of the incident beam; de Broglie wavelength of 15 kV electrons ($0.01 \mu\text{m}$) is considerable less than the wavelength of visible light ($400\text{-}700 \mu\text{m}$) [175], [176]. Care must be taken to prepare the sample being observed due to interactions between electrons and the surface whereas visible light does not interact. The incident beam of electrons causes the ejection of secondary electrons and the back scattering of the original electron along with X-rays from relaxation of excited atoms. Occasionally visible light can be emitted due to cathodoluminescence from low energy relaxation events. An overview of the interactions of electrons with the sample surface that are detectable is shown in Figure 3-8.

To ensure electrons are drawn to the sample the chamber must be evacuated of air and the sample surface must be conductive, for glass and ceramics that are inherent electrical insulators this requires coating with a thin film of carbon. Samples also need to be polished flat to ensure back scattered electron emission is consistent since rough surfaces cause a significant variation in tilt angle of the scattered electrons [177].

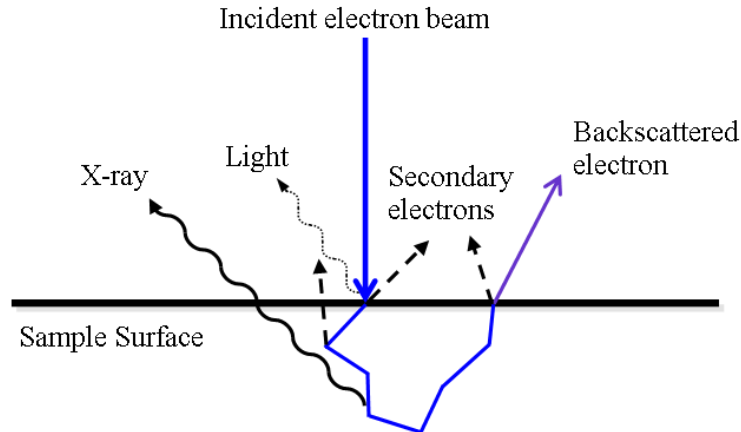


Figure 3-8. Usable signals from electron-surface interactions

The depth of interaction between electrons and the sample surface depends on two main factors, the density of the sample and the incident beam voltage. Many secondary electrons are absorbed into the sample and only those created very near the sample surface can be detected. Likewise some incident, or primary, electrons are absorbed into the sample though thermalisation whilst others manage to escape as backscattered electrons; the depth at which these originate is greater than for secondary electrons. X-rays are the least interacting signal emitted and as such have a much greater depth of origin within the sample; the volume of

material contributing to this is called the interaction volume [175], [176], [178]. The interaction volume for the various signals sources is shown in Figure 3-9.

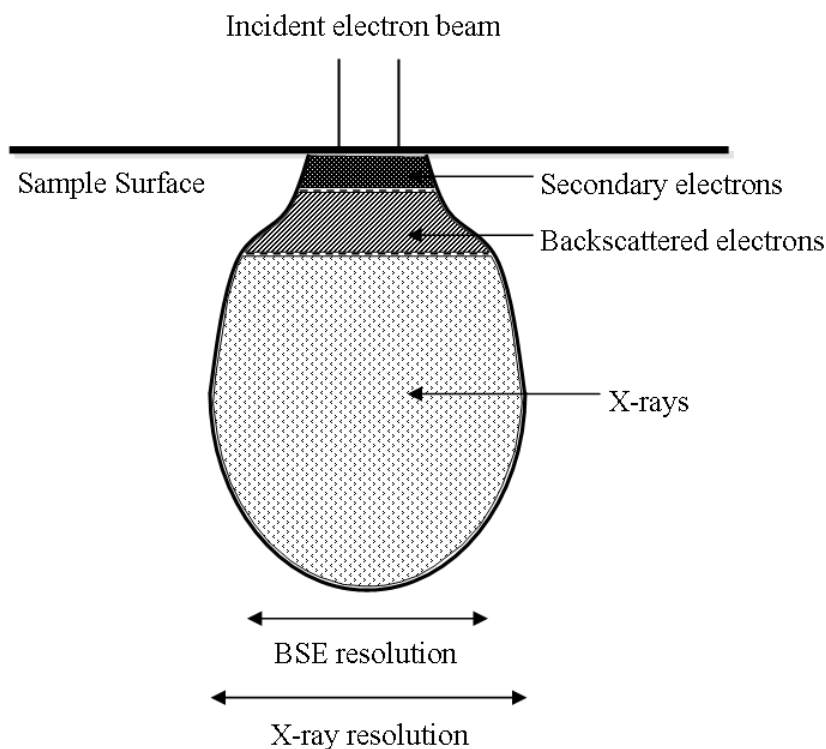


Figure 3-9. Interaction volume from where usable signals are detected

Characteristic X-rays produced from relaxation events within excited atoms can deduce the chemical identity of that atom. A transition of an electron from an outer electron shell to the inner shell vacancy produces an X-ray with an energy quantified to that atom. These X-rays form a spectrum where the peak positions indicate the presence of a particular element. Many elements have several X-ray energies depending on the specific electron orbital shell the transition occurred from. These X-rays are detected in an EDX system simultaneously with imaging.

SEM-EDX data for all projects in this study was collected on a Hitachi TM3030 (15 kV acceleration voltage) equipped with a Bruker XFlash 430H EDX system (30 mm² detector area) capable of detecting all elements between boron and americium; with microanalysis of EDX data on the Bruker Quantax 70 software. All images were obtained with back scattered electrons. To obtain an optically flat sample surface required for SEM-EDX, samples were sectioned and mounted in two part epoxy resin which were ground and polished to a 1 μm finish, as described in Section 3.1.3. To obtain a conductive surface, carbon coating of the samples was employed involving high temperature sputtering of graphite within a vacuum. Samples were then fixed to conductive stainless steel SEM stubs using conductive silver adhesive with a conductive patch running from the base to the conductive surface.

3.5.5. Simultaneous Thermal Analysis

The determination of thermal events, dehydration, de-hydroxylation, de-carbonation, glass transition, crystal formation and melting, can be achieved through various techniques, but most commonly used are differential thermal analysis (DTA), differential scanning calorimetry (DSC) and thermal gravimetric analysis (TGA) [22]. DTA instruments record the temperature difference between a sample and an internal reference whilst heating, such that endothermic events such as melting or a second order glass transition cause the sample temperature to lag behind the reference temperature. Conversely, an exothermic event such as crystallisation or oxidation, cause the sample temperature to increase relative to the reference [179]. DSC equipment operates in very much the same way except the two samples are thermally connected and the energy required to keep the sample and reference at the same temperature is recorded instead, leading to much more accurate results [180]. TGA instruments measure the mass change in a sample as a function of temperature utilising a very accurate calibrated balance; to ensure signals are purely from the sample and not high temperature interactions with air, inert atmospheres are used typically nitrogen or argon [181]. TGA is often combined with DTA or DSC to provide simultaneous thermal analysis (STA) and information on thermal events and associated mass changes in real-time. This provides several benefits including using the same sample ensuring any thermal events can be accurately correlated between data and that the same size, morphology, mass and composition of sample is analysed leading to more accurate interpretation of results [182].

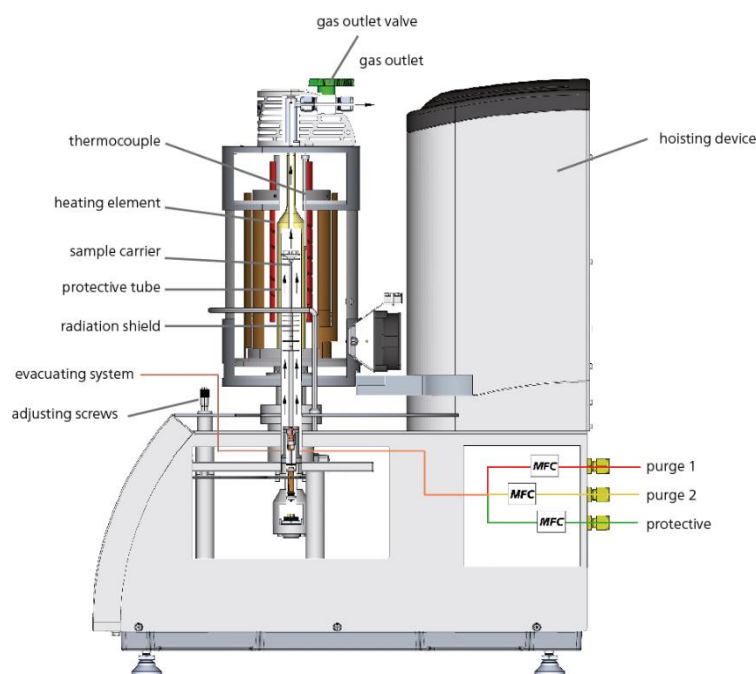


Figure 3-10. STA 449 F3 Jupiter schematic from Netzsch [183]

All thermal data was collected on a Netzsch TG 449 F3 Jupiter simultaneous thermal analyser (Figure 3-10), at temperatures up to 1500 °C under an argon gas atmosphere with a

heating rate of between 5 °C/min and 20 °C/min, depending on the information required. Non-radioactive powdered samples of at least 200 mg were placed in dedicated alumina crucibles for thermal analysis whereas sectioned monoliths of uranium bearing samples were used to reduce the hazard of handling radioactive powders.

3.5.6. Helium Pycnometry

Measurement of a powder sample's volume or density can be determined by gas expansion pycnometry, whereby the difference in pressure due volume expansion can be directly related to the sample volume. Helium is the preferred gas to use for pycnometry due to the small atomic size and lack of reactivity with any sample. Figure 3-11 shows a schematic for a gas expansion pycnometer with a sample cell, pressure monitoring transducer, reference cell and gas valves.

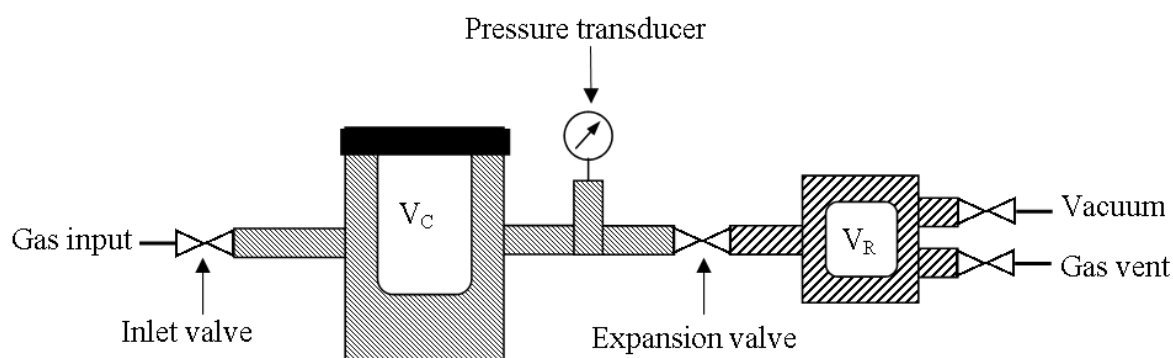


Figure 3-11. Gas expansion pycnometer schematic

The equation for determining the volume of the sample is shown in Equation 6 [184]. The volume of the sample corresponds to the density of the sample through the know mass of the sample, as recorded on a calibrated balance with an accuracy of ± 0.01 g.

$$V_S = V_C + \frac{V_R}{1 - \left(\frac{P_1}{P_2}\right)} \quad \text{Equation 6}$$

Where V_S = volume of the sample, V_R = reference volume, P_1 is the pressure recorded when the sample chamber is filled and P_2 the pressure recorded when the expansion valve is opened.

In all work projects powder samples of know mass were added to a 1 cm³ sample holder insert and placed within a Micrometrics Accupyc II 1340 instrument. Helium gas at a fill pressure of 82.7 kPa was used with 10 purges over 10 cycles and experiments were performed

in room temperature with little variation. The density was calculated automatically from the determined sample volume and recorded sample mass.

3.5.7. X-ray Absorption Spectroscopy

X-ray absorption spectroscopy (XAS) can be described as the sharp increase in absorption of X-rays at specific energies which is unique to that particular element. These sharp increases in absorption are called absorption edges corresponding to the energy required to excite electrons into higher electronic states [185]. This analytical technique uses a synchrotron to generate high energy X-rays which are made monochromatic using a two-bounce, or double crystal, monochromator composed of silicon. The monochromatic beam is focused onto a prepared sample with the transmitted beam, or the detection of fluorescence X-rays, providing information on the local environment of the element being probed [186], [187]. Due to the low concentrations of U probed, coupled with sample attenuation and the hard X-ray absorption edge being investigated, U samples were analysed in fluorescence mode. High concentrations of Ce meant transmission mode was selected for Ce samples. A schematic of the XAS set-up used is shown in Figure 3-12, where I_0 is the intensity of the incident beam, I_T is the intensity of the transmitted beam and I_F is the intensity of the secondary fluorescence photons produced as a result of de-excitation.

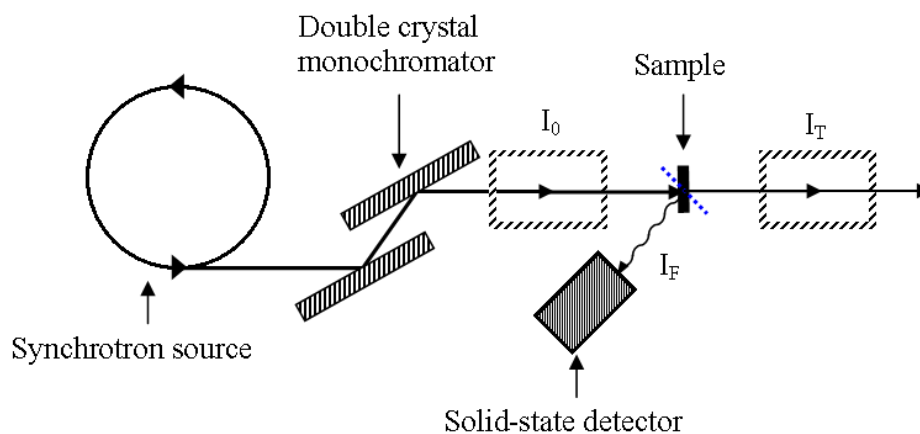


Figure 3-12. XAS experimental set-up schematic (X05LA beamline)

X-ray absorption near edge spectroscopy (XANES) provides information on the oxidation state and coordination of an element whereby the absorption edge and profile/shape changes with increasing or decreasing oxidation state, compared to known standards. This is due to effect of different X-ray energies required to excite electrons into different excited electronic states, such that more energy is required to excite electrons in higher oxidation state samples

[188]. To probe the oxidation state and to understand the behaviour within a material, the main L_3 absorption edge of uranium and cerium was explored in this project.

XANES on uranium bearing samples was performed at the Paul Scherrer Institute at the Swiss Light Source in Switzerland focusing on the U L_3 edge feature at 17,166 eV. The X05LA beamline uses double crystal Si (111) monochromators and Si drift detectors mounted at 45° to the incident beam for detection of fluorescence X-rays. The sample flux was around 400 mA with a flux of 2×10^{12} photons/second on the sample. XANES on cerium niobate samples was performed on the BL-9A beamline at the KEK Photon Factory, High Energy Accelerator Research Organisation in Japan exploring the Ce L_3 edge at approximately 5,723 eV in transmission mode. The beamline is equipped with double crystal Si (111) monochromators and ionisation chamber detectors. Flux on the sample was roughly 6×10^{11} photons/second and with energy of 450 mA. For data reduction and analysis, the Athena Demeter software package (version 0.9.24) was used. XAS sample preparation and raw data collection was performed by Dr Martin Stennett.

3.5.8. Bulk Chemical Analysis

The chemical composition of thermally synthesised materials was required to determine the amount of material in a sample, particularly the target waste or waste simulants, compared to the originally batched composition. Preparation for the chemical analysis required powdered samples with a size fraction less than $75 \mu\text{m}$ to be digested into hydrofluoric acid. This liquid form of sample was fed into a Spectro Ciros Vision inductively coupled plasma emission spectrometer (ICP-ES). The digestion into hydrofluoric acid and ICP-ES analysis was performed by an external laboratory, The University of Sheffield's Department of Chemistry ICP Spectrometry laboratory.

ICP-ES can determine the elemental makeup of a liquid phase by vaporising the liquid sample into high temperature plasma where the sample is decomposed. The high temperatures cause excitation and ionisation of the vaporised sample atoms which release a characteristic radiation when decaying back to the ground electronic state. These emissions are collected and recorded whereby specific wavelengths, or frequencies, of radiation correspond with particular atoms, and hence the make-up of a sample can be determined [189], [190]. Solid state detectors are commonly used for the detection of the emission photons. Figure 3-13 shows a schematic diagram of typical ICP-ES equipment with the plasma torch vaporising a sample and the resulting polychromatic radiation separated and collected in a multiplexer device. For further use of the ICP-ES, see Section 3.5.9.

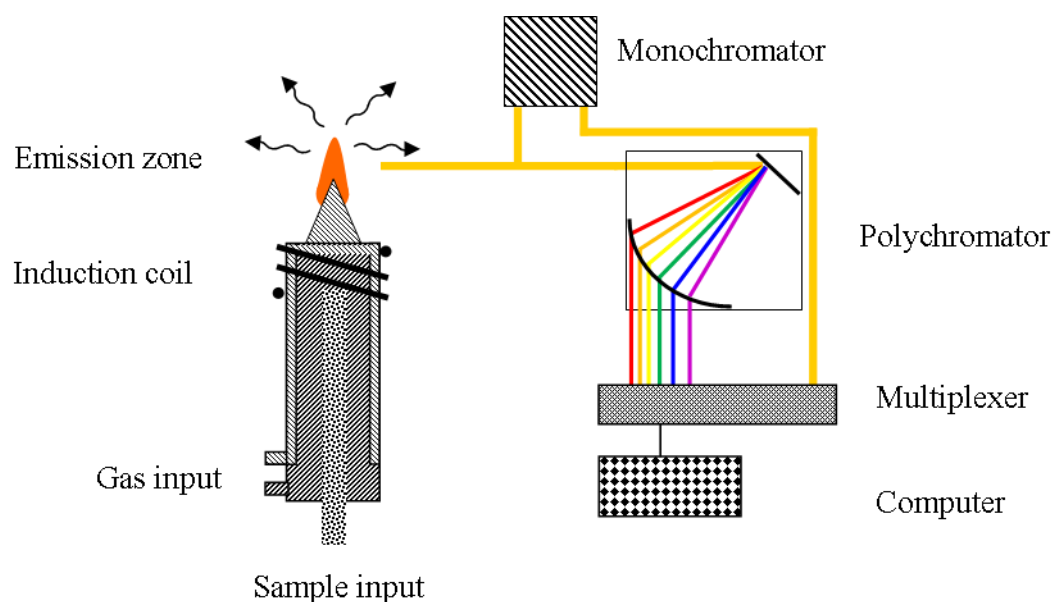


Figure 3-13. Schematic of a typical ICP-ES set-up

3.5.9. Aqueous Dissolution

It is predicted through thermodynamics that glass, a metastable product, will hydrate in the presence of water and exchange constituent glass elements, the rate at which this process occurs is of fundamental importance in the planning and licensing of a nuclear waste facility [77]. Concentrations of chemical species released as a result of dissolution within an aqueous medium under accelerated leaching conditions was performed according to a modified version of the ASTM Product Consistency Test method B (PCT-B) protocol [191]. Relative durability of a test nuclear waste glass can be assessed compared to other homogeneous, phase separated, devitrified or glass-ceramics samples using this method which is commonly used in the literature [76], [128], [192], [193].

The normalised elemental release is often used to determine the loss of each element from a sample subject to a corrosion test and is calculated from Equation 7, where NL_i = normalised elemental release, C_i = concentration of element 'i' in solution, f_i = elemental fraction of element 'i' in the sample and SA/V = reactive surface area of the sample over the volume of leachate used [191]. The concentration of elements in the leachate was originally zero parts per million due to the use of ultra-high quality water. The surface area of the powder samples was calculated on the assumption that the material is spherical with an average particle diameter of 112.5 μm (based on sieving to between 150 and 75 μm).

$$NL_i = \frac{C_i}{(f_i \times \frac{SA}{V})} \quad \text{Equation 7}$$

The fraction of element ‘i’ in each unleached sample was calculated on the basis the constituent elements, derived from bulk chemical analysis (Section 3.5.8), were evenly distributed throughout the sample.

To simulate the length scales nuclear waste glass can expect to be required to remain passive in a GDF, circa 100,000 years (see Section 2.4.2), accelerated leaching experiments were performed on Magnox sludge glass and on simulant Chernobyl LFCM samples.

Alteration of Magnox sludge glass samples utilised the 75 µm – 150 µm size fraction glass powder which was cleaned and rinsed in ASTM-Type 1 compliant (UHQ) water to remove any smaller fines and size fraction of sample. Small volumes of the cleaned glass were placed into high density polyethylene containers such that a constant surface area of glass to volume of solution of 1200 cm⁻¹ was achieved. Samples were run in duplicate using a modified PCT-B test over 28 days at a constant temperature of 90 °C with monitoring of samples on days 1, 3, 7, 14, 21 and 28. Solutions obtained from each container were run through a Thermo Scientific iCAP 6000 Series ICP-ES to obtain the type and concentration of elements present, see Section 3.5.8 for information on the ICP-ES methodology and operation.

Chernobyl LFCM samples were altered using both the method outlined above for a modified PCT-B test and via the vapour hydration test (VHT). This was performed using a modified ASTM C1663 standard [157] with monolithic coupons sectioned to approximately 10 x 5 x 1 mm using a Buehler Isomet Low Speed Saw before being ground and polished to an optical finish using 3 µm diamond suspension (Buehler) on a Planocloth polishing pad and 1 µm diamond suspension (Buehler) on a cashmere polishing pad as outlined in Section 3.3.3.

4. Thermal Treatment of Simulated Magnox Sludge

In this chapter, work on thermal treatment of simulant Magnox sludge waste from the FGMSP and MSSS via vitrification and HIP techniques is explored. Section 4.1 investigates synthesis of samples whereby the uranium content from the expectant wastes (Table 3-1) was replaced with the surrogates neodymium and mischmetal creating a suite of 8 samples to analyse. The expectant wastes were deemed bounding for the potential extremes of waste anticipated within the storage ponds. Section 4.2 discusses the vitrification and analysis of the base magnesium borosilicate and aluminosilicate base glass compositions as well as low activity uranium simulant waste loaded compositions, forming a suite of 6 samples with additional analysis to that in Section 4.1 for oxidation state determination. Section 4.3 explores a ‘once-through’ process for thermal treatment via HIP of simulant Magnox sludge, with similar waste compositions to those described in Sections 4.1 and 4.2, through analysis of the pre-treatment and synthesis conditions. The waste simulant used in this section was hydrothermally altered Magnox fuel elements without uranium content and was provided by the NNL.

4.1. Draft paper: A Comparative Study between Non-Radioactive Surrogates Neodymium and Mischmetal in Magnesium Borosilicate and Aluminosilicate Glasses

This work takes the form of a draft paper ready written in the style of that for the Journal of Nuclear Materials. This work was written by myself with the aid of co-authors for feedback and comments, with all the work performed by myself with the exception of the chemical analysis which was performed on my behalf by Sheffield University Chemistry Department.

The article presented here is presented with references, figures and section numbering adapted to retain continuity with this thesis.

A Comparative Study between Non-Radioactive Surrogates Neodymium and Mischmetal in Magnesium Borosilicate and Aluminosilicate Glasses

Sean T. Barlow¹, Adam J. Fisher¹, Martin C. Stennett¹, Claire L. Corkhill¹, Russell J. Hand¹, Sean P. Morgan² & Neil C. Hyatt¹

*1. Department of Materials Science & Engineering, The University of Sheffield,
Sheffield S1 3JD, UK*

2. Sellafield Ltd., Hinton House, Risley, Warrington WA3 6GR, UK

Abstract: The use of surrogates of uranium for use in the development of novel nuclear wasteforms has often included the lanthanide neodymium (Nd) or the rare-earth alloy mischmetal (Mm). Aluminosilicate and borosilicate glass melts were performed using Nd and Mm with comparable elemental composition and subject to the same analysis regime to determine the effectiveness and validity of using these substitutes in scientific studies of glass microstructure, morphology and dissolution behaviour within aqueous environments. Samples with significant quantities of metallic Nd and Mm (> 4 mol%) caused crystallisation within the glass to various boron and oxide phases which did not significantly affect the chemical durability of the glasses. Borosilicate samples showed the lowest residual dissolution rates, no greater than as $RL_{(B)}: (3.28 \pm 8.85) \times 10^{-2} \text{ g/m}^2/\text{d}$ and comparable to simulant UK high level waste glass. Mischmetal doped samples showed the lowest rates of dissolution, typically an order of magnitude less than neodymium doped glass.

4.1.1. Introduction

The United Kingdom has a significant inventory of hazardous nuclear wastes from its long history in nuclear power generation from 1953 to the present day. These wastes vary in nature but an important component of the inventory is residues and sludges arising from degraded nuclear fuels. To model and understand the key properties of new wasteforms for the immobilisation of such wastes, surrogate materials are utilised to approximate the behaviour of radionuclides in wasteforms when performing early stage feasibility studies, minimising the hazard and dose uptake. Neodymium, along with alloys or mixtures of lanthanides, are often used to replicate the use of uranium and other radionuclides such as americium and plutonium due to comparable ionic radii and oxidation/reduction behaviour [22], [110], [194]–[196]. Mischmetal (Mm), a rare earth alloy with a compositions of circa 50% Ce, 25% La and 25% Nd (trace Pr), also has great potential in this role as a surrogate for spent nuclear fuel [197]–[199]. This study will look to incorporate Nd and Mm surrogates into simulant glass wasteforms for UK Intermediate Level Waste (ILW).

Incorporation of significant quantities of uranium into wastes from the First Generation Magnox Storage Ponds (FGMSP) and Magnox Swarf Storage Silos (MSSS) at Sellafield is a significant problem with work currently underway to move the hazardous material to new safe buffer stores, Sludge Packing Plant 1 (SPP1) [5]. Bounding extremes for the composition of waste anticipated within the FGMSP and MSSS is shown in Table 4-1, with corroded waste representing Magnox fuel that has seen considerable hydrothermal alteration and metallic waste representing Magnox fuel with little corrosion consisting of primarily uranium and magnesium metal. Beyond the initial containment in temporary stores, the approach to final conditioning and disposal of the ILW sludges, is still to be defined. One promising approach, considered here, is thermal treatment via vitrification of sludges to produce a glass or slag like wasteform. Vitrification is often considered promising due to the enhanced passive safety

offered by immobilising radionuclides at the atomic scale within a glass structure, where very low dissolution kinetics can be achieved. The approximately 100,000 years nuclear waste needs to be isolated from the biosphere [70], [200] is potentially problematic for some cementitious materials which remain reactive and could affect the lifetime performance [10], this is not the case for vitrified materials, where natural analogues such as obsidian have been observed to endure these timescales [144], [201].

This study considers the use of uranium surrogates neodymium and mischmetal in comparable glass compositions, based on magnesium borosilicate (MBS) and magnesium aluminosilicate (MAS) pseudo-ternary liquidus phase diagrams [155], [156], [202] where a suitable, low temperature isotherm or glass forming region where ~40 wt% incorporation of MgO was identified in the MBS system and ~20 wt in the MAS system. The results of the synthesis of comparable glass samples containing uranium will be considered in a forthcoming publication.

Table 4-1. Bounding extremes waste composition from FGMSP and MSSS.

Composition	Corroded Waste (wt%)	Metallic Waste (wt%)
Mg	5	12
Mg(OH)₂	80	20
U	5	68
U₃O₈	10	0

4.1.2. Methodology

Borosilicate and aluminosilicate glass compositions doped with either neodymium or mischmetal (Mm) were created with two bounding extremes of the waste anticipated within the FGMSP and MSSS, resulting in the compositions shown in Table 4-2. The bounding waste scenarios, shown in Table 4-1, were used where Nd or Mm surrogates were added at an equivalent molar quantity to the expected U inventory, as Nd, Mm, Nd₂O₃ and Mm₂O₃ (mischmetal oxide).

All borosilicate glasses were batched without alumina; the Al₂O₃ content reported in Table 4-2 arises from corrosion of the alumina crucibles used during thermal synthesis. Aluminosilicate glass compositions included 1.6 mol% B₂O₃ to act as a tracer during dissolution experiments.

Reagents used for batching of glass samples, SiO₂, H₃BO₃ (Sigma-Aldrich 99.5 %), Na₂CO₃ (Alfa Aesar 98%), Al(OH)₃ (Acros 95%), Mg(OH)₂ (Sigma-Aldrich 95%), Nd₂O₃ (Sigma-Aldrich 99.9%), Mg (Acros 99.9%), Nd (Alfa-Aesar 99.1 %) and Mischmetal (Sellafield), were stoichiometrically weighed into sample bags and closely mixed for 1 minute. Each batch was placed into an alumina crucible and melted individually within an Elite Thermal Systems

BRF15/5 furnace. Based on previous work with base glass compositions without simulatant waste, Magnesium borosilicate samples were synthesised at 1250 °C for 3 hours and magnesium aluminosilicate samples at 1500 °C for 5 hours, before casting into bars and annealing for 1 hour. The borosilicate samples were annealed at 610 °C and the aluminosilicate samples at 560 °C. No mechanical stirring or bubbling of the melt was performed and the melts remained static (except for convection currents) during melting.

Elemental analysis of each sample, shown in Table 4-2, were determined by an inductively coupled plasma optical emission spectrometer (ICP-OES) after digestion into hydrofluoric acid, using powdered samples with a size fraction < 75 µm.

Table 4-2. Analysed and batched glass compositions studied.

Sample	Analysed oxide composition (± 0.2 mol%) [as batched]							
	SiO ₂	B ₂ O ₃	MgO	Na ₂ O	Al ₂ O ₃	Nd ₂ O ₃	Ce ₂ O ₃	La ₂ O ₃
MBS-C (Nd)	24.3 [25.2]	22.8 [24.7]	49.2 [49.2]	-	3.3 [0]	0.4 [0.9]	-	-
MBS-M (Nd)	27.1 [24.1]	21.1 [23.7]	42.8 [47.0]	-	4.0 [0]	4.9 [5.2]	-	-
MAS-C (Nd)	45.1 [45.6]	1.2 [1.6]	27.4 [28.3]	18.5 [18.4]	7.6 [5.6]	0.2 [0.5]	-	-
MAS-M (Nd)	42.4 [43.2]	1.3 [1.6]	23.8 [26.8]	16.0 [17.5]	12.2 [5.3]	4.4 [5.6]	-	-
MBS-C (Mm)	21.5 [25.3]	25.9 [24.8]	48.5 [49.4]	-	3.8 [0]	0.1 [0.1]	0.2 [0.3]	0.1 [0.1]
MBS-M (Mm)	21.1 [23.4]	23.3 [23.0]	47.4 [45.8]	-	4.4 [0]	0.9 [1.9]	1.9 [3.9]	1.0 [2.0]
MAS-C (Mm)	41.3 [45.7]	1.5 [1.6]	29.7 [28.4]	18.1 [18.4]	9.2 [5.6]	0.0 [0.1]	0.1 [0.1]	0.1 [0.1]
MAS-M (Mm)	42.3 [43.9]	1.5 [1.6]	25.7 [27.3]	15.9 [17.7]	11.5 [5.4]	0.6 [1.0]	1.7 [2.1]	0.9 [1.0]

Vitrified samples were crushed using a stainless-steel percussion mortar and sieved to a size fraction between 150 and 75 µm. Material less than this was ground using a pestle and mortar for characterisation.

Multi-scale characterisation included powder X-ray diffraction (XRD) using a Bruker D2 Phaser in reflectance mode for identification of any crystalline phases present. Scans over the range $10^\circ \leq 2\theta \leq 60^\circ$ using Cu K α radiation was used with a beam voltage of 30 kV and current of 10 mA. K β radiation was stripped using a built in Ni foil filter. Data were processed using the Bruker DiffracEva 3.0 software package with Crystallography open database [203] and

analysed using standards from the International Centre for Diffraction Data (ICDD) database [162].

Scanning electron microscopy (SEM) was combined with elemental dispersive X-ray spectroscopy (EDS) for identifying any phase separation or crystallisation using a Hitachi TM3030-SEM with semi-quantitative analysis performed by a Bruker Quantax EDS system. Samples were prepared for SEM-EDS by mounting in hard-setting resin and polishing to a 1 μm finish using SiC grit papers followed by diamond suspension polishing solution. To create a conductive surface, samples were splutter carbon coated and earthed using silver paint.

The density of vitrified powder samples was obtained using a Micromeritics Accucyc II 1340 helium pycnometer and 1 cm^3 sample chamber. Experiments were performed at room temperature with fill pressure of 82.7 kPa and 10 purges over 10 cycles with an equilibration rate of 0.034 kPa min^{-1} .

Thermal analysis was performed using a Netzsch TG 449 F3 Jupiter simultaneous thermal analyser, collecting both DTA and thermogravimetric (TG) data. Glass transition, T_g , crystallisation, T_c , and liquidus, T_L , temperatures were recorded. Experiments were performed up to 1500 $^\circ\text{C}$ under an argon atmosphere.

The ASTM Product Consistency Test B (PCT-B) protocol was applied to obtain glass durability [191]. Material with a size fraction between 150 and 75 μm was washed according to the standard protocol and subject to alteration for 28 days in ultra-high quality water at 90 $^\circ\text{C}$ with a surface area to volume ratio of 1200 m^{-1} . At each time point, aliquots of solution were obtained, and the pH was measured prior to acidification (conc. HNO_3) with analysis of dissolved elements by ICP-OES (Thermo-Fisher iCAP6300). The normalised mass loss of elements from the materials was determined according to:

$$N_{L,i} = \frac{C_i}{f_i \times (S_A/V)}$$

where $N_{L,i}$ is the normalised mass loss (g m^{-2}) of element i , C_i is the elementary concentration (mg L^{-1}) in the solution, f_i is the mass fraction of element i , and S_A/V is the ratio (m^{-1}) between the surface area of the glass (m^2) and the volume of solution used (m^3). The normalised dissolution rate, $R_{L,i}$ ($\text{g m}^{-2} \text{d}^{-1}$), is defined as the time-derivative of the normalised mass loss:

$$R_{L,i} = \frac{dN_{L,i}}{dt} = \frac{1}{f_i \times (S_A/V)} \times \frac{dC_i}{dt}$$

4.1.3. Results

Thermal Synthesis & Visual Observation

During melting of the batch material, no foaming or violent reactions between the metallic/corroded waste components and the batch were observed. Corrosion of alumina

crucibles in MBS samples was evident as the melt line on the crucible, causing alumina inclusion into these samples as demonstrated by the analysed composition data in Table 4-2. Corroded waste (-C) samples formed fluid melts and a visually homogenous glass with a blue/purple colour in the case of Nd, or an orange/yellow colour for Mm samples. No apparent crystallinity was observed by visual observation. A noticeable colour change was observed in Nd glass when subjected to different lighting conditions, with fluorescent lighting producing a clear-blue tone whilst natural or incandescent light caused the colour to change to a purple hue as shown in Figure 4-1; this dichromatic effect is due to sharp absorption of yellow and green light [38]. Mm samples did not exhibit this phenomenon.

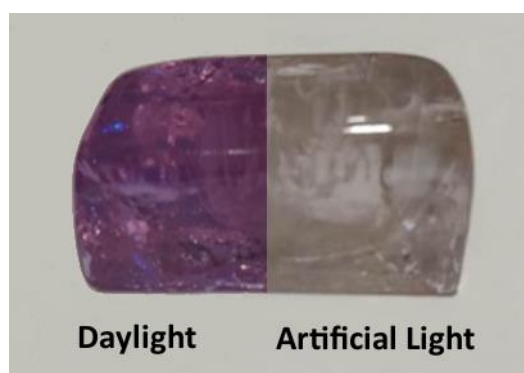


Figure 4-1. Dichromatic neodymium doped glass.

The metallic type waste glasses were more viscous than their corroded waste counterparts and formed a porous glassy-slag phase that was not fully incorporated into the glass melt. This resulted in a lower than batched amount of Nd and Mm uptake into the glass. The component of this melt that was investigated further was that which was successfully poured from the crucibles. The same colouration of samples was observed, with darker, more opaque, hues in the metallic waste samples and lighter hues from corroded waste samples. The metallic-type waste glasses appeared more crystalline by visual observation.

Phase Analysis

Corroded Waste Glass Samples

Corroded waste samples MBS-C (Nd), MBS-C (Mm), MAS-C (Nd) and MAS-C (Mm) were all X-ray amorphous and exhibited diffuse scattering between approximately $20^\circ \leq 2\theta \leq 40^\circ$. Asymmetric diffuse scattering was present in XRD data from MAS samples, split into two distinct components with maxima at 20° and 30° 2θ , indicative of phase separation. Figure 4-2 and Figure 4-3 show the diffraction data for all corroded waste samples, no distinct Bragg reflections caused by crystalline components were detected.

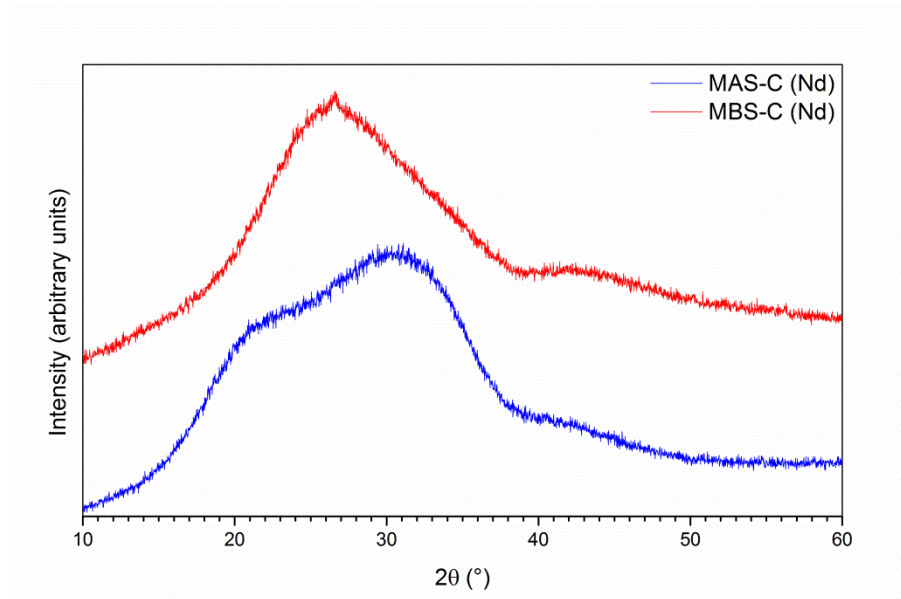


Figure 4-2. Powder X-ray diffraction data for Nd corroded waste samples.

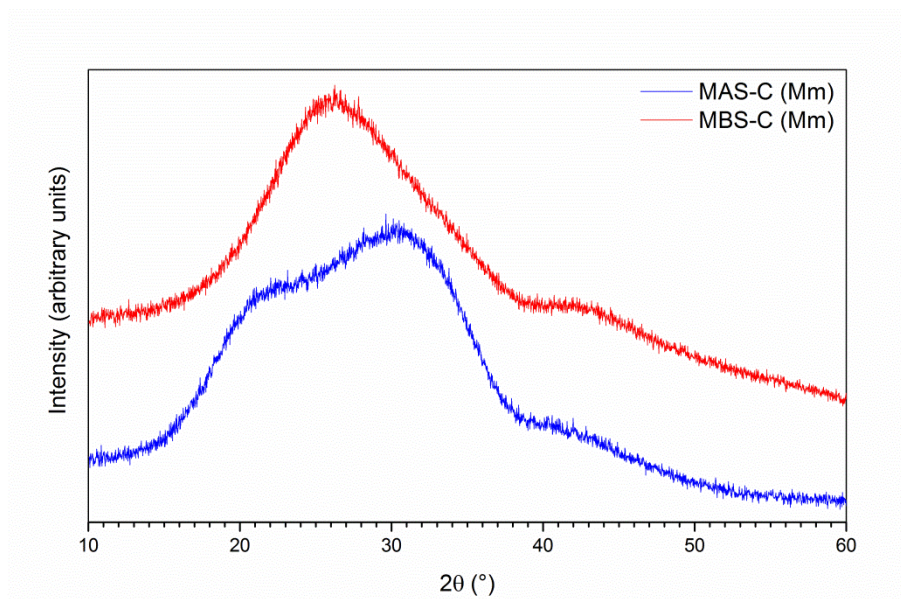


Figure 4-3. Powder X-ray diffraction data for Mm corroded waste samples.

MBS-C (Mm) was observed to exhibit distinct inhomogeneity as verified from variable contrast in back scattered SEM images (Figure 4-4). However, no crystalline inclusions were observed in any corroded waste sample. EDS analysis of the phase separation shows darker regions depleted in Al and mischmetal components, La, Ce and Nd, compared to the lighter phase. All other corroded waste type samples were homogeneous with an even distribution of all elements present, evidenced by the consistent greyscale contrast across the sample, as seen in Figure 4-5.

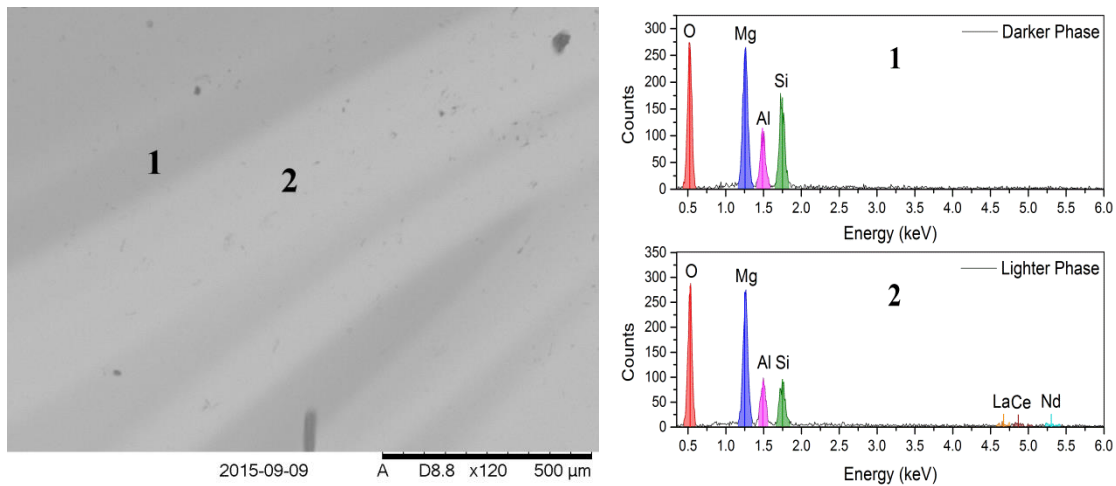


Figure 4-4. Backscattered SEM of inhomogeneous MBS-C (Mm) and EDS spectra for the marked points of interest.

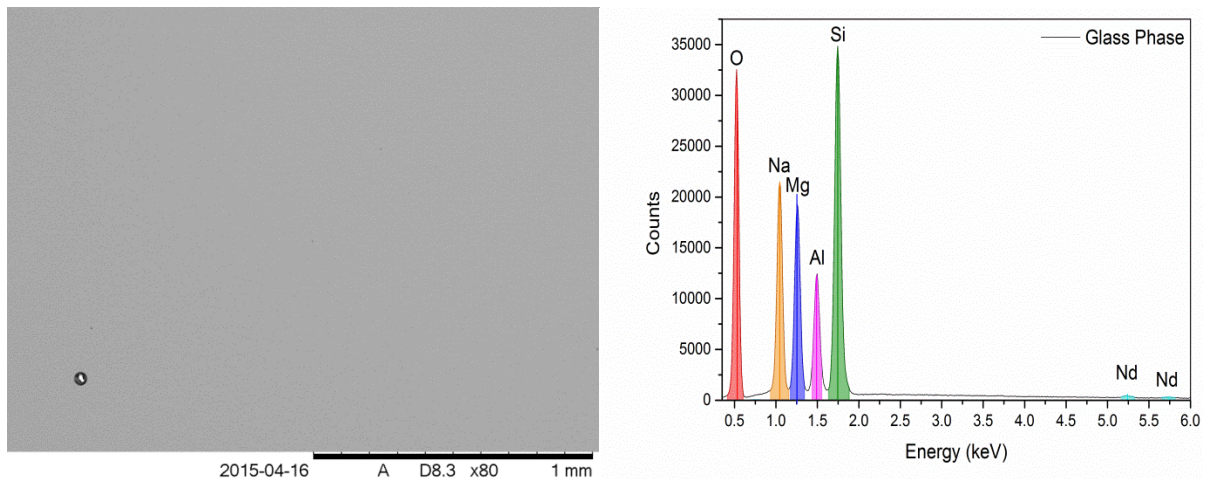


Figure 4-5. Backscattered SEM image of MAS-C (Nd) showing sample consistency. The small (50 μm) bubble in the bottom left corner is a relic from the casting process.

Metallic Waste Glass Samples

Mischmetal Samples

XRD patterns of the metallic mischmetal waste loaded compositions presented clear Bragg reflections present in addition to diffuse scattering arising from the amorphous glass (Figure 4-6). Bragg reflections in the XRD data indicated the presence of $Ce_{1-x}La_xB_{6-x/2}$, where $x=0.5$, in borosilicate compositions and $Ce_{1-x}Nd_xO_{2-x/2}$, where $x=0.3$, in aluminosilicate compositions; both crystalline phases consisted of components from the original mischmetal, namely La, Nd and Ce.

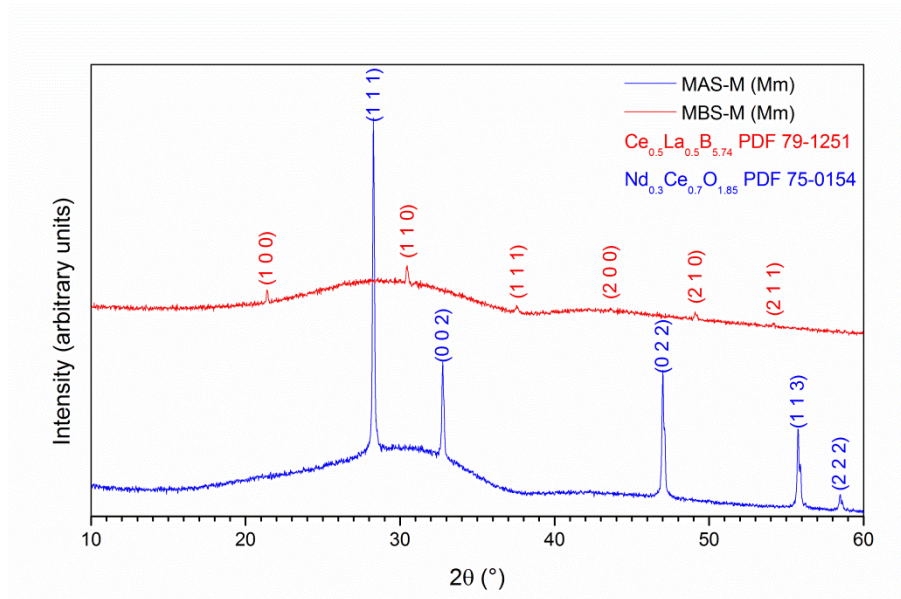


Figure 4-6. Powder X-ray diffraction data for metallic waste loaded Mm glass samples.

Small crystallites, $\sim 0.3 \mu\text{m}$ in diameter, were observed in backscattered SEM images of MAS-M (Mm), with complimentary EDS confirming the presence of Ce and Nd within this phase, see Figure 4-7. Also present were crystals $< 5 \mu\text{m}$ in size, also comprised of Ce, Nd and B, plus an Mg-Al-O phase (Figure 4-9); these phases were too low in concentration to be detected by XRD of the bulk sample. Figure 4-8 shows the presence of large ($< 10 \mu\text{m}$) Ce-Nd-B crystals present in MAS-M (Mm) glass via the backscattered image and EDS element maps whilst Figure 4-9 shows a Mg-Al-O phase present in the sample. In both images the scattered small white crystals are the crystallites shown in Figure 4-7.

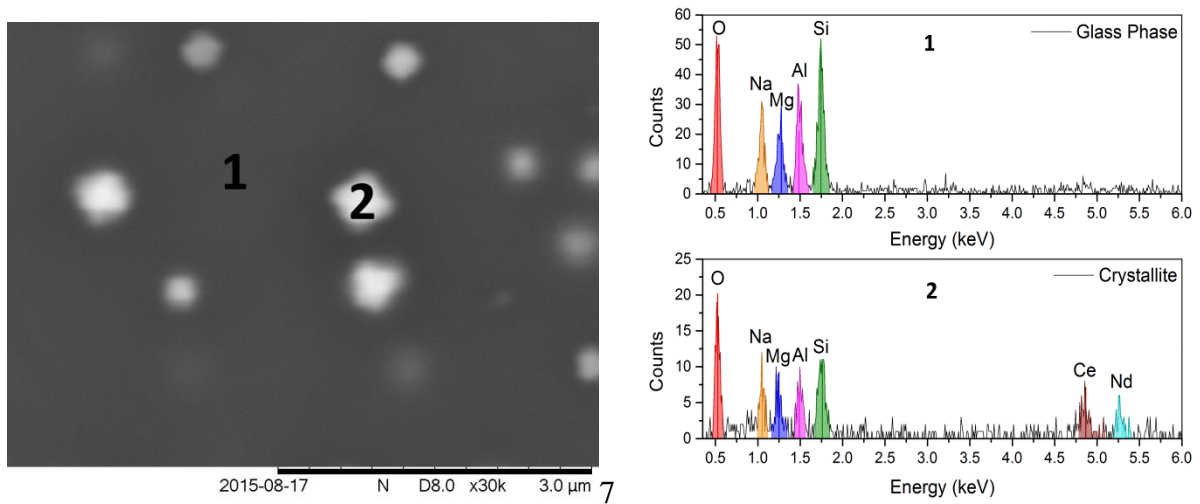


Figure 4-7. Backscattered SEM of MAS-M (Mm) showing $Ce_{1-x}Nd_xO_{2-x/2}$ crystallites and corresponding EDS Spectra.

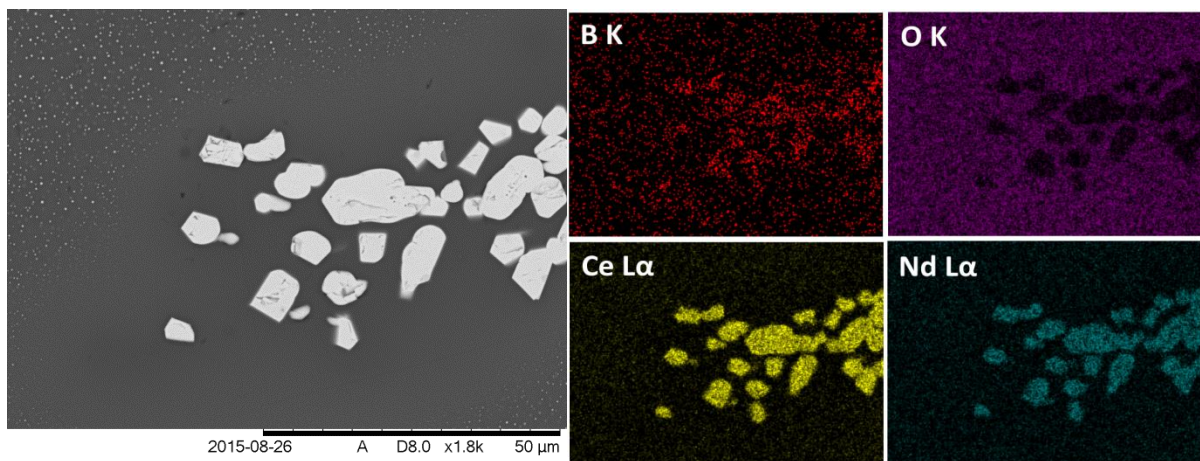


Figure 4-8. Ce-Nd-B crystals within SEM image of MAS-M (Mm) and corresponding EDS element maps.

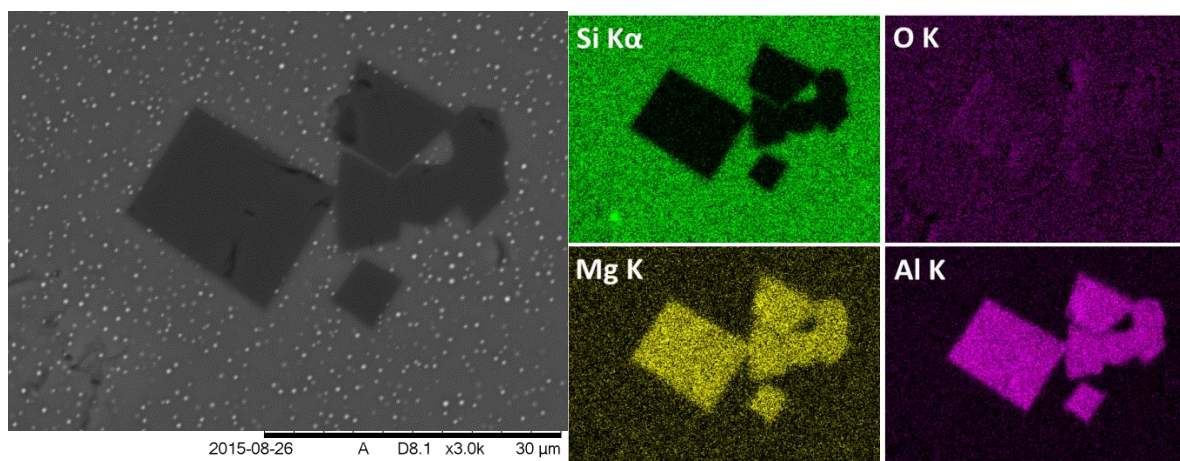


Figure 4-9. Mg-Al-O crystals within SEM image of MAS-M (Mm) and corresponding EDS element maps.

SEM images of MBS-M (Mm) sample shows crystallites $< 5 \mu\text{m}$ that are present in the glass matrix, supplementary EDS indicates these are composed of B, Ce, La and Nd as seen in Figure 4-10. This phase correlates with the $\text{Ce}_{1-x}\text{La}_x\text{B}_{6-x/2}$ phase identified by XRD.

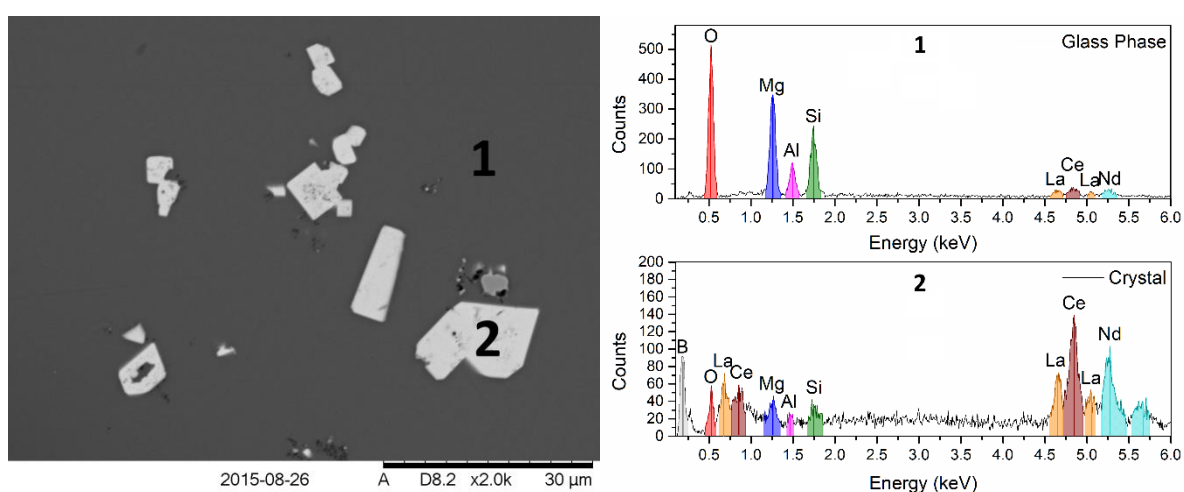


Figure 4-10. SEM image of MBS-M (Mm) and EDS spectra of regions of interest.

Neodymium Samples

XRD of metallic waste loaded neodymium compositions, MBS-M (Nd) and MAS-M (Nd) shows strong Bragg reflections inferring the presence of crystalline inclusions within the glass as seen in Figure 4-11. MBS-M (Nd) contained several crystalline phases with the ICSD database and DiffracEva software identifying $\text{Nd}(\text{OH})_3$, NdB_6 and Nd_2O_3 , whilst MAS-M (Nd) only contained the crystalline phase, $\text{Na}_{1+x}\text{Al}_{1+x}\text{Si}_{1-x}\text{O}_4$ where $x=0.45$. The presence of

$\text{Nd}(\text{OH})_3$ is likely due to hydration of Nd_2O_3 during sample storage and preparation, assisted by the high surface area of powders, $< 75 \mu\text{m}$ particle size, utilised for XRD.

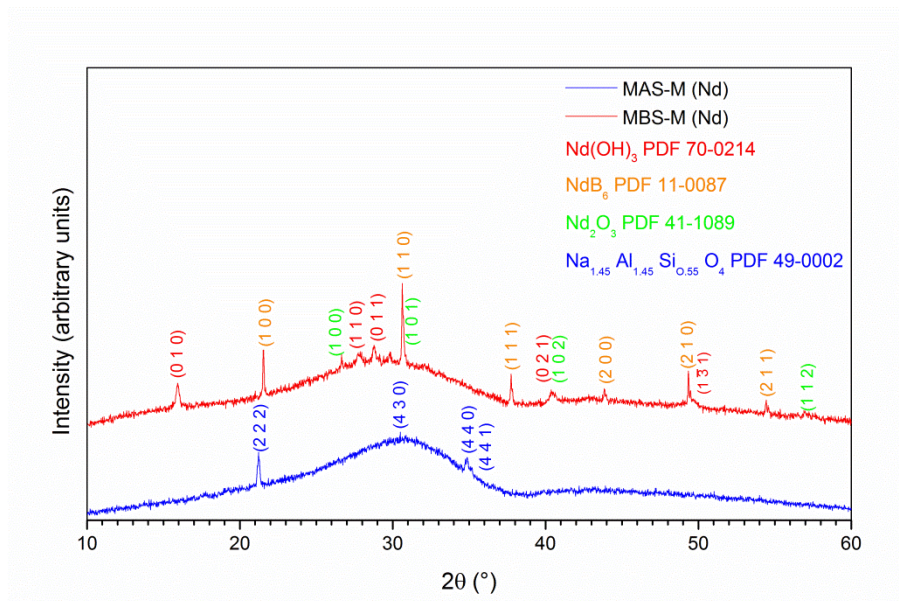


Figure 4-11. Powder X-ray diffraction data for metallic waste loaded Nd glass samples.

MAS-M (Nd) contains fractal-like crystalline formations along with homogeneous glass backscattered, as seen in Figure 4-12 A and Figure 4-12 B. High magnification SEM images and corresponding elemental mapping/EDS spectrum analysis (Figure 4-12 C and Figure 4-12 D) show darker regions are enriched in Si, Na and Al compared to the brighter regions which are enriched in Nd and Mg.

The analogous borosilicate glass, MBS-M (Nd) formed multiple crystalline phases by XRD, however only NdB_6 crystallites were observed in BSE images and from EDS analysis (Figure 4-13). NdB_6 crystallites had a sufficiently high B concentration to allow detection by the EDS system. This sample also exhibited a small amount of liquid-liquid phase separation, differentiated by back scattered electron contrast, however the compositional difference between each phase was too small to be distinguished by EDS as shown in Figure 4-13.

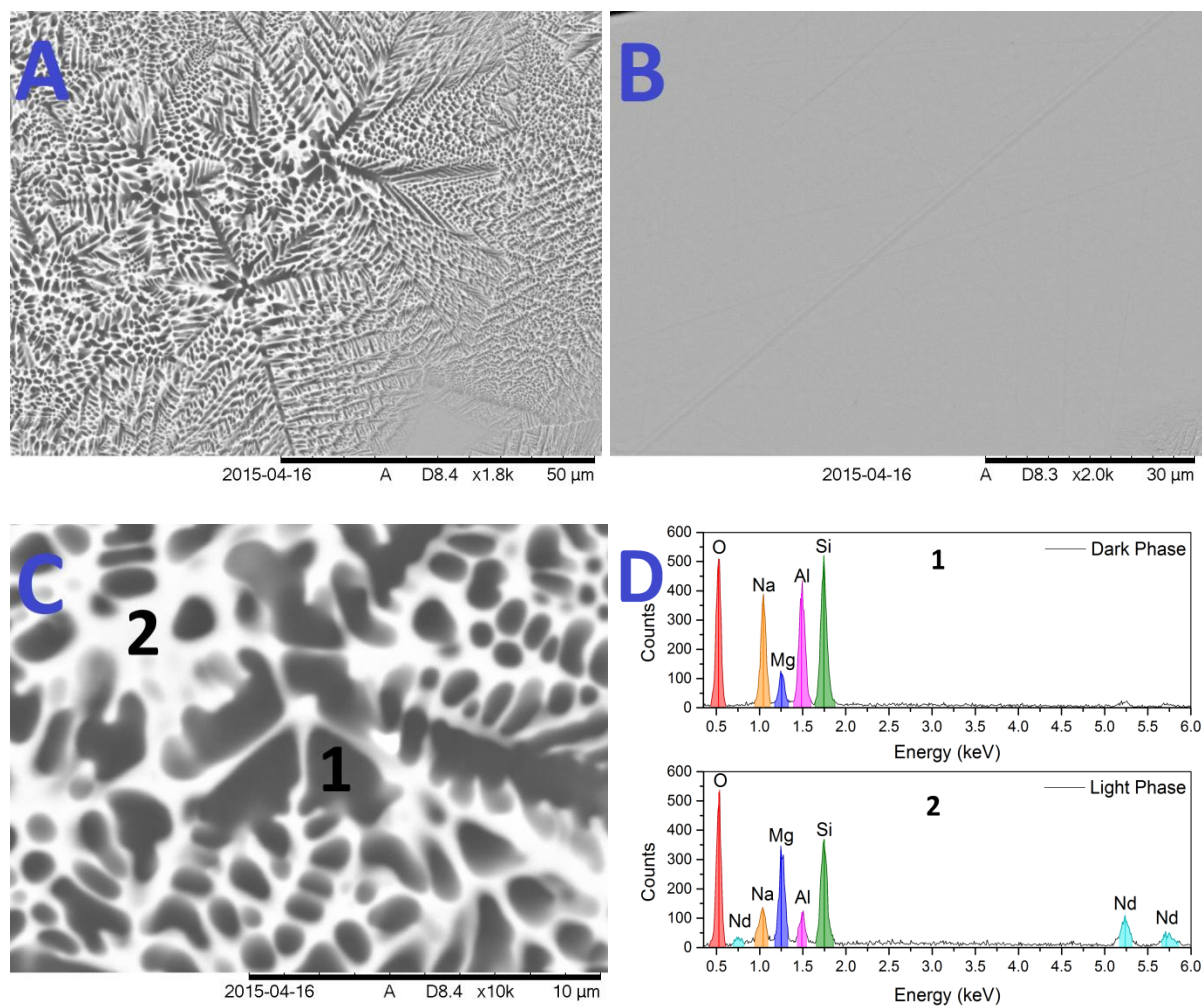


Figure 4-12. BSE micrographs highlighting various morphologies present within MAS-M (Nd). **A** – BSE image of crystalline phase. **B** – BSE micrograph of homogenous phase. **C** – High magnification BSE image of crystalline phase with light and dark phases labelled. **D** - Associated EDS spectra for the light and dark phases shown in C.

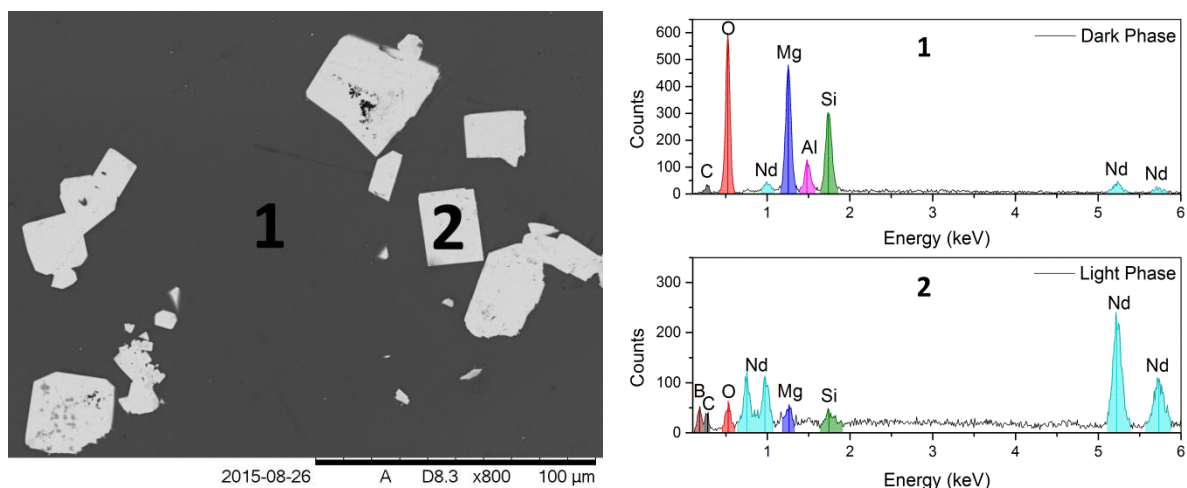


Figure 4-13. BSE images of MBS-M (Nd), exhibiting NdB_6 crystallisation and associated EDS spectra.

Thermal Analysis

A summary of results from thermal analysis are shown in Table 4-3 and DTA data collected is shown in Figure 4-14. Glass transition temperatures (T_g) were obtained from the point of maximum rate of slope for the first thermal event, crystallisation temperatures (T_c) were taken as the point of maximum intensity in exothermic events and the final liquidus temperature (T_{liq}) taken as the lowest point in intensity from the final endothermic event. Complementary thermogravimetric (TG) data showed no noteworthy mass loss upon analysis.

Table 4-3. Extracted thermal event temperatures for all samples.

Sample	Thermal Event ($^{\circ}\text{C}$) $\pm 5^{\circ}\text{C}$			
	T_g	T_{c1}	T_{c2}	T_{liq}
MAS-M (Nd)	669	786	853	1282
MAS-M (Mm)	668	812	846	1269
MAS-C (Nd)	617	837		1154
MAS-C (Mm)	628	834		1210
MBS-M (Nd)	669	810	1100	1130
MBS-M (Mm)	672	908	982	1163
MBS-C (Nd)	670	900		1150
MBS-C (Mm)	668	848		1142

All MAS samples were liquid only above 1200°C whilst all MBS samples were fully melted and liquidus below 1200°C . Crystallisation temperatures depend significantly on the sample composition, varying from 786°C to 1100°C with all metallic waste doped samples forming a second crystallisation peak. All metallic waste-loaded samples were observed to undergo two

exothermic events indicating the formation of multiple crystalline phases within the melt. Glass transition occurred at a similar temperature for all samples studied, with MAS samples having a slightly lower T_g than borosilicate counterparts.

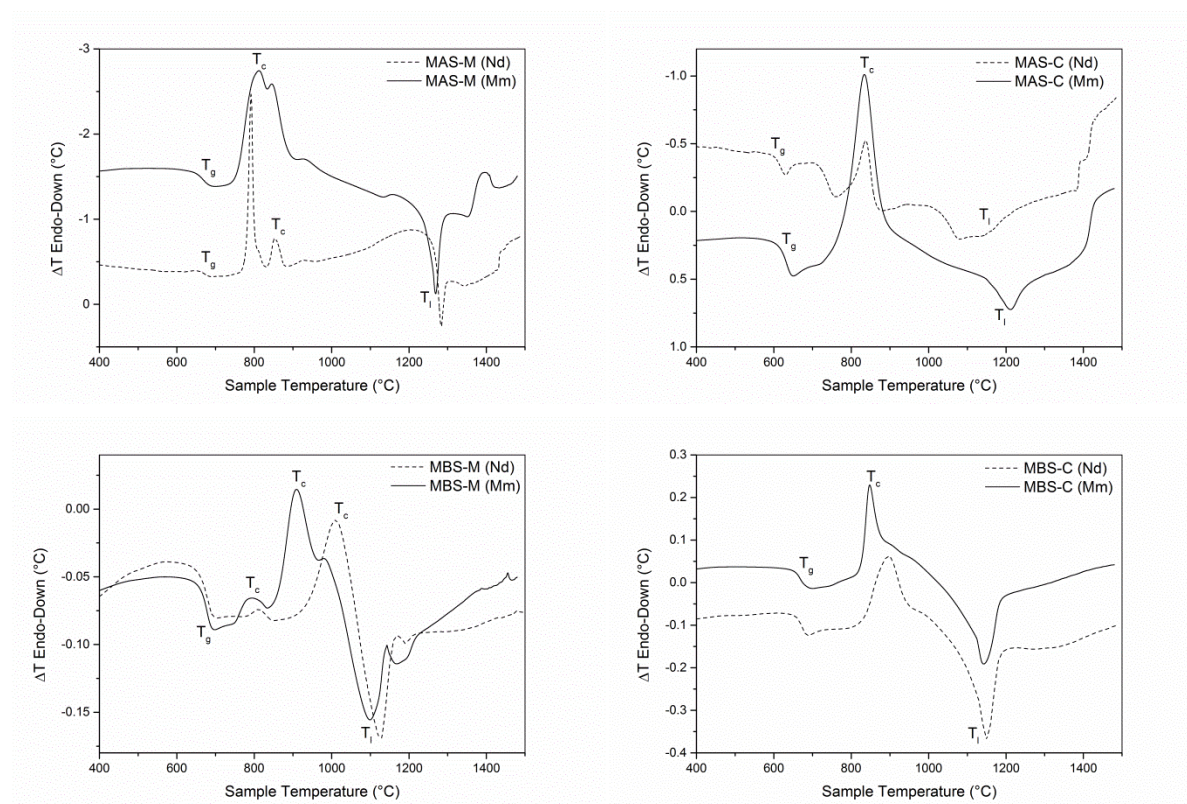


Figure 4-14. Collected DTA for samples created in the study, with glass transition (T_g), crystallisation (T_c) and liquidus points (T_l) labelled.

Helium Pycnometry & Waste Incorporation

Density measurements, by helium pycnometry on powdered samples, identified the metallic-type glasses have a higher density than those from corroded waste. Overall the effect of mischmetal or neodymium has little effect on the density of the glass, as can be seen in Table 4-4, however the determined density of borosilicate compositions are greater than that of the counterpart aluminosilicates glasses.

Incorporation of Nd, in the form of Nd_2O_3 , and Mm, in the form of Ce_2O_3 , La_2O_3 and Nd_2O_3 from both extremes of the waste was near identical in comparable samples (Table 4-2). From the analysed compositions obtained and shown in Table 4-2, the lowest Nd incorporation achieved was 1.2 wt% from MAS-C (Nd) and the highest was 24.1 wt% from MBS-M (Nd) whilst the lowest Mm waste incorporation achieved was 1.4 wt% from MAS-C (Mm) and the highest 18.8 wt% from MBS-M (Mm). It appears that generally Nd is better able to integrate into the glass network compared to Mm, and that borosilicate compositions are able to incorporate more of either Nd or Mm into the glass structure than aluminosilicate compositions.

Table 4-4. Measured density of glass compositions.

Sample	Average density (g.cm⁻³)
MAS-M (Nd)	3.034 ± 0.005
MAS-M (Mm)	2.964 ± 0.005
MAS-C (Nd)	2.625 ± 0.004
MAS-C (Mm)	2.650 ± 0.005
MBS-M (Nd)	3.164 ± 0.007
MBS-M (Mm)	3.101 ± 0.007
MBS-C (Nd)	2.684 ± 0.003
MBS-C (Mm)	2.697 ± 0.006

Aqueous Chemical Durability

The normalised mass loss (NL) of B, Mg and Si were determined for all samples along with the pH of the alteration solution, at various time points from PCT-B experiments. The rate of normalised mass loss of Nd, Ce and La were determined; no appreciable leaching of Ce and La was observed, while Nd leached from only one sample, MAS-C (Nd). A forward (0-7 day) and residual (7-28 day) dissolution rate for B, Si, Mg and Na were calculated and shown in Table 4-5, along with the average solution pH.

Table 4-5. Forward and residual dissolution rates with average pH.

Normalised forward dissolution rates (NR _i , g m ⁻² d ⁻¹)					
Samples	B	Si	Mg	Na	Average pH (±0.1)
MAS-M (Nd)	(1.01 ± 0.20) x 10 ⁰	(1.38 ± 1.95) x 10 ⁻²	-	(5.83 ± 1.84) x 10 ⁻¹	12.1
MAS-M (Mm)	(6.18 ± 3.77) x 10 ⁻²	-	-	(4.36 ± 5.00) x 10 ⁻²	11.6
MAS-C (Nd)	(1.10 ± 0.19) x 10 ⁰	(2.68 ± 0.36) x 10 ⁻¹	(2.57 ± 0.59) x 10 ⁻³	(5.31 ± 1.30) x 10 ⁻¹	12.0
MAS-C (Mm)	(8.64 ± 3.49) x 10 ⁻²	(1.32 ± 1.87) x 10 ⁻³	-	(4.37 ± 3.82) x 10 ⁻²	11.5
MBS-M (Nd)	(2.65 ± 1.02) x 10 ⁻¹	(1.45 ± 0.59) x 10 ⁻³	(3.50 ± 1.18) x 10 ⁻²	-	8.6
MBS-M (Mm)	(6.08 ± 3.42) x 10 ⁻²	-	(4.92 ± 4.54) x 10 ⁻³	-	8.7
MBS-C (Nd)	(5.94 ± 1.61) x 10 ⁻¹	(7.84 ± 2.86) x 10 ⁻⁴	(6.77 ± 1.82) x 10 ⁻²	-	8.7
MBS-C (Mm)	(6.18 ± 4.03) x 10 ⁻²	-	(6.99 ± 5.48) x 10 ⁻³	-	8.6
Normalised residual dissolution rates (NR _i , g m ⁻² d ⁻¹)					
Samples	B	Si	Mg	Na	Average pH (±0.1)
MAS-M (Nd)	(7.12 ± 0.76) x 10 ⁻²	-	-	(4.78 ± 6.41) x 10 ⁻²	12.6
MAS-M (Mm)	(1.27 ± 0.85) x 10 ⁻²	-	-	(1.09 ± 1.01) x 10 ⁻²	11.6
MAS-C (Nd)	(8.32 ± 0.76) x 10 ⁻²	(5.05 ± 2.24) x 10 ⁻³	(3.41 ± 0.45) x 10 ⁻³	(3.40 ± 4.75) x 10 ⁻²	12.5
MAS-C (Mm)	(1.46 ± 0.85) x 10 ⁻²	(1.19 ± 0.70) x 10 ⁻³	-	(1.24 ± 0.82) x 10 ⁻²	11.6
MBS-M (Nd)	(7.06 ± 0.33) x 10 ⁻³	-	(5.69 ± 6.51) x 10 ⁻³	-	8.5
MBS-M (Mm)	(3.11 ± 0.71) x 10 ⁻³	(2.59 ± 0.80) x 10 ⁻⁵	(5.12 ± 8.89) x 10 ⁻⁴	-	8.6
MBS-C (Nd)	(3.28 ± 0.89) x 10 ⁻²	(2.24 ± 1.36) x 10 ⁻⁴	(5.44 ± 10.2) x 10 ⁻³	-	8.6
MBS-C (Mm)	(4.83 ± 0.83) x 10 ⁻³	(3.26 ± 0.54) x 10 ⁻⁵	-	-	8.6

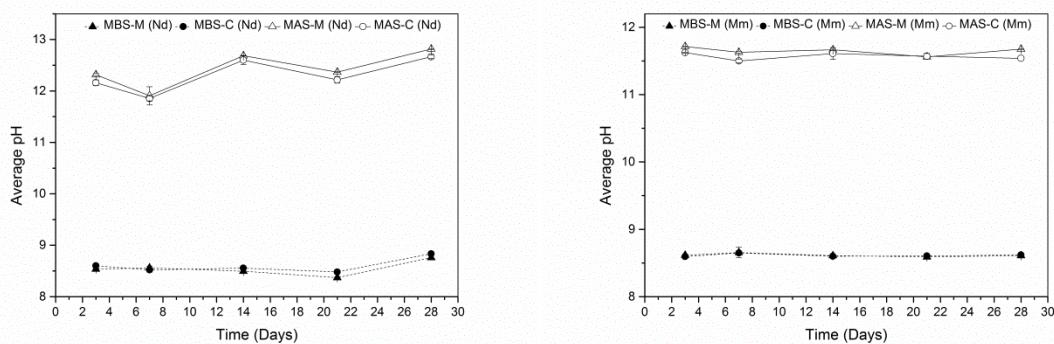


Figure 4-15. Average pH of Nd (left) and Mm (right) samples during PCT-B experiments.

The average pH of the leachate solution from each experiment buffered quickly to an almost constant pH (± 1 pH unit) and did not deviate significantly throughout the 28 days. Leachate from aluminosilicate samples was considerably more alkaline (pH 11.5-12.4) than leachate originating from the borosilicate samples (pH 8.5-8.7), as shown in Figure 4-15. This difference is due to leaching of Na ions from the aluminosilicate glass network; borosilicate samples did not contain Na and consequently the leachate was less alkaline. The initial leachate, and blank samples leachate, was on average pH 6.95.

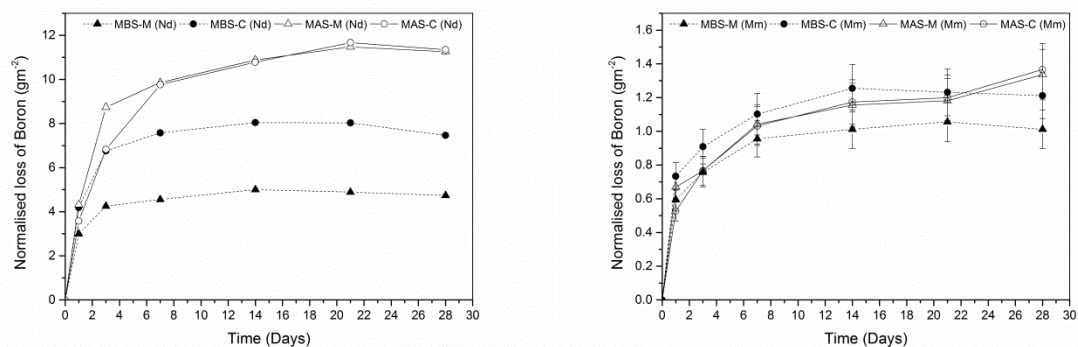


Figure 4-16. Normalised mass loss of B from Nd (left) and Mm (right) samples as a function of time.

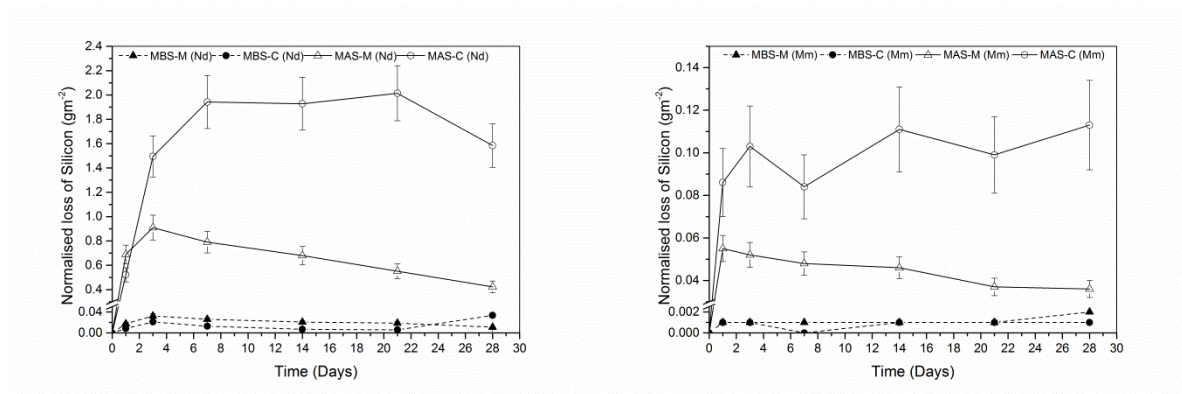


Figure 4-17. Normalised mass loss of Si from Nd (left) and Mm (right) samples as a function of time.

The normalised mass loss of major structural glass components, B and Si, is shown in Figure 4-16 and Figure 4-17. With Nd loaded samples, the normalised mass loss of B from MAS-M (Nd) glass was three times greater than in the borosilicate counterpart MBS-M (Nd), and B release from MAS-C (Nd) was almost twice that of MBS-C (Nd). The normalised mass loss of B from Mm compositions was between 75% and 90% lower than the equivalent Nd loaded compositions. Little to no release of Si was detected from MBS glasses whilst the equivalent MAS compositions released an order of magnitude more Si into solution. The normalised mass loss of Si was reduced by a factor of 20 in Mm glass compositions, compared to their Nd counterparts.

The high normalised mass loss of Na of from MAS compositions results in rapid buffering of the solution to pH 11 – 12, compared to ca. pH 8.5 for MBS compositions, consequently the greater normalised mass loss of Si from MAS compositions is a result of both the higher hydroxide concentration, responsible for nucleophilic attack on and release of Si from the glass network, and greater solubility of silica at high pH [82], [204]. After approximately 7 days the rate of change in mass loss of Si generally decreases, as shown in Figure 4-17, signifying saturation of the leachate and steady state conditions have been approached or that Si has precipitated out of solution and formed passivating alteration layers on the surface of glass particles (as shown in Figure 4-19), increasing the resistance to further dissolution of the glass network.

The normalised mass loss of Mg from both Nd and Mm compositions follow comparable trends with borosilicate glasses leaching more into solution than aluminosilicate counterparts, as seen in Figure 4-18. The rate of normalised loss of Mg reduces after approximately 7 days, akin to B and Si, signifying leachate saturation and the formation of Mg containing alteration layers.

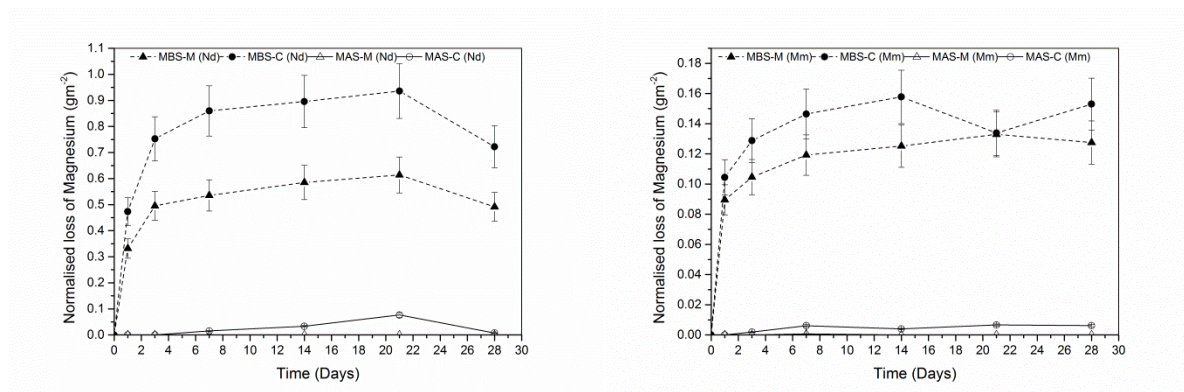


Figure 4-18. Normalised mass loss of Mg from Nd (left) and Mm (right) samples as a function of time.

SEM-EDS analysis of 28 day altered glass samples identified alteration layers in MAS-C (Nd) with a thickness of 8 μm from the pristine glass to water-surface interface; see Figure 4-19. Alteration layers were also observed in MBS-C (Mm), with a thickness no greater than 1 μm (Figure 4-20), too small for detailed EDS analysis. Constituent elements of the glass are present in the alteration layer and distributed evenly throughout, as evidenced by the consistent greyscale in BSE images and distribution of elements from EDS maps shown in Figure 4-19. The only exception was Na where an increased concentration at the water-surface interface occurred. Dehydration of the alteration layer is apparent from shrinkage and pull-away from the bulk glass, evidenced by a dark band in BSE images at the glass-alteration interface in Figure 4-19 and Figure 4-20.

No alteration layers were detected in 28 day aged metallic waste loaded samples from either Nd or Mm glasses, indicating these samples are more resistant to aqueous corrosion. This is evidenced by lower normalised loss of B and Si for metallic waste glass samples as shown in Figure 4-16 and Figure 4-17.

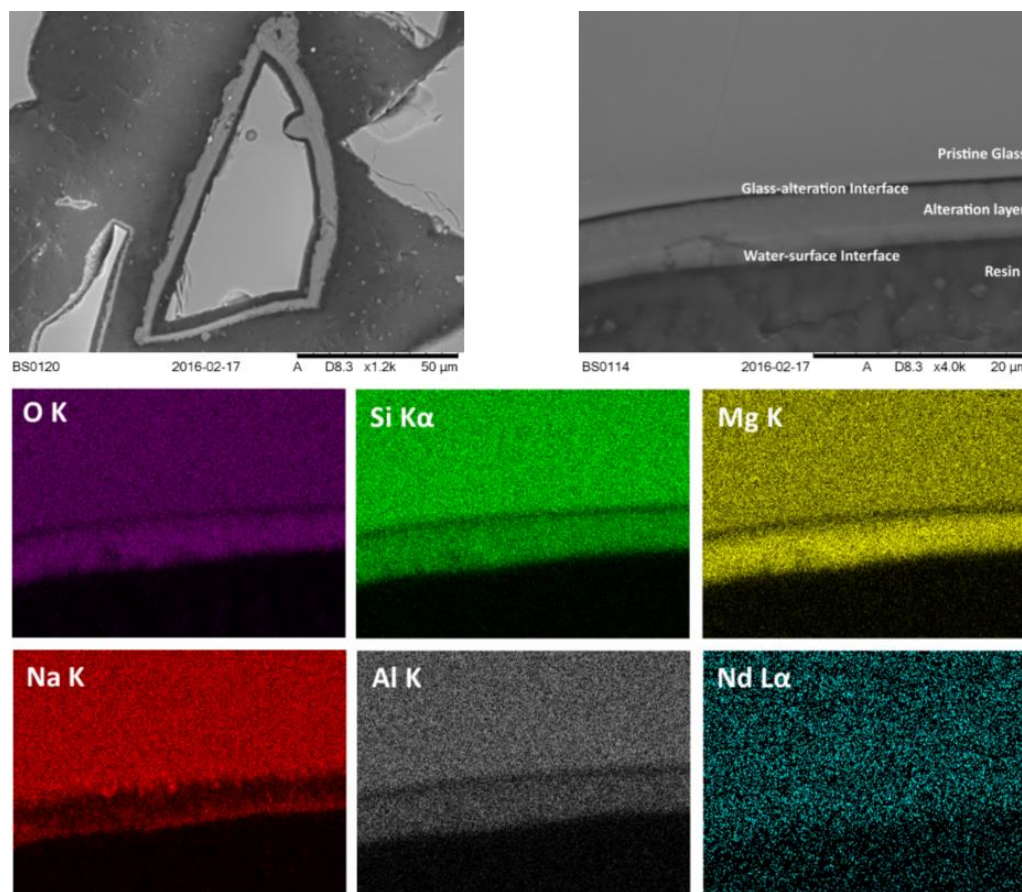


Figure 4-19. BSE micrographs of alteration layers on MAS-C (Nd) glass after 28 days and corresponding EDS maps.

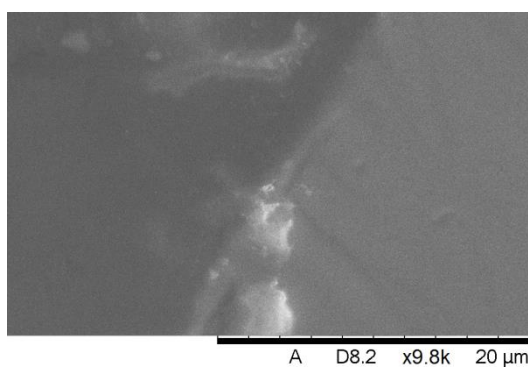


Figure 4-20. BSE image of alteration layers on MBS-C (Mm) after 28 days.

Altered glass samples from the 28 day experiment were analysed by XRD to investigate alteration of the incorporated crystalline phases and the formation of precipitated secondary alteration products. XRD analysis of the 28 day altered Nd samples showed no change in phase

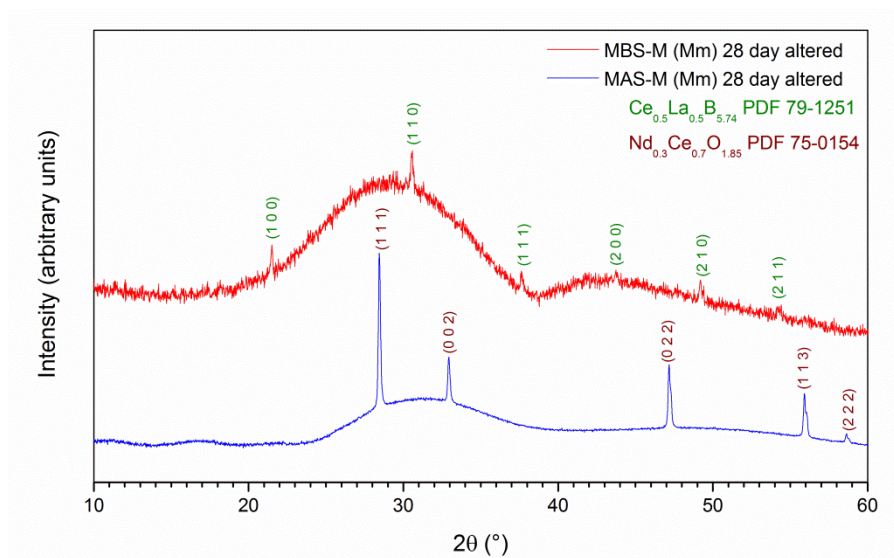


Figure 4-23. XRD pattern for Mm doped metallic waste glasses after 28 day alteration.

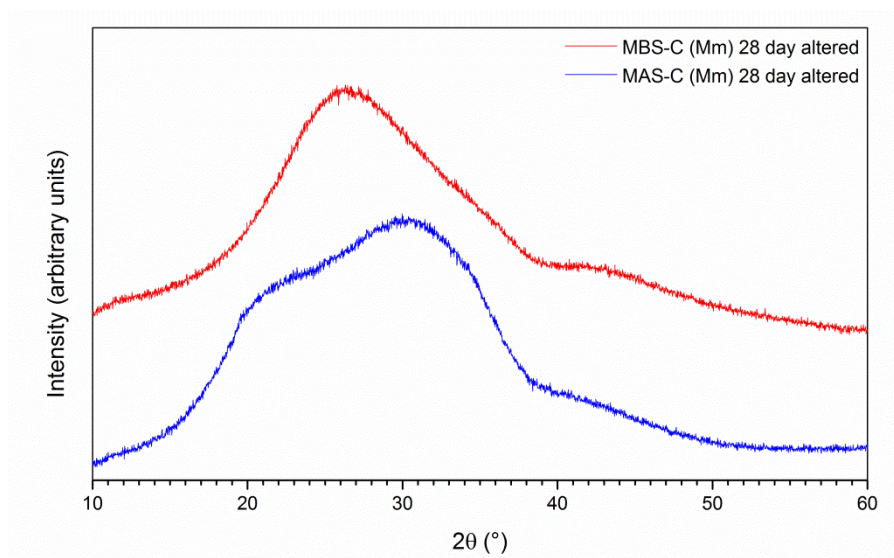


Figure 4-24. XRD pattern for Mm doped corroded waste glasses after 28 day alteration.

4.1.4. Discussion

Thermal Synthesis & Visual Observation

Borosilicate glasses were produced at temperatures comparable with current High level waste (HLW) operations below 1200 °C [200], without the use of typical glass fluxes such as Na, due to the high concentration of boron, > 21 mol% in the final glass (see Table 4-2), allowing lower melting temperatures. Aluminosilicate glasses required temperatures slightly above 1200 °C, based on DTA results, for form a fluid melt due to the more refractory nature of alumina; the presence of Na₂O acts to reduce the melt temperature but Al₂O₃ negates this to necessitate an

increase in temperature. The addition of either Mm or Nd made no effect on the final liquidus temperature, see Table 4-3 and Figure 4-14.

Samples produced from metallic waste formed crystalline glasses and slag-like phases, whilst all corroded waste samples formed visually homogenous glass, free from crystallinity. MBS-M (Mm) reacted with silica to form a slag like phase not incorporated into the bulk glass whereas MBS-C (Mm) is fully vitrified; as evident from the difference between analysed and batched compositions in Table 4-2.

It is unlikely these samples would be reproducible within a conventional glass melter due to the method of introducing glass forming agents into the waste before melting, rather than the conventional waste vitrification techniques of blending waste with a pre-prepared glass frit before vitrification [36]. However, this composition would be reproducible in modern Geomelt or other in-container vitrification technology [197], [205], and has been demonstrated in trials of vitrifying Magnox sludges as outlined by Matlock et.al [194].

Phase Analysis

Metallic waste compositions contained various crystalline phases as observed from XRD analysis, shown in the summary Table 4-6 below; these phases were verified by SEM-EDS analysis. $\text{Na}_{1.45}\text{Al}_{1.45}\text{Si}_{0.55}\text{O}_4$, also known as nepheline, identified from XRD of MAS-M (Nd) was detected as a dark phase in SEM micrographs (Figure 4-12 A & C) and subsequent EDS (Figure 4-12 D). This is a phase known to form in commercial nuclear waste glass, and is generally deleterious for aqueous durability [206]–[208]. The NL_B results obtained show leaching for MAS-M (Nd) was high compared to MAS-M (Mm), which may be linked to the presence of this phase. $\text{Nd}_{0.3}\text{Ce}_{0.7}\text{O}_{1.85}$ from MAS-M (Mm) was observed in SEM micrographs as small crystallites distributed throughout the glass (Figure 4-7), however a Ce, Nd and B crystalline phase and Mg, Al and O phase were also observed (Figure 4-8 & Figure 4-9) that were not detected in XRD data. Since these phases were observed infrequently within the sample they are likely below the detection limit for XRD.

Various phases including $\text{Nd}(\text{OH})_3$, NdB_6 and Nd_2O_3 were present within MBS-M (Nd) by XRD analysis, with the boride phases observed in SEM micrographs and EDS spectra, note the carbon content within the EDS map (Figure 4-13) was due to carbon coating of samples to ensure sample surface conductivity. $\text{Nd}(\text{OH})_3$ is likely formed from exposing Nd_2O_3 , during the crushing process in order to create powdered samples, which hydrated to form small quantities of $\text{Nd}(\text{OH})_3$. These phases were not observed in MAS-M (Nd) due to the higher temperature melt conditions fully oxidising and digesting Nd into the glass with no Nd oxide phases formed (Figure 4-11).

All corroded waste samples, with either Mm or Nd feed, were X-ray amorphous by XRD analysis, indicating successful oxidation and incorporation of metallic components into the bulk glass with no resulting crystallinity or sharp Bragg reflections. Striations observed from BSE images of MBS-C (Mm) were caused by the sample not being fully homogenised due to

insufficient mixing of the melt by thermal currents alone; mechanical stirring or bubbling of the melt would reduce this, improving the mixing of the mischmetal components identified in the lighter phase into the bulk glass. Such heterogeneous glass samples are often seen in the nuclear industry with waste glass often possessing a heterogeneous microstructure, and do not pose a fundamental challenge to disposability [209], [210]. The increased Al and Mm content in the lighter phase of MBS-C (Mm) was likely to have resulted from interaction between the alumina crucible and Mm components at the melting temperature. This was not observed in the Nd doped counterpart despite uptake of a similar amount of Al₂O₃ from corrosion of the crucible (Table 4-2), suggesting more agitation of the melt is required to incorporate Mm compared to Nd. Higher temperatures required by the equivalent aluminosilicate samples resulted in greater thermal currents and better mixing of the melts resulting in a more homogenous sample, as observed in Figure 4-5.

Table 4-6. Summary of phases observed in all samples by XRD analysis.

Sample	Phases Present by XRD
MAS-M (Nd)	Na _{1.45} Al _{1.45} Si _{0.55} O ₄
MAS-M (Mm)	Nd _{0.3} Ce _{0.7} O _{1.85}
MAS-C (Nd)	Amorphous
MAS-C (Mm)	Amorphous
MBS-M (Nd)	Nd(OH) ₃ , NdB ₆ , Nd ₂ O ₃
MBS-M (Mm)	Ce _{0.5} La _{0.5} B _{5.74}
MBS-C (Nd)	Amorphous
MBS-C (Mm)	Amorphous

Thermal Analysis

Similar (± 50 °C) glass transition temperatures for all samples were obtained from extracted DTA data, however the first exothermic recrystallisation point occurred at a higher temperature in borosilicate glasses than aluminosilicates (Table 4-3). A second exothermic event was only observed in metallic waste samples, this temperature is likely associated with the growth of the crystalline phases observed from XRD and SEM-EDS data, since amorphous samples were obtained from glass that exhibited no second T_c. Higher melting temperatures were required to create liquidus aluminosilicate melts compared to borosilicates, this is reflected in DTA data showing T₁ above 1200 °C in most cases. This increase in temperature is due to the presence of Al₂O₃ and SiO₂ in greater concentrations and lower B₂O₃ content compared to borosilicates samples, which is assumed to create a more polymerised melt due to the increased content of network-forming cations. The flux effect from Na₂O is offset by the greater concentration of refractory Al₂O₃. No significant mass loss from thermogravimetric analysis indicates volatilisation of the batch components has not occurred upon melting, improving the safety case for these glass compositions were they to be employed commercially.

Dissolution & alteration

Release of Na in significant quantity, $> 4 \times 10^{-2} \text{ g m}^{-2} \text{ d}^{-1}$, is responsible for the increased pH of leachate from the aluminosilicate samples compared to that from borosilicate samples. This impacts the overall glass durability with higher pH conditions increasing nucleophilic attack and solubility, with glass dissolution increased as a result, as observed in the forward and residual dissolution rates of boron (Table 4-5) and the from the normalised loss of boron in Figure 4-16. The presence of the crystalline phase nepheline in MAS-M (Nd) is one potential cause for the high leaching rates observed for this sample, having the second highest boron dissolution rate and the highest sodium dissolution rate.

In general, corroded waste samples had a higher normalised loss of B, Si and Mg than their metallic waste counterparts, and corresponded with the presence of alteration layers shown in Figure 4-19 and Figure 4-20. The lack of alteration layers and lower leach rates in metallic waste samples indicate these samples are more resistant to aqueous corrosion.

Compared to the HLW simulant glass MW-25, with a reported boron release rate of $2.4 \times 10^{-2} \text{ g m}^{-2} \text{ d}^{-1}$ [209], the rates observed in this study are comparable and for all borosilicate samples are lower than that of the HLW simulant, which is considered promising from a disposability standpoint. The total activity of vitrified Magnox HLW, according to the NDA waste stream datasheets [211] is $\sim 170 \text{ TBq m}^{-3}$ of α and $\sim 35,600 \text{ TBq m}^{-3}$ of $\beta\gamma$ nuclides whilst for ILW glasses, using the Magnox sludge wastes described in this study [89], [212] with waste loading of 25%, the total activity would be $\sim 1 \text{ TBq m}^{-3}$ of α and $\sim 43 \text{ TBq m}^{-3}$ of $\beta\gamma$ nuclides, over 2 orders of magnitude lower than HLW glass wasteforms. Taken together, these data imply that the repository source term of the conceptual vitrified borosilicate glass wasteforms developed here for Magnox sludges, should meet the expected waste acceptance criteria.

No detectable release of Nd, Ce and La was observed from any of the conceptual wasteforms, except for MAS-C (Nd) where the maximum loss of Nd did not exceed 0.012 g m^{-2} over the 28 days. The leaching of Nd from this composition is likely due to the high NL_{Si} experienced during dissolution effectively breaking down the glass structure. In other compositions, negligible leaching of the waste simulants indicates these components remain in or with the wasteform possibly in an alteration layer as a stable phase. Unfortunately, no such phase could be observed from SEM-EDS of 28 day altered samples, Figure 4-19 and Figure 4-22 revealing mostly homogenous alteration regions and X-ray amorphous glass within the only sample to demonstrate leaching of any waste component. The concentration of Na was enriched at the water-surface interface of glass alteration layers indicating sodium ions have freely migrated from the glass into solution, evidenced by the high pH observed for all aluminosilicate samples. This enrichment is likely due to the samples solution reaching saturation in Na and precipitating back onto the water-surface interface as Stage II dissolution. Due to this effect, it is likely the alteration layers are non-passivating.

B and Si leaching was over ten times greater from Nd samples compared to Mm doped samples (Figure 4-16 & Figure 4-17) implying mischmetal creates a more connected glass

network and is therefore more durable with lower overall rates of dissolution of the key glass components.

Alteration layers observed on aluminosilicate glass samples were clearly apparent, see Figure 4-19 and Figure 4-20, whilst lower rates of dissolution were observed for borosilicate glasses. It is therefore assumed the alteration layers formed are not fully passivating since their formation between day 1 and day 7 acts only to reduce the dissolution to the steady state regime, along with saturation of the leachate solution. Single-pass flow-through tests would remove the effects of sample saturation and help to understand the dissolution kinetics further [78], [213].

Analysis of 28 day leached samples from the PCT experiment shows no change in the XRD pattern for any sample. A subtle shift in peak positions for the $Ce_{0.5}La_{0.5}B_{5.74}$ phase is evident when compared to the unaltered sample, which could be linked a change in the stoichiometry of this phase due to hydrothermal alteration. Since this particular sample has low rates of dissolution, as identified from Table 4-5, the change in stoichiometry of this phase does not affect the overall glass durability. No mischmetal or neodymium components were identified implying the waste components preferentially remain in the glass phase, or form crystalline phases in such low quantities to avoid detection by either XRD or SEM-EDS.

4.1.5. Conclusions

Presented in this work are two glass networks, magnesium borosilicate and magnesium aluminosilicate, that have been doped with mischmetal or neodymium in two waste loading regimes, corroded or metallic waste, forming a suite of 8 samples. The samples were successful in demonstrating incorporation of waste simulant components into glassy products that suffered crystallisation when loaded with a majority of metallic waste yet formed amorphous glass when loaded with corroded type waste. This effect was evident with the use of either surrogate waste material.

Magnesium borosilicate samples, with either mischmetal or neodymium, could be melted and cast below 1200 °C, but often consisted of inhomogeneity from lack of mechanical stirring or mixing of the melt, whilst aluminosilicate samples required higher melting temperatures but could self-mix effectively. Lower temperatures preferred by the nuclear industry necessitate the use of borosilicate samples going forward [36], [214], stirring or bubbling of the melts would improve the homogeneity of the product. However it is noted that scaling up the volume of a glass melt would increase thermal currents enabling better mixing. Nevertheless, heterogeneous wasteforms are typical products of pilot scale ILW vitrification trials and compositional gradients and occluded porosity are not considered to be a fundamental challenge to the safety case for storage and disposal [215].

The effectiveness of mischmetal as a surrogate for uranium on studies on microstructure and morphology can be validated by observation of oxide crystalline phases, as observed in studies

on uranium loaded compositions [216] whilst neodymium samples formed both oxide and boride phases. By comparison of dissolution rates of key elements from this study with that of other studies [209], both neodymium and mischmetal result in analogous rates. The processing temperatures of both glass systems are comparable to that of real ILW [217]

Crystallinity observed in mischmetal doped samples MAS-M (Mm) and MBS-M (Mm) did not significantly alter the chemical durability of the glass system, with these samples having the lowest normalised loss of key elements and lower rates of glass dissolution compared to those doped with neodymium. In general, metallic waste loaded samples had greater durability than corroded sample, with an exception is made for MAS-M (Nd) where nepheline formation results in higher NL_B and NL_{Na} (Table 4-5 & Figure 4-16). The formation of altered regions on the glass-water interface did not significantly suppress dissolution rates over the 28 day test and sodium ions were found to pass through the layer and accumulate at the water-surface interface. Overall borosilicate glass, with either mischmetal or neodymium, were found to be more chemically durable than the aluminosilicate equivalents with a performance analogous to UK HLW simulant glass, supporting the use of borosilicate samples in future trials and experiments.

Mischmetal samples were more chemically durable than those with neodymium and showed little alteration over 28 days of accelerated leaching however would require mechanical mixing to form a homogenous glass unlike those doped with neodymium. A more simplistic range of oxide crystalline phases were formed within mischmetal doped glasses whereas crystallisation within neodymium glasses was more complex, forming both oxide and boride phases within the same composition, not commonly observed in uranium bearing waste glasses. The use of both neodymium and mischmetal can be seen as effective dependent on the composition being studied and the conditions of the experiment

4.1.6. Acknowledgments

The authors would like to thank the EPSRC (Grant EP/G037140/1) for funding this research which was performed in part at the MIDAS Facility, at the University of Sheffield, established with support from the Department of Energy and Climate Change.

4.2. Draft Paper: Thermal Treatment of Magnox Sludge Intermediate Level Nuclear Waste through Vitrification

This work takes the form of a draft paper written in the style for publishing in the Journal of Hazardous Materials. This work was written by myself with the aid of co-authors for feedback and comments. All of the sample preparation and analysis was performed by myself with the exception of the acquisition of chemical composition of glass which was performed on my behalf by Sheffield University Chemistry Department and the collection of X-ray absorption spectroscopy data which was performed by co-authors Daniel Bailey and Martin Stennett at the Paul Scherrer Swiss Light Source Facility, Switzerland.

The article presented here is has references, figures and section numbering adapted to retain continuity with this thesis.

Thermal Treatment of Magnox Sludge Intermediate Level Nuclear Waste through Vitrification

Sean T. Barlow¹, Adam J. Fisher¹, Daniel J. Bailey¹, Martin C. Stennett¹, Claire L. Corkhill¹, Russell J. Hand¹, Sean P. Morgan² & Neil C. Hyatt¹

1. Department of Materials Science & Engineering, The University of Sheffield, Sheffield S1 3JD, UK

2. Sellafield Ltd., Hinton House, Risley, Warrington WA3 6GR, UK

Abstract: Magnesium aluminosilicate and magnesium borosilicate wasteforms were investigated for the vitrification of intermediate level Magnox sludge waste accumulated on the Sellafield site over 50 years. Base glass compositions were doped with two bounding waste simulants for sludges from the First Generation Magnox Storage Ponds, including up to 12 wt% metallic magnesium and 68 wt% metallic uranium. Borosilicate compositions demonstrate suitably high waste loadings of over 27 wt% by oxidising and digesting metallic waste elements into an amorphous glass. Simulants with a high metallic waste fraction afforded partially devitrified glasses with crystalline UO₂ and U₃O₈ which did not adversely impact chemical durability. Borosilicate compositions showed dissolution rates comparable to high level and intermediate level waste glass with $RL_{(B)} = (3.32 \pm 2.98) \times 10^{-1} \text{ g m}^{-2}\text{d}^{-1}$. Uranium speciation within glass was investigated by X-ray absorption near edge spectroscopy; borosilicate compositions were characterised by a slightly lower mean U oxidation state 5.0 ± 0.1 than aluminosilicate counterparts 5.2 ± 0.1 . Aluminosilicate glass compositions were determined to be unsuitable for application due to high dissolution rates and unfavourable processing conditions. This work establishes proof of concept of vitrification of hazardous

Magnox sludge waste in borosilicate glass formulations, with the potential to achieve an 80% reduction in conditioned waste volume, over the current site baseline plan.

4.2.1. Introduction

The United Kingdom operated Magnox nuclear reactors for electricity production from 1953 to 2015. These first generation graphite moderated, carbon dioxide cooled reactors used natural, unenriched uranium metal fuel clad in a *magnesium non-oxidising* (Magnox) alloy [25], [39]. Although all Magnox reactors are now in the process of being decommissioned, wastes arising from Magnox spent fuel management continue to pose a significant radiological risk.

Magnox spent fuel is currently reprocessed, to recover uranium and plutonium, at the Magnox Reprocessing Plant, Sellafield, UK. Reprocessing operations are expected to continue until 2020 by which point all Magnox spent nuclear fuel (SNF) should have been reprocessed [48], [63]. Historically, Magnox SNF was stored in open air water-filled cooling ponds prior to reprocessing, called the First Generation Magnox Storage Ponds (FGMSP) and sheared cladding also stored underwater in Magnox Swarf Storage Silos (MSSS). Increased throughput of nuclear fuel at Magnox stations (required as a result of industrial action by coal miners during the 1970s and 1980s) combined with lengthy shutdowns at the reprocessing facility led to a build-up of SNF in the FGMSP resulting in storage of the SNF for periods longer than originally anticipated [39], [63], [84]. Increased storage times led to considerable corrosion of the Magnox alloy fuel cladding and natural uranium fuel forming a radiologically hazardous layer of magnesium hydroxide sludge on the bottom of the cooling pond [85]:



Uranium inclusion into the 3,148 m³ of sludge within the First Generation Magnox Storage Ponds (FGMSP) and Magnox Swarf Storage Silos (MSSS) is one of the biggest problems facing the Sellafield nuclear site, requiring urgent decommissioning to reduce the hazard posed [88]–[90].

Current plans for Magnox sludge remediation are retrieval from the ponds and storage in an engineered facility prior to encapsulation in a cement matrix, consistent with treatment of other intermediate level wastes (ILW) [63]. Although cost effective in the short term, cementation increases the volume of waste requiring disposal thereby increasing the storage, transport and overall cost of a deep geological disposal facility (GDF), the UK's preferred disposal option. Due to the long-lived radiotoxicity of elements contained in Magnox sludge, there are also concerns that cement wasteforms may not be durable enough, over the timescales required, to prevent release of hazardous radionuclides to the biosphere [10]. Due to swelling of metallic Magnox containing waste containers from production of hydrogen gas, cement wasteform compatibility with metallic wastes is also of concern [85], [218], [219].

Vitrification is the current industry standard for the treatment of high level waste (HLW). Interest in the vitrification of ILW wastes has grown in recent years because of the improved waste loading and durability relative to cement wasteforms, significant volume reduction and enhanced passive safety offered by vitreous wasteforms [209]. Vitrification chemically bonds radiotoxic elements into the structure of a glass, oxidises waste components and eliminates water and other volatile species. This project was aimed at producing a single chemically durable vitreous wasteform capable of immobilising Magnox sludge wastes with a diverse composition and consistency.



Figure 4-25. First Generation Magnox Storage Ponds, Sellafield, Cumbria UK [83]

4.2.2. Experimental procedures

Two suitable base glass compositions were determined through study of the low temperature isotherms of magnesium borosilicate (MBS) and magnesium aluminosilicate (MAS) pseudo-ternary liquidus phase diagrams [155], [156]. Bounding extremes of the waste found within the FGMSP were investigated, as can be seen below and in Table 4-7.

Metallic: waste consisting of mostly intact uranium metal fuel and cladding material.

Corroded: waste containing highly corroded Magnox cladding with uranium oxide contamination.

Combination of the base glass systems and the bounding extreme wastes shown above resulted in a suite of six samples: **M**agnesium **B**oro**S**ilicate base glass (MBS), **M**agnesium **B**oro**S**ilicate with **C**orroded waste (MBS-C), **M**agnesium **B**oro**S**ilicate with **M**etallic waste (MBS-M), **M**agnesium **A**lumino**S**ilicate base glass (MAS), **M**agnesium **A**lumino**S**ilicate with **C**orroded waste (MAS-C) and **M**agnesium **A**lumino**S**ilicate with **M**etallic waste (MAS-M) as

shown in Table 4-8. Aluminium is present in analysed MBS compositions from the corrosion of alumina crucible used and boron present in MAS samples as a tracer for glass dissolution.

Table 4-7. Bounding waste compositions for FGMSP.

	Mg	Mg(OH) ₂	U	U ₃ O ₈
Metallic waste (wt%)	12.0	20.0	68.0	0.0
Corroded waste (wt%)	5.0	80.0	5.0	10.0

Stoichiometric amounts of SiO₂, H₃BO₃ (Sigma-Aldrich 99.5%), Na₂CO₃ (Alfa Aesar 98%), Al(OH)₃ (Acros 95%), Mg(OH)₂ (Sigma-Aldrich 95%), Mg (Acros 99.9%), U₃O₈ and U (BDH) were batched and mixed together for 1 minute before melting in alumina crucibles within an Elite Thermal Systems BRF15/5 muffle furnace. Magnesium content in base glass samples was replaced, on a molar basis, with the proportion of magnesium and uranium found in the bounding waste compositions, shown in Table 4-7, and renormalized to create the waste loaded formulations. For waste bearing glasses, the magnesium content was substituted for the waste elements shown in Table 4-7. MBS compositions were melted at 1250 °C for 3 hours, MAS compositions were melted at 1500 °C for 5 hours in order to form fluid melts. The composition of the processed glass compositions was determined via total dissolution in hydrofluoric acid and analysis by inductively coupled plasma optical emission spectroscopy (ICP-OES).

Materials were characterised by powder X-ray diffraction (XRD) using a Bruker D2 X-ray diffractometer in reflection mode over the range $10^\circ < 2\theta < 60^\circ$ using Cu K α radiation (30 kV, 10 mA); K β radiation was stripped using a Ni foil filter. XRD data were processed using the Bruker DiffracEva 3.0 software package with Crystallography Open Database [203] and the International Centre for Diffraction Data (ICDD) database [162].

The microstructure of representative sample cross-sections were characterised by scanning electron microscopy and energy dispersive X-ray spectroscopy (SEM-EDX) using a Hitachi TM3030-SEM equipped with a Bruker Quantax EDX system. Samples were prepared for SEM analysis by mounting in cold-setting resin and polishing to an optical finish (1 μ m) using progressively finer grades of SiC papers and diamond suspension. Samples were sputter coated in carbon to avoid surface charging effects.

Glass transition (T_g), crystallisation (T_c) and liquidus (T_l) temperatures were determined from differential thermal analysis (DTA) of representative samples using a Netzsch TG 449 F3 Jupiter simultaneous thermal analyser. A temperature within 50 °C of T_g was taken as the annealing temperature for each sample; 560 °C for MAS samples and 610 °C for MBS samples.

X-ray absorption near-edge spectroscopy (XANES) was performed in micro-focus mode to determine the oxidation state of uranium at regions of interest in waste loaded samples [220]. Samples were measured in fluorescence mode at the X05LA beamline, Paul Scherrer Institute Swiss Light Source, Switzerland, U L₃ edge. Representative samples were fixed into cold-

setting resin and thin sectioned before mounting on a Spectrasil slide. Measurements took place on a motorised 3D stage allowing scanning of samples with a beam spot size of approximately $1 \mu\text{m}^2$ and photon energy tuned using a double crystal Si (111) monochromator. Regions of interest were selected based on the representation of the sample morphology from previous SEM-EDX analysis. Multiple XANES spectra for each sample were measured and averaged at the regions of interest over the range $30 \text{ eV} \leq U \text{ L}_3 \text{ edge} \leq 250 \text{ eV}$. X-ray fluorescence was measured using a Si drift detector (KETEK) mounted 45° to the incident beam, creating XRF maps to aid selecting regions of interest. Data reduction and XANES analysis were performed using the Athena Demeter 0.9.24 software package [221]. Uranium oxidation state was determined by linear regression with respect to standards of known oxidation state: UTi_2O_6 (U^{4+}), $\text{U}_{0.5}\text{Y}_{0.5}\text{Ti}_2\text{O}_6$ (U^{5+}) and CaUO_4 (U^{6+}).

Glass durability was assessed using a modified ASTM Product Consistency Test B (PCT-B) protocol [191]. Powdered samples with a size fraction between $75 \mu\text{m}$ and $150 \mu\text{m}$ were dissolved in ultra-high quality water at 90°C for 28 days with a surface to volume ratio of 1200 m^{-1} . Sampling of the solution took place on days 1, 3, 7, 14, 21 and 28. Concentration of elements within solution was found by inductively coupled plasma optical emission spectroscopy (ICP-OES) using a Thermo-Fisher 6000iCAP and comparison with standards of known concentration.

Density was determined by helium pycnometry using a Micromeritics Accupyc II 1340 with powder samples. Measurements were run at room temperature in a 1 cm^3 chamber with a fill pressure of 82.7 kPa and were purged 10 times over 10 cycles with an equilibration rate of 0.034 kPa/min .

4.2.3. Results

Melting behaviour and composition

No violent or unduly vigorous reactions between the waste simulants, including the metallic content, and glass were observed; however, significant corrosion of the alumina crucibles did occur resulting in higher than nominally batched Al_2O_3 (See Table 4-8). Metallic waste melts, in particular MBS-M, were viscous and formed glassy slag-like fractions which did not incorporate into the bulk glass, resulting in low uranium uptake, seen in Table 4-8. Corroded waste melts were fluid forming a homogeneous glass with good vitrification of the waste simulants and no crystallinity. Base glass samples MAS and MBS also formed fluid melts and homogenous glass. Typically, a waste loaded glass would have a lower amount of glass matrix constituents (SiO_2 , B_2O_3 and MgO) than the corresponding base composition, however since these samples utilised MgO from the waste stream this is not the case in this study. The high waste loaded MAS-M sample is an exception where the concentration of B_2O_3 is greater to aid glass formation.

Table 4-8. Analysed glass compositions from ICP-OES and batched compositions in mol%.

	Component Analysed (± 0.2 mol%) [as batched]						
	SiO ₂	B ₂ O ₃	MgO	UO ₃	Na ₂ O	Al ₂ O ₃	Total
MAS	46.4 [48.0]	1.8 [2.0]	20.5 [20.0]	-	20.6 [20.0]	10.7 [10.0]	100.0
MAS-M	42.8 [40.8]	3.3 [3.7]	23.7 [25.4]	4.1 [8.7]	15.6 [13.2]	10.5 [5.0]	100.0
MAS-C	44.7 [45.5]	1.3 [1.6]	27.6 [28.3]	0.5 [0.6]	18.8 [18.4]	7.1 [5.6]	100.0
MBS	24.4 [25.4]	24.1 [25.0]	47.6 [49.6]	-	-	3.9 [0]	100.0
MBS-M	23.2 [21.7]	21.7 [21.3]	41.7 [42.4]	6.9 [14.5]	-	6.5 [0]	100.0
MBS-C	24.5 [24.1]	23.1 [24.7]	47.4 [49.1]	0.7 [1.0]	-	4.3 [0]	100.0

Phase analysis and microstructure

Base glass and corroded waste samples

X-ray powder diffraction of the base glass and corroded waste doped glass compositions revealed the presence of diffuse scattering indicative of an amorphous material between $20^\circ < 2\theta < 40^\circ$ for the borosilicates and between $15^\circ < 2\theta < 45^\circ$ for the aluminosilicates, see Figure 4-26 and Figure 4-27. No sharp Bragg reflections constant with crystalline components are present. The diffuse scattering of the MAS glass compositions in the range $15^\circ < 2\theta < 45^\circ$ is clearly composed of two components, and that of the MBS compositions shows some asymmetry, indicative of phase separation.

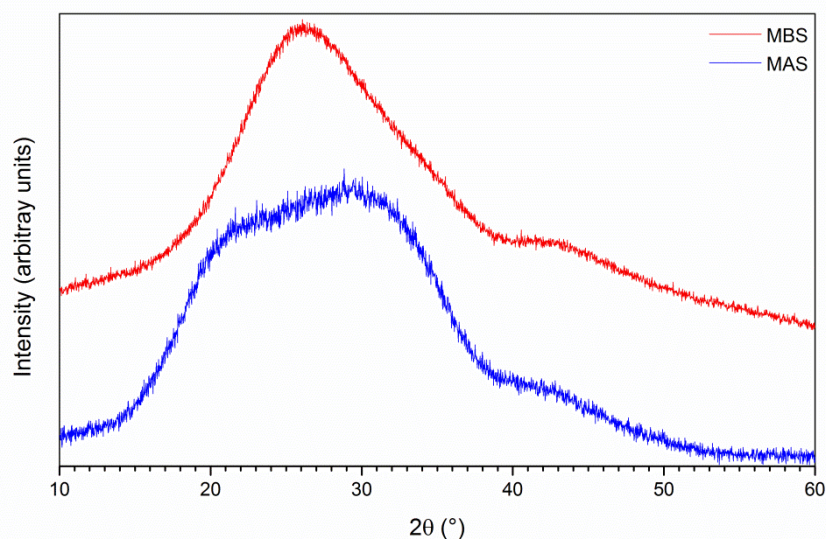


Figure 4-26. Powder X-ray diffraction data of MAS and MBS base glasses.

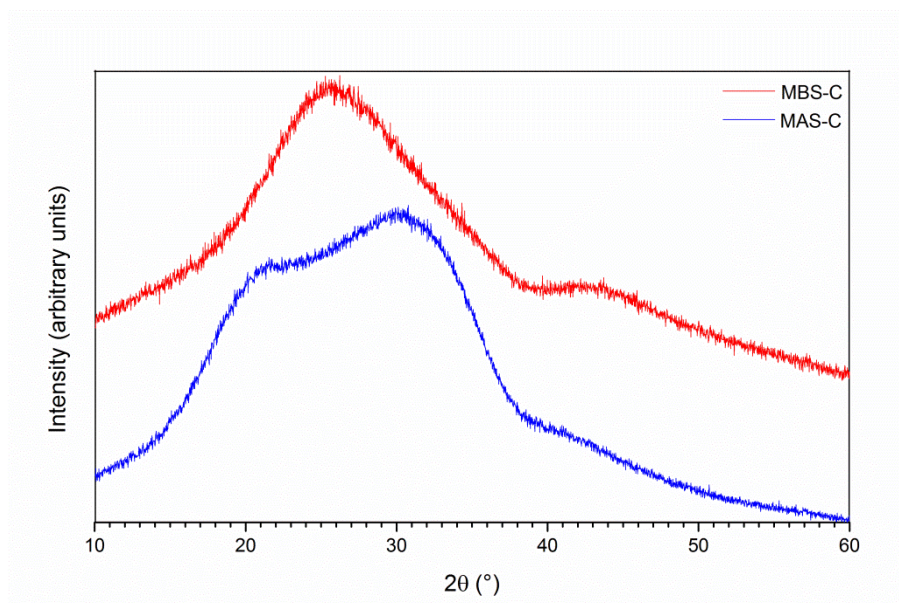


Figure 4-27. Powder X-ray diffraction data of MAS and MBS base glasses loaded with corroded waste simulant.

Back scattered electron imaging of the microstructure of the MBS-C composition loaded with corroded waste simulant, Figure 4-28, revealed striations in greyscale contrast, confirming the presence of phase separation suggested by XRD data. EDX analysis showed the phase of bright contrast to be enriched in aluminium and uranium, whereas these elements were depleted in the regions of dark contrast, as seen in Figure 4-28. No crystalline inclusions were evident in this material, in agreement with the absence of sharp Bragg reflections in XRD data. Back scattered electron imaging of the microstructure of the MAS base glass and MAS-C composition loaded with corroded waste simulant, did not demonstrate obvious striations in imaging contrast, which implies that phase separation must occur at fine scale and involve two phases of similar composition, see Figure 4-29. Uranium was found to be distributed homogeneously throughout the glass matrix.

Both base glass compositions were observed homogeneous by SEM-EDX (Figure 4-30 and Figure 4-31), with no apparent phase separation. The presence of Al within MBS samples, as observed from chemical analysis Table 4-8, is confirmed in the EDX element maps on Figure 4-30.

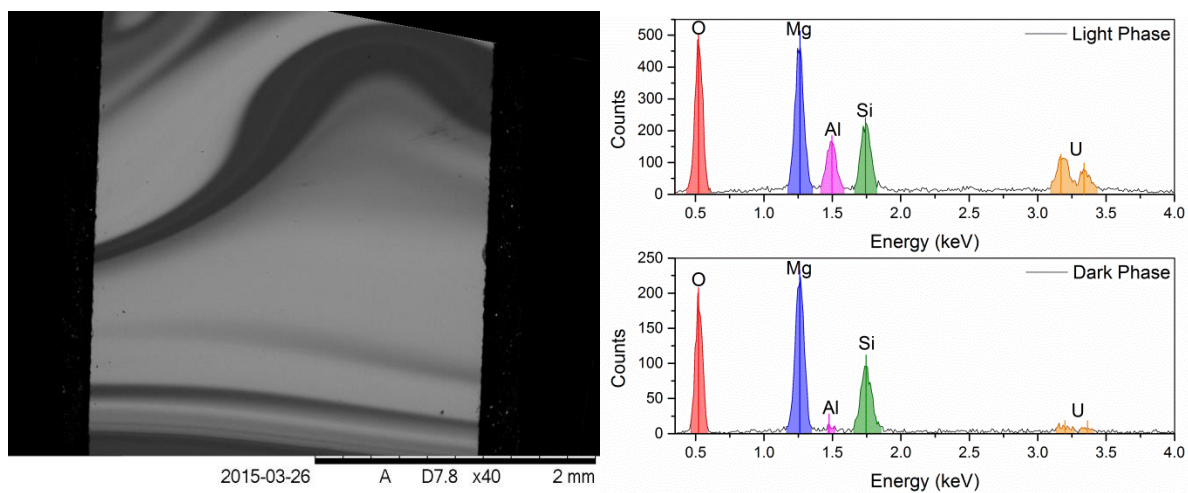


Figure 4-28. Low magnification back-scattered SEM image and close-up EDX spectra showing microstructure and composition within MBS-C; Top EDX spectra for light phase; Bottom EDX spectra for dark phase.

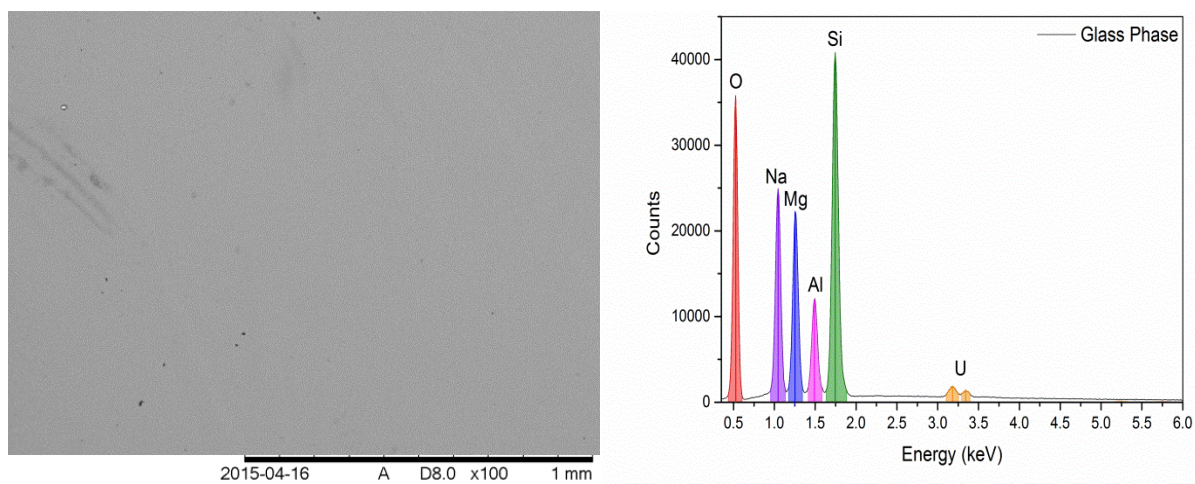


Figure 4-29. Back-scattered SEM image showing homogenous MAS-C glass & corresponding EDX spectra; similar results were obtained for both base glass samples.

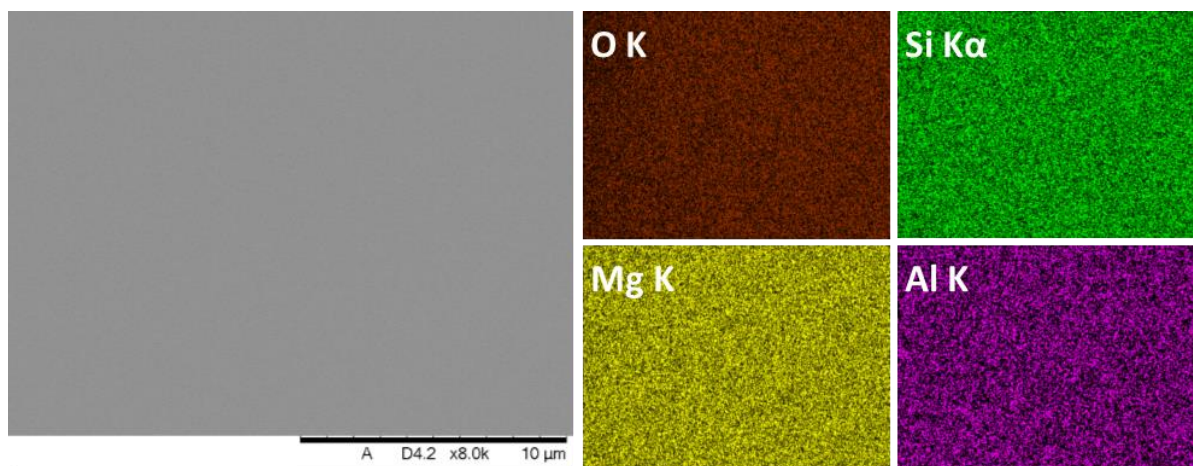


Figure 4-30. EDX maps for key components of MBS base glass.

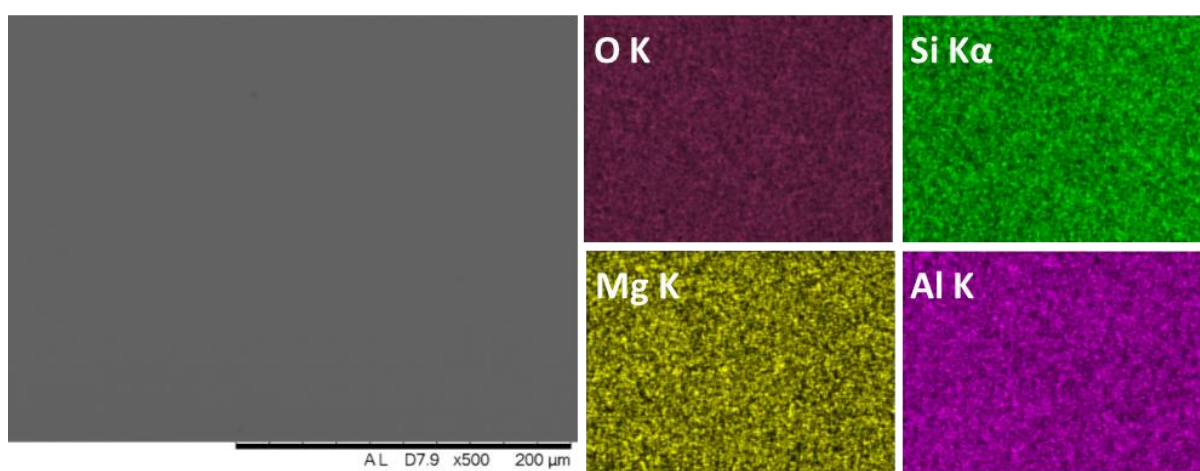


Figure 4-31. EDX maps for key components of MAS base glass.

Metallic waste samples

The XRD data of glass formulations incorporating metallic waste simulant, MBS-M and MAS-M, exhibit sharp Bragg reflections confirming the presence of crystalline phases in addition to diffuse scattering associated with amorphous phases, see Figure 4-32. XRD data of the borosilicate MBS-M glass confirmed the presence of crystalline UO_2 and U_3O_8 phases whilst only UO_2 was apparent in the aluminosilicate MAS-M counterpart. SEM images confirm the presence of such inclusions, revealing dendritic and fused forms of the crystallites within the glass matrix, as shown in Figure 4-33. Dendritic crystallites formed repeating structures in a natural, fractal pattern (Figure 4-34) whilst fused crystals formed larger structures (Figure 4-35). Voids and air bubbles were also detected in metallic waste glass samples due to higher viscosity of the melts trapping air bubbles in the final product. EDX spectra obtained on the phases verify the presence of U and O (other components arise from sampling of the encapsulating glass matrix by the electron beam). Note that the apparent low intensity of the O

$K\alpha$ X-ray emission in the presence of high uranium content is due to attenuation by the matrix. The MAS-M composition exhibited a predominance of dendritic crystallites ca. 1.5 μm across, whereas the MBS-M composition showed a predominance of fused crystallites ca. 3.5 μm across.

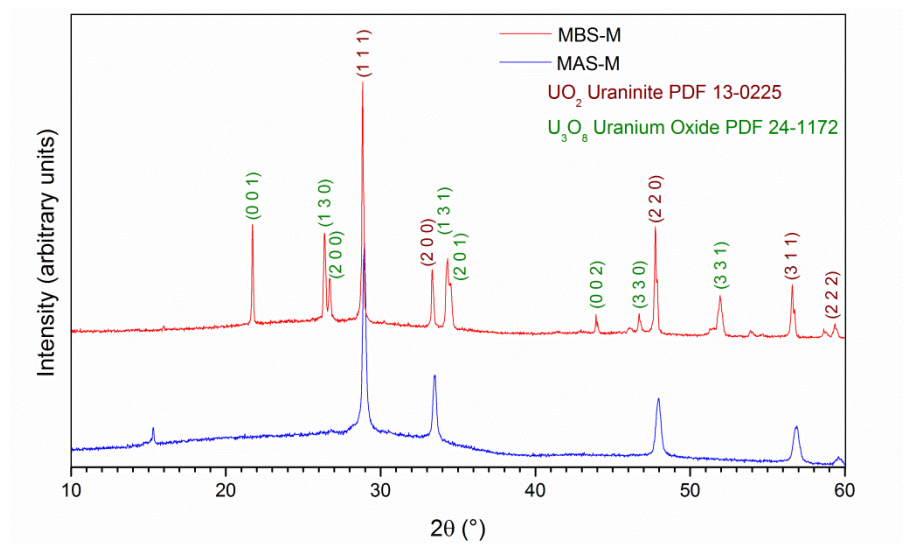


Figure 4-32. Powder X-ray diffraction data of samples loaded with metallic wastes.

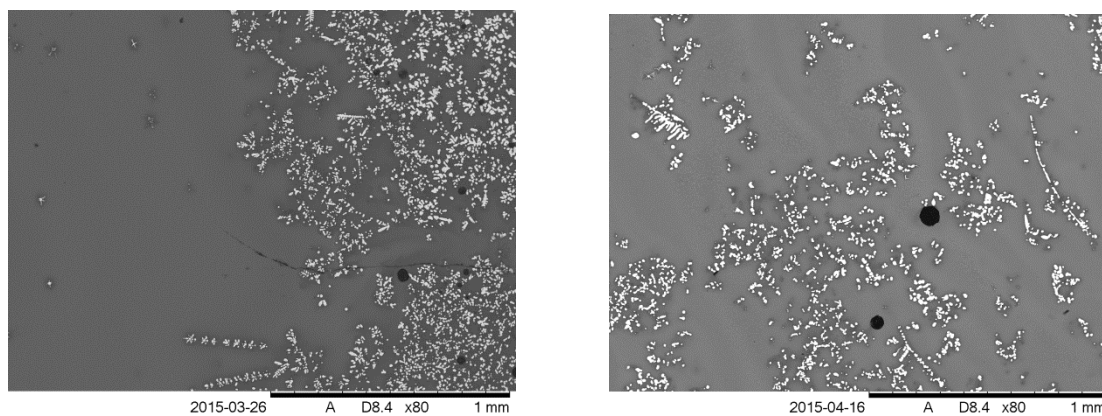


Figure 4-33. Back-scattered SEM micrographs of MBS-M (left) and MAS-M (right).

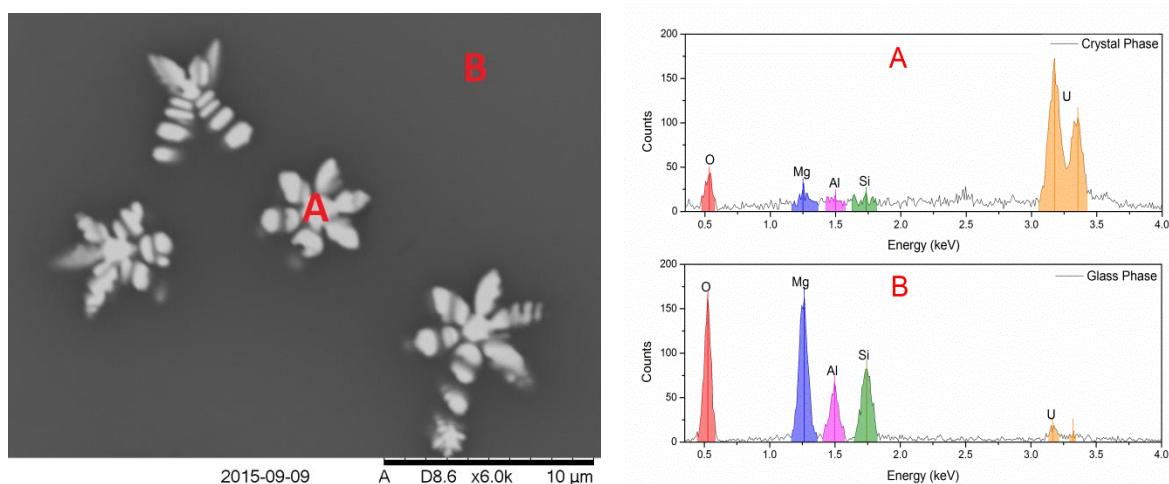


Figure 4-34. Back-scattered SEM image and EDX spectra showing dendritic crystals within MBS-M; Top EDX spectra for bright crystalline inclusion (A); Bottom EDX spectra for dark glass phase (B).

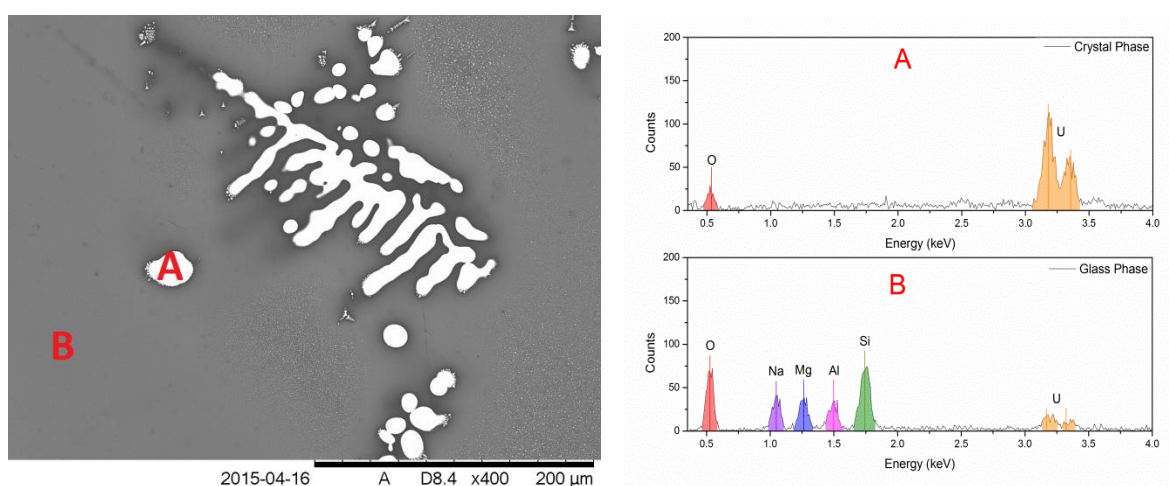


Figure 4-35. Back-scattered SEM image and EDX spectra showing fused crystals within MAS-M; Top EDX spectra for bright crystalline phase; Bottom EDX spectra for dark glass phase.

Thermal analysis

The results of thermal analysis are summarised in Table 4-9 and representative DTA data are shown in Figure 4-36.

Table 4-9. Extracted values for glass transition (T_g), crystallisation points (T_c) and liquidus temperature (T_l).

Sample	T_{g1}	T_{g2}	T_{c1}	T_{c2}	$T_l (\pm 5 \text{ } ^\circ\text{C})$
MAS	614	740	846	965	1375
MAS-M	631	673	712	945	1420
MAS-C	617	675	754	943	1418
MBS	665	770	841	970	1151
MBS-M	672	767	856	1000	1153
MBS-C	672	848	914	995	1135

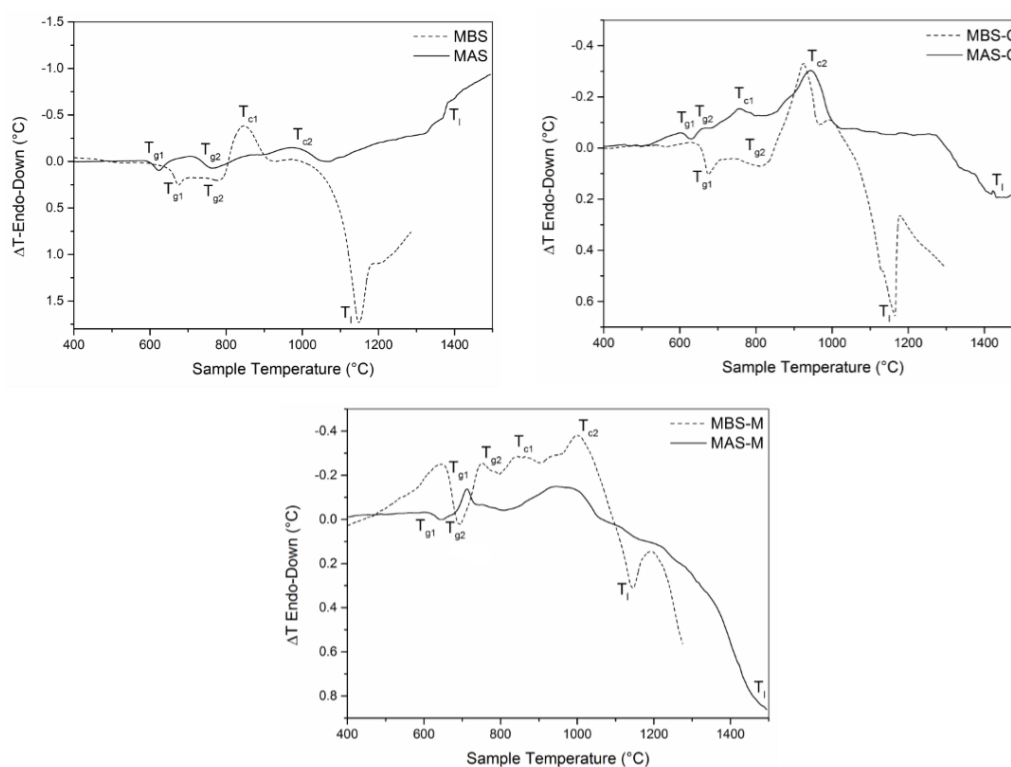


Figure 4-36. Thermal analysis of samples created in this study showing T_g , T_c and T_l .

Liquidus temperatures (T_l) as determined by DTA showed borosilicate compositions were fully melted from between 1150 - 1200 °C whilst aluminosilicate compositions were only liquidus above 1375 °C. Two distinct glass transition temperatures were observed in all samples with T_g in aluminosilicate samples typically ~50 °C lower than in borosilicate counterparts. Crystallisation points extracted from DTA data reflect the multiple crystalline phases formed in the samples. A second exothermic peak (T_{c2}), from 945 – 1000 °C, is observed in all samples which suggest that T_{c2} is an inherent feature of these glass systems. Simultaneous thermogravimetric (TG) analysis showed no significant loss of mass upon heating.

Uranium incorporation

Figure 4-37 shows the background subtracted and normalised U L₃ X-ray Absorption Near Edge Spectroscopy (XANES) data for the MAS and MBS wasteforms, compared with data from reference compounds characterised by U⁴⁺ – UO₂, U⁵⁺ – U_{0.5}Y_{0.5}Ti₂O₆, and U⁶⁺ – CaUO₄ species. These data were corrected to the absolute energy scale using the known edge position (E₀) of Zr foil measured simultaneously using a reference ion-chamber. To first order the precise energy of the absorption edge, E₀, is correlated with oxidation state and a calibration line, based on the reference compounds, can be utilised to extract the mean uranium oxidation state of an unknown, see Figure 4-37. The precise absorption edge and inferred bulk mean uranium oxidation state for the MAS and MBS wasteforms are summarised in Table 4-10. The mean uranium oxidation state in the MBS-M and MAS-M formulations, 4.9 ± 0.1 and 5.2 ± 0.1, respectively, confirms effective oxidation of the uranium metallic feed in the thermal treatment process. The mean uranium oxidation states in the MBS-C and MAS-counterparts are higher, 5.5 ± 0.1 and 5.7 ± 0.1, respectively, reflecting the more oxidised nature of the waste simulant. Uranium is more oxidised in the aluminosilicate formulations, compared to borosilicate counterparts, as a result of the higher processing temperature used for the former (1500 °C) compared to the latter (1200 °C).

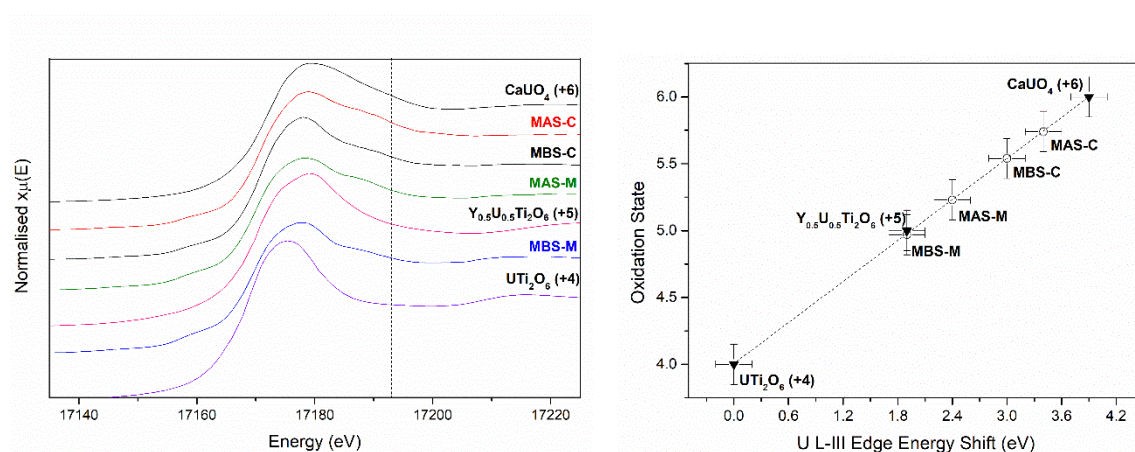


Figure 4-37. XANES plots for each sample (left) and oxidation state versus E₀ energy shift, Error bars +/-0.1 (right).

Table 4-10. Extracted E_0 values and corresponding oxidation state from XANES.

Sample	E_0 (eV)	Oxidation State (± 0.1)
UTi₂O₆ (4+)	17166.4	4.0
MBS-M	17168.3	5.0
Y_{0.5}U_{0.5}Ti₂O₆ (5+)	17168.3	5.0
MAS-M	17168.8	5.2
MBS-C	17169.4	5.5
MAS-C	17169.8	5.7
CaUO₄ (6+)	17170.3	6.0

Core-hole lifetime broadening of U L₃ edge XANES data makes a definitive assessment of the relative contributions of U⁴⁺, U⁵⁺ and U⁶⁺, to the average oxidation state difficult. In addition, it is clear that bulk measurement of uranium oxidation state also includes a contribution from UO₂ and U₃O₈, where present as crystalline phases. Also, compositions with a mean oxidation state in excess of 5.0, will likely have some contribution from U⁴⁺, which is typically incorporated in silicate glasses as the uranyl species UO₂²⁺ [222], [223]. The uranyl species presents a diagnostic post-edge resonance at ca. 15 eV above E₀, in U L₃ edge XANES, arising from scattering by the uranyl O=U=O oxygens [224], [225], this is also evident in the U L₃ XANES data of CaUO₄ reference, which is characterised by the presence of uranyl species. This feature is also discernible in the U L₃ XANES of the most oxidised glass composition, MAS-C, from which the presence of uranyl species is inferred.

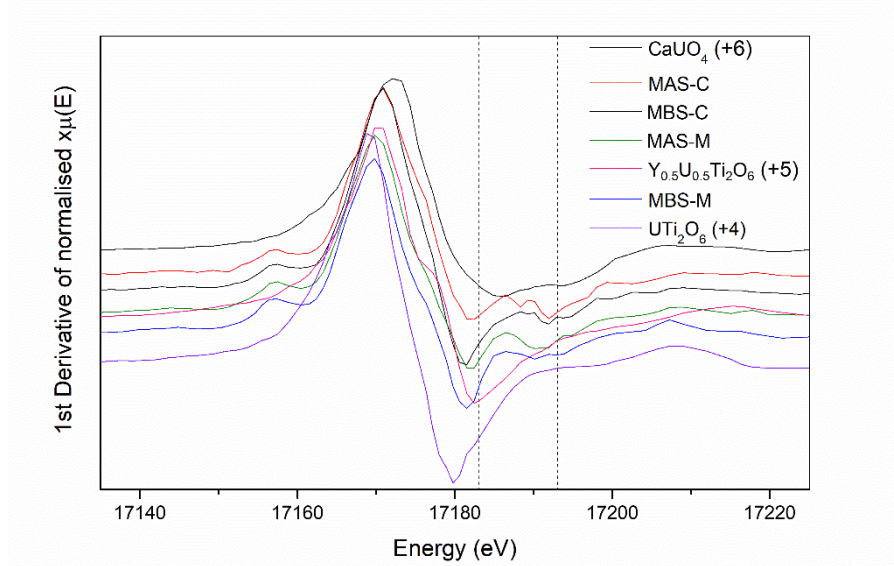


Figure 4-38. First derivative of XANES data highlighting uranyl.

Post-edge resonance observed in the region between 17183 eV and 17193 eV (highlighted between the dashed lines in Figure 4-37 and Figure 4-38) fingerprints the U speciation as uranyl-like $(\text{UO}_2)^{2+}$ with samples closely resembling the spectra of CaUO_4 and $\text{U}_{0.5}\text{Y}_{0.5}\text{Ti}_2\text{O}_6$ and indicate an oxidation state between 5+ and 6+ is dominant [222], [224]. Linear regression of extracted normalised, absorption edge position, referenced to standards of known oxidation state, gave the oxidation state for each sample as shown in Table 4-10 [226]. It is apparent corroded waste glass samples have higher U oxidation states than corresponding metallic waste glasses and borosilicate samples have lower U oxidation state than the comparative aluminosilicate system.

Density and waste loading

Helium pycnometry showed waste doped glasses have higher density than the respective base composition as expected, and that borosilicate samples are denser than aluminosilicate counterparts (see Table 4-11).

The lowest uranium waste loading achieved was 2.32 wt% for MAS-C and the highest was 27.2 wt% for MBS-M. Magnesium waste was incorporated into the glass network in greater concentrations with the lowest waste loading being 13.69 wt% for MAS-M and the highest being 33.96 wt% for MBS-C. It is apparent the aluminosilicate compositions is not able to incorporate Mg or U in as high a concentration as their borosilicate counterparts, which thus exhibit higher density.

Table 4-11. Calculated density of synthesised glass compositions.

Sample	Average density (g m^{-2})
MAS	2.5803 ± 0.0033
MAS-M	3.2356 ± 0.0055
MAS-C	2.6763 ± 0.0022
MBS	2.6330 ± 0.0012
MBS-M	3.7212 ± 0.0020
MBS-C	2.7606 ± 0.0007

Chemical durability

Normalised release rates of B, Na, Si and Mg were calculated for base glass compositions, along with uranium for waste bearing samples, from results of solution analysis of PCT-B experiments (Figure 4-40). The initial forward (3 -7 day) dissolution rates for key elements, B, Na, Si and Mg were calculated and summarised in Table 4-12 alongside the average pH of the leachate during the experiment. Saturation indexes calculated during the dissolution of waste glass from modelling are shown in Table 4-13.

Table 4-12. Normalised forward dissolution rates for boron and uranium in $\text{g m}^{-2}\text{d}^{-1}$ with average pH of solution.

Normalised forward dissolution rates (NR_i , $\text{g m}^{-2}\text{d}^{-1}$)						
Samples	Si	B	U	Mg	Na	pH
MAS	$(4.50 \pm 5.45) \times 10^{-2}$	$(1.53 \pm 0.91) \times 10^{-2}$	-	-	$(1.28 \pm 0.76) \times 10^{-2}$	12.1
MAS-M	$(4.60 \pm 5.09) \times 10^{-2}$	$(6.08 \pm 2.86) \times 10^{-1}$	$(5.75 \pm 1.27) \times 10^{-2}$	$(2.62 \pm 0.29) \times 10^{-3}$	$(2.99 \pm 2.01) \times 10^{-1}$	11.8
MAS-C	$(1.03 \pm 0.73) \times 10^{-1}$	$(7.05 \pm 3.46) \times 10^{-1}$	$(1.45 \pm 0.31) \times 10^{-1}$	$(1.02 \pm 0.14) \times 10^{-2}$	$(4.24 \pm 2.23) \times 10^{-1}$	12.5
MBS	$(-1.66 \pm 0.55) \times 10^{-3}$	$(3.32 \pm 2.98) \times 10^{-1}$	-	$(2.49 \pm 3.65) \times 10^{-2}$	-	8.4
MBS-M	$(0.11 \pm 3.05) \times 10^{-3}$	$(2.72 \pm 2.09) \times 10^{-1}$	-	$(2.21 \pm 2.27) \times 10^{-2}$	-	8.3
MBS-C	$(-1.56 \pm 0.61) \times 10^{-3}$	$(2.99 \pm 2.66) \times 10^{-1}$	-	$(1.74 \pm 3.28) \times 10^{-2}$	-	8.6

Table 4-13. Saturation indexes (SI) calculated during the dissolution of waste glass compositions at 90°C in UHQ water.

Phase	SI (MBS-M)	SI (MBS-C)	SI (MAS-M)	SI (MAS-C)	Formula
Anthophyllite	18.5	24.07	52.11	53.54	$\text{Mg}_7\text{Si}_8\text{O}_{22}(\text{OH})_2$
Brucite	1.18	2.25	7.62	8.51	$\text{Mg}(\text{OH})_2$
Chrysotile	10.7	13.43	27.15	28.62	$\text{Mg}_3\text{Si}_2\text{O}_5(\text{OH})_4$
Saponite-H			25.25	25.33	$\text{H}_{0.33}\text{Mg}_3\text{Al}_{0.33}\text{Si}_{3.67}\text{O}_{10}(\text{OH})_2$
Saponite-Mg			28.04	28.27	$\text{Mg}_{3.165}\text{Al}_{0.33}\text{Si}_{3.67}\text{O}_{10}(\text{OH})_2$
Saponite-Na			27.57	28.03	$\text{Na}_{0.33}\text{Mg}_3\text{Al}_{0.33}\text{Si}_{3.67}\text{O}_{10}(\text{OH})_2$
Sepiolite	0.6	12.2	26.51	26.36	$\text{Mg}_4\text{Si}_6\text{O}_{15}(\text{OH})_2 \cdot 6\text{H}_2\text{O}$
Talc	11.57	13.82	25.15	25.41	$\text{Mg}_3\text{Si}_4\text{O}_{10}(\text{OH})_2$
Schoepite	0.6	0.25	0.73		$\text{UO}_3 \cdot 2\text{H}_2\text{O}$
Soddyite	3.75	2.81	2.58		$(\text{UO}_2)_2(\text{SiO}_4) \cdot 2\text{H}_2\text{O}$
$\text{UO}_3 \cdot 9\text{H}_2\text{O}(\alpha)$	0.5	0.15	0.63		$\text{UO}_3 \cdot 9\text{H}_2\text{O}$
$\text{UO}_3 \cdot 2\text{H}_2\text{O}$	0.6	0.25	0.73		$\text{UO}_3 \cdot 2\text{H}_2\text{O}$

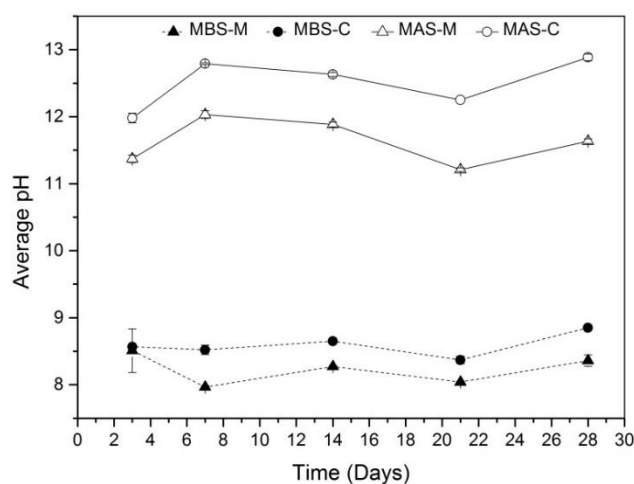


Figure 4-39. pH of all sample solutions over the experimental period.

The pH of all solutions in contact with sample saturated rapidly and did not change markedly during the course of the experiments, as shown in Figure 4-39. The average solution pH from borosilicate samples was pH 8.4 whilst average pH from aluminosilicate samples was pH 12.1 (Figure 4-39). This increase in pH is consistent with the leaching of Na; detected in solution from aluminosilicate samples in significant quantities, $NL_{Na} > 5 \text{ gm}^{-2}$ after 7 days. Borosilicate samples did not contain Na and consequently the leachate was considerably less alkaline.

The normalised mass loss (NL_i) of all major structural glass components are shown in Figure 4-40 overleaf. Boron is commonly considered as a tracer for glass dissolution, since once dissolved it is not re-incorporated within the gel layer or within precipitated secondary alteration phases [76]. After 28 days, the NL_B of the MAS-C composition was a factor of two greater than the MBS-C counterpart, whereas the NL_B of the MAS-M composition was a factor of 5 greater than the MBS-M counterpart. The normalised mass loss of Si, NL_{Si} , was always lower than NL_B , indicative of incongruent dissolution and consistent with the phase separated nature of the glasses, and typically an order of magnitude greater in MAS compositions than the MBS counterparts. All compositions show a decrease in NL_{Si} and NL_{Mg} at 21-28 days, whilst NL_B remains effectively constant, suggesting the precipitation of magnesium (alumino)silicate alteration phases. Over the duration of the experiments significant uranium release was observed only for the MAS compositions, and is greater for the MAS-C composition, compared to MAS-M, as shown in Figure 4-40. In contrast, the mass loss of U from the MBS glasses was found to be at least two orders of magnitude lower than those from the counterpart MAS glasses, detectable in very low concentrations only on day 28.

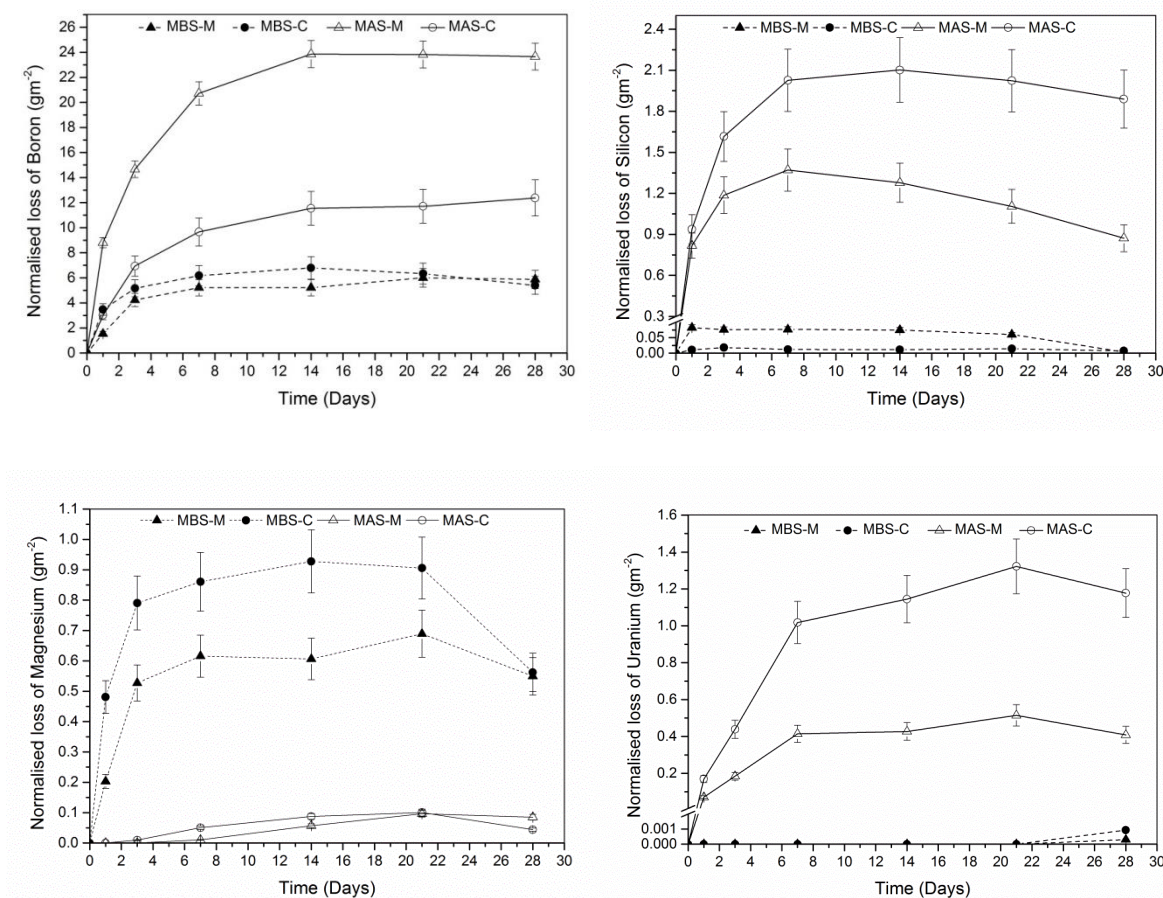


Figure 4-40. Normalised mass loss of boron, silicon, magnesium and uranium (g m^{-2}) versus time for all waste glass samples.

Recovered glass powders from 28-day dissolution experiments were embedded in resin and polished back to study the formation of surface alteration layers, by SEM-EDX. Glass powders of MAS compositions altered for 28 day were observed to have formed alteration layers over 10 μm thick from pristine glass to water-surface interface, whereas MBS compositions exhibited an alteration layer only 1 μm thick. Bright regions found in the backscattered SEM image of MAS-C (Region 'A' of Figure 4-41) are associated with enrichment of U when compared to EDX maps (Figure 4-41 bottom and Figure 4-42). All major glass constituents were detected within the altered region and distributed evenly, apart from sodium and uranium, which accumulate at the water-surface and glass-alteration interfaces respectively. Alteration layers formed on borosilicate glasses were composed major glass constituents and were uniform in composition (Figure 4-43).

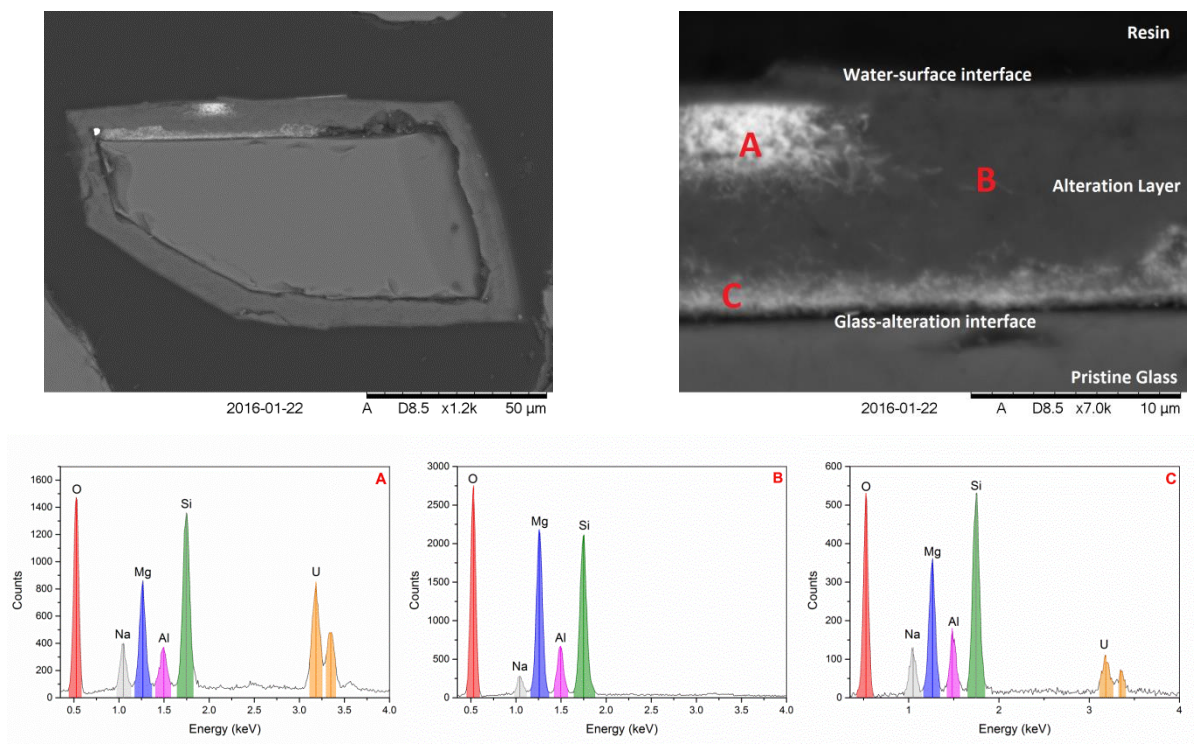


Figure 4-41. SEM micrographs of MAS-C glass showing alteration layers after 28 day dissolution (top) and EDS spectra of from points A, B and B (bottom).

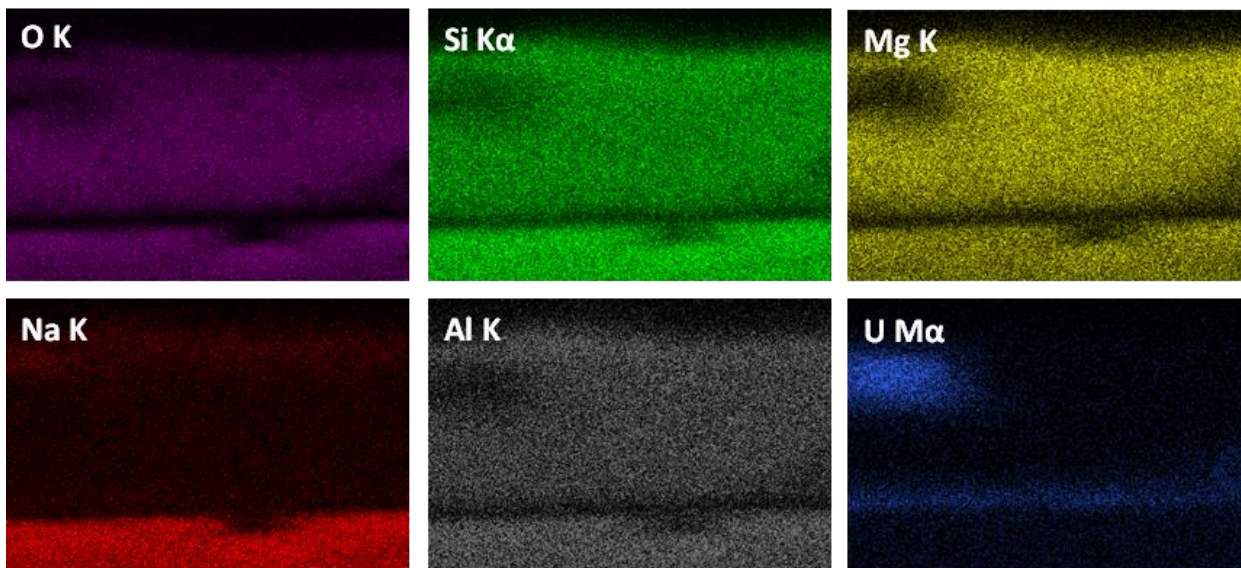


Figure 4-42. EDX maps of MAS-C glass alteration layer.

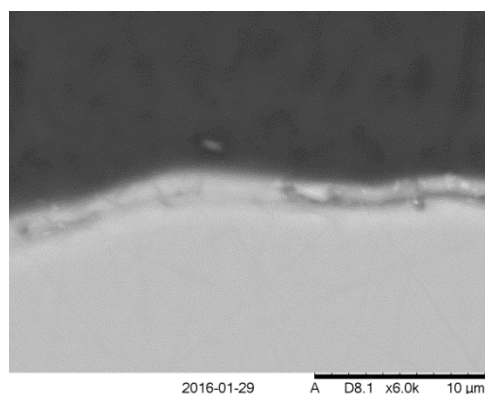


Figure 4-43. SEM micrograph of MBS-C showing 28 day alteration layer.

Geochemical modelling using the Phreeqc software package indicated numerous phases are thermodynamically favourable to form within the test conditions (Table 4-13), including clay-like minerals talc [$\text{Mg}_3\text{Si}_4\text{O}_{10}(\text{OH})_2$], sepiolite [$\text{Mg}_4\text{Si}_6\text{O}_{15}(\text{OH})_2 \cdot 6\text{H}_2\text{O}$], chrysotile [$\text{Mg}_3\text{Si}_2\text{O}_5(\text{OH})_4$] as well as brucite [$\text{Mg}(\text{OH})_2$] and hydrated uranium oxide phases $\text{UO}_3 \cdot 0.9\text{H}_2\text{O}$ and $\text{UO}_3 \cdot 2\text{H}_2\text{O}$. Phase analysis of XRD data from 28 day altered waste loaded samples identified the same crystalline phase assemblage in both metallic samples with the addition of minor reflections indicative of $\text{UO}_4 \cdot 4\text{H}_2\text{O}$ within MAS-M that were not present before alteration, see Figure 4-44. Also evident in MAS-M XRD data is a shift of the UO_2 peaks, compared to MBS-M, consistent with an increase in oxidation number to $\text{UO}_{2.34}$. Both corroded waste samples were still X-ray amorphous after the leaching experiment with no crystalline Bragg reflections detected (Figure 4-45).

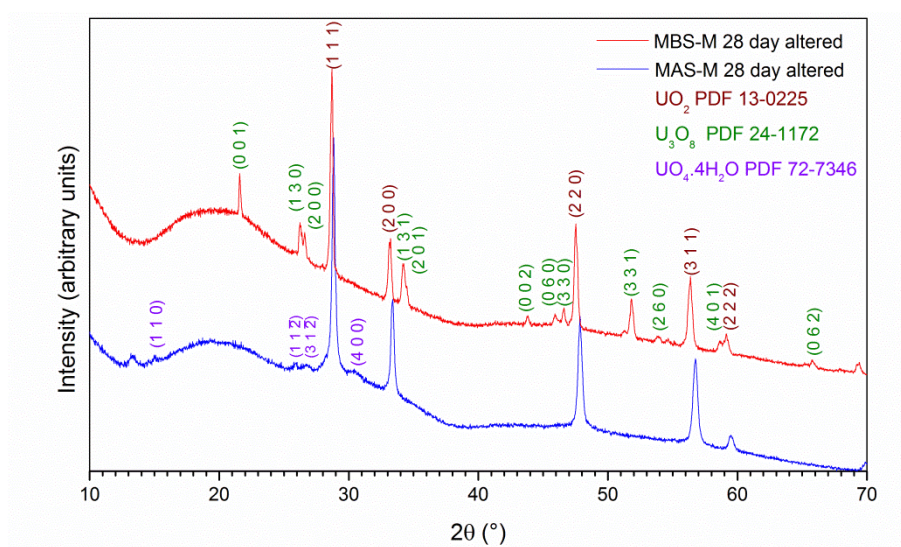


Figure 4-44. XRD trace of MBS-M and MAS-M after 28 day alteration experiment.

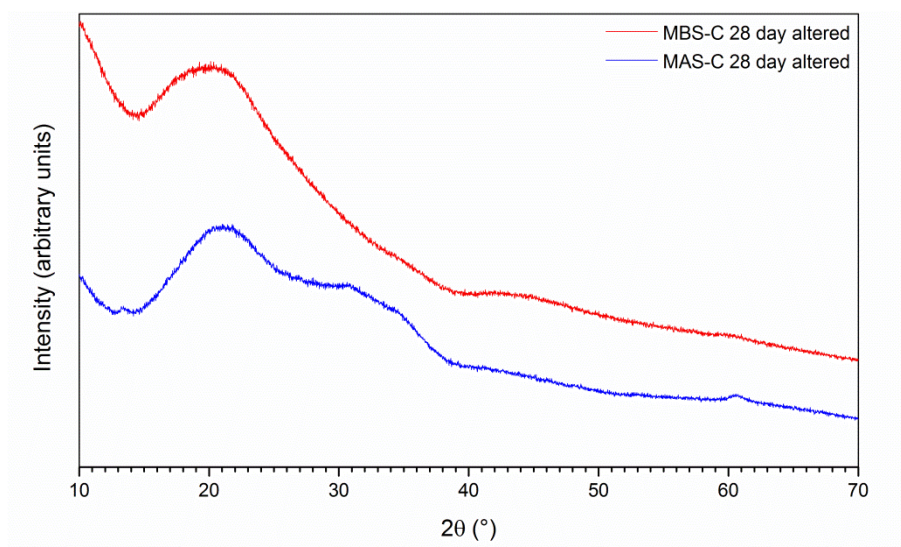


Figure 4-45. XRD trace of MBS-C and MAS-C after 28 day alteration experiment.

4.2.4. Discussion

Melting behaviour and waste loading

The presence of B_2O_3 in high concentrations, >20 mol%, allowed melting of borosilicate glass compositions at lower temperatures compared to aluminosilicate counterparts, see Table 4-8 [134]. Lower melt temperatures are preferable in waste glasses due to compatibility with industrial vitrification plants, which typically operate below 1200 °C, and volatility of radionuclides, particularly Cs radioisotopes [108], [214], which will be present at low concentration as a fission product in these degraded fuel residues. For this reason aluminosilicate glass compositions, $T_1 > 1375$ °C, are likely to be unsuitable for immobilisation of Magnox sludge wastes.

Samples produced from the corroded waste stream were visually homogenous whereas samples from metallic waste were found to be crystalline and slag-like. The partial crystallisation of glasses produced from the metallic waste simulant, does not pose a fundamental barrier to vitrification of FGMP wastes in these glass compositions, given the low fissile material content. A definitive assessment would require a pilot scale demonstration experiment, e.g. using Joule heated batch melter technology, where realistic melt convection would provide understanding of the distribution and fraction of crystalline components. If necessary, the waste loading could be reduced to achieve an acceptable crystalline component.

Typical glass production involves vitrification of a waste with a glass frit, however as the Mg content in these vitrified wasteforms is derived from the waste stream, these samples would only be reproducible with a frit of SiO_2 and B_2O_3 . This may have implications on the production process and would need to be investigated further.

Phase analysis

Both the MAS and MBS base glasses and their derivatives incorporating the corroded waste simulant were demonstrated to be amorphous, showing no crystalline inclusions. In contrast, MAS and MBS derivatives incorporating the metallic waste simulant comprised a glass matrix encapsulating either UO_2 or UO_2 and U_3O_8 , respectively. The corroded waste simulant was apparently completely oxidised and incorporated within the wasteform. The XRD data of the MAS and MBS glasses, and their derivatives, showed evidence for phase separation in the diffuse scattering apparent in XRD data and chemical gradients apparent in SEM-EDX observations. The phase separated nature of the materials was also apparent in differential thermal analysis data (Figure 4-36 and Table 4-9); two glass transition temperatures were apparent implying two separate glass networks [227]. Phase separated glasses often consist of a less durable (modifier rich) second phase which can reduce the overall durability of a wasteform [141], [201], [228]. The data obtained in this study is consistent with this hypothesis where corroded waste samples exhibited higher overall rates of dissolution compared to metallic waste doped samples. Conversely, the crystalline content in the metallic waste doped sample does not reduce the durability of the wasteforms.

Corrosion of the alumina crucibles by the glass melts resulted in Al_2O_3 content in all products exceeding that batched, as shown in Table 4-8. Interestingly, Al_2O_3 incorporation within the borosilicate glass melt is associated with preferential uptake of uranium, as shown by the SEM-EDX analysis in Figure 4-28. This suggests that elaboration of the glass composition to explore addition of Al_2O_3 as a minor component, may assist further incorporation of uranium and potentially eliminate phase separation.

Crystalline phases detected in metallic waste samples, UO_2 and U_3O_8 , were correspondingly observed in SEM micrographs (Figure 4-33). Two forms of inclusion were found, fused crystals and dendritic crystallites, both of which were formed during the initial casting and cooling of the glass, as un-reacted batch material was not detected. Complementary EDX spectra (Figure 4-34 and Figure 4-35) detected uranium and oxygen in the crystalline inclusions analogous with UO_2 or U_3O_8 proving uranium metal has been oxidised within the melt. There was no evidence for magnesium incorporation in any crystalline phase by either XRD or SEM-EDX, indicating Mg metal and $\text{Mg}(\text{OH})_2$ simulant waste constituents were completely oxidised or dehydroxylated, and digested into the melt as MgO. The presence of crystalline phases is expected to cause increased rates of dissolution due to crystals creating grain boundaries that could act as pathways to accelerated leaching [201]. Metallic waste samples were also observed to contain high amounts of porosity which would be potentially deleterious to the performance of waste glasses if reproduced in full scale products; since the available surface area of the glass for chemical attack is increased thereby leading to increased rates of dissolution. However, chemical durability data for metallic waste loaded samples (Figure 4-40) do not show

significant normalised mass loss (except for boron), therefore porosity and crystallisation does not therefore appear to have a deleterious effect on these glasses.

Geochemical modelling, using Phreeqc [36], identified various potential phases can be present as a result of alteration. In MAS-M, the previous crystalline UO_2 phase pre-28 day leaching was transformed to a higher oxidation state, where a transformation from UO_2 to hyper-stoichiometric $\text{UO}_{2.34}$ was observed. Low intensity peaks were also detected in MAS-M that index consistently with studtite, $\text{UO}_4 \cdot 4\text{H}_2\text{O}$, a hydrated U (6+) phase that has been observed in previous work on alteration of UO_2 [229]–[231] and observed on aged glass-ceramic samples of lava-like fuel containing materials formed from the Chernobyl nuclear disaster [99], [232]. This hydrated uranium species is possible through radiolysis of the leachate solution to form oxidising reactants such as hydrogen peroxide. This phase was only observed in MAS-M demonstrating the phase is formed through alteration of UO_2 crystals present in the glass; this was not observed in the borosilicate counterpart due to the lower rates of dissolution observed in this sample overall (Figure 4-40). No alteration products predicted by Phreeqc modelling were observed in XRD data, indicating that either the alteration products are not forming, or that they are low in concentration and therefore below the detection limit for XRD, or present as quasi crystalline materials. Neither corroded sample showed any change with no crystalline phases detected by XRD, indicating the alteration regions shown in Figure 4-41 and Figure 4-42 are X-ray amorphous, or below the detection limit of XRD.

Thermal analysis

High melting temperatures were required for aluminosilicate samples due to a combination of higher Al_2O_3 and SiO_2 content coupled with less B_2O_3 resulting in a more polymerised melt and resultant glass. When compare to corroded waste samples, a general trend of increased liquidus temperatures for all metallic waste samples is apparent, most likely due to the high concentration of uranium in such systems acting as an intermediate oxide [135]. Alternative glass making systems such as in-container vitrification or the use of adequate air filtration could be used to negate the effects of increased melt temperature, with corrosion resistant lining required for aluminosilicate compositions.

Uranium incorporation

Results from XANES experiments demonstrate both metallic and corroded waste can be passively oxidised and digested into the glass melt without mechanical stirring or bubbling. This simplifies the production of glass and reduces the amount of secondary waste produced but results in striations within the samples as observed in Figure 4-28, arising from phase separation. Due to the increased melting temperature and melt duration, U in aluminosilicate samples was more oxidised than in the equivalent borosilicate sample as higher temperatures

provide more oxidising conditions. Similarly, corroded waste samples were found to have higher U oxidation states than metallic waste glasses, caused by the initial batch components containing previously oxidised uranium (U_3O_8) and only small amounts of metal whereas metallic waste glass was batched with larger quantities of metallic U. The observed crystalline phase UO_2 (U^{4+}) within MBS-M sample is a contributing factor to the lower average oxidation state compared to the corroded waste counterpart sample. Oxidation state of uranium influences the mobility of the radionuclide in aqueous environments, such that U^{6+} is more mobile and therefore hazardous, than U^{4+} , hence glass compositions with U in low oxidation states would be preferential for disposal [233]. The observation of the U^{6+} studtite-like phase by XRD of 28 day altered MAS-M could be an underlying factor in the high rate of uranium dissolution in this sample, compared to MBS-M. The presence of studtite and the shift in peak position from UO_2 to $UO_{2.34}$ within 28 day altered MAS-M indicates uranium can oxidise within the hydrothermal conditions of a PCT-B test. Further studies of sample oxidation state post leaching could be useful in determining the exact change in oxidation state due to hydrothermal alteration.

Dissolution and alteration

Increased pH of leachate from aluminosilicate samples is linked to sodium release which is responsible for the greater mass loss of boron, silicon and uranium as observed by Corkhill *et al.* [76]. Upon reaching saturation, the B leaching rate observed in borosilicate glasses was almost identical to that of aluminosilicate compositions implying the same dissolution process is occurring in both sets of samples, however the normalised mass loss was significantly higher in aluminosilicate glasses. The durability of these samples was found to be comparable to that of other ILW and HLW glasses observed over similar conditions and timescales, with HLW simulant MW-25 having a boron release rate of $2.4 \times 10^{-2} \text{ g m}^{-2} \text{ d}^{-1}$ [209]. As the magnesium aluminosilicate and borosilicate samples produced in this study are intended for the Magnox ILW, where the radioactive hazard is two orders of magnitude lower than that of HLW, the safety case of these samples is strengthened significantly. UK HKW glass

Normalised mass loss of magnesium is considerably lower than the loss of boron, and since the long term radiotoxic hazard is due to U, the leaching of Mg is not a significant problem. Mass loss of U was considerably higher in aluminosilicate samples due to the increased pH from the Na content and higher oxidation state, as previously mentioned.

Leaching of U was observed to be greater in corroded waste samples, where the average oxidation state nears U^{6+} , when likened to the comparable metallic waste doped samples. Correspondingly, aluminosilicate glasses leach more uranium than borosilicates counterparts, partly due to the difference in U oxidation state between samples.

Alteration layers formed on glass particles after 28 days (Figure 4-41) which were found to be homogenous in the case of borosilicate samples. No concentration of uranium was detected

in this region and it is therefore assumed this behaves as a passivating layer reducing further dissolution of the glass as the system enters the steady state dissolution regime, improving the passive safety of the system. Sodium and uranium accumulated on the water the water-surface and glass-alteration interfaces for aluminosilicate samples which indicate this alteration region is not passivating allowing uranium to accumulate in this unstable region, allowing uptake into solution and impairing the function of the aluminosilicate waste form. This alteration region was not detected by XRD on 28 day samples.

4.2.5. Conclusions

In this study MgO-B₂O₃-SiO₂ and MgO-Al₂O₃-SiO₂ glass systems were produced that passively oxidised and incorporated metallic uranium and magnesium representative of wastes present in the First Generation Magnox Storage Ponds. Two extremes of the waste encompassing the whole spectrum anticipated were incorporated into a single composition demonstrating the flexibility of the system studied and simplifying the process of making safe the ponds on the Sellafield site.

MgO-B₂O₃-SiO₂ compositions melted below 1200 °C; whilst this is compatible with the glass melter technology currently used at Sellafield, technology such as in container vitrification or Joule heated melters would likely be used for this application. MgO-Al₂O₃-SiO₂ compositions required melting temperatures in excess of 1300 °C which would necessitate adaption to existing melting facilities, or more likely the use of the technologies mentioned above, however the increased temperature could lead to the volatilisation of problematic fission products such as Cs and hence a borosilicate composition is most preferential.

Borosilicate glasses were found to be more chemically durable than their aluminosilicate counterparts with lower average U oxidation state and performance comparable to current UK HLW glass. Formation of alteration layers was observed to be enhanced in aluminosilicate glasses relative to borosilicate samples and the creation of the potentially deleterious studtite phases on aluminosilicate samples help to conclude that magnesium borosilicate glass compositions would be more suitable for the immobilisation of Magnox sludges.

If the borosilicate system proposed in this study was used to treat the 3,148 m³ of sludge waste in the FGMSP, calculations show a net reduction in the volume of waste to be disposed by 25% compared to the raw sludge and a reduction in 80% compared with the current baseline plan of cementation. Since the cost of disposal for ILW in a GDF is estimated at £8,990 per m³ [234], the financial saving from disposing vitrified waste over cemented waste was calculated at approximately £82 million.

4.2.6. Acknowledgments

The authors would like to thank the EPSRC (Grant EP/G037140/1) for funding this research which was performed in part at the MIDAS Facility, at the University of Sheffield, established with support from the Department of Energy and Climate Change.

4.3. Further Work – Hot Isostatic Pressing of Sludge Waste

Hot isostatic pressing of wet Magnox sludge residues was researched with the intention to develop a single can process route by which wet sludge waste could be thermally synthesised into a durable waste form. This would be possible by conversion of sludge and residues into solids using the HIP via ‘in-can’ hydration of oxides into hydroxides as outlined in Section 3.2. The proceeding sections look at the work done in exploring this novel option for nuclear waste disposal.

4.3.1. Introduction

A simple, once-through process for treatment and safe immobilisation of hazardous sludge wastes would be of great benefit to the UK nuclear industry. Hot Isostatic Pressing (HIPing) is one such potential approach to thermal treatment of sludge wastes. A desk study was conducted into the feasibility of wet HIPing simulant Magnox Sludge identifying a couple of key issues. The first being that free water entrained within a sealed HIP can would transform to steam at the temperatures exposed to during a HIP cycle, causing pressurisation within the can which would impede densification. A second concern was for the safety and longevity of the pressure vessel equipment, with a breach or rupture of a can causing significant damage to the pressure vessel and the furnace within, especially since the can internal pressurisation and high temperature water/steam could weaken the welds used to manufacture and seal the can.

However, negating all these factors, a study into the best available material with which to sequester any free water was performed with the conclusion that this process would lead to a significant increase in the total waste to be disposed and hence was not an efficient process: the most effective sequestering material was identified as sodium metasilicate (waterglass) leading to a 1.6x increase in volume to absorb the water present in the raw sludge. It must be noted however that this would be comparable to encapsulation within a cement.

It was therefore decided that drying and or calcining of the wet sludge waste would be required to remove free water and bound waters of hydration and assist in the development of a viable product to dispose. Two samples utilising Magnox sludge calcined at 600 °C and 1000 °C were developed from the borosilicate glass composition outlined in the previous section. The objective for this experiment was to produce a durable glass product akin to that produced in Section 4.2. For the methodology used to produce HIP samples the reader is referred to Section 3.2.

4.3.2. Results

Melting Behaviour and Composition:

Of the two samples produced from the HIP thermal synthesis, the 1000 °C calcined sludge sample (MBS-1000) produced a can that appeared to have little densification and shrinkage as would have been expected. This particular sample was repeated three times with the same result. A 600 °C calcination sample (MBS-600) was deformed in the manner expected, from experience of other HIP synthesis experiments [151]. Figure 4-46-A shows MBS-1000 after the HIP cycle with deformation of the lid and discolouration of the outer surface. Upon close inspection the presence of dark black, glossy spots was present on the surface of the HIP can along the bottom weld (Figure 4-46-B). MBS-600 did not suffer these effects. Cutting open MBS-1000 revealed a deep-blue glass sat atop a white powder material with a friable consistency as shown in Figure 4-47-A. The interior of the HIP can was heavily corroded with deep pitting and a distinct 'neck line' present (Figure 4-47-B), as observed similarly on glass melting crucibles from highly corrosive melts. The corrosion extends approximately 1 mm into the stainless-steel HIP can wall. Again, this was not observed in the MBS-600 sample.

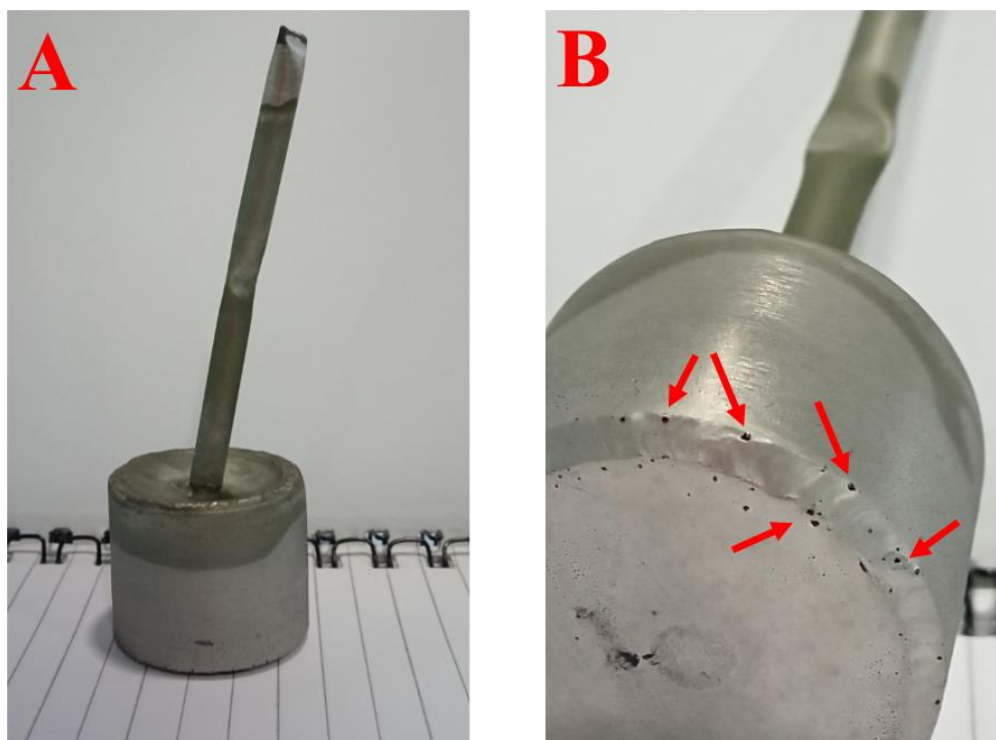


Figure 4-46. Post-HIP MBS-1000 sample; surface deformation and discolouration (A) and highlighted glossy black spots (B).

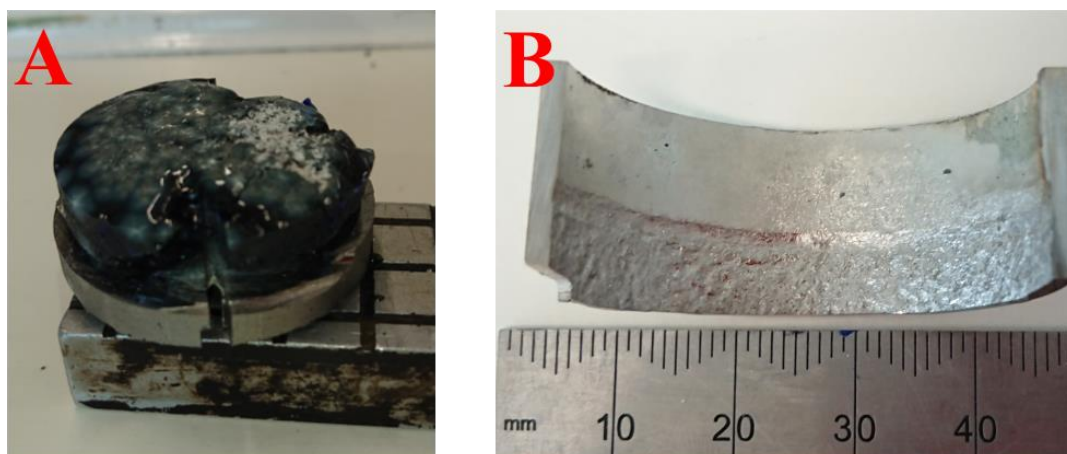


Figure 4-47. Sectioned can from MBS-1000 sample; Blue glass surrounding white powdery material (A) and heavily corroded internal HIP can (B)

Volume reduction obtained from the pre-HIPed can was determined by water displacement, with 38.6% volume reduction for MBS-600 sample and 36.2% reduction for MBS-1000.

Phase Analysis and Microstructure:

XRD of 600 °C and 1000 °C calcined Magnox sludge simulant is shown in Figure 4-48. In both cases the wet $\text{Mg}(\text{OH})_2$ was dehydroxylated to MgO , with the peaks for associated this phase more pronounced and sharper after 1000 °C calcination indicating a more ordered/structured material has formed [173]. The insets show a region over the range $30^\circ < 2\theta < 65^\circ$ highlighting a minor MgAl_2O_4 spinel phase present within the MgO . Due to the Magnox AL80 material used to create the simulant sludge, which contains 0.8% Al [235], this minor spinel phase is likely due to the process of reacting the Mg and Al during calcination.

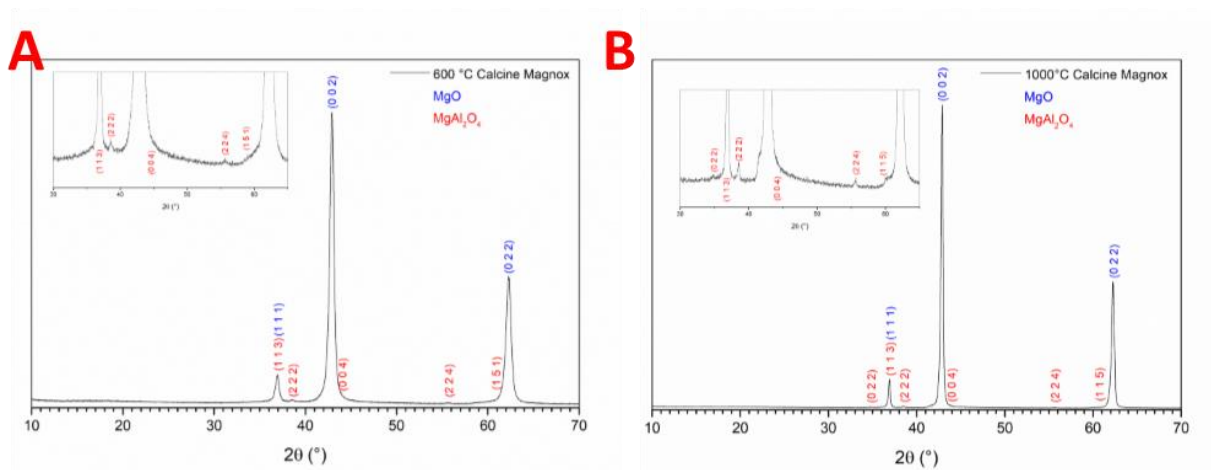


Figure 4-48. XRD data of calcined simulant Magnox sludge at 600 °C (A) and 1000 °C (B)

The XRD analysis of the HIPped wasteforms revealed a heavily crystallised glass product had been produced, evidenced by diffuse scattering between $15^\circ \leq 2\theta \leq 30^\circ$ shown in Figure 4-49 and Figure 4-50. The added batch components SiO_2 and B_2O_3 are present combined with the MgO yielding a $MgO-B_2O_3-SiO_2$ glass, plus forming a crystalline $Mg_2B_2O_5$, demonstrating reaction has occurred at the synthesis temperatures. A significant SiO_2 phase was also present in both samples, occurring due to either incomplete reaction with the other batch components or crystallising out of a glass melt during cooling. The SiO_2 phase is evidently more prevalent in MBS-1000 sample evidenced by the intense (011) peak indexed to SiO_2 in Figure 4-50.

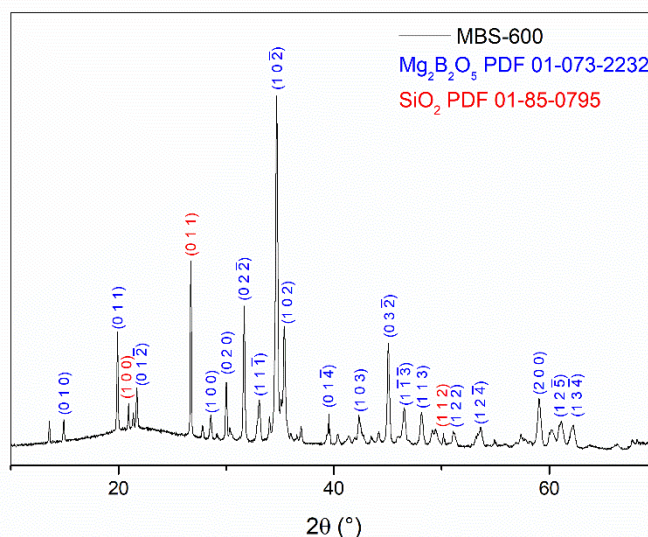


Figure 4-49. XRD data for MBS-600 after HIP synthesis

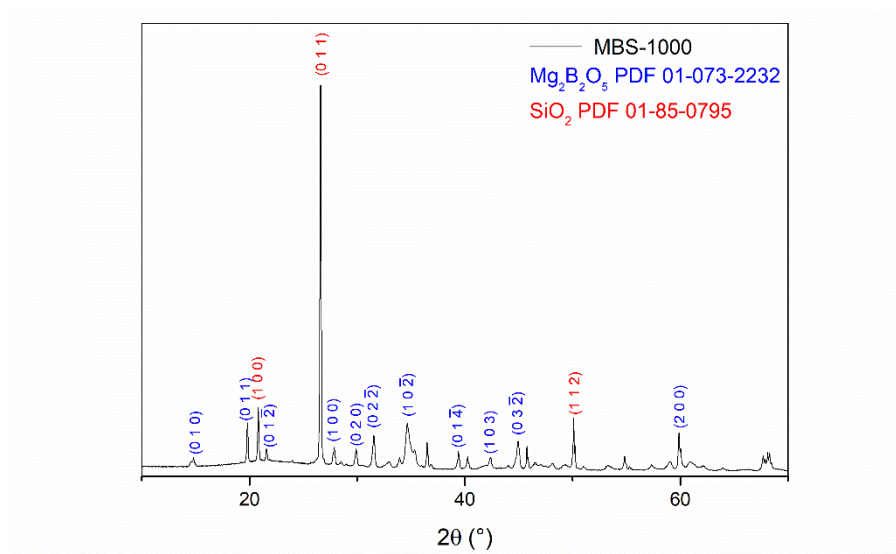


Figure 4-50. XRD for MBS-1000 after HIP synthesis

SEM of the HIPped MBS-600 and MBS-1000 wastefoms revealed multiple phases present within the glassy materials produced, see Figure 4-51. Very little homogenous glass was observed in either sample, confirming the visual observations that heterogenous samples had been created. The detailed microstructure of the samples was not investigated by EDS analysis however a basic EDS spot analysis determined a high concentration of Si-O regions, likely SiO_2 , and Fe-Mo-Cr spinels in both samples whilst being more prevalent in the MBS-1000 composition.

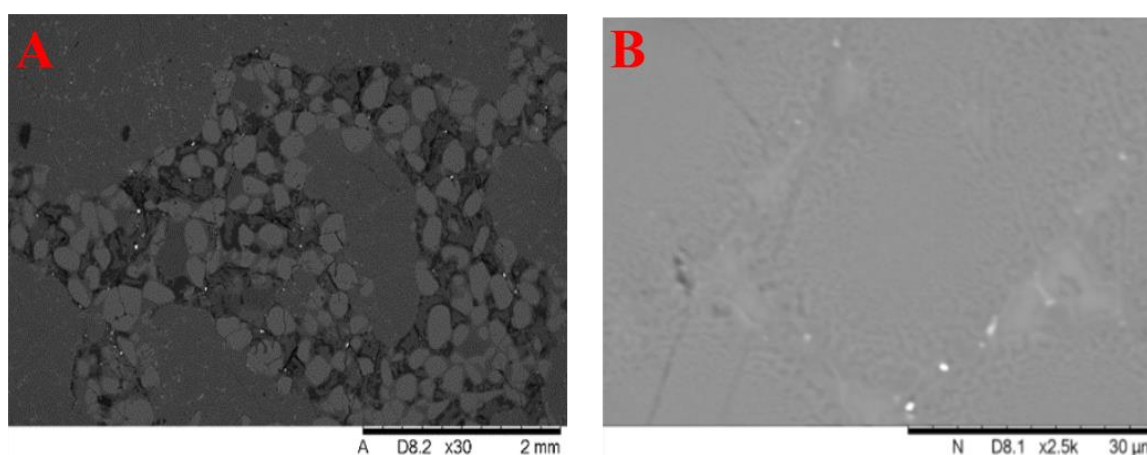


Figure 4-51. SEM micrographs showing SiO_2 phase present in MBS-600 (A) and a Si-Al rich region within MBS-1000 (B). Note the bright spots corresponded to a Fe-Cr-Mo spinel like phase.

Thermal Analysis:

Simulant Magnox sludge material was analysed by DTA-TG (Figure 4-52), determining $\text{Mg}(\text{OH})_2$ undergoes de-hydroxylation into MgO between 350 °C and 500 °C. The associated mass change from this thermal event was around 32% of the original mass, with mass loss due to release of H_2O .

Material extracted from MBS-600 was also analysed by DTA-TG to determine the points at which thermal events occurred within the sample during heating. Figure 4-53 shows the DTA and TG data obtained over the temperature range 100 °C to 1500 °C. The data obtained is comparable to that from the base glass discussed earlier (Section 4.2). A second order glass transition event was observed at circa 565 °C, followed by an exothermic event assigned as a crystallisation event at 683 °C. A further second order event is present at 984 °C indicating a second glass transition region, before the final liquidus temperature occurring from 1220 °C.

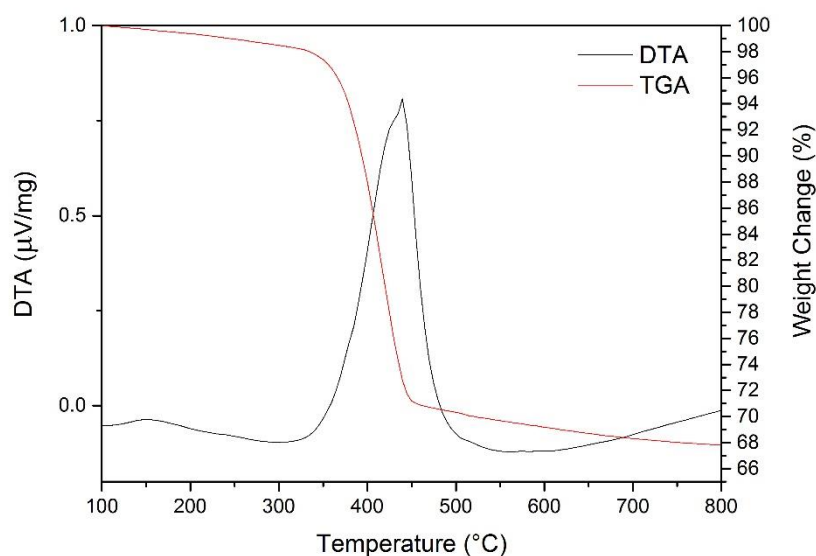


Figure 4-52. STA of Simulant Magnox Sludge

Mass loss of up to 4 wt% occurred rapidly during the initial heating to approximately 600 °C likely due to the presence of residual $\text{Mg}(\text{OH})_2$ in this sample. A steady mass was then maintained until melting and the release of volatiles reduced the mass further albeit at a much lower rate. Material was not extracted from MBS-1000 for DTA-TG experiments.

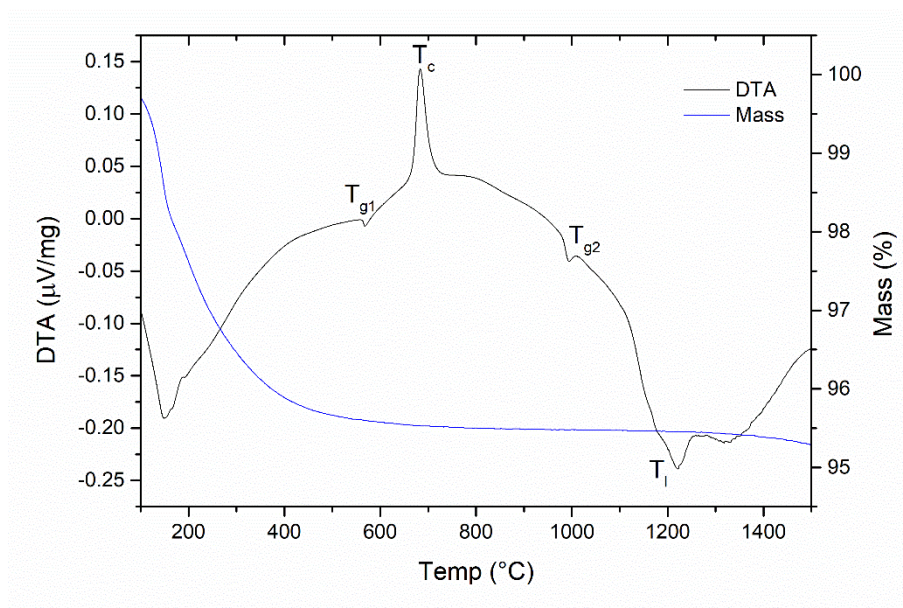


Figure 4-53. DTA-TG data from MBS-600

4.3.3. Discussion

Thermal synthesis of magnesium borosilicate glass via HIP method was found to be more complex than expected, forming a heterogeneous wasteform and evident reaction with the steel HIP can/welds which led to can failure. Calcination at 600 °C was determined to be sufficient for near complete de-hydroxylation of the sludge to MgO, whilst calcination at 1000 °C produces so called ‘hard-burned’ magnesia, which has low reactivity [86], [236]. Due to unreactive MgO not incorporated in the melt within MBS-1000, a glass composition of SiO₂-B₂O₃ would have formed. The SiO₂-B₂O₃ pseudo-ternary liquidus phase diagram [237] identifies formation of a liquid glass phase above 600 °C, therefore formation of a high B₂O₃ content glass melt would be corrosive at high temperatures. The blue colouration and distinct glassy phase present from MBS-1000 samples can be linked to this corrosion with significant incorporation of the steel components from the HIP can (Figure 4-47). This effect is akin that observed in the neckline of alumina crucibles from conventional thermal synthesis in a glass melting furnace (Section 4.2). Unlike a conventional glass melting, the HIP can is a sealed system, not allowing volatilisation of the B₂O₃. Evidence of Fe-Mo-Cr spinel phases in the samples also indicate uptake of material from the HIP can walls. The small dark black, glossy spots present on the exterior of the MBS-1000 HIP can were too small to be extracted and analysed but noting the severe corrosion on the interior of the can are likely a result of the corrosive glass attack on pin hole welds, especially as these occur along the weld line. Calcination of sludge at 600 °C produces MgO which is more reactive assisting MgO incorporation into the glass melt as it forms, maintaining a high liquidus and therefore less

aggressive melt. It is suggested that any further work on the wastefrom development should utilise 600 °C calcined material.

It would be assumed that the higher temperature calcined material would perform better due to the removal of all bound waters of hydration, however as has been discussed the formation of 'hard-burned' magnesia effectively increases corrosion though alteration of the target glass phase. It is also likely that re-hydroxylation and carbonation of calcined material upon cooling in air may have occurred. This would be more prevalent in MBS-1000 due to the longer time taken to cool and batch into a HIP can compared to MBS-600. To conclusively determine this process, the use of an inert gas or vacuum furnace would be required to calcine the sludge simulants.

From the intensity of the crystalline peaks of SiO_2 and the $\text{Mg}_2\text{B}_2\text{O}_5$ phases identified by XRD, it can be deduced that a very inhomogeneous material has been created. The two phases present coincide with unreacted/partially reacted original batch material, with the original MgO and B_2O_3 content combining into an oxide phase. It is hypothesised that reaction of a small quantity of the batch components into the target glass phase did occur (evidenced by the homogenous regions in Figure 4-51), producing the intended magnesium borosilicate phase, although this is likely incorporating elements pulled out from the corrosion of the steel HIP cans used (Figure 4-47). Glass melts often require agitation or mixing and this is often in the form of natural convection currents through a melt. In the sealed environment of the HIP can, of the size used in this project, this is unlikely to happen and hinders the production of the glass melt.

Thermal analysis was only performed on the MBS-600 sample as it was noted the experiment was performed under an inert gas and without external pressure applied, as would have been the case in the HIP during the synthesis process and therefore is of limited value. The DTA data obtained reveals a melting temperature comparable to that of the original MBS base glass developed and investigated in Section 4.2, however it would be expected that during a HIP cycle this temperature would be reduced due to the high pressure exerted upon the batch. The glass transition should have been comparable to the base glass, however it was observed to be circa 100 °C higher, likely due to the alteration of the glass composition due to the uptake of stainless-steel components. A second glass transition was also observed occurring, indicating a second, higher temperature glass phase had formed however no evidence of this was found in SEM micrographs nor was there any second region of diffuse scattering present in XRD data.

4.3.4. Conclusions

It is concluded that the HIP technique would not be suitable for the production of the magnesium borosilicate glass studied, without further research. The high content of boron

created a corrosive melt which lead to a large uptake of material from the HIP can wall into the glassy melt. The lack of any mixing resulted in an inhomogeneous material with incomplete reaction of the batch components into a glass product. Further refinement of the glass batch composition may yield better results with the use of less boron being key for future compositions. The calcination temperature/conditions for the simulant Magnox sludge could also be modified to assist in the final product quality.

5. Thermal Treatment of Simulated Chernobyl Lava-Like Fuel Containing Materials

This section explores the application of thermal treatment to produce simulant LFCM, representative of that from the Chernobyl Unit 4 meltdown, and the subsequent characterisation of the materials. The simulants were produced on a laboratory scale using low activity uranium to reduce the risk of exposure whilst maintaining the properties of the original lava material. These LFCM materials are described in detail over two papers in this chapter along with the work done to recreate them in the laboratory.

The first paper discusses the initial development of LFCM samples whilst the second paper discusses the evolution of the batching and synthesis process to create representative material.

5.1. Initial Development - Published Paper: Synthesis of simulant ‘lava-like’ fuel containing materials (LFCM) from the Chernobyl reactor Unit 4 meltdown

This work takes the form of a published paper submitted to the MRS Advances Journal and published on 23/12/2016. This work was performed and written by myself with the aid of co-authors for feedback and comments.

The article presented here is 'Reprinted with permission' in its entirety with the copyright notice 'MRS Advances © 2016 Materials Research Society' [238]. Figure and section numbering including referencing have been adapted to retain continuity with this thesis.

Synthesis of simulant ‘lava-like’ fuel containing materials (LFCM) from the Chernobyl reactor Unit 4 meltdown

Sean T. Barlow, Daniel J. Bailey, Adam J. Fisher, Martin C. Stennett, Claire L. Corkhill and Neil C. Hyatt

Department of Materials Science and Engineering, The University of Sheffield, S1 3JD, UK.

Abstract: A preliminary investigation of the synthesis and characterization of simulant ‘lava-like’ fuel containing materials (LFCM), as low activity analogues of LFCM produced by the melt down of Chernobyl Unit 4. Simulant materials were synthesized by melting batched

reagents in a tube furnace at 1500 °C, under reducing atmosphere with controlled cooling to room temperature, to simulate conditions of lava formation. Characterization using XRD and SEM-EDX identified several crystalline phases including ZrO_2 , UO_x and a Zr-U-O mixed oxide phase with spherical metal particles encapsulated by a glassy matrix. The UO_x and ZrO_2 phase morphology was very diverse comprising of fused crystals to dendritic crystallites from the crystallization of uranium initially dissolved in the glass phase. This project aims to develop simulant LFCM to assess the durability of Chernobyl lavas and to determine the rate of dissolution, behavior and evolution of these materials under shelter conditions.

5.1.1. Introduction

On the 26th of April 1986, an accident during an experimental power failure test destroyed Unit 4 of the Chernobyl Nuclear Power Plant, Ukraine. During the accident, temperatures reached in excess of 1600 °C resulting in melting of the nuclear fuel and zirconium cladding [97]. Interaction of the molten fuel mass with the structural materials of the reactor resulted in the formation of several lava-like flows. These lava-like flows formed glassy materials upon cooling in the basement levels beneath the ruined reactor [239]. These so called lava-like fuel containing materials (LFCM) are essentially glass-ceramic composite materials [96]. Accumulations of LFCM are located in numerous sub-reactor rooms beneath Unit 4, amounting to approximately 1250 tons [97]. LFCM masses are primarily brown or black and contain considerable porosity and compositional heterogeneity. However, granulated and pumice-like materials have also been observed. Solidified metallic spheres of varying diameter have been found in brown and black type lavas. Granulated and pumice-like materials are hypothesized to be the result of lava flows interacting with cold water, causing instant foaming and the formation of highly porous material [96].

Following the accident, an interim shelter was constructed to contain the ruined reactor and protect its contents. Although designed to last 30 years, degradation of the shelter structure has led to the ingress of substantial volumes of water. Interaction of water with LFCM within the shelter has caused weathering of substantial portions of the LFCM and formation of numerous secondary uranium compounds, studtite ($UO_4 \cdot H_2O$), rutherfordine (UO_2CO_3), schoepite ($(UO_2)_8O_2(OH)_{12} \cdot 12H_2O$) and paulscherrite ($UO_2(OH)_2$). Constant wetting and drying of LFCM materials and associated secondary uranium mineral phases leads to the formation of fine radioactive aerosol particles; a significant respirable hazard within the shelter and a possible source of airborne contamination [94], [240]. The study of the alteration of LFCM under shelter conditions is vital to understanding the long term behaviour of these materials, the hazard LFCM presents and the eventual remediation of the site. Due to the large amounts of spent nuclear fuel contained within LFCM, study of actual LFCM is hazardous and not without considerable challenge. Study of low activity simulant LFCM, derived from actual lava compositions, is needed to understand the durability of LFCM materials and to determine the alteration behavior of these materials. This study was therefore conceived to design and

synthesize representative simulant LFCM to allow the behavior of LFCM to be studied without the additional complications of high radioactivity. The findings of this project could also assist in the development of glass wastefoms in engineered repositories via the use of low activity simulants to enable synthesis and characterisation on the durability of wastefoms encountered in the civil waste industry.

5.1.2. Review of LFCM and Compositions as Synthetic Targets

Brown LFCM contains metallic iron in the form of spherical droplets within the glass matrix and ~11 wt% uranium. In general the degree of crystallisation and proportion of Fe-bearing phases is greater in the Brown LFCM along with the uranium content [6], [96], [97], [99]. Analysis of LFCM by the Khlopin Radium Institute revealed several crystalline inclusions including non-stoichiometric UO_2 , ZrO_2 , from the fuel cladding materials, and a high uranium zircon phase termed Chernobylite. Dendrite-like inclusions of $(\text{Zr}_{1-x}\text{U}_x)\text{O}_2$ were reported, representing recrystallization of LFCM after cooling, along with phases of a fused morphology from the interaction between droplets of UO_x and Zirconium alloy cladding [6]. Compositions of brown and black LFCM have been reported in numerous publications, but each differ with regards to major glass components [7], [95]–[97], [241]. Consequently, averaged compositions were determined and used to produce the simulant materials in this study. Synthesized simulant compositions are shown in Table 5-1.

Table 5-1. Synthesized LFCM compositions

Component	Brown LFCM (mol%)	Black LFCM (mol%)
SiO_2	65.6	67.9
CaO	7.3	8.2
ZrO_2	3.3	3.0
Na_2O	5.3	5.8
BaO	0.1	0.1
Al_2O_3	4.2	5.1
MnO	0.5	0.4
Fe_2O_3	0.5	-
MgO	10.7	8.4
UO_2	2.5	1.2

5.1.3. Experimental Procedure

Stoichiometric amounts of SiO_2 (Lochaline Quartz Sand 99.6%), CaCO_3 (Fisher 98%), ZrO_2 (Aldrich 99%), Na_2CO_3 (Alfa Aesar 98%), BaCO_3 (Alfa Aesar 99%), $\text{Al}(\text{OH})_3$ (Acros 95%),

Mn₂O₃ (Aldrich 99%), Fe/Cr₁₈/Ni₁₀/Mo₃ (Goodfellow), Mg(OH)₂ (Sigma-Aldrich 99.9%) and UO₂ (British Drug Houses) were batched accordingly to produce both black and brown compositions. Batched compositions were carefully mixed prior to melting in alumina ‘boat’ crucibles within an Elite Thermal Systems TSH 15/50/450 tube furnace under flowing H₂/N₂. Reducing conditions were utilized to simulate formation conditions during the accident. Samples were melted at 1500 °C for 4 hours and cooled to room temperature at 1 °C/min.. Initial samples were prone to spontaneous fracturing and an intermediate annealing step was successfully applied by heating to 690 °C for 70 hrs with cooling to room temperature at 5 °C/min, reducing the residual stresses within the glass and obtaining monolithic samples.

X-ray powder diffraction (XRD) was performed to determine the crystalline phases present within synthesized materials. Measurements were conducted using a Bruker D2 X-ray diffractometer in reflectance mode over the range $10^\circ < 2\theta < 60^\circ$ with Cu K α radiation (30 kV, 10 mA). Subsequent data was processed using the Bruker DiffracEva 3.0 software package and the PDF-2 database used for peak identification.

Representative cross-sections of synthesized LFCM were produced by sectioning melted glasses using a Buehler Isomet Low Speed Saw. Crystalline phase assemblage of the cross-sections was studied by scanning electron microscopy (SEM) using a Hitachi TM3030 SEM. Partitioning of key elements within the simulant samples was determined by energy dispersive X-ray spectroscopy (EDX) using a Bruker Quantax EDX system coupled to the SEM. Samples were prepared for SEM-EDX by mounting in cold-setting epoxy resin and polishing with SiC and diamond paste to a 1 μ m finish. Samples were sputter coated with carbon to avoid surface charge effects.

5.1.4. Results & Discussion

LFCM Synthesis:

Produced ‘Brown’ and ‘Black’ LFCM compositions formed highly crystalline, glassy products. Brown type simulants were dark brown in color with a cracked and mottled surface with low porosity. Black simulant compositions formed a dark blue glass with a thin pale-blue surface layer that was glassy in appearance. The pale blue colored surface is not reported as present in the actual LFCM samples, found in the Chernobyl sub-reactor rooms, and the bulk was much darker in coloration. However, one particular LFCM variant, termed polychromatic ceramic, located in the upper levels of the destroyed Unit 4, was described as “a sealing-wax brown color with bright blue veinlets” [242]. Overall, the visual appearance of the simulants is comparable with reported LFCM.

Phase Analysis:

Results of powder X-ray diffraction analysis showed simulant LFCM to be glassy materials with significant crystalline content, as shown in Figure 5-1. The strong diffuse intensity is typical of glassy materials and the observed reflections were indexed to zirconium oxide (ZrO_2), a uranium-zirconium mixed oxide phase ($\text{U}_{0.8}\text{Zr}_{0.2}\text{O}_2$) and cristobalite (SiO_2). Brown compositions were also found to contain a spinel phase, nominally $\text{Fe}(\text{Fe}_{1.96}\text{Cr}_{0.03}\text{Ni}_{0.01})\text{O}_4$ from the oxidation of $\text{Fe}/\text{Cr}_{18}/\text{Ni}_{10}/\text{Mo}_3$ steel phase added to the batch.

The pale blue surface phase observed on black simulant lava was removed and characterized by XRD however no significant difference compared to the bulk was detected. This phase is believed to contain uranium in the U (IV) oxidation state, due to its blue coloration. A full analysis of the average oxidation state within the lavas will be carried out at a later date.

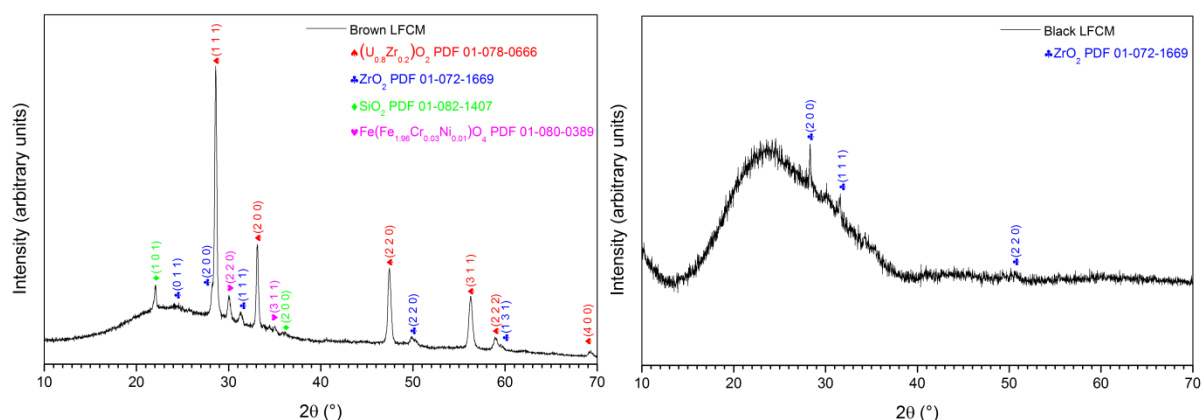


Figure 5-1. XRD plot of simulant brown (left) and black (right) LFCM

Scanning electron microscopy of black and brown simulant lavas found the microstructure to consist of a majority glass matrix with various minor phases dispersed throughout as distinguished by their contrast. Minor phases rich in U and Zr were present as dendritic and fused crystals. Spherical particles of metal were also found throughout the glass matrix of brown LFCM simulants, likely formed as droplets of molten metal trapped within the glass matrix during melting, as shown in Figure 5-2. Complementary EDX analysis highlights elemental partitioning with the samples in correspondence with the crystalline phases identified by XRD. EDX maps for the key elements indicate uranium and zirconium are evenly distributed throughout the glass matrix and concentrated within their representative crystal phases as shown in Figure 5-3.

Comparison of the experimental data presented in this study with the results of analysis of actual LFCM shows good agreement between the simulant and real materials [7], [95]–[97], [241]. Morphology, crystalline content and microstructure were found to be consistent with those observed in actual LFCM samples with the notable exception of the crystalline phase zircon (ZrSiO_4). These results would suggest that, although the simulant materials are a good approximation, further refinement is necessary to produce more representative simulant LFCM.

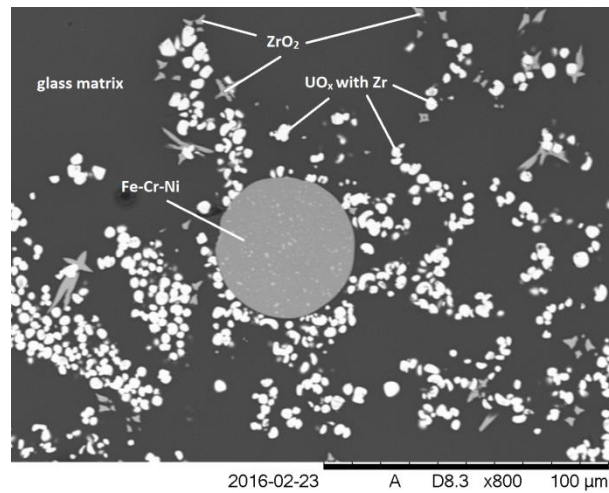


Figure 5-2. Back-scattered SEM micrograph of simulant brown LFCM labeling the crystalline phases present.

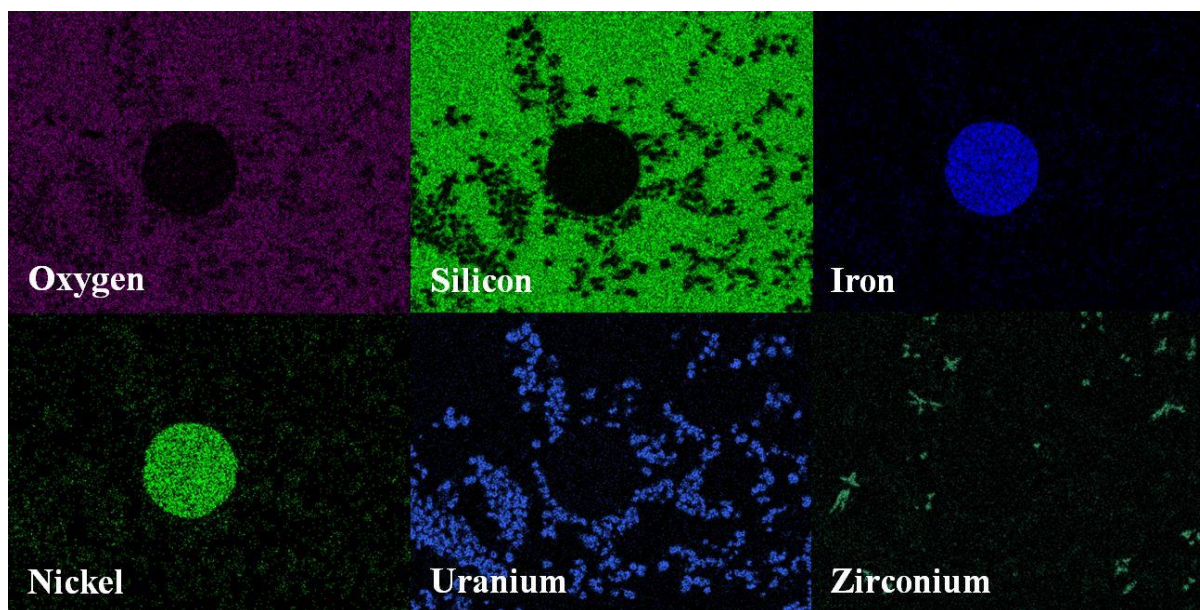


Figure 5-3. EDS maps of key elements in brown LFCM

5.1.5. Conclusions

This study demonstrates the successful synthesis of simulant ‘lava-like’ fuel containing materials. The morphology and microstructure have both been recreated successfully in the simulant material and the crystalline content has been found to be largely similar with the exception of zircon. Further refinement of the composition and synthesis procedure is ongoing; production of adjusted LFCM compositions to reproduce the zircon phase is underway with promising results so far.

5.1.6. Acknowledgements

The authors would like to thank the EPSRC (Grants EP/G037140/1, EP/N017374/1, EP/L014041/1) for financial support for this research, which was performed at the MIDAS Facility, at the University of Sheffield, established with support from the Department of Energy and Climate Change. We also acknowledge financial support from the EPSRC allocation to University of Sheffield from its Global Challenges Research Fund.

5.2. Development of Representative Samples – Submitted Paper: Synthesis, characterisation and corrosion behaviour of simulant Chernobyl nuclear meltdown materials

This work takes the form of a draft paper submitted to the journal *npj Materials Degradation* on 02/04/19. This work was written by myself with the aid of co-authors for feedback and comments. All the experimental work was performed by myself with the exception of the acquisition of chemical compositional data which was performed on my behalf by Sheffield University Chemistry Department, X-ray absorption spectroscopy data collection which was performed by the co-author Martin Stennett at the KEK Photon factory, High Energy Accelerator Research Organisation Facility, Japan, and chemical durability testing which were performed by co-authors Claire Corkhill, Daniel Bailey and Clemence Gausse.

The article presented here is reproduced with figure and section numbering adapted to retain continuity with this thesis.

Synthesis, characterisation and corrosion behaviour of simulant Chernobyl nuclear meltdown materials

Sean T. Barlow¹, Daniel J. Bailey¹, Adam J. Fisher¹, Martin C. Stennett¹, Clemence Gausse¹, Claire L. Corkhill^{1*}, Viktor A. Krasnov², Sergey Yu. Sayenko³ and Neil C. Hyatt¹

¹NucleUS Immobilisation Science Laboratory, Department of Materials Science and Engineering, The University of Sheffield, S1 3JD, UK.

²Institute for Safety Problems of Nuclear Power Plants, National Academy of Sciences of Ukraine, Kyiv oblast, Ukraine.

³National Science Center Kharkov Institute of Physics and Technology, National Academy of Sciences of Ukraine, Kharkov, Ukraine.

Abstract: Understanding the physical and chemical properties of materials arising from nuclear meltdowns, such as the Chernobyl and Fukushima accidents, is critical to supporting decommissioning operations and reducing the hazard to personnel and the environment surrounding the stricken reactors. Relatively few samples of meltdown materials are available for study, and their analysis is made challenging due to the radiation hazard associated with handling them. In this study, small-scale batches of low radioactivity (i.e. containing depleted uranium only) simulants for Chernobyl Lava-like Fuel Containing Materials (LFCMs) have been prepared and were found to closely approximate the microstructure and mineralogy of real LFCM. The addition of excess of ZrO₂ to the composition resulted in the first successful synthesis of high-uranium zircon (chernobylite) by crystallisation from a glass melt. Use of

these simulant materials allowed further analysis of the thermal characteristics of LFCM and the corrosion kinetics, giving results that are in good agreement with the limited available literature on real samples. It should, therefore, be possible to use these new simulant materials to support decommissioning operations of nuclear reactors post-accident.

5.2.1. Introduction

On the 26th of April 1986, Reactor 4 of the Chernobyl nuclear power plant underwent a catastrophic failure whilst undergoing an experimental power failure test. The reactor experienced uncontrolled fission and water flashed into steam causing an explosion, which exposed the reactor to the atmosphere and caused ignition of the graphite core. It took several days to eventually quell the fire, in which time, radioactive particles were emitted into the surrounding area and the atmosphere, to be spread across the region (now Ukraine, Belarus and Russia) and parts of Europe. This event, classified as Level 7 on the International Nuclear Event Scale (INES), was arguably the most serious nuclear incident to affect the world to date; it is known to have caused 31 direct deaths and a mass-evacuation from a 30 km exclusion zone surrounding the reactor, that remains in place today.

During the melt-down of the reactor core, temperatures reached in excess of 1600 °C, which caused the uranium nuclear fuel to melt with the zirconium cladding [4], [6]. This molten material interacted with structural reactor building materials including steel, concrete, serpentine and sand, forming ~100 tons of a glass-like lava that was transported under its own weight to sub-reactor rooms, solidifying in large masses, such as the widely reported “elephants foot” [6], [96], [101], [243]. Known as Lava-like Fuel Containing Materials (LFCM), these highly crystalline, radioactive, glass-like slags, were found in two main forms, known as Brown and Black lavas [6]. Crystalline phases observed in both types of LFCM include non-stoichiometric UO_2 and ZrO_2 from fuel and cladding materials, a U-Zr-O mixed oxide phase and high uranium zircon ($\text{Zr}_{1-x}\text{U}_x$) SiO_4 , referred to as “chernobylite” [6], [244]–[247]. The glassy material in which these crystalline phases reside is a Mg-bearing (from serpentine minerals used in the reactor construction) Ca-aluminosilicate glass [6], [244] although the actinide and minor fission product content of the glass is not well known. The main differences between Brown and Black lavas are the extent of crystallisation (greater in the Brown LFCM), the presence of a significant proportion of Fe-bearing phases (Brown LFCM only) and the uranium content (higher in the Brown LFCM). Owing to the heterogeneous nature of LFCM, bulk analysis has yielded a range of compositions, as shown in Table 2-1.

While analysis of samples taken from Chernobyl LFCM was performed over 20 years ago [4], [6], [96], [101], [232], [239], [243]–[245], [248]–[252] the highly radioactive nature of the materials limited the types of characterisation performed. Samples of the material are limited due to the difficulties and dangers associated with their collection (unstable building, high

radiation levels) and only a few specimens of the lava that were sampled from within the reactor building have been studied. Despite recent studies [7], [247], [253], little is known about the condition of Chernobyl LFCM, especially now, 33 years after the accident. To overcome this lack of information, past attempts to simulate low-activity LFCMs (i.e. containing no fission products, only depleted uranium) have been made to help understand the conditions within the reactor during the accident, however, this work was unable to accurately approximate the microstructure, morphology and mineralogy of LFCM [238], [254]–[256].

One important aspect of LFCM behaviour that has not yet been investigated in detail is its corrosion behaviour within the reactor building. It is known that, due to the condensation of water inside the roof of the original Chernobyl sarcophagus (as a result of the temperature differential within and outside the structure), and the presence of holes in the sarcophagus roof, a significant proportion of water has dripped onto the LFCM causing it to corrode [251], [257]. This is apparent from the presence of yellow secondary alteration products formed on the surface of LFCM, known to include: paulscherrite ($\text{UO}_2(\text{OH})_2$); studtite ($\text{UO}_4 \cdot 4\text{H}_2\text{O}$); $\text{UO}_3 \cdot 2\text{H}_2\text{O}$ (epiianthinite); rutherfordine ($\text{UO}_2 \cdot \text{CO}_3$); schoepite ($(\text{UO}_2)_8\text{O}_2(\text{OH})_{12} \cdot 12\text{H}_2\text{O}$), $\text{Na}_4(\text{UO}_2)(\text{CO}_3)_3$ and the sodium carbonate phases $\text{Na}_3\text{H}(\text{CO}_3)_2 \cdot 2\text{H}_2\text{O}$ and $\text{Na}_2\text{CO}_3 \cdot \text{H}_2\text{O}$ [6], [232], [239], [253]. These phases have potential to generate significant amounts of radioactive, uranium-bearing dust when the humidity within the sarcophagus falls below 85% [257]–[259].

Understanding the corrosion behaviour of LFCM and developing a detailed evaluation of the kinetics and mechanisms of dissolution, are vital to support ongoing decommissioning efforts – both at Chernobyl and also at the Fukushima Daiichi Nuclear Power Plant, where LFCM-type materials are thought to have formed and remain submerged in water used to cool the melted core. As such, in this study, we present the results of an investigation to synthesise low-radioactivity, representative simulant LFCMs and perform a preliminary evaluation of their corrosion behaviour.

5.2.2. Experimental Procedure

Synthesis:

A survey of the literature was used to ascertain the composition of Black and Brown lavas from Chernobyl; an average of all analysed samples in the literature (Table A1) was used to produce the batched compositions shown in Table 5-2. When compared to the literature values, excess ZrO_2 was added to the batch in order to force zircon crystallisation by increasing the concentration until this phase formed. Stoichiometric amounts of the reagents for each of the elements present within the LFCM samples were used (SiO_2 (Lochaline Quartz Sand 99.6%), CaCO_3 (Fisher 98%), ZrO_2 (Aldrich 99%), Na_2CO_3 (Alfa Aesar 98%), BaCO_3 (Alfa Aesar 99%), $\text{Al}(\text{OH})_3$ (Acros 95%), Mn_2O_3 (Aldrich 99%), Fe/Cr₁₈/Ni₁₀/Mo₃ (Goodfellow), $\text{Mg}(\text{OH})_2$ (Sigma-Aldrich 99.9%) and UO_2 (BDH)). Batches were intimately mixed for at least one minute. Thermal synthesis of the loose batched powders was performed in alumina boat crucibles under a reducing atmosphere ($\text{H}_2(5\%) - \text{N}_2(95\%)$ gas) at 1500 °C for 4 h and

subsequently 720 °C for 72 h. The ramp rate was 3 °C min⁻¹ at the beginning and end of the synthesis, and 1 °C min⁻¹ between 1500 °C and 720 °C steps. The second heating step was necessary to prevent shattering of the alumina crucible and to facilitate crystallite growth. The composition of the resulting materials was determined by ICP-OES (Spectro Ciros Vision) after digestion in aqua regia, as shown in Table 5-2. The elevated concentration of Al₂O₃ is due to corrosion of the alumina crucible during thermal treatment.

Table 5-2. Composition of simulatant Lava-like Fuel Containing Material compositions (mol %), as batched and as determined by ICP-OES after aqua regia digest of thermally treated samples.

Component	Brown LFCM	Brown LFCM	Black LFCM	Black LFCM
	(mol%) <i>Batched</i>	(mol%) <i>Analysed</i>	(mol%) <i>Batched</i>	(mol%) <i>Analysed</i>
SiO ₂	62.2	59.8	64.2	65.3
CaO	7.3	7.1	7.7	6.4
ZrO ₂	7.6	8.4	8.1	7.2
Na ₂ O	7.9	6.8	7.3	4.7
BaO	-	-	0.1	0.1
Al ₂ O ₃	1.9	4.0	3.2	5.6
MnO	-	-	0.4	0.5
Fe ₂ O ₃	0.6	0.7	-	0.5
MgO	10.1	10.0	7.9	8.2
UO ₂	2.4	3.2	1.2	1.5
TOTAL	100.0	100.0	100.0	100.0

Characterisation:

The crystalline phase assemblage was determined by powder X-ray diffraction (XRD) using a Bruker D2 Phaser X-ray diffractometer in reflectance mode over the range $10^\circ \leq 2\theta \leq 70^\circ$ with Cu K α radiation (30 kV, 10 mA). Representative cross-sections were prepared by mounting monolith samples in resin and polishing to a 1 μ m finish using successive SiC grit papers and diamond suspension polishing solution. The morphology of the crystalline phase assemblage was imaged using a Hitachi TM3030 Scanning Electron Microscope (SEM) with semi-quantitative analysis of mineral composition using a built-in Bruker XFlash 430H Energy Dispersive X-ray Spectroscopy (EDS) system. Thermal characterisation of the LFCMs was performed using Differential Thermal Analysis (DTA) of representative powdered samples using a Netzsch TG 449 F3 simultaneous thermal analyser. The glass transition (T_g), crystallisation (T_c) and liquidus (T_l) temperatures were determined, with the annealing temperature of the samples taken to within 50 °C of the T_g observed. Helium pycnometry analysis gave densities of 3.054 ± 0.004 g cm⁻³ and 2.998 ± 0.003 g cm⁻³ for Brown and Black simulatant LFCM, respectively.

X-ray absorption near edge spectroscopy (XANES) analysis of the U L_{III} edge was performed on Black and Brown lava samples, on beamline BL-27 at the Photon Factory synchrotron facility (Tsukuba, Japan) [260], to evaluate the bulk uranium oxidation state. XANES spectra were collected between 16865 and 18265 eV with an accumulation time of 1 s step⁻¹ and energy steps of 4 eV (16865 – 17115), 1 eV (17115 – 17665), 4 eV (17665 – 17965), and 1 eV (17965 – 18265). Multiple spectra were averaged to improve the signal to noise ratio and a fluorescence spectrum of a Zr foil was acquired simultaneously with each sample to ensure accurate energy calibration. Three crystalline standards were also measured using the same conditions. All samples were prepared by mixing finely ground powders with polyethylene glycol (PEG) and pressing into cylindrical disks of 13mm diameter. The PEG to powder ratio was optimised to give a suitable edge step over the U L_{III} absorption edge. Data reduction and analysis performed using the Athena software package [221]. Linear regression of the U L_{III} edge energy position (defined as the energy where the edge step is equal to 0.5) with respect to standards of known oxidation state (UO₂, Yb_{0.5}U_{0.5}Ti₂O₆, and CaUO₄), confirmed the uranium oxidation state within the sample [261].

Corrosion analysis:

Two ASTM standard methods were used as the basis of corrosion experiments. Firstly, a modified ASTM Product Consistency Test B (PCT-B) protocol (ASTM C1205-14) [191] utilising a surface area to volume ratio of 120 m⁻¹, was performed to give insight to dissolution kinetics. LFCM materials were crushed and sieved to a powder of 75 to 150 μm in size. Washed powders were placed in Teflon vessels and 10 mL of UHQ water (in equilibrium with CO₂ in the air) was added. Vessels were tightened and placed inside an oven at 50 ± 1 °C for 28 days. At several time intervals, aliquots of solution were taken for elemental analysis using inductively coupled plasma-mass spectroscopy (Agilent 4500) and the pH was measured.

The normalised mass loss of elements within the LFCMs was determined according the following equation:

$$N_{L,i} = \frac{C_i}{f_i \times (S_A/V)} \quad \text{Equation 8}$$

where $N_{L,i}$ is the normalised mass loss (g m⁻²) of element i , C_i is the elementary concentration (mg L⁻¹) in the solution, f_i is the mass fraction of element i , and S_A/V is the ratio (m⁻¹) between the surface area of the glass (m²) and the volume of solution used (m³). The normalised dissolution rate, R_{Li} (g m² d⁻¹), is defined as the time-derivative of the normalised mass loss:

$$R_{L,i} = \frac{dN_{L,i}}{dt} = \frac{1}{f_i \times (S_A/V)} \times \frac{dC_i}{dt} \quad \text{Equation 9}$$

Analysis of the experimental data was performed using the geochemical speciation software PHREEQC, using the Lawrence Livermore National Laboratory thermodynamic database, LLNL-TDB. Data used in the LLNL-TDB are valid for temperatures ranging from 0 – 300 °C. The corroded samples were further characterised by XRD.

The second method of corrosion analysis was Vapour Hydration Testing (VHT), performed using a modified ASTM C1663 [157] to develop insight to the secondary phases formed on LFCMs during corrosion. Monolith coupons, 10 x 5 x 1 mm in size, were polished to an optical finish with successive SiC grit papers. Samples were suspended within stainless steel pressure vessels using stainless steel wire, such that all surfaces of the coupons were in contact with water vapour during the experiment. Vessels were tightly sealed and placed within a temperature controlled oven at 200 °C for 28 days. At the end of the experiment, samples were mounted in cross-section in epoxy resin for SEM/EDX analysis, as described above.

5.2.3. Results

Lava-like Fuel Containing Material microstructure and phase analysis:

Analysis of Brown and Black LFCMs revealed a microstructure and mineralogy consistent with real Chernobyl LFCM materials as observed by Burakov et al. [6]. A glass-like material containing crystallites was confirmed for both materials by XRD (Figure 5-4), with a region of diffuse scattering present between $15^\circ < 2\theta < 35^\circ$ and Bragg reflections indexed as: UO_2 [PDF 71-0258]; monoclinic ZrO_2 [PDF 78-1807]; cubic ZrO_2 [PDF 81-1550]; ZrSiO_4 [PDF 72-0402]; and albite ($\text{NaAlSi}_3\text{O}_8$) [PDF 41-1480]. The expanded unit cell parameter of the cubic ZrO_2 phase, $a = 5.150(4) \text{ \AA}$, compared with the reference data, $a = 5.135(9) \text{ \AA}$, is consistent with the formation of cubic $(\text{Zr}_{1-x}\text{U}_x)\text{O}_2$. The reflections indexed as ZrSiO_4 appeared to be more intense in the Black LFCM. The presence of these phases was confirmed by SEM/EDS analysis of each material, as shown in either Figure 5-5, Figure 5-6 and Appendix Figure A1. Phases containing Zr and U (i.e. $(\text{Zr}_{1-x}\text{U}_x)\text{O}_2$) had a cubo-octahedral or fused morphology (Figure 5-6) or dendritic morphology (Appendix Figure A1). The morphology is consistent with that observed in real LFCM [6], [7], [248]. Furthermore, spherical inclusions containing Fe, Cr, Ni and Mo were observed, arising from the addition of stainless steel to the samples prior to thermal treatment.

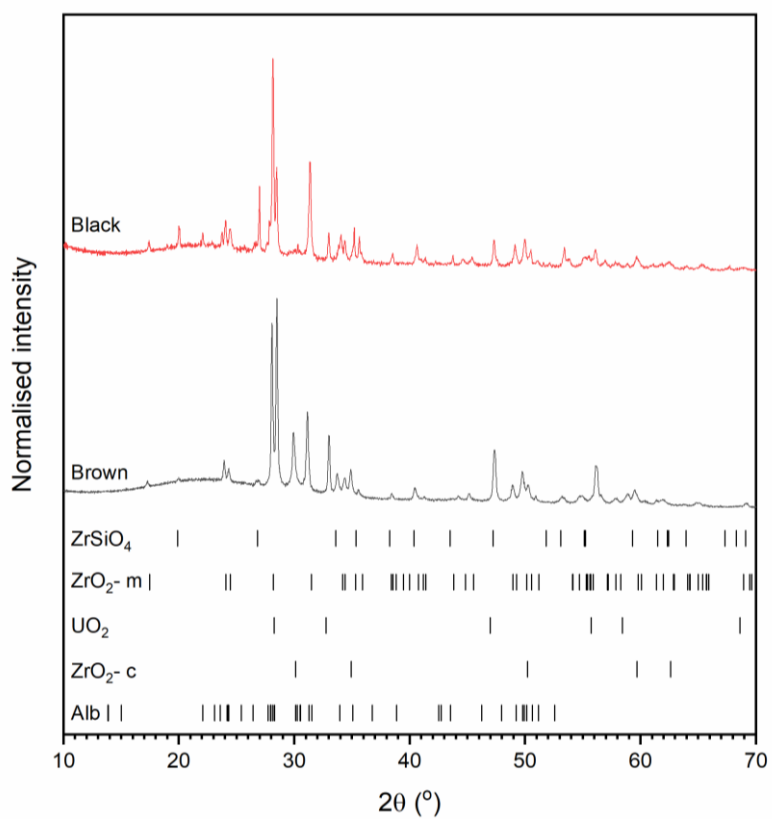


Figure 5-4. Powder x-ray diffraction data obtained for simulant Brown and Black LFCM compositions.

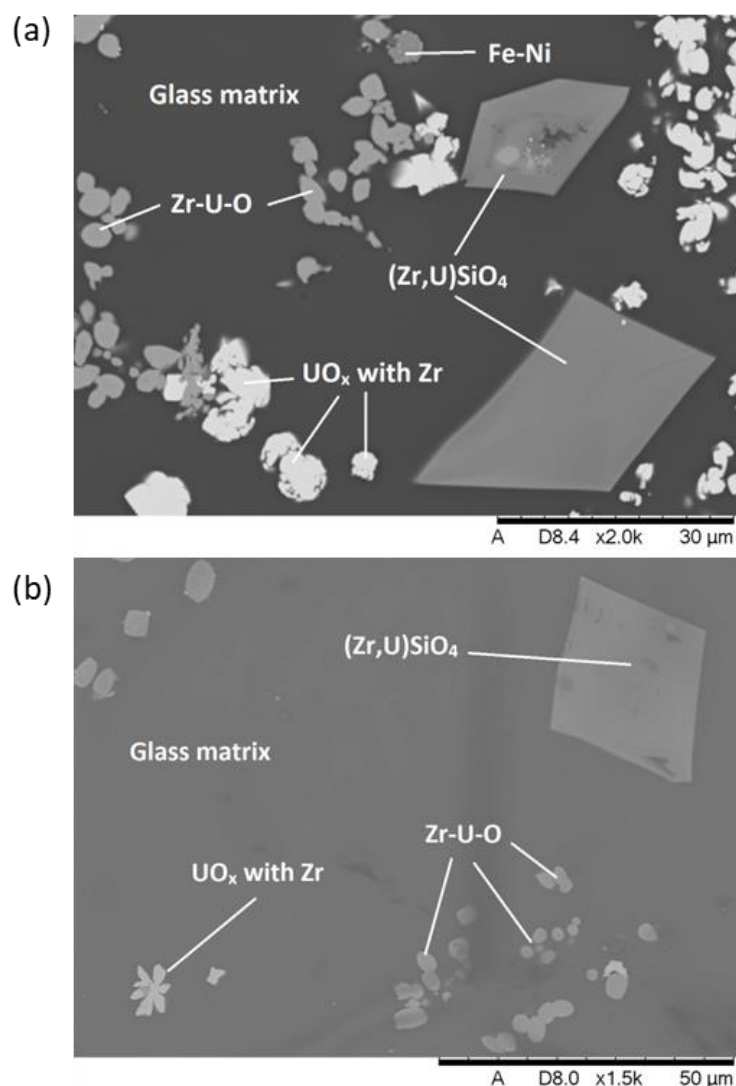


Figure 5-5. Labelled back-scattered electron images of simulant (a) Brown; and (b) Black LFCM compositions, highlighting phases identified with the aid of EDX and XRD.

Previous studies that aimed to simulate LFCM were unable to promote the formation of U-rich zircon, often referred to as chernobylite [(Zr_{1-x},U_x)SiO₄], which is present in real LFCM [254]–[256]. Since most of the Zr present in the LFCM partitions into crystalline phases, and the reported Zr concentrations of real LFCM (Table 2-1) are averaged electron probe microanalysis or EDS measurements across the whole, heterogeneous sample (including lower Zr-content glass), it is possible that previous attempts to force crystallisation of chernobylite were unsuccessful due to an under-estimation of the Zr content required to force zircon crystallisation. In the present study, through the addition of excess ZrO₂ (Table 5-2) it was possible to promote crystallisation of high-uranium zircon, as shown in Figure 5-6. The U-containing zircon had a characteristic bi-pyramidal shape with distinct growth zonation; EDS data averaged over several U-bearing zircon crystallites gave an approximate composition of

$(\text{Zr}_{0.95}\text{U}_{0.05})\text{SiO}_4$ for the Black LFCM and approximately $(\text{Zr}_{0.90}\text{U}_{0.10})\text{SiO}_4$ for Brown LFCM. The incorporation of ~5 wt% and 10 wt% U in zircon from simulated Black and Brown lavas is in good agreement with literature values (5.6 wt% and 11.3 wt%, respectively) [7]. At the centre of several of the zircon crystals, small Zr-bearing inclusions were observed (e.g. Figure 5-6c). Such inclusions were observed in real Brown LFCM, thought to be relict ZrO_2 inclusions from the crystallisation of Zr-U-O phases into high uranium-zircon [6], [245]. The presence of monoclinic ZrO_2 , in the form of baddeleyite, is rare in the previous analysis of real LFCM [6], [245]; its relative abundance in the present study (Figure 5-4, Appendix Figure A1) may be due to the addition of more ZrO_2 than was required to form the zircon phase. The presence of albite ($\text{NaAlSi}_3\text{O}_8$), as large dendrites within the glassy matrix, is in accordance with previous observations of pyroxene-like minerals with a composition of $(\text{Ca}_{0.08}\text{Fe}_{0.02}\text{Cr}_{0.02}\text{Zr}_{0.02})\text{Al}_{0.18}\text{Mg}_{1.86}\text{Si}_{1.82}\text{O}_{5.97}$, in particles of real LFCM [7].

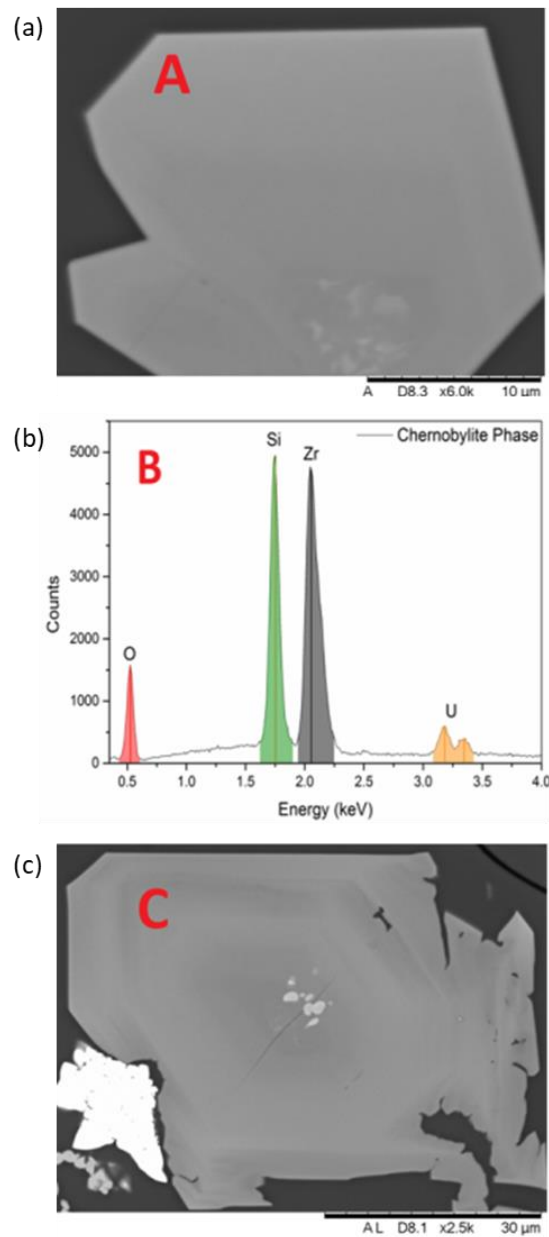


Figure 5-6. Back Scattered Electron micrographs of high uranium zircon (chernobylite, $(\text{Zr}_{0.90}\text{U}_{0.10})\text{SiO}_4$) within simulant Brown LFCM; (a) agglomerated crystals; (b) EDS data showing incorporation of uranium in the zircon phase; and (c) evidence of zoning within zircon and presence of Zr-rich particles in the centre of the zircon.

Thermal analysis of simulant LFCM, as determined by DTA, gave values for T_g of 722 ± 5 °C and 732 ± 5 °C for the Brown and Black compositions, respectively (Table 5-3, Appendix Figure A2). This is somewhat lower than previously estimated values for LFCM [262]. Two distinct crystallisation peaks were observed in both materials, the first occurring at between 1006 ± 5 °C and 1020 ± 5 °C, and the second at $\sim 1245 \pm 5$ °C. By application of Ti-

thermometry, Poml et al. [247] estimated the temperature of high-uranium zircon crystallisation in LFCM to be ~ 1250 °C, suggesting that the T_c of $\sim 1245 \pm 5$ °C observed in the present work may be related with crystallisation and growth of zircon. This is consistent with zircon crystallisation in geological formations, where zircon is known to form at temperatures between 1300 °C and 1600 °C [263], [264]. The identified crystallisation temperature (T_{c1}) should therefore be associated with the formation and growth of Zr-U-O-containing phases. The samples became liquid at temperatures $> 1213 \pm 5$ °C and heating to more 1359 ± 5 °C was required to obtain a crystal-free melt. This is somewhat lower than the estimations of the melt temperature of LFCM within the Chernobyl reactor, which range between 1400 °C and 1550 °C and may be explained by the compositional heterogeneity of real LFCM. Other than the exclusion of fission products, the primary difference in composition between the real LFCM and the simulant materials analysed here is the source of Zr. During the accident, it is thought that the first portion of liquid phases formed at ~ 1400 °C as a result of melting of U and Zr into a U,Zr alloy [4], after which the melt interacted with the reactor construction materials forming LFCM; in the current study, this stage of melting is not observed, due to the addition of Zr in oxide form. Thermogravimetric data obtained simultaneously with thermal analysis showed no appreciable mass change upon heating.

Table 5-3. Temperatures of key thermal events within simulant Brown and Black LFCM.

		Sample	
		Brown LFCM	Black LFCM
Thermal Event (°C) ± 5 °C	T_g	722	732
	T_{c1}	1006	1020
	T_{c2}	1247	1243
	T_{l1}	1226	1213
	T_{l2}	1281	1359

Analysis of the U L_{III} edge XANES spectra acquired from bulk simulant Brown and Black LFCM samples and oxidation state standards are shown in Figure 5-7. The position of the absorption edge (E_0), and the similarity in the post edge features with those of UO_2 , suggest that the average uranium oxidation state in both lava samples is close to four. Comparison of the extracted edge position of the lava samples to reference samples of known oxidation state backs this suggestion (Figure 5-7, Appendix Table A1). The mean U oxidation state was determined to be 4.1 ± 0.2 for the Black LFCM and 4.3 ± 0.2 for the Brown LFCM, which is in agreement with previous analysis of real LFCM particles by XANES [7].

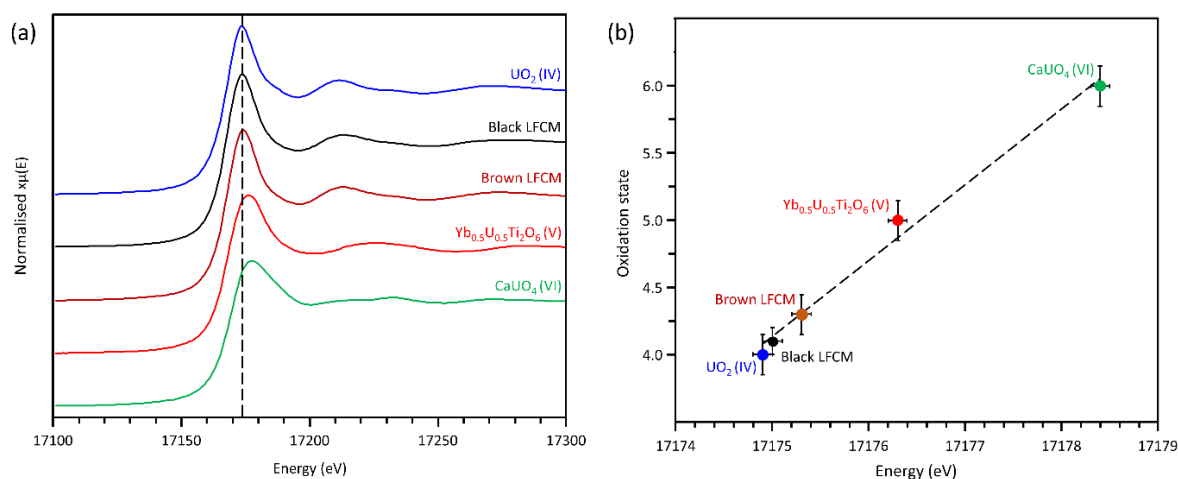


Figure 5-7. Uranium L_{III} edge XANES data for simulant Brown and Black LFCMs, with reference to uranium standards of known oxidation state, (a) showing full XANES spectra; and (b) linear regression of the extracted normalised edge position of standards and samples.

Lava-like Fuel Containing Material corrosion behaviour:

The extent of corrosion of each of the LFCM samples in UHQ water at 50 °C was found to be comparable, as shown in Figure 5-8 and Appendix Figure A3. For both samples, the pH averaged at approximately pH 5 throughout the experiment (Appendix Figure A3), which is ~1 – 2 pH units lower than in the corresponding blank solutions. The normalised mass loss of Na (N_{Na}), typically used as a tracer in the dissolution of glass materials, indicated that the corrosion rate of the Black LFCM was greater than the Brown LFCM (Figure 5-8, Table 5-4). The normalised mass loss of U was also higher in the Black LFCM, consistent with the marginally higher oxidation state of uranium in this material, however the normalised corrosion rate of U was lower since the sample reached saturation (Figure 5-8 & Table 5-4), suggesting that U may be incorporated in secondary phases within the Black LFCM to a greater extent than the Brown LFCM. Zirconium was highly resistant to leaching in both materials.

Table 5-4. Normalised corrosion rates for elements observed to increase in concentration over 28 day corrosion period.

LFCM	Normalised Corrosion Rate (N_{Ri} , $\text{g m}^{-2} \text{d}^{-1}$)			
	Si	Mg	Na	U
Brown	$(4.42 \pm 0.43) \times 10^{-3}$	$(4.22 \pm 0.47) \times 10^{-3}$	$(4.36 \pm 0.67) \times 10^{-3}$	$(9.28 \pm 1.19) \times 10^{-5}$
Black	$(1.47 \pm 0.30) \times 10^{-3}$	$(1.49 \pm 0.10) \times 10^{-3}$	$(5.70 \pm 0.64) \times 10^{-3}$	$(7.28 \pm 5.51) \times 10^{-5}$

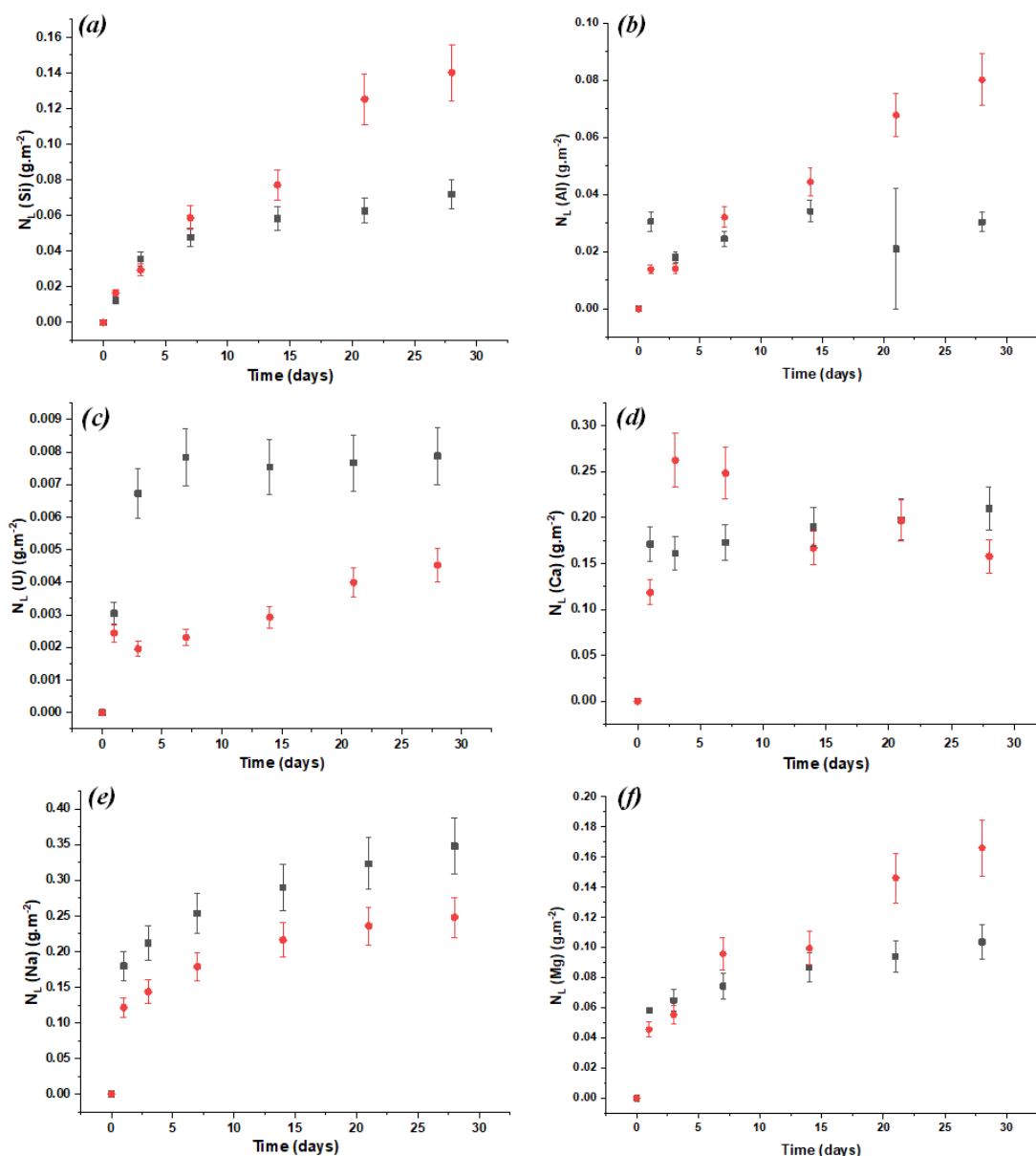


Figure 5-8. Graphs of N_{Li} for (a) Si; (b) Al; (c) U; (d) Ca; (e) Na; and (f) Mg for Black (■) and Brown (●) LFCM leached in UHQ water at 50 °C.

The decrease in the concentration and N_{Li} of the different elements in solution is indicative of a change in the degree of saturation of the solution with respect to these elements. For example, the concentration of Ca leached into solution from the Brown LFCM was observed to decrease after an initial increase. Saturation phenomena could lead to the formation of secondary phases on the surface of the material. Geochemical modelling of the elemental solution concentrations using the Phreeqc software package indicated several phases are thermodynamically favourable to form and become saturated in solution including smectite clay (beidellite with a general formula of $(Ca,Na,K,Mg_{0.5})_xAl_{4+x}Si_{8-x}O_{20}(OH)_{4.n}H_2O$), the phyllosilicate, kaolinite ($Al_2Si_2O_5(OH)_4$), and hematite (Fe_2O_3). Also, the uranium-bearing phase, soddyite [$(UO_2)_2SiO_4 \cdot 2H_2O$] was predicted to be in equilibrium with the solution

(Appendix Table A2). XRD analysis of the LFCM samples after 28 days of corrosion in UHQ water at 50 °C (Figure A4) showed no change in the crystalline phase assemblage when compared to the pre-leached samples, suggesting that any secondary phases formed were non-crystalline or present only in small (<3 wt%) quantities. SEM-EDS analysis of samples subject to corrosion under PCT (UHQ water, 50 °C) and VHT conditions (UHQ water, 200 °C) gave evidence for the formation of Na, Si and Al-bearing alteration products for both LFCM materials (Figure 5-9, Figure 5-10 and Figure A5), consistent with geochemical modelling predictions. The alteration layer was found to range from ~ 1 µm to 10 µm in thickness for both LFCM compositions. No uranium-bearing alteration products were observed in either type of corrosion experiment.

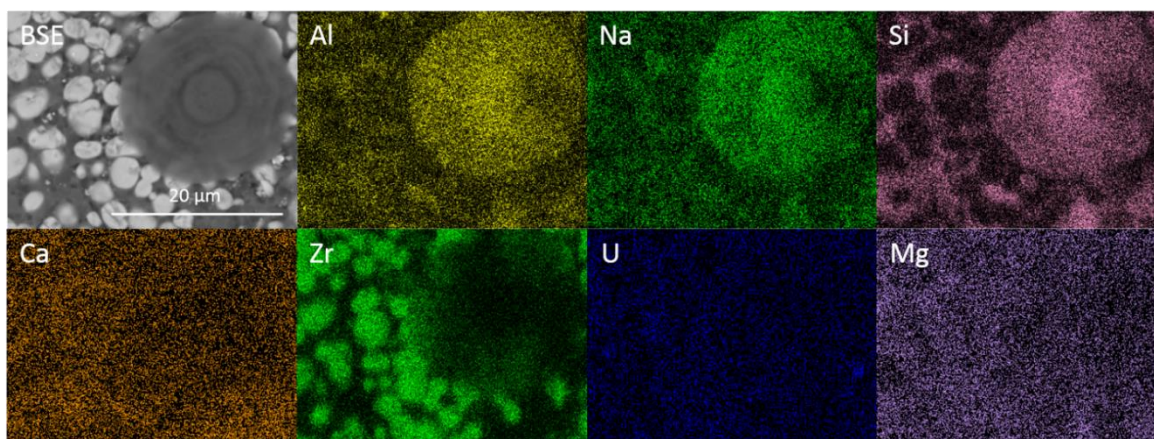


Figure 5-9. SEM-EDS analysis of Black LFCM after 28 days of corrosion using the VHT method, showing the formation of a spherical alteration phase.

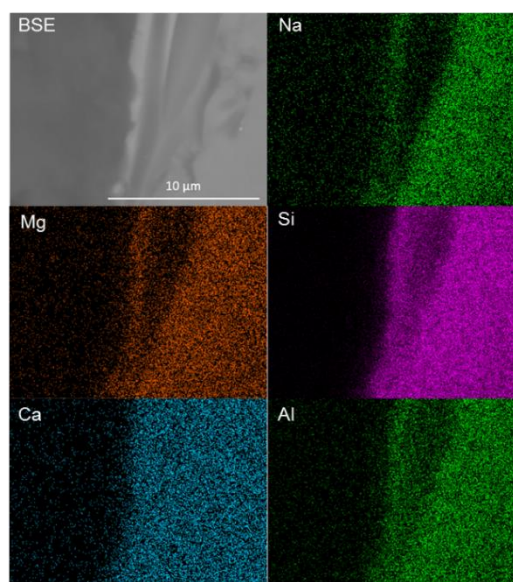


Figure 5-10. SEM-EDS analysis of Black LFCM particles samples after 28 days of leaching at 50°C in water.

5.2.4. Discussion

Replication of Chernobyl Lava-like Fuel Containing Material:

The data presented in this study confirm that the synthesis of realistic low-activity (i.e. containing depleted uranium as the only radioactive isotope) simulants for Chernobyl LFCM is achievable at a small, batch scale, in the laboratory. The microstructure and mineralogy of the resulting materials were the same as found in real Brown and Black LFCMs, containing the same range of phases, including the high-uranium zircon, chernobylite, which previous studies of simulants have been unable to form [254]–[256]. It was previously proven possible to synthesise this phase through high-temperature heat treatment of U-Zr-Si-O gels [265],

however, to our knowledge, the present study is the first to successfully crystallise this phase from a glass melt. The LFCM simulants synthesised here additionally contained Zr-U-O-phases, UO_2 , ZrO_2 and Fe,Ni,Cr,Mo-bearing metallic inclusions, also found in real LFCM. The identification of small inclusions of ZrO_2 at the centre of chernobylite grains confirms previous hypotheses that this phase is the product of reaction between Zr-U-O and the silicate melt [6], [245].

One advantage of being able to create low-activity simulants is the ability to perform measurements that are otherwise difficult to conduct within a hot-cell environment. In the present study, we have been able to further elucidate the thermal characteristics of LFCM, determining the glass phase transition, liquidus temperature and the crystallisation temperatures of zircon and Zr-U-O-containing phases. The latter values are consistent with those measured for natural minerals, and the former may differ slightly from real LFCM due to the use of ZrO_2 as a precursor rather than zircaloy cladding composed of alloying metals which could alter the transition temperatures and provide reducing conditions beyond that of the supplied H_2N_2 atmosphere. The preparation of low-activity samples is also advantageous for analysis at user facilities, for example, synchrotron beamlines. The present study confirmed, by XANES, that the oxidation state of uranium in the simulant samples, which was initially added to the batch as UO_3 , was U(IV), as observed in real LFCM [7]. In the absence of zircaloy cladding, the melting of which is thought to have partially reduced UO_2 during the accident, our study required the application of a reducing atmosphere during synthesis to create the desired oxidation state.

There is a further benefit of being able to synthesise small (25 g) batches of realistic simulant LFCM. The use of large-scale demonstrators, where experiments are conducted to understand the interaction of molten fuel and cladding with structural building materials, such as the VULCANO facility in France [266] are expensive and hazardous to operate. Having a reliable, small-scale synthesis procedure may be helpful in screening compositions and experimental matrices so that the use of the large-scale demonstrator can be reduced to only those most important experiments; this may prove highly useful in the ongoing assessment of molten corium-concrete interaction (MCCI) products at the Fukushima Daiichi Nuclear Power Plant in Japan, ahead of fuel retrieval operations.

Steps towards understanding Lava-like Fuel Containing Material corrosion behaviour:

The corrosion behaviour of LFCM is of significant concern with regards to decommissioning of the Chernobyl reactor. This is due to the large amounts of radioactive dust generated from the secondary alteration products when the humidity within the sarcophagus falls; the removal of water from the LFCM surfaces can significantly intensify UO_2 oxidation and dehydrate hydrous uranium-containing oxidation products, forming dust [259]. Some estimates suggest that the maximum rate of dust formation in the last 33 years was on the order of 1 to 10 kg y^{-1} [259]. Several studies have been performed to elucidate the corrosion rate of LFCM and to ascertain the nature of the secondary alteration phases that are formed during corrosion. Many

of these have been concerned specifically with the leaching rate of various fission products (e.g. ^{106}Ru , ^{137}Cs , etc.) however, relatively few have focused on the corrosion rate of other elements in the LFCM, including uranium – the source of the radioactive dust hazard.

Using simulant LFCM, we were able to ascertain that the uranium release rate to water (initial pH 6.5) at 50 °C was $(9.28 \pm 1.19) \times 10^{-5} \text{ g cm}^{-2} \text{ d}^{-1}$ for Brown lava (Table 5-4). This is in reasonable agreement with the only comparable data for real LFCM (Brown), which gave a uranium release rate of $1.8 \times 10^{-5} \text{ g cm}^{-2} \text{ d}^{-1}$ after 22 days of leaching in in $0.4 \text{ mol L}^{-1} \text{ NaCl}$ solution (initial pH 6.5), at *room temperature* [249]. In agreement with our findings, the study of real LFCM also showed that the corrosion rate of Brown LFCM was lower than that of Black LFCM [249] although it should be noted that other studies have shown no real difference between the two compositions [253]. These uranium release rates obtained are approximately one order of magnitude greater than those for uranium leached from spent nuclear fuel under oxidative conditions [267], but are comparable with those for U_3O_8 -doped borosilicate glass [268]. The corrosion rates of Na and Si from the simulant LFCM compositions are also of the same order of magnitude as borosilicate high level nuclear waste glass compositions such as MW25 [76] or the non-radioactive simplified surrogate of French high level waste glass, the International Simple Glass [82]. The presence of a silicate alteration layer observed after corrosion (Figure 5-10) suggests that the mechanism of corrosion of LFCMs is, at least in part, similar to that of silicate glasses.

Comparing the corrosion of simulant LFCM with available data in the literature for real LFCM, the pH of the solutions of both were observed to decrease by 1 – 2 pH units, relative to the blank, over the 28 days duration of leaching. This is somewhat unusual behaviour for alkali-aluminosilicate glasses (where the release of alkali elements to solution from the corroding glass and subsequent complexation with alkali elements raises the pH to alkaline values), and points to the formation of pH-influencing secondary alteration phases, such as those that incorporate hydroxide ions (removal of which may lower pH), or those which complex with carbonate ions. Within the Chernobyl sarcophagus, the carbonate concentration was found to vary between 370 – 2900 mg L^{-1} and uranyl carbonate phases were observed to form, [6], [232], [239], [251], [253] which may effectively lower the pH. However, the present experiments contained significantly less carbonate (only that in equilibrium with CO_2 in the air) and such phases were neither observed, nor predicted, by geochemical modelling. It is possible that colloidal complexes containing carbonate may have formed, which were not detectable using the analytical techniques applied here, however, it seems that the removal of OH^- ions into secondary phases is the most plausible explanation for the observed pH decrease in the current study.

Further work is required to fully understand the corrosion behaviour of LFCM simulants; in particular, uranium-bearing secondary precipitates, as seen on real LFCM, were apparently absent from the simulant samples. In the present work, three key factors may contribute to the

lack of formation of these phases: (1) the pH may be too low to promote the formation of Na-uranyl carbonate phases – the pH of the water within the sarcophagus was measured as pH 8.5 – 10 [251] higher than in the present study; (2) as mentioned above, the carbonate concentration within these experiments is significantly lower than within the sarcophagus; and (3) most significantly, the simulant samples do not contain any alpha-emitting isotopes. Radiolysis of water by alpha particles is known to promote the formation of hydrogen peroxide (in addition to other radical species), which is known to have a significant influence on the oxidative dissolution of UO_2 [269]. Furthermore, studtite ($\text{UO}_4 \cdot 4\text{H}_2\text{O}$), which has been observed on real LFCM samples, is a peroxide-containing mineral that forms by incorporating hydrogen peroxide created by alpha-radiolysis, thus requires radiation for its formation [230]. Further studies are currently being performed to explore these factors, and to develop further understanding of the corrosion, and dust generation capacity of LFCMs and other fuel debris.

5.2.5. Acknowledgments

The authors wish to acknowledge funding for this research from EPSRC through grant agreement numbers EP/L015390/1, EP/R01924X/1, EP/M026566/1 and EP/P013600/1. CLC is grateful to EPSRC for the award of an Early Career Research Fellowship (EP/N017374/1) and NCH is grateful for support from the University of Sheffield Global Challenges Research Fund. This research was performed in part at the MIDAS Facility, at the University of Sheffield, established with support from the Department of Energy and Climate Change. Collection of the XAS data was performed under the approval of the Photon Factory Advisory Committee (Proposal No. 2017G187); the support of Yoshihiro Okamoto (JAEA) and Noriko Usami (KEK) during the experiment is gratefully acknowledged. We thank Dr. Boris Burakov and Dr. Sergei Shiryayev for useful discussions throughout these experiments, the International Atomic Energy Agency for financial support to attend meetings on the Coordinated Research Project on the Management of Severely Damaged Spent Fuel and Corium, and also Julia Wallenius and Alex Corkhill for assistance with Russian to English translation.

6. Thermal Treatment of Americium Residues

This chapter explores the thermal synthesis of Am, extracted from civil stockpiles of Pu waste, into a ternary oxide phase; utilising Ce as a surrogate for Am. Ce_3NbO_7 was selected for investigation due to an existing gap in the current literature and the potential for use as an RTG by ESA making it a compound of interest. This section is written in the form of a draft paper to be published shortly.

6.1. Draft Paper: Synthesis and characterisation of rare Ce_3NbO_7 weberite-type compounds by neutron powder diffraction and X-ray absorption spectroscopy

This work is in the form of a draft paper written in the style of the journal *Inorganic Chemistry*. This work was written by myself with the aid of co-authors for feedback and comments. All the work was performed by myself with the exception of neutron diffraction data collection which was performed in my presence at the ISIS neutron source facility, electron diffraction data collection performed by Dr Heath Bagshaw with my assistance at the University of Manchester, magnetic susceptibility which was performed by co-author Emma McCabe at the School of Physical Sciences, University of Kent, and X-ray absorption spectroscopy data collection which was performed by co-author Shi-kuan Sun at the KEK Photon factory, High Energy Accelerator Research Organisation Facility, Japan.

The article presented here is reproduced in its entirety with references, figures and section numbering adapted to retain continuity with this thesis.

Synthesis and characterisation of rare Ce_3NbO_7 weberite-type compounds by neutron powder diffraction and X-ray absorption spectroscopy

Sean T. Barlow[†], Shi-kuan Sun[†], Dashnor Beqiri[‡], Emma McCabe[‡], Heath Bagshaw[§], Martin C. Stennett[†] and Neil C. Hyatt^{*†}

[†]*Department of Materials Science & Engineering, University of Sheffield, Sheffield S1 3JD, UK*

[‡]*School of Physical Sciences, University of Kent, Canterbury, CT2 7NH, UK*

[§]*School of Earth and Environmental Sciences, University of Manchester, Manchester, M13 9PL, UK*

Abstract: Ce_3NbO_7 weberite-type materials are a potential inactive analogue for $^{241}\text{Am}_3\text{NbO}_7$ which could be utilised in americium radioisotope thermoelectric generators to be developed by the European Space Agency for scientific missions beyond the orbit of Jupiter. Ceramics with greater than 99% purity were synthesised by thermal solid-state reaction and analytically characterised by X-ray diffraction, neutron diffraction, helium pycnometry, and X-ray absorption spectroscopy. The magnetic behaviour of the material was measured and the Weiss temperature and magnetic moment per unit volume derived, in good agreement with theoretical values. Electron diffraction imaging and Rietveld refinement using neutron powder diffraction data were employed to confirm the crystal structure and X-ray absorption spectroscopy confirmed that cerium exists in the +III oxidation state in Ce_3NbO_7 .

6.1.1. Introduction

In recent years, the global availability of plutonium-238 for use in radioisotope thermoelectric generators (RTGs), has been challenged, due to a gap in production of ca. 30 years and increasing demand for application in deep space probes. For example, ^{238}Pu powered RTGs were used for the New Horizons mission to Pluto, the Mars Science Laboratory rover Curiosity and the Voyager probes, both now operating from interstellar space, impossible to achieve with conventional solar powered craft [110], [270]. RTGs convert radioactive decay heat into

electricity via the thermoelectric Seebeck effect with an efficiency of around 6% [107] providing electrical power to spacecraft systems for decades. Whilst plans are underway to resume the production of ^{238}Pu in the United States of America, the European Space Agency (ESA) plans to use an alternative radionuclide, ^{241}Am , citing availability within European nations, endurance from the longer half-life (^{241}Am 433 years vs. ^{238}Pu 88 years) and comparable heat output to ^{238}Pu (^{241}Am 155 W_t/kg vs. ^{238}Pu 568 W_t/kg) [105], [106], [109], [271]. The UK National Nuclear Laboratory have demonstrated successful laboratory scale americium extraction from UK stockpile of civil separated plutonium derived from spent nuclear fuel, ensuring a readily available supply of ^{241}Am for ESA use [272], [273].

The specific material formulation for ^{241}Am RTG sources has yet to be decided, potential candidates are AmO_2 and Am_2O_3 [115], and a range of cermet or metal matrix type composites, which offer the advantage of reducing system mass compared to the current method of cladding ceramic pellets within iridium casings and carbon heat shields, in case of atmospheric re-entry [109], [110], [113], [274]. For ceramic heat sources, a further consideration, is control of Am redox, and hence oxygen stoichiometry, during material processing and over the service lifetime, since associated dimensional changes may pose a challenge to the integration of the ceramic material and overall safety of the RTG system [116]. For example, autoreduction of AmO_2 is known occur at high temperature under 1 atm O_2 [275], resulting in non-stoichiometric AmO_{2-x} . To help avoid these issues surrounding the use of binary compounds, our research programme is therefore oriented at understanding the synthesis and structure of refractory actinide ternary oxides, as potential ceramic heat sources. Given the similar ionic radii of trivalent actinides and lanthanides, one potential family of compounds for such applications adopt the weberite structure with composition Ln_3MO_7 (Ln = lanthanide, M = Nb or Ta), with the intention of Am^{3+} substitution for Ln^{3+} . Given the challenge, hazard and expense of working with transuranic elements it is common to utilize a non-radioactive surrogate element in early research and development studies. Previous work has utilized $\text{Ce}^{3+/4+}$ as a surrogate for $\text{Am}^{3+/4+}$ and $\text{Pu}^{3+}/\text{Pu}^{4+}$, given the similar ionic radii of these species for a given co-ordination environment [116], [276], [277]. This work investigated the synthesis and crystal structure of Ce_3NbO_7 , as an analogue for Am_3NbO_7 , acknowledging the similar 8-coordinate cationic radii of Ce^{3+} (1.01 Å) and Am^{3+} (0.98 Å).

Americium compounds usually assume the +III oxidation state with IV, V and VI requiring extra effort to produce, hence in this project ceramic materials with trivalent actinides were targeted [114].

Weberite-type niobates, Ln_3NbO_7 (where Ln = lanthanide), compounds have been the subject of previous investigation [117]–[119], due to their interesting electrical and magnetic properties. However, the precise assignment of room temperature space group symmetry of these compounds remains the subject of contention, due, at least in part, to the choice of diffraction method applied. For example, La_3NbO_7 was originally determined to adopt $Cmcm$ symmetry based on analysis of laboratory X-ray diffraction data, but subsequently shown to adopt $Pm\bar{c}n$ symmetry based on high resolution synchrotron X-ray diffraction data [117],

[120]. As discussed later in this contribution, the *Cmcm* and *Pmcn* weberite crystal structures are related by a subtle rotation and distortion of the MO_6 octahedra, giving rise to additional super-cell reflections in *Pmcn*. Consequently, neutron and electron diffraction techniques are required to definitively establish the true space group symmetry, being more sensitive to scattering and displacement of oxygen atoms.

A systematic synchrotron X-ray diffraction study of the room temperature crystal structures of Ln_3NbO_7 weberite compounds proposed space group *Pmcn* for $\text{Ln} = \text{La} - \text{Nd}$ (*bca* setting of space group 62, *Pnma*) and *Ccmm* for $\text{Ln} = \text{Sm} - \text{Gd}$ (*ba \bar{c}* setting of space group 63, *Cmcm*) structures [117]. Whereas, compounds with $\text{Ln} = \text{Tb} - \text{Lu}$ were found to adopt an average defect fluorite structure, space group *Fm-3m*, but with evidence of diffuse scattering indicative of some short range order characteristic of the weberite structure (supported by analysis of Raman modes) [117]. Previous work, utilizing laboratory X-ray diffraction, had assigned compounds with $\text{Ln} = \text{Sm} - \text{Tb}$ to adopt space group *C222₁*, a sub-group of *Cmcm* [159], [278]. Recent high resolution synchrotron X-ray and neutron diffraction studies have shown that La_3NbO_7 and Nd_3NbO_7 exhibit a continuous phase transition between *Pmcm* and *Cmcm* aristotypes at 360 K and 450 K respectively [124]. Synchrotron X-ray diffraction also established a related phase transition for Gd_3NbO_7 , from *Cmcm* to *Cm2m*, at 340K [279]. The presence of such phase transitions, close to room temperature, in Ln_3NbO_7 materials, poses an additional challenge for structure determination since small variations in ambient conditions, thermometry, and stoichiometry may result in assignment of alternate aristotypes.

During the progress of this work, Inabayashi et al. reported an investigation of the synthesis, crystal structure and magnetic behavior of Ce_3NbO_7 under flowing H_2 atmosphere [123], with the room temperature structure determined to adopt space group *Pnma*, based on laboratory X-ray diffraction data. An earlier report of $\text{Ce}_3\text{NbO}_{7+\delta}$, reported this material to adopt a cubic defect fluorite structure, *Fm-3m* symmetry, with disorder of both $\text{Ce}^{3+}/\text{Nb}^{5+}$ and oxygen/vacancies over the available atom positions [122]. The report of Inabayashi *et al* is more consistent with expectation for larger lanthanides but, as argued above, neutron and electron diffraction studies are required for a definitive assessment, having greater sensitivity to site disorder and subtle supercell reflections diagnostic of the underlying symmetry.

In this contribution, the solid state synthesis and characterisation of Ce_3NbO_7 ceramics is reported. Using X-ray, neutron and electron diffraction, the room temperature crystal structure of this compound is determine to adopt space group *Pmcn*. Ce L_3 edge X-ray Absorption Spectroscopy and magnetic susceptibility measurements confirmed the presence of Ce^{3+} , exclusively, within Ce_3NbO_7 . The compound shows Curie Weiss paramagnetism with a Weiss temperature of -143 ± 1 K, demonstrating weak antiferromagnetic interactions.

6.1.2. Experimental

Crystalline Ce_3NbO_7 was synthesised by conventional solid state oxide reaction in the presence of a reducing atmosphere of 5% H_2 -95% N_2 , required to induce reduction of Ce^{4+} to Ce^{3+} . CeO_2 (Acros Organics, 99.9%) and Nb_2O_5 (BDH, 99.5%) were calcined at 1073 K for 12 h before wet grinding in a planetary ball mill for 5 mins and subsequently dried at 383 K for 3 h. Dry powders were uniaxially pressed into cylindrical ‘green body’ pellets 10 mm by 6 mm under a pressure of 41 MPa, placed in alumina crucibles and covered in excess sacrificial batch material as an oxygen-getter to prevent adventitious oxidation of the pellets during thermal synthesis. Reaction took place at 1523 K for 24 h under flowing 5% H_2 -95% N_2 gas mixture. After reaction the outer layer (< 1 mm) of each pellet was visibly darker in hue from the interior and was abraded off using SiC grit paper (Figure B1). Finished pellets were milled to a fine powder using a planetary mill and powder X-ray diffraction (XRD) was used to determine the crystalline phase assemblage and phase purity. Multiple calcinations were necessary to create phase pure samples (> 95%). XRD was collected on a Bruker D2 diffractometer in reflectance mode over the range $10^\circ < 2\theta < 70^\circ$ and also on a STOE STADI P in transmission mode over the range $10^\circ < 2\theta < 120^\circ$, both utilizing Cu $K\alpha$ radiation. Quantitative Energy Dispersive X-ray analysis of Ce_3NbO_7 was performed on a polished sintered pellet, using a Hitachi TM3030 SEM equipped with a Bruker Quantax EDX detector.

High-resolution neutron powder diffraction (NPD) was performed at the ISIS spallation neutron source (Rutherford Appleton Laboratory (UK)) using the HRPD time of flight (TOF) instrument. Diffraction was measured on 2.364 g of powder from 30 ms to 130 ms using the NBS silicon backscattering detector bank with the 2 hour scan delivering an 80 μA neutron beam current. Rietveld refinement was carried out using the GSAS refinement suite [171], [172], with unit cell parameters, atomic coordinates and isotropic temperature factors typically refined, as well as a background function, scale factor and profile parameters. Data were acquired at room temperature, 298 K.

A FEI Techni F30 TEM with 300 KeV accelerating voltage was utilised to facilitate the identification of the correct orthorhombic space group via electron diffraction imaging on thin powder samples. Finely ground, powdered Ce_3NbO_7 was placed onto a holey carbon TEM grid and manipulated within the TEM via a double tilt sample holder. Diffraction patterns were collected using a Gatan Orius CCD camera with 5 second exposure time and analysed using SingleCrystal v3.1.1 software.

X-ray absorption spectroscopy (XAS) experiments were completed at the KEK Photon Factory (PF), High Energy Accelerator Research Organization (Japan) focusing on the Ce L-III edge (5,723 eV). XAS spectra were collected from 5600 eV to 6000 eV with data reduction and analysis performed using the Athena Demeter 0.9.24 software package. Linear regression with respect to standards of known oxidation state, CeO_2 and CePO_4 , confirmed cerium oxidation state within the sample.

Magnetic susceptibility measurements were taken with the temperature-dependence relationship measured over the temperature range of $2 \text{ K} \leq T \leq 300 \text{ K}$ with an applied field of

0.1 T, using a Quantum Design MPMS (SQUID magnetometer). Susceptibility measurements were performed under field-cooled and zero-field-cooled and conditions.

The thermal stability of Ce_3NbO_7 was investigated by thermogravimetric analysis (TGA) and Differential thermal analysis (DTA, with combined mass spectroscopy of evolved gas). Data were acquired using a Netzsch TG 449 F3 simultaneous thermal analyser (STA) over the temperature range 470 – 1770 K with a heating rate of 5 K min^{-1} . Nitrogen gas was used during the DTA data acquisition and to purge the sample chamber before the heating cycle, whilst an air atmosphere was used during TGA data acquisition.

Density measurements were obtained by helium pycnometry using Micromeritics Accupyc II 1340 on powdered samples. Data was collected at $23 \text{ }^\circ\text{C}$ within a 1 cm^3 chamber, fill pressure of 82.7 kPa with 10 purges over 10 cycles and an equilibration rate of $0.034 \text{ kPa min}^{-1}$.

6.1.3. Results

Solid state synthesis and crystal structure:

Ce_3NbO_7 was successfully formed under the reducing conditions of the flowing 5% H_2 -95% N_2 atmosphere as shown in the XRD data in Figure 6-1 and Figure 6-2. Reacted pellets were dark red/brown in coloration, typical of a reduced cerium oxidation state, with a minor yellow coloured precipitate on the outer surface visible after 24 hours reaction at 1523 K (Figure B1). The yellow impurity phase was identified as $\text{CeNbO}_{4+\delta}$ by initial XRD analysis, as shown by the indexed patterns in Figure 6-1 and Figure 6-2. $\text{CeNbO}_{4+\delta}$ adopts the monoclinic Fergusonite structure (I21/a) which can accommodate a variable oxygen stoichiometry [280]. The best fit to the observed reflections associated with $\text{CeNbO}_{4+\delta}$, were the reported diffraction data corresponding to $\text{CeNbO}_{4.00}$ [281]. Notably, single crystals of $\text{CeNbO}_{4+\delta}$ with $\delta = 0$ were reported to be yellow in colour, whereas oxidized regions exhibited a dark green colouration [282]; polycrystalline materials were reported to be yellow-green and dark green in the case of compositions with $\delta = 0$ and $0.08 < \delta < 0.25$, respectively [281]. The enrichment of the $\text{CeNbO}_{4+\delta}$ impurity phase at the surface of our materials, at the solid/gas interface, suggests scavenging of trace oxygen from the gas atmosphere may be responsible for its stabilization, most likely during cooling since elevated temperatures are known to decompose $\text{CeNbO}_{4+\delta}$ to CeNbO_4 [283]. Consideration of the reference diffraction data for yellow-green colour phase [281], suggests $0 < \delta \ll 0.08$ for our sample; for simplicity this impurity phase is referred to as stoichiometric CeNbO_4 . The intensity of the Bragg reflections associated with CeNbO_4 phase did not change appreciably with extended reaction time. Removing the outer layer of the reacted pellets, by gentle abrasion, was found to yield an essentially single phase material by XRD analysis, see Figure 6-2. Quantitative EDX analysis performed on a polished sintered pellet, confirmed the presence of Ce and Nb in a 3:1 ratio, as expected.

Structure refinement of Ce_3NbO_7 considered both candidate space groups, $Cmcm$ and $Pm\bar{c}n$, shown schematically in Figure 6-3. The crystal structure comprises infinite bands of corner sharing NbO_6 octahedra and edge sharing $\text{Ce}(1)\text{O}_8$ cubes separated by 7-fold co-ordinate $\text{Ce}(2)$ ions. As described below, rotation and distortion of the NbO_6 octahedra, lowers the symmetry from $Cmcm$ to $Pm\bar{c}n$. The two space groups are distinguished by reflections with hkl $h+k=2n$ and $h0l$ $h=2n$ or $l=2n$, which are allowed for $Pm\bar{c}n$ but systematically absent in $Cmcm$.

A Le Bail analysis of laboratory XRD data afforded a similar quality of fits for both $Cmcm$ and $Pm\bar{c}n$ space groups, with a modest improvement in fit favouring assignment of $Pm\bar{c}n$ symmetry: $R_{\text{wp}}=14.77\%$ for $Cmcm$, 14.10% for $Pm\bar{c}n$ from reflection mode $\text{Cu K}\alpha$ XRD; and $R_{\text{wp}}=5.75\%$ for $Cmcm$, 4.01% for $Pm\bar{c}n$ from transmission mode $\text{Cu K}\alpha_1$ XRD; see Appendix Figure B2 and Figure B3. This is consistent with the presence of additional weak reflections satisfying the conditions hkl $h+k=2n$ and $h0l$ $h=2n$ or $l=2n$ in the X-ray diffraction data.

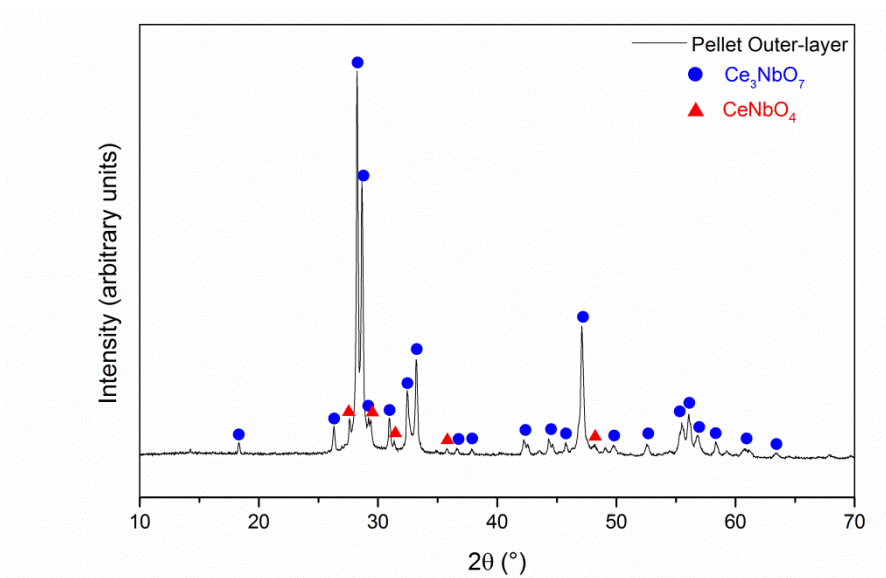


Figure 6-1. XRD pattern acquired from the surface of a pellet of composition Ce_3NbO_7 , post reaction in 5% H_2 -95% N_2 for 24h, showing enrichment in CeNbO_4 .

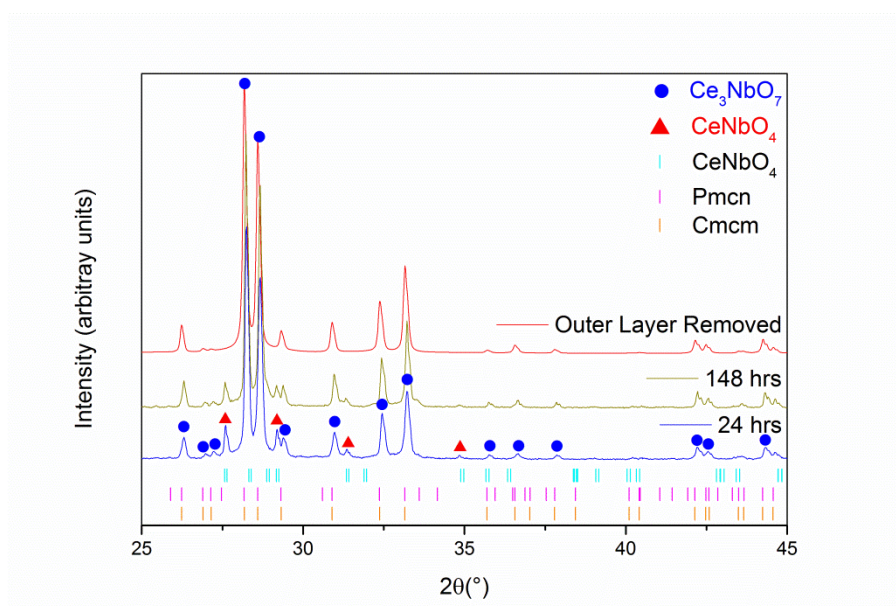


Figure 6-2. XRD pattern acquired from the surface of a pellet of composition Ce_3NbO_7 , post reaction in 5% H_2 -95% N_2 , showing enrichment in CeNbO_4 , and after 148 h with the surface layer removed.

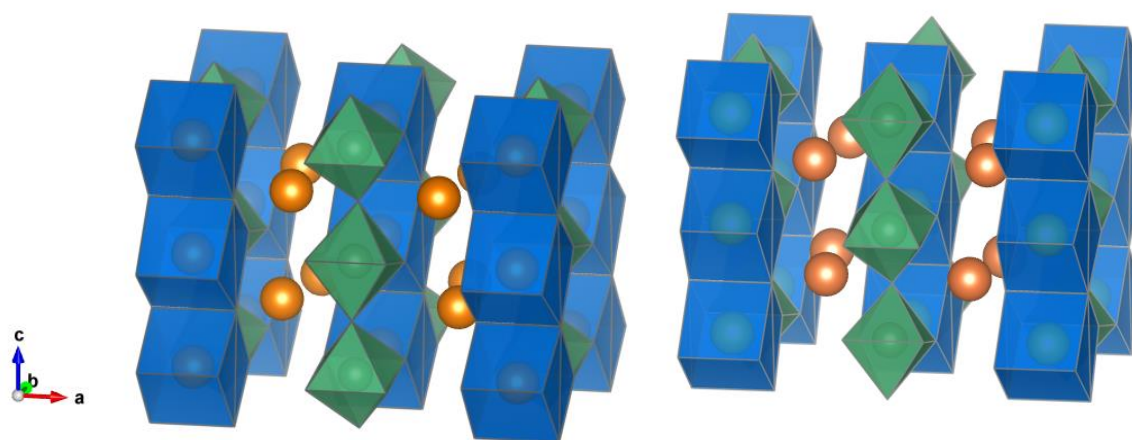


Figure 6-3. Schematic crystal Structure for Ce_3NbO_7 in Cmc spacegroup (left) and $Pmcn$ (right). $\text{Ce}(1)\text{O}_8$ units are revealed as blue cubes, $\text{Ce}(2)$ ions shown by orange spheres and NbO_6 octahedra represented by green octahedra.

Electron Diffraction:

Selected Area Electron Diffraction (SAED) patterns were acquired from crushed grains of Ce_3NbO_7 to make an unambiguous determination of space group. Figure 6-4 shows the indexed SAED pattern obtained from the $[0\ 2\ 1]$ zone axis whilst the Appendix Figure B4 shows the corresponding simulated SAEDs for the $[0\ 2\ 1]$ zone axis in the Cmc and $Pmcn$ space groups.

The observation of hkl $h+k \neq 2n$ reflections (e.g. $h2-4$ $h \neq 2n$; $h3-6$ $h \neq 2n$) which are systematically absent for $Cmcm$ symmetry, confirm the assignment of the primitive $Pm\bar{c}n$ space group for Ce_3NbO_7 at room temperature.

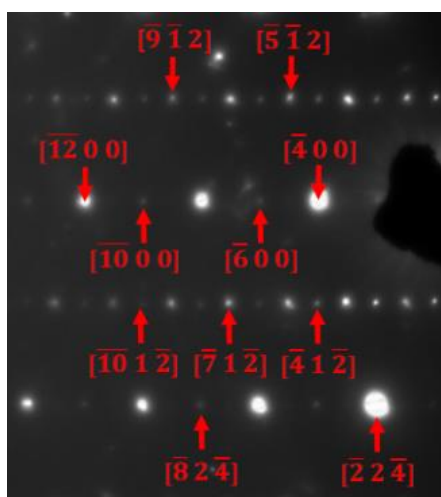


Figure 6-4. Electron diffraction pattern obtained in the 0 2 1 plane.

Neutron diffraction:

Rietveld analysis of room temperature neutron diffraction data acquired from Ce_3NbO_7 , in space group $Pm\bar{c}n$, afforded an excellent fit of the refined structure model to the data, with $\chi^2 = 3.00$, $R_{wp} = 5.80\%$, $R_p = 5.37\%$, for 51 variables, as shown in Figure 6-5. The refined structural parameters are summarized in Table 6-1. The sample was determined to contain a small residual amount of $CeNbO_4$ impurity phase (0.21% by weight). It was noted that anisotropic peak broadening was required to adequately fit asymmetry of reflections in the range $2.25 < d < 2.55$ Å. We also attempted to fit our data with a model incorporating two Ce_3NbO_7 phases of $Pm\bar{c}n$ and $Cmcm$ symmetry or both of $Pm\bar{c}n$ symmetry. Although this also adequately modeled the aforementioned reflection asymmetry, refinement of a single Ce_3NbO_7 phase in $Pm\bar{c}n$ symmetry, with anisotropic peak broadening, always produced superior goodness of fit metrics. No evidence for atom site vacancies or cation anti-site defects was established by refinement of site occupancies (with appropriate constraints). Taken together, these observations may point to some small degree of compositional variation in our material, as discussed below.

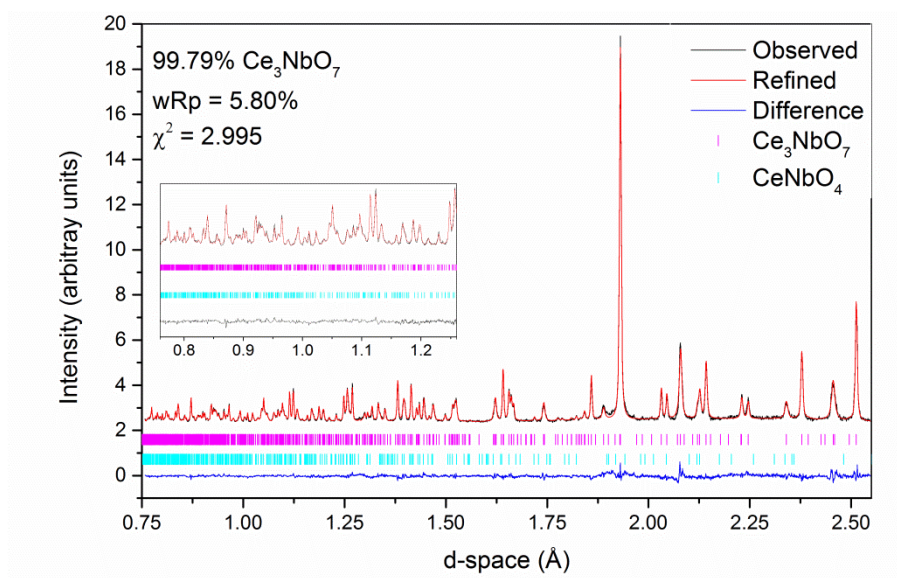


Figure 6-5. Final fit of refined structural model for Ce_3NbO_7 in space group $Pmcn$ to neutron diffraction data, showing observed, fitted and difference profiles; tick marks show allowed reflections for Ce_3NbO_7 and CeNbO_4 .

Key bond lengths for the Ce_3NbO_7 structure are summarised in Table 6-2 along with bond valance analysis. By utilizing reference bond lengths of $r_0=2.151 \text{ \AA}$ for Ce^{3+} [284] and $r_0=1.911 \text{ \AA}$ for Nb^{5+} [285], the calculated bond valance sum (BVS) for 8 coordinate Ce(1) was 2.79 v.u. and 3.14 v.u. for 7 coordinate Ce(2), whilst the BVS of 6 coordinate Nb was 4.84 v.u. The determined mean bond valance sums for the Nb and Ce sites are within a few percent of the formal oxidation states, and hence there was no evidence for significant structural strain.

The theoretical density for Ce_3NbO_7 calculated from the refined NPD data was 6.445 g/cm^3 with the minor impurity phase having a density of 5.464 g/cm^3 leading to an overall calculated density of 6.443 g/cm^3 for the material. This is in close agreement with the powder density of $6.5029 \pm 0.0051 \text{ g/cm}^3$ determined by helium gas pycnometry.

Table 6-1. Rietveld refined structural parameters output for *Pmcn* (#62) Ce_3NbO_7 from room temperature NPD data; $R_{\text{wp}} = 5.80\%$, $R_{\text{p}} = 5.37\%$, $\chi^2 = 2.995$.

Ce₃NbO₇ – 99.79 Wt. %					
Atom	Site	X	y	z	$U_{\text{iso}} \times 100$ (\AA^2)
Ce1	4c	0.2500	0.7571(9)	0.0104(1)	0.44(8)
Ce2	8d	0.4769 (1)	0.4540(2)	0.2497(1)	0.32(4)
Nb	4c	0.2500	0.2503(8)	-0.0043(9)	0.15(5)
O1	8d	0.8706(3)	0.9451(4)	0.9667(6)	0.94(9)
O2	8d	0.3796(3)	0.4251(4)	0.9630(6)	0.89(9)
O3	8d	0.3806(1)	0.7259(2)	0.2496(1)	0.45(4)
O4	4c	0.2500	0.3191(3)	0.2497(1)	0.80(5)
<i>a</i>	11.0492(4) \AA	<i>b</i>	7.5561(3) \AA	<i>c</i>	7.7180(3) \AA

Table 6-2. Select interatomic bond lengths in Ce₃NbO₇ calculated from refined NPD data;
Average Ce BVS: 2.96, Average Nb BVS: 4.84.

<i>Atoms</i>	<i>Bond Length (Å)</i>	<i>Bond Valence Sum (v.u.)</i>	<i>Coordination</i>
Ce1-O1	2.621(7) (x2)	2.79	8
Ce1-O2	2.912(7) (x2)		
Ce1-O3	2.355(9) (x2)		
Ce1-O3	2.481(9) (x2)		
Ce2-O1	2.495(7) (x1)	3.14	7
Ce2-O1	2.485(8) (x1)		
Ce2-O2	2.470(8) (x1)		
Ce2-O2	2.458(7) (x1)		
Ce2-O3	2.312(2) (x1)		
Ce2-O3	2.334(3) (x1)		
Ce2-O4	2.706(2) (x1)		
Nb-O1	2.010(6) (x2)	4.84	6
Nb-O2	1.965(6) (x2)		
Nb-O4	2.028(1) (x1)		
Nb-O4	1.970(1) (x1)		

Ce L₃ edge XANES:

Figure 6-6 shows the background subtracted and normalized Ce L₃ edge XANES data of Ce₃NbO₇ is compared with that of reference compounds CePO₄ and CeO₂, containing Ce³⁺ and Ce⁴⁺, respectively. The absolute energy position (E₀) of the Ce L₃ absorption edge is a function of oxidation state, with a chemical shift of ca. 3.6 eV between the E₀ determined for CePO₄ and CeO₂ reference compounds, determined as the energy corresponding to -μ_x = 0.59 i.e. half height of the edge step), see Table 6-3. Additionally, Ce L₃ edge XANES of Ce³⁺ species are characterised by a single intense white line feature, whereas the XANES of Ce⁴⁺ species are characterised by three white line features of comparable intensity, as exemplified by Figure 6-6. The electronic states associated with these characteristic features have been established as discussed by Stennett et al. [286]. The E₀ and profile of the Ce L₃ edge XANES data of

Ce_3NbO_7 are very similar to those of the CePO_4 reference compound, as demonstrated by Figure 6-6 and Table 3, consistent with the presence of Ce^{3+} . Assuming a linear dependence of E_0 to oxidation state, interpolation from the reference compounds affords an estimated Ce oxidation state of 3.1 ± 0.1 eV for Ce_3NbO_7 . Linear combination fitting of the Ce L_3 edge XANES data of CePO_4 and CeO_2 , to that of Ce_3NbO_7 , determined an estimated Ce oxidation state of 3.1 ± 0.1 eV for Ce_3NbO_7 .

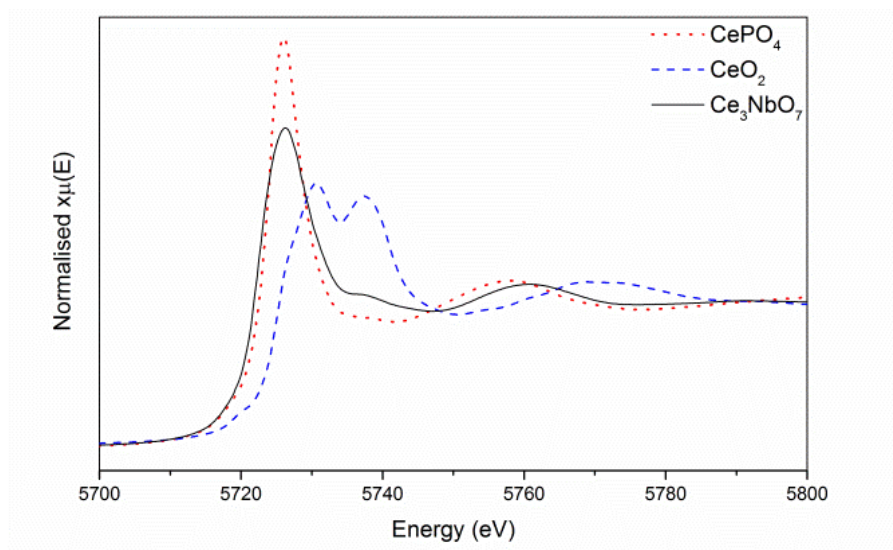


Figure 6-6. XAS spectra for Ce_3NbO_7 and two reference samples

Table 6-3. Extracted E_0 values and corresponding oxidation state.

Sample	E_0 (eV)	Oxidation State (± 0.15)
CePO_4 (Ce^{3+})	5722.2	3.0
Ce_3NbO_7	5722.8	3.1
CeO_2 (Ce^{4+})	5725.8	4.0

Magnetic properties:

The temperature dependence of the magnetic susceptibility of Ce_3NbO_7 is shown in Figure 6-7. Long range magnetic ordering was not observed over the temperature range studied however Curie-Weiss fitting was successfully applied between 185 K and 281 K, revealing a calculated Weiss temperature of -143 ± 1 K. The effective magnetic moment per Ce^{3+} was calculated as $2.51 \pm 0.01 \mu_B$, in excellent agreement with the theoretical value of $2.54 \mu_B$.

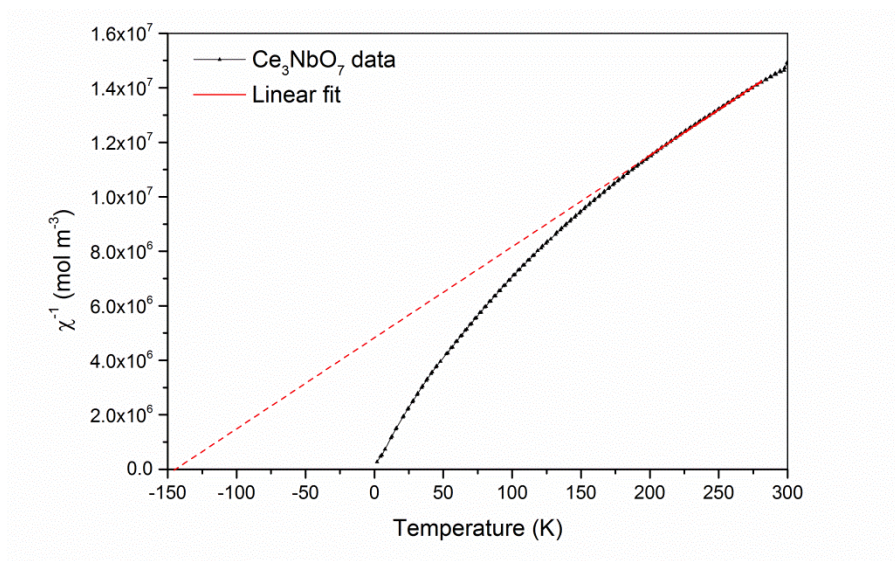


Figure 6-7. Reciprocal magnetic susceptibility for Ce_3NbO_7 over the range $2 \text{ K} \leq T \leq 300 \text{ K}$.

Thermogravimetric and Differential Thermal Analysis:

DTA data of Ce_3NbO_7 on heating under N_2 atmosphere to is shown in Figure 6-8 alongside TGA data upon heating under an air atmosphere. These data show a continuous weight gain on heating above ca. 400 K, associated with adventitious oxidation of the sample. The recovered material was green in colour and did not show evidence of melting, but powder X-ray diffraction, Figure 6-9, demonstrated decomposition of Ce_3NbO_7 to yield a mixture of $\text{CeNbO}_{4+\delta}$ and $2(\text{CeO}_2)$. The d-spacing of the reflections corresponding to $\text{CeNbO}_{4+\delta}$ were consistent with an increase in unit cell volume, relative to $\delta = 0$, as previously observed for $\delta = 0.08$ and $\delta = 0.25$ [281], providing a close match to the $\delta = 0.25$ reported data for this phase. Assuming decomposition to stoichiometric CeO_2 plus $\text{CeNbO}_{4+\delta}$, the observed weight increase of 3.2 wt%, could correspond to a gain of 1.2 formula units of oxygen ($\text{Ce}_3\text{NbO}_{8.2}$), implying $\delta \approx 0.2$ for $\text{CeNbO}_{4+\delta}$, consistent with interpretation of XRD data of $\delta \approx 0.25$.

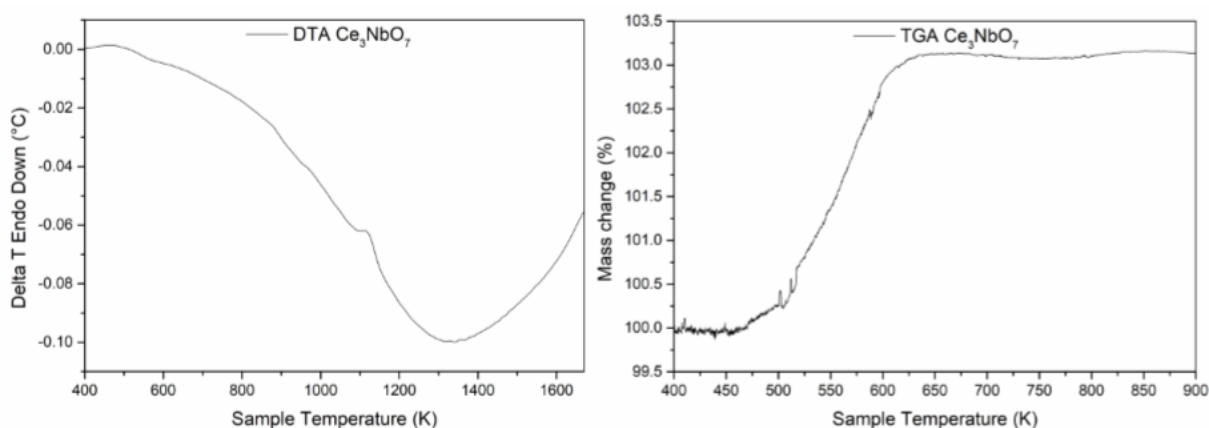


Figure 6-8. DTA data (400 – 1670 K) and TGA (400 – 900 K) data for Ce_3NbO_7 .

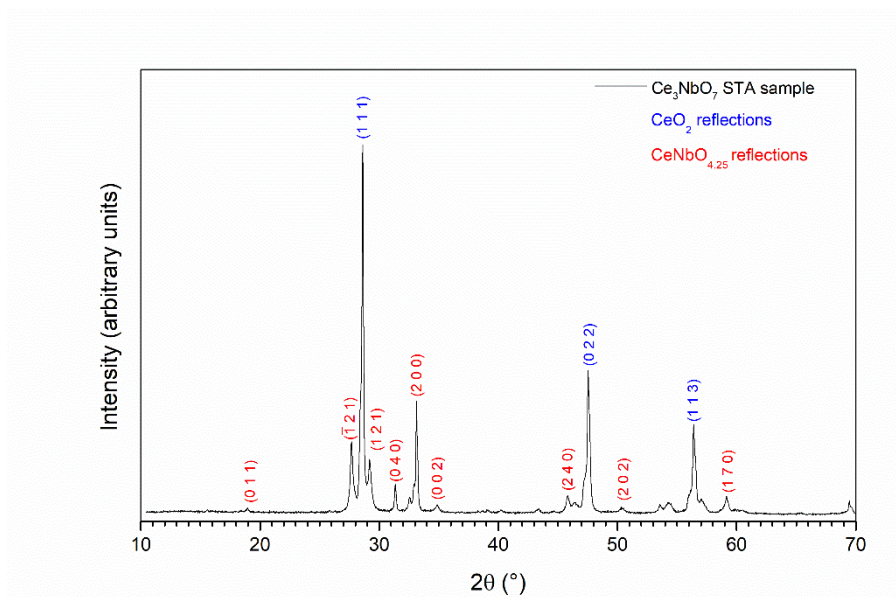


Figure 6-9. Powder XRD of sample after thermal analysis showing transformation into other indexed phases.

6.1.4. Discussion

Ce_3NbO_7 was successfully synthesized from CeO_2 and Nb_2O_5 at 1523 K for 24 h, under flowing 5% H_2 -95% N_2 gas mixture to effect reduction of Ce^{4+} to Ce^{3+} . Nevertheless, the material will scavenge even trace oxygen, during synthesis, yielding a surface layer enriched in CeNbO_4 on ceramic bodies, even when buried within a bed of sacrificial powder. Gentle abrasion of the surface of Ce_3NbO_7 , to remove the CeNbO_4 rich surface layer, yielded an essentially single phase material.

Analysis of combined neutron, electron and X-ray diffraction demonstrate that Ce_3NbO_7 adopts a weberite structure in space group $Pm\bar{c}n$ (#62) rather than $Cmcm$ (#63), as observed for counterpart Ln_3NbO_7 compounds with relatively large lanthanides $\text{Ln} = \text{La}, \text{Pr}$ and Nd [120], [121], [124], [287]. The two candidate structural models (Figure 6-3) are very similar, and differ only in slight rotation of NbO_6 octahedra; described by the Y_2^- mode distortion from $Cmcm$ to $Pnma$ (alternative setting to $Pm\bar{c}n$) using the ISODISTORT program [288]. Distortions to other subgroups of $Cmcm$ (e.g. $C222_1$, $Cmc2_1$, $Ama2$ and $Amm2$ from Γ_1^- , Γ_2^- , Γ_3^- and Γ_4^- irreps, respectively) as described by ISODISTORT [288] were also considered but these centred models are inconsistent with the reflections observed in ED. Overall, this is consistent with previous analysis of the crystal structure of Ce_3NbO_7 , based on laboratory X-ray diffraction data, [123] although it is important to emphasise that both electron and neutron diffraction data are essential to be confident of this conclusion. Bond valence sum analysis and Ce L_3 edge XANES data (by comparison to data from CePO_4 and CeO_2 reference compounds) confirm the presence of Ce^{3+} in Ce_3NbO_7 , consistent with the deep red-brown colour of this material in powder form.

As noted above, asymmetric line broadening observed in neutron diffraction data suggest some subtle compositional variation within our material, but this could not be attributed to cation or vacancies, or Ce/Nb disorder. Quantitative EDX analysis, Ce L_3 edge XANES and magnetic susceptibility data are consistent with the presence of a bulk stoichiometry of Ce_3NbO_7 . However, our preliminary investigation of the high temperature behaviour of Ce_3NbO_7 has shown that the compound will undergo adventitious oxidation under an air atmosphere, finally decomposing to yield CeO_2 and $\text{CeNbO}_{4+\delta}$ ($\delta \approx 0.25$). These observations are broadly consistent with those of Inabayashi et al., who report continuous oxidation of Ce_3NbO_7 under O_2 gas [123]. Taken together, these data suggest a plausible explanation for the asymmetric line broadening in our neutron diffraction data (apparent due to the high resolution), involving the presence of a small oxygen excess giving rise to a compositional gradient from the core to rim of powder grains. This would be expected to induce some crystallographic strain, giving rise to the observed asymmetric line broadening, but be consistent with a stoichiometric bulk composition and our structure determination.

Magnetic susceptibility data revealed no evidence for long range magnetic ordering in Ce_3NbO_7 at low temperature. However, the negative Weiss temperature implies underlying antiferromagnetic interactions between Ce^{3+} ions, although, evidently, the exchange interaction is not sufficiently strong to give rise to long-range magnetic order. Our derived magnetic effective magnetic moment per Ce^{3+} of $2.51 \pm 0.01 \mu_B$ was in excellent agreement with the theoretical value of $2.54 \mu_B$. Recent work by Inabayashi et al. [123] also reported the absence of magnetic ordering in Ce_3NbO_7 , but determined a smaller effective magnetic moment per Ce^{3+} ion of $1.77 \mu_B$, from fitting the Curie-Weiss Law magnetic susceptibility data; this was attributed to the effect of local crystal field. Interestingly, Inabayashi et al. also determined a Weiss temperature of -13.4K , compared to our determination, of -143K , which suggests weaker underlying antiferromagnetic exchange interactions. These differences are difficult to rationalize, given the evidence to demonstrate the single phase or near single phase nature of

the reported compounds. As noted above, a gradient of oxygen interstitials at the grain boundaries of our material might explain the observed asymmetric line broadening, revealed by the high resolution neutron diffraction, but a significant bulk concentration of such interstitials would be inconsistent with our determined magnetic moment and Ce L₃ edge XANES data.

As highlighted in the introduction to this contribution, Guogang et al. reported the synthesis of the phase Ce₃NbO_{7+δ}, in a mixture with CeNbO_{4+δ}, from solid state reaction between CeO₂ and Nb₂O₅ in a 6:1 mole ratio, under air atmosphere. Ce₃NbO_{7+δ} was reported to adopt space group *Fm-3m* and unit cell parameter $a = 5.4053 \text{ \AA}$, based on X-ray diffraction data [122]. This report is apparently inconsistent with the synthesis of Ce₃NbO₇ under reducing atmosphere, and the sensitivity of this material toward adventitious oxidation at high temperature. The reported unit cell parameter of Ce₃NbO_{7+δ} is close to that of CeO₂ NIST Standard Reference Material 647b, $a = 5.4152 \pm 0.0030 \text{ \AA}$ [289]. These observations suggest that the cubic Ce₃NbO_{7+δ}, phase identified by Guogang et al. [122], was in fact CeO₂, as expected from consideration of stoichiometry and conditions of synthesis, and consistent with data presented in Figure 6-9, herein.

Previous consideration of A₂²⁺B₂⁵⁺O₇ and A₂³⁺B₂⁴⁺O₇ compounds has shown that the cation radius ratio, r_A/r_B – with A and B cations in 8-fold and 6-fold coordination respectively, is a useful metric for predicting the relative stability of the weberite, pyrochlore and defect fluorite structures. Counterpart A₃³⁺B⁵⁺O₇ compounds (A = Lanthanide and Y; B = Nb, Sb, Ta, Re, Os, Ir and Ru) adopt either the weberite or defect fluorite structure, depending on composition. Therefore, we also considered the r_A/r_B ratio as a potentially useful metric to predict adoption of the weberite or defect fluorite structure for Ln³⁺B⁵⁺O₇ compounds. For simplicity, one can equate r_A with the ionic radius for the Ln³⁺ ion in 8-fold co-ordination, since, in the weberite structure, the ratio of 8-fold to 7-fold co-ordinate Ln sites is 2:1. For this analysis, the ICSD database was screened for relevant compounds, constrained to room temperature structures and quality assured crystallographic data. Figure 6-10 shows the resulting structure field map for Ln₃³⁺B⁵⁺O₇ compounds, which shows reasonably well-defined fields for weberite and defect fluorite structured compounds [162]. In addition, the weberite structure field is well delineated between examples which adopt the La₃NbO₇ and Y₃TaO₇ aristotypes, which differ in the mode of tilting of the MO₆ octahedra (respectively: *Cmcm* or *Pcnm* with Y₂⁻ irrep; and *Ccmm* or *C222₁* with Γ₁⁻ irrep). The La₃NbO₇ and Y₃TaO₇ aristotypes are evidently adopted for large and intermediate r_A/r_B ratios, respectively, whereas the defect fluorite structure is stabilized only for the smallest r_A/r_B ratios. Of particular interest is the fact that Ce₃NbO₇ falls within the La₃NbO₇ type weberite structure field based on ionic size considerations. This analysis also demonstrates that there remain many as yet unreported Ln³⁺B⁵⁺O₇ compounds and/or structures which would be worthy of experimental and theoretical study.

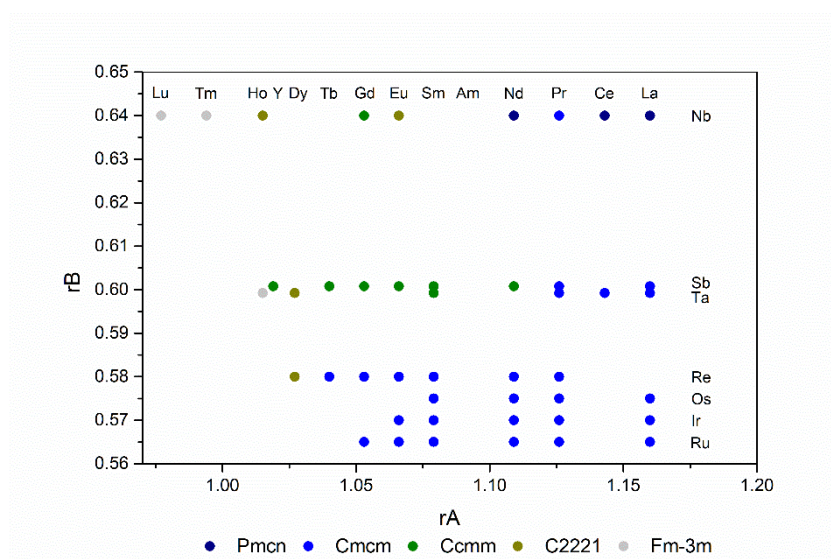


Figure 6-10. Structure field map for $\text{Ln}^{3+}\text{B}^{5+}\text{O}_7$ compounds, Grey = Defect fluorite type, Green = Y_3TaO_7 type, Blue = La_3NbO_7 type

Our interest in synthesizing Ce_3NbO_7 was stimulated by the need to explore the structure-property relations of refractory actinide ternary oxides, as potential ceramic heat sources for use RTGs for deep space probes. This study, and the work of Inabayashi et al. [123], have shown that $\text{Ce}_3(\text{Nb},\text{Ta})\text{O}_7$ is prone to oxidation at high temperature, associated with transformation of Ce^{3+} to Ce^{4+} , resulting in decomposition. Similar behaviour would naturally be expected for the Am^{3+} weberite analogue and, since the overarching aim is to maintain Am redox during materials processing and in service, in particular avoiding associated component dimensional changes, Am_3NbO_7 weberite would not seem well suited to this application. Consideration of the possibility of a defect fluorite structured Am_3NbO_7 compound is more appealing, since occupancy of the vacant anion position could provide a mechanism for accommodating $\text{Am}^{3+}/\text{Am}^{4+}$ redox, and isotropic unit cell expansion, without leading to decomposition. The structure field map derived above shows that Am_3NbO_7 would be expected to adopt either the La_3NbO_7 or Y_3TaO_7 weberite structure and lies well away from the defect fluorite phase field. Nevertheless, both La_3NbO_7 and Y_3TaO_7 structures may be considered as ordered derivatives of a parent defect fluorite structure and it can be hypothesised that α -recoil damage in Am_3NbO_7 could effect a transition from a weberite to defect fluorite or amorphous structure, through accumulation of atomic displacements, as observed for counterpart $\text{A}_2\text{B}_2\text{O}_7$ pyrochlores [290]–[292]. As yet, the radiation damage behaviour of Ln_3BO_7 phases has not been documented but would certainly be of particular interest in support of ceramic disposition of separated plutonium stockpiles which require immobilisation and disposal. Experimental and theoretical studies of the stability of Am_3BO_7 compounds would also be a worthy pursuit, since the radius ratio considerations point to compatibility with the weberite structure. However, the utility of weberite structured Am_3NbO_7 for RTG applications seems doubtful.

6.1.5. Conclusions

Ce_3NbO_7 was successfully synthesized by solid state reaction under 5% H_2 -95% N_2 atmosphere at 1523 K. Neutron and electron diffraction data demonstrate this compound to adopt the weberite *Pmcn* aristotype structure, with Ce^{3+} ions occupying sites which are 8-fold and 7-fold co-ordinated by oxygen, confirmed by Ce L_3 edge XANES. The compound shows Curie Weiss paramagnetism with a Weiss temperature of -143 ± 1 K, demonstrating weak antiferromagnetic interactions. The effective magnetic moment per Ce^{3+} was calculated as $2.51 \pm 0.01 \mu_{\text{B}}$, in excellent agreement with the theoretical value of $2.54 \mu_{\text{B}}$. Ce_3NbO_7 will undergo adventitious oxidation at high temperature, eventually decomposing to a mixture of CeO_2 and $\text{CeNbO}_{4+\delta}$. Consideration of cation radius ratios for Ln_3BO_7 compounds has shown this to be a useful metric for discriminating the relative stability of weberite and defect fluorite structures. This empirical analysis suggests that hypothetical Am_3BO_7 compounds are compatible with weberite related structures.

6.1.6. Acknowledgements

The authors would like to thank the EPSRC (Grant EP/G037140/1) for funding this research which was performed in part at the MIDAS Facility, at the University of Sheffield, established with support from the Department of Energy and Climate Change. X-ray absorption experiments were performed under the approval of Proposal No. 2015P013 from the Photon Factory Advisory Committee. Also acknowledged is the help of Dr Heath Bagshaw at the University of Manchester for his expert use of the TEM and for the ED imaging work. We are grateful to Alex Gibbs for assistance with neutron diffraction, and to the ISIS neutron and muon source for provision of beamtime.

7. Conclusions and Recommended Future Work

This section aims to bring together the conclusions and discussion from each of the previous Chapters, identifying how they meet the objectives of this research and the further work that can follow from the results obtained. It is apparent from the previous Chapters that the application of thermal treatment for fuel residues and problematic nuclear waste is diverse resulting in the production of wasteform materials requiring a wide suite of analysis to fully comprehend. In Chapter 2 a selection of wastes and fuel residues were identified for further research, namely Magnox sludge wastes, Chernobyl fuel residues and Am build-up from civil Pu stockpiles, each seemingly quite different yet all of which are linked by the requirement to ensure long term immobilisation and safety. All synthesised materials were subject to a common suite of characterisation techniques, often using the same instrumentation, demonstrating the versatility of these resources. The research in this thesis all demonstrate the use of simulants to aid thermal synthesis of simulated nuclear fuel residues and problematic nuclear wastes and the importance of this is outlined in the Section 7.1 below.

As with any scientific subject, the pursuit of further knowledge is key to better understanding the materials discussed in this Thesis, and therefore this very much an ‘open book’, with both potential and ongoing further work discussed in Section 7.2.

7.1. Overall Conclusions

In Chapter 4 durable magnesium borosilicate glass wasteforms were successfully developed, capable of immobilising the wide envelope of nuclear fuel residues anticipated from the sludge waste ponds and silos at the Sellafield site. Whilst the base glass composition was amorphous, the preferred option for a nuclear waste glass since the radionuclide content is dispersed evenly through the material, loading with high levels of metallic waste lead to partial crystallisation. This crystallisation occurred with Mm, Nd and U and is likely due to the time/temperature conditions of the thermal treatment process as well as the sample reaching saturation in the concentration of waste components that can be accommodated in the glass structure. In most cases, the observed crystallisation did not significantly alter the chemical durability of the glass system; metallic waste loaded samples showed the lowest leaching rates of glass components compared to glass with corroded waste. For the Magnox wastes evaluated in this Thesis, the borosilicate glass developed was found to have chemical durability analogous to current UK HLW simulant glass subject to similar conditions. The total activity content for the ILW in question is approximately 2 orders of magnitude lower than for HLW, therefore the overall source term of the magnesium borosilicate wasteform is considerably less and the conditions

of acceptance for these materials within a geological repository could be less onerous. Thermal treatment of these sludge wastes creates a significant net reduction in the volume of waste to be disposed, circa 80% compared with the current UK's baseline plan of cementation. Such a reduction in volume would result in less space required in a geological repository. Assuming ILW costs for disposal with a single GDF of £8,990 per m³ [234], the associated disposal cost saving compared to cementation is approximately £82 million. However as these costs are based on September 2008 money and undiscounted, it is likely the cost savings may be greater. Similar thermal treatment techniques could be applied to other wastes at Sellafield and across the UK leading to further volume reduction and therefore saved repository space which could reduce the sizing of a proposed GDF, currently estimated at a fixed cost of £4401 million. It is anticipated the financial benefits of implementing ILW thermal treatment via vitrification would outweigh the costs of developing and running such a treatment facility. The human factors in the development of thermal treatment options for ILW is uncountable with non-financeable benefits such as improved passive safety and potentially increased public support owing to less nuclear material requiring transportation. This could have the knock-on effect of gaining a communities acceptance for the construction and operation of a GDF, a key stepping stone in the UK's plan for long term disposal of nuclear waste.

Section 4.1 showed the presence of Mm suppressing dissolution of MAS and MBS compositions whilst forming non-complex crystallinity, Mm simulants wastefoms produced oxide based or boride based crystalline phases during synthesis, with each never-coexisting in the same sample. However, when doped with Nd, simulants waste forms produced both boride and oxide phases simultaneously. From Section 4.2, it was found oxide phases were present in U doped samples exclusively. For Nd and Mm doped glass, it was found the magnesium borosilicate composition has an affinity towards boride phases whilst oxide phases were found in both MAS and MBS systems. It is hypothesised that the effect of the simulants Nd and Mm on a wasteform could be utilised best for applications where considerable quantities of fission products are present in the waste. One such example is the treatment of irradiated spent nuclear fuel, where research into creating simulants nuclear fuel (SIMfuel) involves significant use of many lanthanides to simulate the array of fission products built up over use in a reactor [293], [294]. For the type Magnox sludge wastes studied in this project, the amount of fission products present in the real material is low and hence, the use of Mm and Nd as simulants for this particular nuclear waste would not be ideal, considering the effect this has on the chemical durability. The use of low activity U, as shown in Section 4.2, demonstrated simulants representative of ILW can be synthesised safely on the laboratory scale. As can be seen by comparison between the dissolution data of U doped, Nd doped and Mm doped compositions, the leaching behaviour of the simulants is different, with no leaching of Mm components Ce and La, very little Nd leaching yet appreciable leaching of U, likely due to the additional effects of U redox on solubility. Therefore, the use of Nd or Mm in these samples could lead to the false impression that these materials do not leach from their wasteform whilst results from Section 4.2 show otherwise. This demonstrates the importance of using simulants for the correct purpose. In Chapter 5, the development of representative LFCM materials would not

be possible through the use of simulants; the ability to form a high-uranium zircon phase was dependent on the availability of U within the glass melt and replacement with a simulant would not replicate this phase. Likewise in Chapter 6 the use of the simulant Ce for Am was important to recreate the effects of oxidation at high temperatures.

One of the major cross-cutting questions that has developed from this thesis is the extent to which one can trust the use of simulants. To answer this accurately the scenarios in which simulant are to be used and the purpose of the research need to be thoroughly understood. As previously mentioned, the use of low activity U was used in this research for immobilising Magnox sludge waste due to the need to develop an understanding of the long-term behaviour of the material with the aqueous conditions expected within a GDF. However, if the content of fission products in the waste was deemed to be high, relative to the other materials in the waste stream, the use of Mm and/or Nd alongside low activity U would be justified in long-term durability experiments as we would expect to learn the effect the components have on the leaching of key elements of the waste product, which could then allow for redevelopment of the original wastefrom. However, no simulant can ever replace the need to conduct real world testing and/or pilot studies before implementation, however the more realistic an experiment can be, the lower the risk of failure and re-work. This has both time and cost savings associated. In some circumstances, such as Chapter 6, the use of a highly radioactive and contaminable component in early stage research could prove both costly and unsafe, therefore simulants may have to be used so far as they do not impede the original aim of the research.

Using a HIP thermal synthesis process on the same base MBS glass composition from Sections 4.1 and 4.2, it was concluded in Section 4.3 that the technique would not be suitable without additional research. The high content of B in the batch composition caused significant corrosion on the HIP can wall leading to a large uptake of refractory material into the glassy melt. Insufficient mixing of the batch during synthesis, via thermal convection, resulted in incomplete reaction of the original batch and an inhomogeneous material. Utilising the wastefrom considered in this project, it is unlikely the wastes from FGMSF would be suited to HIP thermal synthesis, however the use of a less corrosive composition may improve the quality of the wastefrom. The MAS glass studied in Section 4.2 contained very little B (just as a tracer for dissolution experiments) and may be suitable if the HIP equipment used is capable of operating at temperatures upto 1500 °C. Subtle compositional changes in this base glass via the addition of glass fluxes such as LiO₂ may reduce the liquidus temperature and hence operating temperature of the HIP equipment. If the disposal conditions to be placed on these wastes are not particular onerous and the requirements on wastefrom acceptance relaxed, pressing the sludges into solid pucks of material, encapsulated in the HIP can may suffice as an acceptable wastefrom. Due to the high costs and small processing volumes anticipated through this method, conventional thermal synthesis via vitrification as outlined in Section 4.2 may prove to be more economically viable, providing a durable, homogenous or slightly heterogenous glassy product. However, the disadvantages of vitrification include a need to calcine the material and scrub any off-gas produced from a radioactive glass melt, which would create another secondary waste in the off-gas filtration system and the wastes associated with

dismantling a vitrification facility including highly refractory material that would be difficult to incorporate into another waste product. The effect of these disadvantages can be reduced via small batch processing in single use glass melting units, however this would come at a cost and could be comparable to pressing similar sized batches in a HIP unit, with the added benefit of a HIP can providing an initial barrier to the environment via the multi-barrier principle (Figure 2-13) and potentially greater volume reduction. Development of large industrial HIP facilities and pressing of sludge material is ongoing research, with previous work by Heath et.al. [154] demonstrating the technique as a viable route for disposal, whilst the technique currently remains an interesting albeit novel process for thermally treating small volumes of other problematic wastes.

The development of representative simulants for Chernobyl LFCM in Chapter 5 demonstrates successful thermal synthesis of material analogous to the multiphase wastefoms that may be produced from thermal treatment of nuclear fuel residues. By replicating these fuel residue wastefoms with low activity simulants, the detailed durability in sub-optimal conditions that may be expected within a GDF facility in the long term can be studied and simulated. Through investigating the effects of water, oxidising or reducing conditions and interaction with other geological elements, researchers can gain insight in to the long-term behaviour of thermally treated fuel residue wastefoms, ensuring enduring passive safety whilst reducing the hazard to the researchers. In Section 5.2 successful synthesis of simulant LFCM was achieved with a typical morphology and microstructure representative of that found in real brown and black type LFCM including formation of the distinctive Chernobylite phase from a glass melt, such phases could be realistically expected in wastefoms produced from fuel residues. This demonstrates that we can precisely recreate composition, phase assemblage and microstructure of highly active materials with low active simulants though thoughtful consideration of the original synthesis process. As shown in Section 4.2, detailed analysis and discussion can be performed on material utilising low activity U and can be compared to other work in the literature to develop an understanding of the simulants created. The knowledge developed from creating representative LFCM may be of use in the clear up operations taking place at Chernobyl and the Fukushima Daiichi Nuclear Power Plant in Japan, allowing planners to make more informed decisions on the fate of such materials including the priority of the removal from site based on the rate at which it is degrading and the effect of the local environment on the materials durability. By considering the microstructure and morphology of the materials, potential thermal treatment of the Chernobyl LFCM fuel residues in a glass or glass-ceramic wastefom may be considered as a viable option for the long term storage of the material. Further work on the durability of Chernobyl and Fukushima LFCM is ongoing (Section 7.2)

Another problematic radioactive product and residue investigated via the use of simulants was the Pu stockpiles at Sellafield; decaying into Am over time. A novel Ce_3NbO_7 compound was successfully produced, with near 100% phase purity, as a simulant for a potential Am_3NbO_7 ceramic phase; which could be used as a radioactive heat source to power spacecraft, converting civil waste into an asset. Chapter 6 showed that successful reduction of Ce^{4+} to Ce^{3+}

occurred during synthesis however oxidation at high temperature occurs and would also be expected for the Am^{3+} weberite structure, changing the redox of Am during processing and in service, therefore rendering Am_3NbO_7 weberite ceramics as unsuitable for this application. However, the work has opened new avenues of research including radiation damage behaviour in Ln_3BO_7 phases which has yet to be documented and would assist in the deposition of ceramic based separated plutonium stockpiles which require immobilisation and disposition.

7.2. Recommended and Ongoing Future Work

To improve the Mg and U metallic waste incorporation into the amorphous phase of MAS and MBS glass, further refinement of the compositions and the thermal synthesis process is required. Al_2O_3 incorporation within the MBS melt was associated with preferential uptake of uranium suggesting the addition of Al_2O_3 as a minor component, combined with mixing of the glass melt during synthesis may increase the incorporation of U and remove phase separation.

Advancing the leaching and dissolution understanding of MAS and MBS glass would help ascertain the long-term behaviour of the samples under varying conditions. By using a single-pass flow-through test, the effects of sample saturation would be removed and the forward rate dissolution kinetics along with accurate comparisons with existing HLW and ILW simulants could be determined. Further studies of the post leaching oxidation state of MAS and MBS glass could determine the exact change in oxidation state due to hydrothermal alteration vital to the development of the safety case for implementing vitreous wastefoms. Research on this with other compositions and materials is currently underway by the University of Sheffield Immobilisation Science Laboratory.

Further improvement in the HIP glass batch composition and processing may yield better results in creating a solid monolithic glass or glass ceramic material. The use of less corrosive boron and more resistant HIP can construction would be of importance for future experiments. In this research it was found a 600 °C calcine of Magnox sludge waste was sufficient in converting $\text{Mg}(\text{OH})_2$ to MgO whilst retaining a degree of magnesia reactivity to ensure the target composition was created, further work to refine the pre-HIP treatment process would be required for development of this thermal synthesis technique. By finely adjusting the calcination temperature and cooling the calcined material within an inert dry atmosphere to remove the effect of rehydration or carbonation, the final HIPed product quality would be improved.

For LFCM samples produced, excess ZrO_2 beyond that reported in the literature was required to promote crystallisation of the Chernobylite phase, which also inadvertently led to the formation of a ZrO_2 phase in the form of baddeleyite, not frequently observed in analysis of real LFCM therefore further refinement of the batch will be required to reduce the ZrO_2 content

whilst retaining the Chernobylite phase. Uranium-bearing secondary precipitates were absent on simulant samples after alteration, yet they are found on real LFCM, therefore further work is required to fully understand the corrosion behaviour of LFCM simulants. This would include increasing the pH of the solution to approximately pH 8.5 – 10 as well as increasing the carbonate content in order to promote the formation of Na-uranyl carbonate phases. Doping the simulant samples with alpha-emitting isotopes would also assist in the precipitation of U-bearing secondary phases such as studtite with radiolysis of water known to promote the formation of hydrogen peroxide. Further studies at the University of Sheffield Immobilisation Science Laboratory are currently being performed to explore these factors, and to develop further understanding of the corrosion behaviour and dust generation capacity of LFCMs along with other similar fuel residues.

The behaviour of Ln_3BO_7 phases under irradiation conditions have not been documented and point to a gap in the current literature knowledge yet would be helpful to support other ceramic wastefrom candidates for the disposal of separated plutonium stockpiles, another problematic fuel product and residue. These radiation damage experiments would also be of interest for the MAS and MBS samples, along with a reassessment of their durability after irradiation and investigation into any changes into the crystalline phase assemblage of these materials.

Appendix A

The following is the supplementary information provided with the Development of Representative Samples paper in Section 5.2.

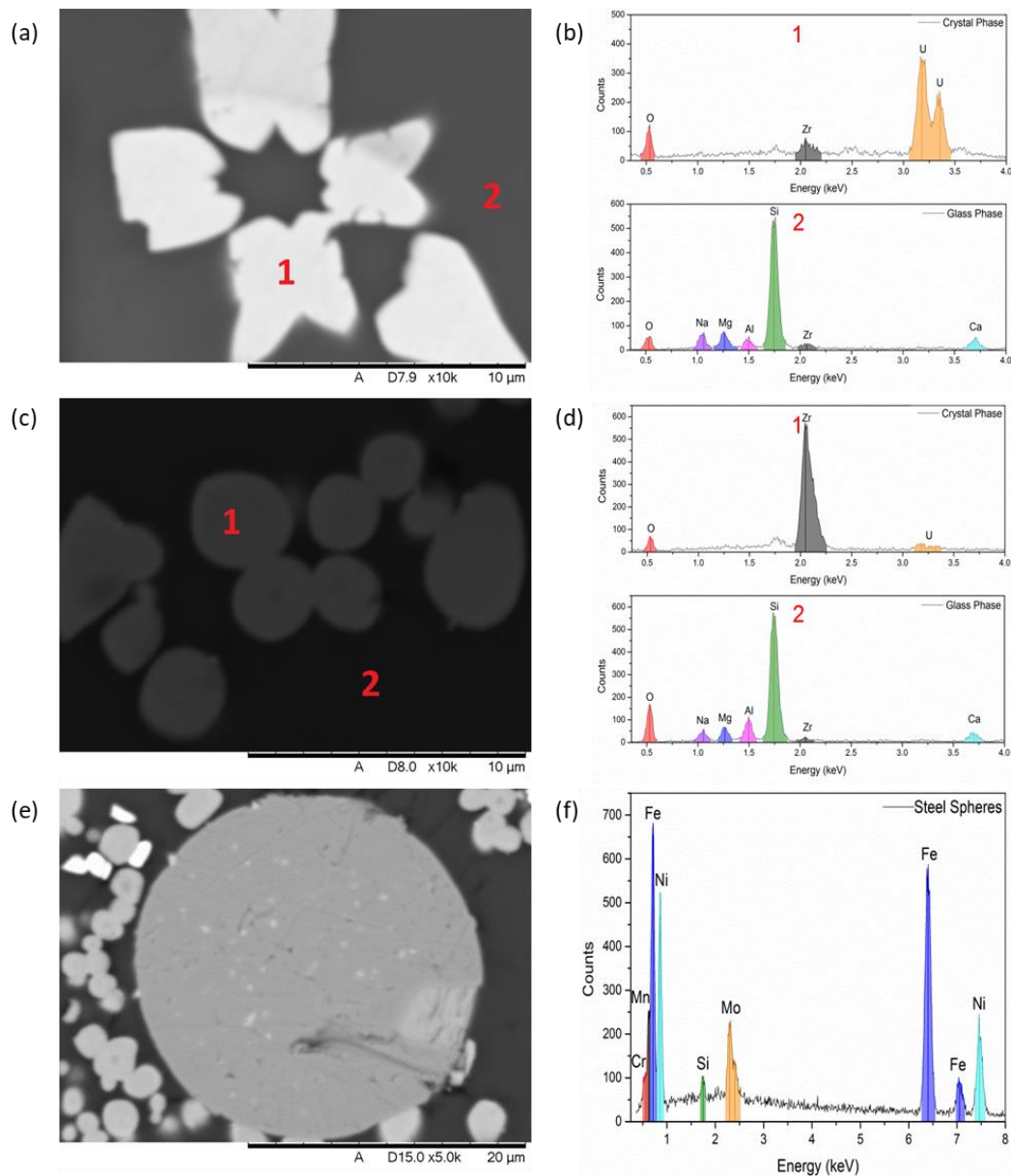


Figure A1. SEM-EDS analysis of (a) and (b) U-Zr crystals present within simulant Brown LFCM; (c) and (d) Zr crystals present within simulant Black LFCM; and (e) and (f) steel sphere inclusion within Black LFCM.

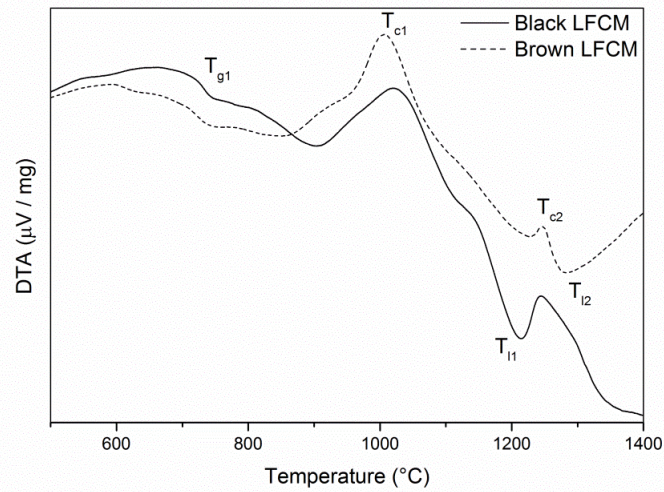


Figure A2. Simulant LFCM thermal analysis highlighting T_g , T_c and T_1 (Endo-down).

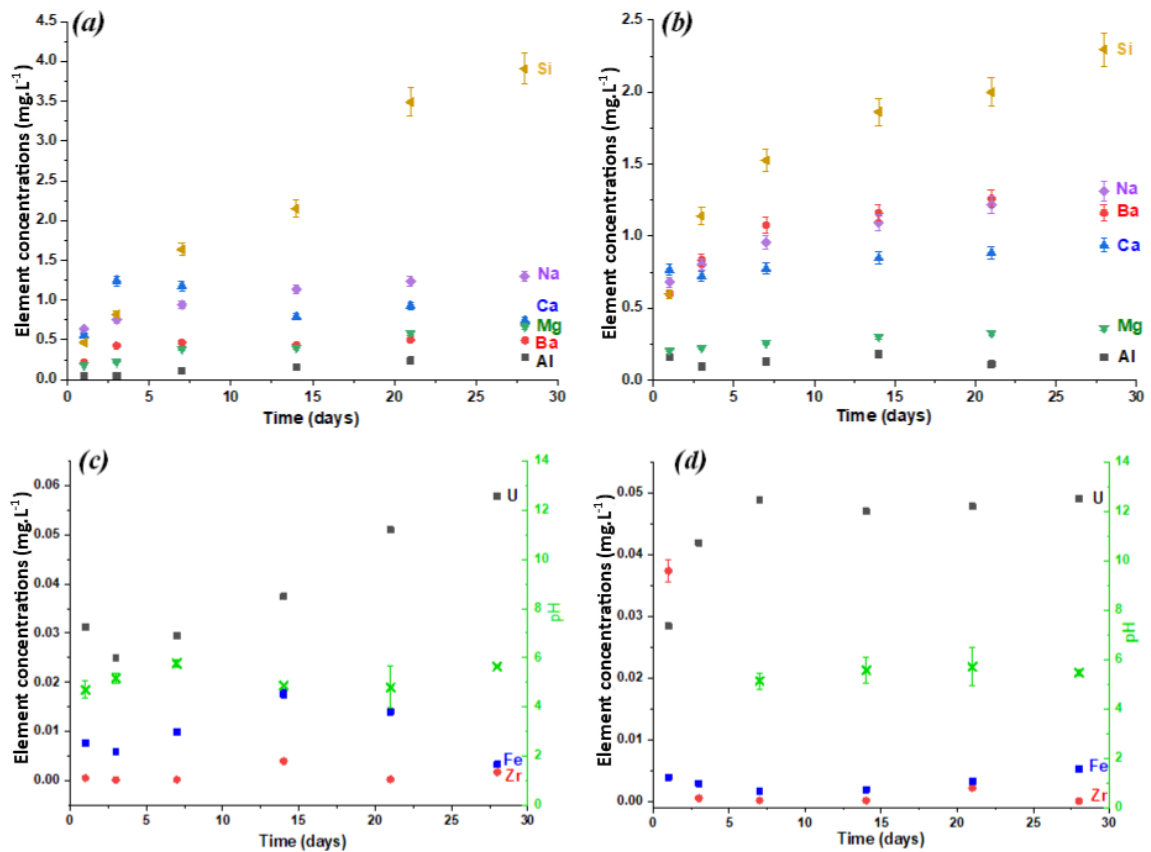


Figure A3. Evolution of the element concentrations C_{Si} (\blacktriangleleft), C_{Na} (\blacklozenge), C_{Ca} (\blacktriangle), C_{Mg} (\blacktriangledown), C_U (\blacksquare), C_{Fe} (\blacksquare) and C_{Zr} (\bullet) and pH (\times) of the simulant Brown (a ; c) and Black (b ; d) LFCM in pure water at 50°C.

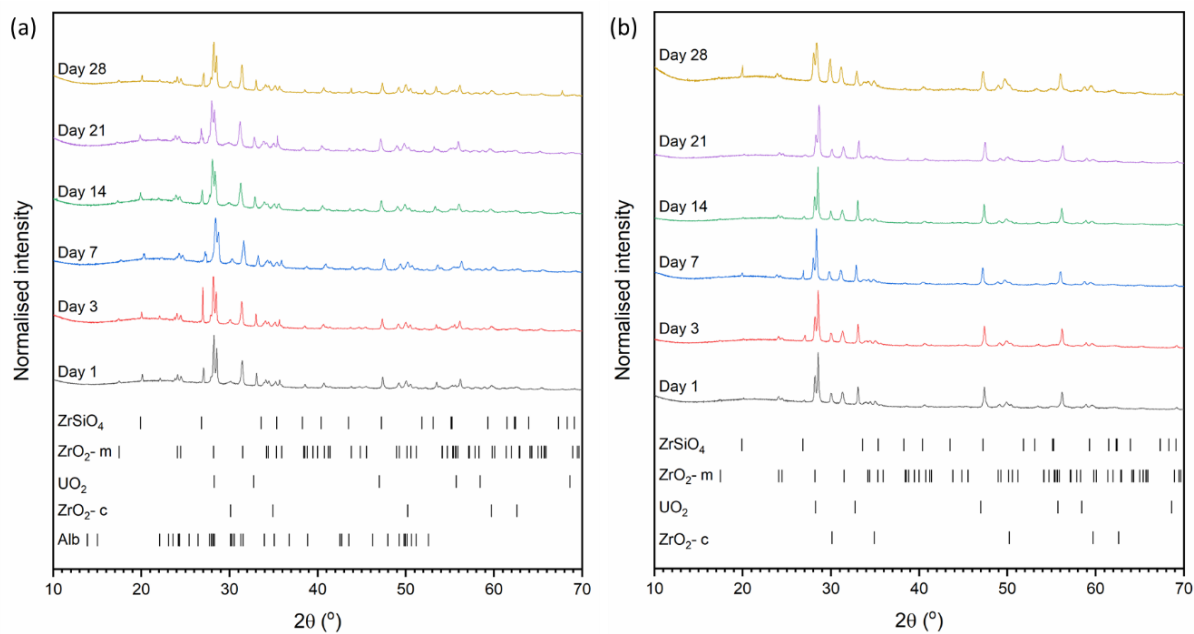


Figure A4. XRD patterns of LFCM samples after 28 days of leaching at 50°C in water, (a) Black lava; and (b) Brown lava.

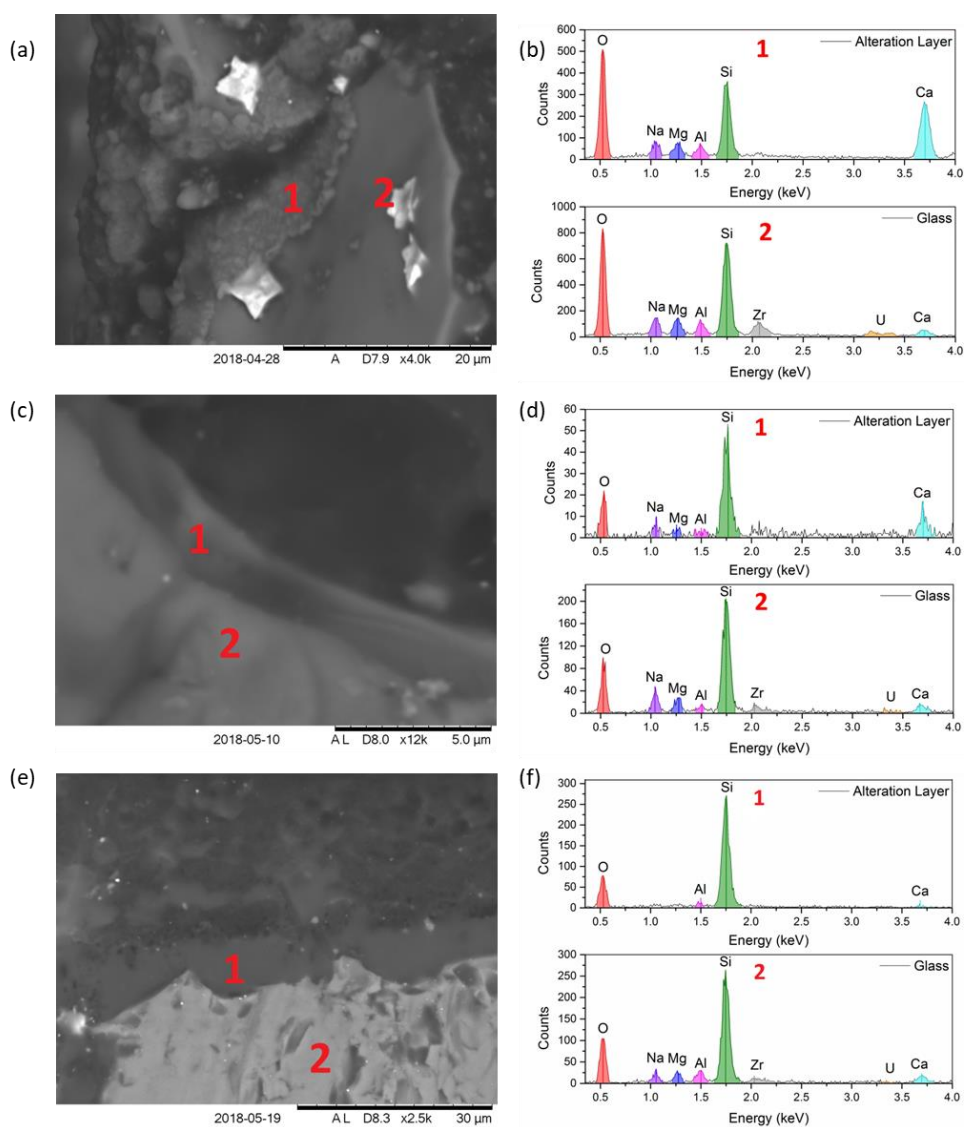


Table A1. Extracted E_0 values and corresponding oxidation state from XAS.

Sample	Extracted E_0 (eV)	Oxidation State (± 0.2)
UO₂ (IV)	17174.9	4.0
Black LFCM	17175.0	4.1
Brown LFCM	17175.3	4.3
Yb_{0.5}U_{0.5}Ti₂O₆ (V)	17176.3	5.0
CaUO₄ (VI)	17178.4	6.0

Table A2. Saturation indexes (SI) relative to the main secondary phases during the dissolution of Black and Brown LFCM at 50°C in UHQ water.

Phase	SI (Brown LFCM)	SI (Black LFCM)	Formula
Beidellite-Ca	2.84	1.39	Ca _{0.165} Al _{2.33} Si _{3.67} O ₁₀ (OH) ₂
Beidellite-H	2.83	1.36	H _{0.33} Al _{2.33} Si _{3.67} O ₁₀ (OH) ₂
Beidellite-Mg	2.95	1.44	Mg _{0.165} Al _{2.33} Si _{3.67} O ₁₀ (OH) ₂
Beidellite-Na	2.08	0.61	Na _{0.33} Al _{2.33} Si _{3.67} O ₁₀ (OH) ₂
Kaolinite	4.60	3.60	Al ₂ Si ₂ O ₅ (OH) ₄
Boehmite	2.77	2.52	AlO ₂ H
Hematite	8.48	8.89	Fe ₂ O ₃
Soddyite	0.98	0.46	(UO ₂) ₂ SiO ₄ ·2H ₂ O
Pyrophyllite	2.02	0.58	Al ₂ Si ₄ O ₁₀ (OH) ₂

Appendix B

The following is the supplementary information provided with the Cerium (III) Immobilisation paper in Section 6.1.

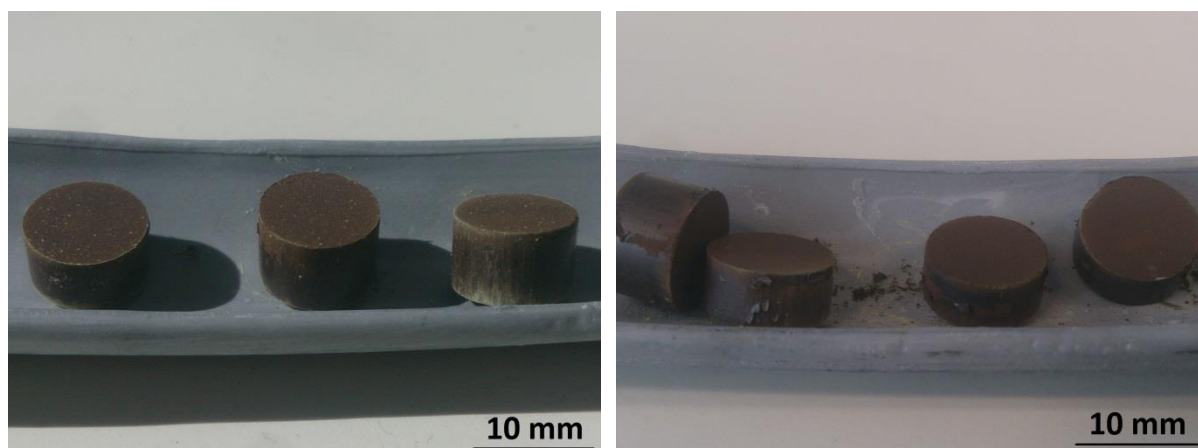


Figure B1. Synthesised pellets after 24 and 148 hours showing yellow precipitates on outer surface (left) from 24 hour reacted samples. These are not apparent in 148 hour reacted samples (right).

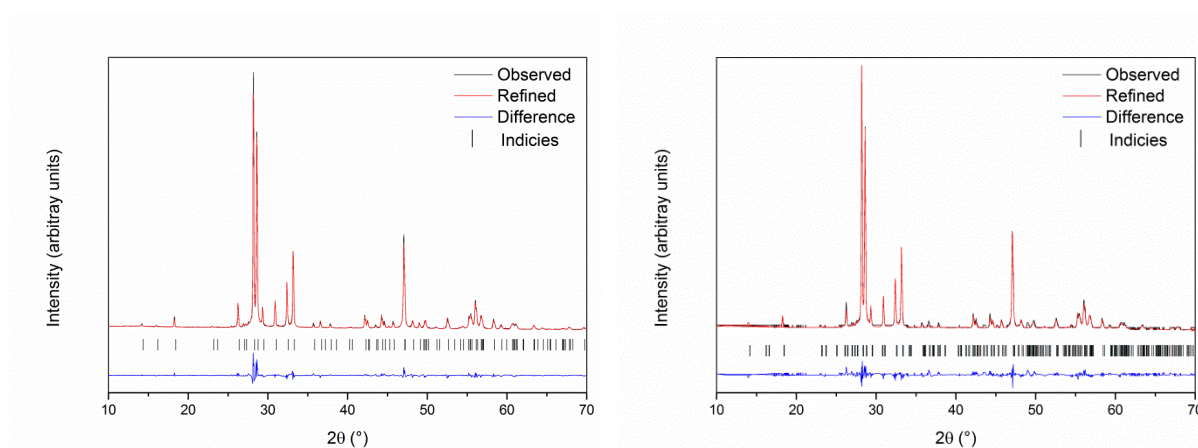


Figure B2. Reflectance mode XRD of bulk Ce_3NbO_7 with Cmcm (left) and Pmcn (right) refinements overlaid.

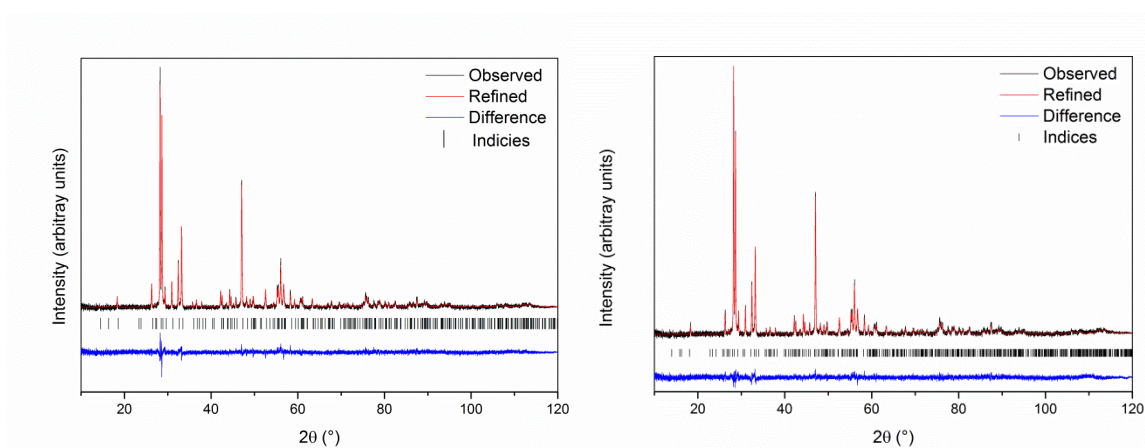


Figure B3. Transmission mode XRD of bulk Ce_3NbO_7 with $\text{Cmc}21$ (left) and $\text{Pm}21n$ (right) refinements overlaid.

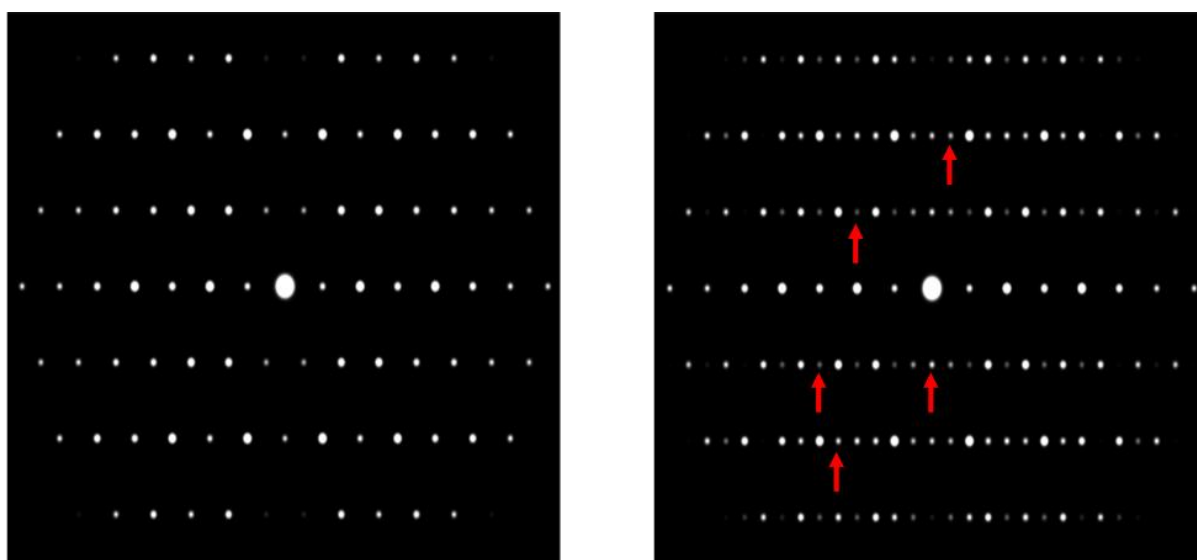


Figure B4. $[0\ 2\ 1]$ zone axis simulated electron diffraction pattern for $\text{Cmc}21$ (left) and $\text{Pm}21n$ (right) space groups of Ce_3NbO_7 . Note the lack of intensity for the sub-lattice on the simulated $\text{Cmc}21$ system.

References

- [1] M. Hill *et al.*, “CoRWM Meeting with NDA on Legacy Ponds and Silos,” no. January, pp. 1–9, 2011.
- [2] A. N. Leigh and N. Routledge, “Preparation for Fuel Storage Pond Clean Up British Nuclear Group Sellafield Site A.N.,” in *WM’07 Conference*, 2007.
- [3] M. W. Peres, “A Comparison of Challenges Associated with Sludge Removal, Treatment and Disposal at Several Spent Fuel Storage Locations,” in *WM’07 Conference*, 2007.
- [4] S. V. Ushakov, B. E. Burakov, S. I. Shabalev, and E. B. Anderson, “Interaction of UO₂ and Zircaloy during the Chernobyl accident,” *Materials Research Society Symposium - Proceedings*, vol. 465, no. January 1996, pp. 1313–1318, 1997.
- [5] Nuclear Decommissioning Authority, “Priority Programmes and Major Projects: Performance Report,” 2015.
- [6] B. E. Burakov *et al.*, “The Behavior of Nuclear Fuel in First Days of the Chernobyl Accident,” *Materials Research Society, Symposium Proceedings*, vol. 465, no. August, pp. 1297–1308, 1997.
- [7] A. A. Shiryaev *et al.*, “Physico-chemical properties of Chernobyl lava and their destruction products,” *Progress in Nuclear Energy*, vol. 92, no. 2016, pp. 104–118, 2016.
- [8] N. C. Hyatt, “Plutonium management policy in the United Kingdom: The need for a dual track strategy,” *Energy Policy*, vol. 101, no. 2017, pp. 303–309, 2017.
- [9] R. Ambrosi *et al.*, “Americium-241 Radioisotope Thermoelectric generator development for space applications,” in *2013 International Nuclear Atlantic Conference*, 2013.
- [10] C. Utton and I. H. Godfrey, “Review of stability of cemented grouted ion-exchange materials, sludges and flocs,” 2010.
- [11] O. Hahn, “The Discovery of Fission,” *Scientific American*, vol. 198, no. 2, pp. 76–84, 1958.
- [12] L. Meitner and O. R. Frisch, “Disintegration of Uranium by Neutrons: A New Type of Nuclear Reaction,” *Nature*, vol. 143, pp. 239–240, 1939.
- [13] O. R. Frisch, “Physical Evidence for the Division of Heavy Nuclei under Neutron Bombardment,” *Nature*, vol. 143, no. 3616, pp. 276–276, Feb. 1939.
- [14] H. Von Halban, F. Joliot, and L. Kowarski, “Number of Neutrons Liberated in the Nuclear Fission of Uranium,” *Nature*, vol. 143, no. 3625, pp. 680–680, Apr. 1939.
- [15] OpenStax College, “Chemistry,” *OpenStax CNX*, 2015. [Online]. Available: <https://openstaxcollege.org/textbooks/chemistry>. [Accessed: 21-Jan-2016].
- [16] K. T. Bainbridge, “Trinity,” 1976.

- [17] M.A.U.D Committee, “Report by M.A.U.D Committee on the use of Uranium for a Bomb,” 1941.
- [18] I. Hore-Lacy, *Nuclear Energy in the 21st Century*, vol. 1, no. 1. Academic Press, 2006.
- [19] M. A. Lusted, *Nuclear Energy*. ABDO Publishing Company, 2013.
- [20] R. L. Murray, *Nuclear Energy: An Introduction to the Concepts, Systems and Applications of Nuclear Processes*, 6th ed. Oxford: Elsevier, 2008.
- [21] R. Michal, “Fifty years ago in December: Atomic reactor EBR-I produced first electricity,” *Nuclear News*, vol. 44, no. 12, pp. 28–29, 2001.
- [22] I. W. Donald, *Waste Immobilization in Glass and Ceramic Based Hosts*. Chichester, UK: John Wiley & Sons, 2010.
- [23] “Calder Hall Power Station,” *The Engineer*, vol. 202, no. 5254, pp. 464–468, 1956.
- [24] Sellafield Ltd, “Challenge,” 2016. [Online]. Available: <http://www.sellafieldsites.com/challenge/>. [Accessed: 22-Jan-2016].
- [25] D. G. Cacuci, *Handbook of Nuclear Engineering- Volume 1 Nuclear Engineering Fundamentals*, 1st ed. Springer US, 2010.
- [26] S. Morley, “National Grid: Live Status,” 2015. [Online]. Available: <http://nationalgrid.stephenmorley.org/>. [Accessed: 16-Nov-2015].
- [27] E. Nonbel, “Description of the Advanced Gas Cooled Type of Reactor (AGR),” 1996.
- [28] Nuclear Decommissioning Authority, “Waste Inventory Data for Wylfa,” 2015. [Online]. Available: <http://www.nda.gov.uk/ukinventory/site/wlyfa/>. [Accessed: 23-Nov-2015].
- [29] N. Lakin, “Heysham power station bosses ‘delighted’ by seven year extension,” *The Visitor*. Morcambe, 16-Feb-2016.
- [30] Seymour Chartered surveyors, “Portfolio item - Sizewell B Power Station,” 2016. [Online]. Available: <http://seymoursurveyors.com/portfolio-item/sizewell-b-power-station/>. [Accessed: 19-Apr-2016].
- [31] T. Fenwick, “UK new build nuclear power: delivering best value,” 2014.
- [32] B. Brooks, “New build,” *Nuclear Future*, vol. 11, no. 2, pp. 10–11, 2015.
- [33] T. Abram and S. Ion, “Generation-IV nuclear power: A review of the state of the science,” *Energy Policy*, vol. 36, no. 12, pp. 4323–4330, 2008.
- [34] K. Tuček, J. Carlsson, and H. Wider, “Comparison of sodium and lead-cooled fast reactors regarding reactor physics aspects, severe safety and economical issues,” *Nuclear Engineering and Design*, vol. 236, no. 14–16, pp. 1589–1598, 2006.
- [35] C. A. Sharrad, L. M. Harwood, and F. R. Livens, “Nuclear Fuel Cycles: Interfaces with the Environment,” in *Nuclear Power and the Environment*, Vol 32., R. E. Hester and R. M. Harrison, Eds. Cambridge: Royal Society of Chemistry Publishing, 2011, pp. 40–56.
- [36] M. I. Ojovan and W. E. Lee, *An Introduction to Nuclear Waste Immobilisation*, 2nd Ed. Oxford: Elsevier, 2014.

- [37] M. H. Klaproth, "Chemical Investigation of Uranium, a newly discovered metallic substance," *Chemical Annals for the Friends of Nature, Medicine, Domestic Art and Manufactures*, vol. 2, pp. 387–403, 1789.
- [38] J. Emsley, "Neodymium," in *Nature's Building Blocks: An A-Z Guide to the Elements*, 1st ed., Oxford: Oxford University Press, 2001, p. 480.
- [39] R. E. Hester and R. M. Harrison, *Nuclear Power and the Environment*, vol. 32. Royal Society of Chemistry Publishing, 2011.
- [40] IAEA, "Methods of exploitation of different types of uranium deposits - IAEA-TECDOC-1174," 2000.
- [41] National Research Council, *Uranium Mining in Virginia: Scientific, Technical, Environmental, Human Health and Safety, and Regulatory Aspects of Uranium Mining and Processing in Virginia*. National Academies Press, 2012.
- [42] IAEA, "In Situ Leaching of Uranium: Technical, Environmental and Economic Aspects - IAEA-TECDOC-492," 1989.
- [43] J. S. Morrell and M. J. Jackson, *Uranium processing and properties*, 1st ed. Springer New York, 2013.
- [44] I. W. Donald, R. N. J. Taylor, and B. L. Metcalfe, "The immobilization of high level radioactive wastes using ceramics and glasses," *Journal of Materials Science*, vol. 32, no. 22, pp. 5851–5887, 1997.
- [45] S. Villani, *Uranium Enrichment*. Springer, 1979.
- [46] J. P. Banks and C. K. Ebinger, *Business and Nonproliferation: Industry's Role in Safeguarding a Nuclear Renaissance*. Brookings Institution Press, 2011.
- [47] Office for Nuclear Regulation, "Review of Magnox Reprocessing Separation Plant Regulatory Strategy - ONR-SEL-PAR-15-004," 2015.
- [48] Nuclear Decommissioning Authority, "NDA Business Plan 2017 to 2020 - SG/2017/24," 2017.
- [49] A. Ramanujam, "Purex and Thorex Processes (Aqueous Reprocessing)," *Encyclopedia of Materials: Science and Technology (Second Edition)*, vol. 2, pp. 7918–7924, Jan. 2001.
- [50] International Atomic Energy Agency, *Storage and Disposal of Spent Fuel and High Level Radioactive Waste*, no. February. 2006, pp. 1–6.
- [51] C. Golinelli and J. L. Guillet Cogema, "MOX In France: Status and Prospects," in *IAEA Technical Committee Meeting on Recycling of Pu and U in Water Reactor Fuel*, 1995, pp. 17–23.
- [52] Department for Business Enterprise & Regulatory Reform, "Meeting the Energy Challenge: A White Paper on Energy," 2008.
- [53] DEFRA & Department of the Environment, "Managing Radioactive Waste Safely A Framework for Implementing," 2008.
- [54] DEFRA, DTI, and Devolved Administrations, *Policy for the long term management of*

- solid low level radioactive waste in the United Kingdom*. London: Department for Environment, Food and Rural Affairs, 2007.
- [55] R. O. A. Rahman, R. Z. Rakhimov, N. R. Rakhimova, and M. I. Ojovan, "Radioactive Waste Cementation," in *Cementitious Materials for Nuclear Waste Immobilization*, vol. XXXIII, no. 2, Chichester, UK: John Wiley & Sons, Ltd, 2014, pp. 127–157.
- [56] LLW Repository Ltd, "National Waste Programme: Services," 2016. [Online]. Available: <http://llwrsite.com/national-waste-programme/services/>. [Accessed: 13-Jan-2016].
- [57] Office for Nuclear Regulation, "Basic principles of radioactive waste management: An introduction to the management of higher activity radioactive waste on nuclear licensed sites," 2015.
- [58] Radioactive Waste Management Ltd., "What will go into a GDF?," Oct. 2017.
- [59] Nuclear Decommissioning Authority, "Radioactive Waste Strategy September 2019," Sep-2019. [Online]. Available: <https://www.gov.uk/government/consultations/nda-radioactive-waste-management-strategy/outcome/radioactive-waste-strategy-september-2019>. [Accessed: 04-Apr-2020].
- [60] D. Gore, "Radioactive Waste: Some Topical Issues," London, 1996.
- [61] Poyry Energy Limited and Amec plc, "The 2013 UK Radioactive Waste Inventory," 2013.
- [62] Nuclear Decommissioning Authority, "2016 UK Radioactive waste and materials inventory: UK radioactive waste inventory report," NDA, 2017.
- [63] Sellafield Ltd, "Sellafield Performance Plan," 2015.
- [64] Sellafield Ltd, "Waste Management: ILW Treatment and Storage," 2016. [Online]. Available: <http://www.sellafieldsites.com/solution/waste-management/ilw-treatment-and-storage/the-plan>. [Accessed: 13-Jan-2016].
- [65] Dounreay Site Restoration Ltd, "Higher activity waste," 2016. [Online]. Available: <http://www.dounreay.com/waste/radioactive-waste/higher-activity-waste>. [Accessed: 13-Jan-2016].
- [66] BBC News, "In pictures: First high-level waste shipment," 2010. [Online]. Available: http://news.bbc.co.uk/1/hi/in_pictures/8469708.stm. [Accessed: 14-Jan-2016].
- [67] Department of Energy & Climate Change, "Implementing Geological Disposal," 2014.
- [68] H. Feiveson, Z. Mian, M. V. Ramana, and F. von Hippel, "Spent Fuel from Nuclear Power Reactors: An Overview of a New Study by the International Panel on Fissile Materials," 2011.
- [69] Nuclear Decommissioning Authority, "Progress on plutonium consolidation, storage and disposition," 2019.
- [70] T. Blees, "Critique of The Future of the Nuclear Fuel Cycle : An Interdisciplinary MIT Study," 2011.
- [71] United Kingdom Nirex, "Review of CoRWM Document No . 627 Disposal in

- subduction zones,” 2005.
- [72] United Kingdom Nirex, “Review of CoRWM Document No . 625 Sub seabed disposal,” 2005.
- [73] D. P. Whitmire and D. P. Wright, “Nuclear waste spectrum as evidence of technological extraterrestrial civilizations,” *Icarus*, vol. 42, no. 1, pp. 149–156, 1980.
- [74] West Cumbria: Managing Radioactive Waste Safely, “Geological Disposal Facility Gallery,” 2013. [Online]. Available: <http://www.westcumbriamrws.org.uk/page/119/Geological-Disposal-Facility-Gallery.htm>. [Accessed: 14-Jan-2016].
- [75] Radioactive Waste Management, “Geological Disposal: Generic Specification for waste packages containing high heat generating waste,” Oxford, 2016.
- [76] C. L. Corkhill, N. J. Cassingham, P. G. Heath, and N. C. Hyatt, “Dissolution of UK High-Level Waste Glass Under Simulated Hyperalkaline Conditions of a Colocated Geological Disposal Facility,” *International Journal of Applied Glass Science*, vol. 4, no. 4, pp. 1–16, Dec. 2013.
- [77] J. D. Vienna, J. V. Ryan, S. Gin, and Y. Inagaki, “Current Understanding and Remaining Challenges in Modeling Long-Term Degradation of Borosilicate Nuclear Waste Glasses,” *International Journal of Applied Glass Science*, vol. 4, no. 4, pp. 283–294, Dec. 2013.
- [78] E. M. Pierce, E. A. Rodriguez, L. J. Calligan, W. J. Shaw, and B. Pete McGrail, “An experimental study of the dissolution rates of simulated aluminoborosilicate waste glasses as a function of pH and temperature under dilute conditions,” *Applied Geochemistry*, vol. 23, no. 9, pp. 2559–2573, 2008.
- [79] E. Vernaz, S. Gin, C. Jégou, and I. Ribet, “Present understanding of r7t7 glass alteration kinetics and their impact on long-term behavior modeling,” *Journal of Nuclear Materials*, vol. 298, no. 1–2, pp. 27–36, 2001.
- [80] C. Jégou, S. Gin, and F. Larché, “Alteration kinetics of a simplified nuclear glass in an aqueous medium: Effects of solution chemistry and of protective gel properties on diminishing the alteration rate,” *Journal of Nuclear Materials*, vol. 280, no. 2, pp. 216–229, 2000.
- [81] P. Frugier *et al.*, “SON68 nuclear glass dissolution kinetics: Current state of knowledge and basis of the new GRAAL model,” *Journal of Nuclear Materials*, vol. 380, no. 1–3, pp. 8–21, 2008.
- [82] D. J. Backhouse, A. J. Fisher, J. J. Neeway, C. L. Corkhill, N. C. Hyatt, and R. J. Hand, “Corrosion of the International Simple Glass under acidic to hyperalkaline conditions,” *npj Materials Degradation*, vol. 2, p. 29, 2018.
- [83] Sellafield Ltd., “First Generation Magnox Storage Pond,” <Http://Www.Sellafieldsites.Com>, 2016. [Online]. Available: www.sellafieldsite.com. [Accessed: 15-Apr-2016].
- [84] D. Mason and A. Buchan, “Sellafield Legacy Wastes Update,” 2007.
- [85] J. Cronin and N. Collier, “Corrosion and expansion of grouted Magnox,” *Mineralogical*

- Magazine*, vol. 76, no. 8, pp. 2901–2909, Dec. 2012.
- [86] M. A. Shand, *The Chemistry and Technology of Magnesia*. Hoboken, NJ, USA: John Wiley & Sons, Inc., 2006.
- [87] C. Delegard and A. Schmidt, “Uranium Metal Reaction Behaviour in Water, Sludge and Grout Matrices- Technical Report, PNNL-17815,” 2008.
- [88] Nuclear Decommissioning Authority, “UK Radioactive Waste Inventory - 2D22 Magnox Cladding and Miscellaneous Solid Waste,” 2014.
- [89] Nuclear Decommissioning Authority, “UK Radioactive Waste Inventory - 2D24 Magnox Cladding and Miscellaneous Solid Waste,” 2014.
- [90] Nuclear Decommissioning Authority, “UK Radioactive Waste Inventory - 2D35 Magnox Cladding and Miscellaneous Solid Waste,” 2014.
- [91] Y. Onishi, O. V. Voitsekhovich, and M. J. Zheleznyak, *Chernobyl - What Have We Learned?: The Successes and Failures to Mitigate Water Contamination Over 20 Years*, 1st ed. Springer Netherlands, 2007.
- [92] R. . Mould, *Chernobyl Record: The Definitive History of the Chernobyl Catastrophe*. CRC Press, 2000.
- [93] E. I. Grishanin, “The Role of Chemical Reactions in the Chernobyl Accident,” *Physics of Atomic Nuclei*, vol. 73, no. 14, pp. 2296–2300, 2010.
- [94] A. A. Borovoi, “Nuclear fuel in the shelter,” *Atomic Energy*, vol. 100, no. 4, pp. 249–256, 2006.
- [95] Y. A. Olkhoviyk and M. I. Ojovan, “Corrosion Resistance of Chernobyl NPP Lava Fuel-Containing Masses,” *Innovations in Corrosion and Materials Science*, vol. 5, no. 1, pp. 36–42, 2015.
- [96] E. M. Pazukhin, “Fuel-Containing Lavas of the Chernobyl NPP 4th Block Topography physicochemical properties and formation scenario,” *Radiochemistry*, vol. 36, no. 2, pp. 109–154, 1994.
- [97] A. Bilyk, A. Novikov, K. Shefer, V. Kashtanov, L. Dodd, and Y. Appolonskyu, “‘Shelter’ Object Safety Status Report / Отчет О Состоянии Безопасности Объекта « Укрытие »,” 2008.
- [98] V. N. Pavlovych, “Fuel-Containing Masses of Chernobyl Unit 4: Multiplying Properties and Neutron Characteristics,” *Nuclear Science and Engineering*, vol. 133, pp. 301–313, 1999.
- [99] R. V Harutyunyan, L. A. Bolshov, A. A. Borovoy, E. P. Velikhov, and A. O. Klyuchnikov, *Nuclear Fuel in a Facility of the Chernobyl Shelter*, 1st ed. Moscow: Nauka, 2010.
- [100] International Atomic Energy Agency, “Management of Severely Damaged Nuclear Fuel and Related Waste,” Vienna, 1991.
- [101] S. A. Bogatov, A. A. Borovoi, A. S. Lagunenkov, E. M. Pazukhin, V. F. Strizhov, and V. A. Khvoshchinskii, “Formation and spread of Chernobyl lavas,” *Radiochemistry*, vol. 50, no. 6, pp. 650–654, 2008.

- [102] Serco, "Literature Review of Partitioning and Transmutation," 2011.
- [103] Organisation for Economic Co-operation and Development, "Spent Nuclear Fuel Assay Data for Isotopic Validation," 2011.
- [104] S. Nathan, "Prism project: A proposal for the UK's problem plutonium," 2013. [Online]. Available: <https://www.theengineer.co.uk/issues/energy-and-sustainability-special/prism-project-a-proposal-for-the-uks-problem-plutonium/>. [Accessed: 24-Jan-2018].
- [105] M. J. Sarsfield *et al.*, "A European Radioisotope Production Facility for Power Sources in Space," in *European Nuclear Conference 2012*, 2012, pp. 4–8.
- [106] L. Summerer and K. Stephenson, "Nuclear power sources: A key enabling technology for planetary exploration," *Proceedings of the Institution of Mechanical Engineers, Part G: Journal of Aerospace Engineering*, vol. 225, no. 2, pp. 129–143, 2011.
- [107] M. A. Prelas, C. L. Weaver, M. L. Watermann, E. D. Lukosi, R. J. Schott, and D. A. Wisniewski, "A review of nuclear batteries," *Progress in Nuclear Energy*, vol. 75, pp. 117–148, 2014.
- [108] D. Harris and J. Epstein, "Properties of Selected Radioisotopes," National Aeronautics and Space Administration, Greenbelt, MD, NASA SP-7031, 1968.
- [109] R. C. O'Brien, R. M. Ambrosi, N. P. Bannister, S. D. Howe, and H. V. Atkinson, "Safe radioisotope thermoelectric generators and heat sources for space applications," *Journal of Nuclear Materials*, vol. 377, no. 3, pp. 506–521, 2008.
- [110] H. R. Williams, H. Ning, M. J. Reece, R. M. Ambrosi, N. P. Bannister, and K. Stephenson, "Metal matrix composite fuel for space radioisotope energy sources," *Journal of Nuclear Materials*, vol. 433, no. 1–3, pp. 116–123, Feb. 2013.
- [111] R. Ambrosi *et al.*, "Development and Testing of Americium-241 Radioisotope Thermoelectric Generator: Concept Designs and Breadboard System," *Nuclear and Emerging Technologies for Space*, no. 2012, pp. 1–2, 2012.
- [112] NASA Jet Propulsion Laboratory, "Billion-Pixel View of Mars Comes From Curiosity Rover," 2013. [Online]. Available: <http://www.jpl.nasa.gov/news/news.php?release=2013-205>. [Accessed: 22-Jul-2014].
- [113] R. C. O'Brien, R. M. Ambrosi, N. P. Bannister, S. D. Howe, and H. V. Atkinson, "Spark Plasma Sintering of simulated radioisotope materials within tungsten cermets," *Journal of Nuclear Materials*, vol. 393, no. 1, pp. 108–113, Aug. 2009.
- [114] W. H. Runde and B. J. Mincher, "Higher oxidation states of americium: Preparation, characterization and use for separations," *Chemical Reviews*, vol. 111, no. 9, pp. 5723–5741, 2011.
- [115] E. J. Watkinson *et al.*, "Sintering trials of analogues of americium oxides for radioisotope power systems," *Journal of Nuclear Materials*, vol. 491, pp. 18–30, 2017.
- [116] E. J. Watkinson *et al.*, "Cerium neodymium oxide solid solution synthesis as a potential analogue for substoichiometric AmO₂ for radioisotope power systems," *Journal of Nuclear Materials*, vol. 486, pp. 308–322, 2017.

- [117] K. P. F. Siqueira *et al.*, “Synchrotron X-ray diffraction and Raman spectroscopy of Ln₃NbO₇ (Ln=La, Pr, Nd, Sm-Lu) ceramics obtained by molten-salt synthesis,” *Journal of Solid State Chemistry*, vol. 209, no. 2014, pp. 63–68, 2014.
- [118] S. A. Kovyazina, L. A. Perelyaeva, I. A. Leonidov, and Y. A. Bakhteeva, “High-Temperature Structural Disorder in R₃NbO₇,” *Journal of Structural Chemistry*, vol. 44, no. 6, pp. 975–979, 2003.
- [119] J. G. Allpress and H. J. Rossell, “Fluorite-Related Phases Ln₃MO₇, Ln = Rare Earth, Y or SC, M = Nb, Sb or Ta I. Crystal Chemistry,” *Journal of Solid State Chemistry*, vol. 27, no. 1, pp. 105–114, 1979.
- [120] H. J. Rossell, “Fluorite-Related Phases Ln₃MO₇, Ln = Rare Earth, Y or SC, M = Nb, Sb or Ta II. Structure Determination,” *Journal of Solid State Chemistry*, vol. 27, no. 1, pp. 115–122, 1979.
- [121] J. F. Vente, R. B. Helmholtz, and D. J. W. Ijdo, “The Structure and Magnetic Properties of Pr₃MO₇ with M=Nb, Ta and Sb,” *Journal of Solid State Chemistry*, vol. 108, pp. 18–23, 1994.
- [122] Z. Guoguang, L. Qin, and F. Qianfeng, “Structure and Dielectric Study of Ce₃NbO₇,” *Journal of Rare Earths*, vol. 25, pp. 730–733, 2007.
- [123] M. Inabayashi, Y. Doi, M. Wakeshima, and Y. Hinatsu, “Synthesis, crystal structures and magnetic properties of fluorite-related compounds Ce₃MO₇ (M = Nb, Ta),” *Journal of Solid State Chemistry*, vol. 254, no. July, pp. 150–154, 2017.
- [124] L. Cai and J. C. Nino, “Synchrotron and neutron powder diffraction study of phase transition in weberite-type Nd₃NbO₇ and La₃NbO₇,” *Journal of Solid State Chemistry*, vol. 184, no. 8, pp. 2263–2271, 2011.
- [125] A. N. Klimenko, Y. S. Kozlov, V. S. Sergeev, and E. A. Pastukhov, “High temperature phase transitions in rare-earth element niobates R₃NbO₇,” *Thermochimica Acta*, vol. 209, pp. 331–338, 1992.
- [126] P. A. Bingham, N. C. Hyatt, R. J. Hand, and C. R. Wilding, “Glass Development for Vitrification of Wet Intermediate Level Waste (WILW) from Decommissioning of the Hinkley Point ‘A’ Site,” in *Materials Research Society Symposium Proceedings*, 2009, vol. 1124.
- [127] M. Kelly, D. A. Lever, C. R. W. D. Applegate, and R. Hand, “Consideration of Vitrified ILW in a Geological Disposal Facility,” Oxford, 2009.
- [128] P. A. Bingham, N. C. Hyatt, R. J. Hand, and S. D. Forder, “Vitrification of UK intermediate level radioactive wastes arising from site decommissioning. Initial laboratory trials,” vol. 54, no. 1, pp. 1–19, 2013.
- [129] N. C. Collier and N. B. Milestone, “The encapsulation of Mg(OH)₂ sludge in composite cement,” *Cement and Concrete Research*, vol. 40, no. 3, pp. 452–459, Mar. 2010.
- [130] W. E. Lee, M. I. Ojovan, M. C. Stennett, and N. C. Hyatt, “Immobilisation of radioactive waste in glasses, glass composite materials and ceramics,” *Advances in Applied Ceramics*, vol. 105, no. 1, pp. 3–12, 2006.
- [131] A. K. Varshneya, *Fundamentals of Inorganic Glasses*, 1st ed. Academic Press, 1994.

- [132] W. E. Lee, M. I. Ojovan, M. C. Stennett, and N. C. Hyatt, "Immobilisation of radioactive waste in glasses, glass composite materials and ceramics," *Advances in Applied Ceramics*, vol. 105, no. 1, pp. 3–12, 2006.
- [133] A. J. Connelly, R. J. Hand, P. A. Bingham, and N. C. Hyatt, "Mechanical properties of nuclear waste glasses," *Journal of Nuclear Materials*, vol. 408, no. 2, pp. 188–193, 2011.
- [134] J. E. Shelby, *Introduction to Glass Science and Technology*, 2nd Editio. Cambridge: The Royal Society of Chemistry, 2005.
- [135] C. D. Wirkus and D. R. Wilder, "Uranium glasses : I . Fundamental considerations," 1960.
- [136] E. El-Meliegy and R. Noort, *Glasses and Glass Ceramics for Medical Applications*. New York, NY: Springer New York, 2012.
- [137] W. H. Zachariasen, "The atomic arrangement in glass," *Journal of the American Chemical Society*, vol. 54, no. 10, pp. 3841–3851, 1932.
- [138] W. H. Zachariasen, "The Vitreous State," *The Journal of Chemical Physics*, vol. 3, pp. 162–163, Mar. 1935.
- [139] W. Vogel, *Glass Chemistry*, 2nd ed. Springer-Verlag, 1994.
- [140] D. G. KARRAKER, "Actinide Valences in Borosilicate Glass," *Journal of the American Ceramic Society*, vol. 65, no. 1, pp. 53–55, 1982.
- [141] B. M. Wright and J. E. Shelby, "Phase separation and the mixed alkali effect," *Physics and Chemistry of Glasses*, vol. 41, no. 4, pp. 192–198, 2000.
- [142] M. O. Prado, A. A. Campos, P. C. Soares, A. C. M. Rodrigues, and E. D. Zanotto, "Liquid-liquid phase separation in alkali-borosilicate glass: An impedance spectroscopy study," *Journal of Non-Crystalline Solids*, vol. 332, no. 1–3, pp. 166–172, 2003.
- [143] M. I. Ojovan, *Handbook of Advanced Radioactive Waste Conditioning Technologies*. Woodhead Publishing, 2011.
- [144] M. I. Ojovan and W. E. Lee, "Glassy Wasteforms for Nuclear Waste Immobilization," *Metallurgical and Materials Transactions A*, vol. 42, no. 4, pp. 837–851, 2011.
- [145] G. J. Mccarthy, "Quartz matrix isolation of radioactive wastes," *Journal of Materials Science*, vol. 8, no. 9, pp. 1358–1359, Sep. 1973.
- [146] M. L. Carter, H. Li, Y. Zhang, E. R. Vance, and D. R. G. Mitchell, "Titanate ceramics for immobilisation of uranium-rich radioactive wastes arising from 99Mo production," *Journal of Nuclear Materials*, vol. 384, no. 3, pp. 322–326, 2009.
- [147] M. James *et al.*, "Crystal chemistry and structures of (Ca,U) titanate pyrochlores," *Journal of the American Ceramic Society*, vol. 93, no. 10, pp. 3464–3473, 2010.
- [148] L. S. Bozadzhiev, G. T. Georgiev, and R. L. Bozadzhiev, "A glass-ceramic material for fixation of radioactive waste," *Science of Sintering*, vol. 43, no. 2, pp. 225–229, 2011.
- [149] C. B. Boyer, "Historical Review of HIP Equipment," in *Proceedings of the Third International Conference*, 1991, pp. 465–510.

- [150] R. M. Govindarajan and N. Aravas, "Deformation processing of metal powders: Part II—Hot isostatic pressing," *International Journal of Mechanical Sciences*, vol. 36, no. 1, pp. 359–372, 1994.
- [151] S. M. Thornber, P. G. Heath, G. P. Da Costa, M. C. Stennett, and N. C. Hyatt, "The effect of pre-treatment parameters on the quality of glass-ceramic wasteforms for plutonium immobilisation, consolidated by hot isostatic pressing," *Journal of Nuclear Materials*, vol. 485, pp. 253–261, 2017.
- [152] T. Y. Chen, E. R. Maddrell, N. C. Hyatt, A. S. Gandy, M. C. Stennett, and J. A. Hriljac, "Transformation of Cs-IONSIV® into a ceramic wasteform by hot isostatic pressing," *Journal of Nuclear Materials*, vol. 498, pp. 33–43, 2018.
- [153] E. R. Vance, M. W. A. Stewart, and S. Moricca, "Advanced Ceramics and Glass-Ceramics for Immobilisation of ILW and HLW," *MRS Proceedings*, vol. 1475, pp. imrc11-1475-nw35-il12, Jan. 2012.
- [154] P. G. Heath, M. W. A. Stewart, S. Moricca, and N. C. Hyatt, "Hot-isostatically pressed wasteforms for Magnox sludge immobilisation," *Journal of Nuclear Materials*, vol. 499, pp. 233–241, 2018.
- [155] E. M. Levin, C. R. Robbins, and H. F. McMurdie, *Phase Diagrams For Ceramists: Volume 1*. Columbus, Ohio: The American Ceramic Society INC, 1964.
- [156] E. M. Levin, C. R. Robbins, and H. F. McMurdie, *Phase Diagrams For Ceramists: Volume 2 - 1969 Supplement*. Columbus, Ohio: The American Ceramic Society INC, 1969.
- [157] ASTM International, "Standard Test Method for Measuring Waste Glass or Glass Ceramic Durability by Vapor Hydration Test," 2017.
- [158] H. Nishimine, Y. Doi, Y. Hinatsu, and M. Sato, "Phase transition of Ln_3IrO_7 (Ln=Pr, Nd, Sm, Eu) and its low-temperature structure," *Journal of the Ceramic Society of Japan*, vol. 155, no. 10, pp. 577–581, 2007.
- [159] Y. Doi, Y. Harada, and Y. Hinatsu, "Crystal structures and magnetic properties of fluorite-related oxides Ln_3NbO_7 (Ln=lanthanides)," *Journal of Solid State Chemistry*, vol. 182, no. 4, pp. 709–715, 2009.
- [160] M. Wakeshima, H. Nishimine, and Y. Hinatsu, "Crystal structures and magnetic properties of rare earth tantalates RE_3TaO_7 (RE = rare earths)," *Journal of Physics: Condensed Matter*, vol. 16, no. 23, pp. 4103–4120, 2004.
- [161] W. T. Fu and D. J. W. IJdo, "On the crystal structures of Ln_3MO_7 (Ln=Nd, Sm, Y and M=Sb, Ta)-Rietveld refinement using X-ray powder diffraction data," *Journal of Solid State Chemistry*, vol. 182, no. 9, pp. 2451–2455, 2009.
- [162] FIZ Karlsruhe, "Inorganic Crystal Structure Database," ICSD, 2017. [Online]. Available: <https://icsd.fiz-karlsruhe.de/search/>. [Accessed: 01-Dec-2017].
- [163] H. A. Hauptman, "History of X-ray crystallography," *Chemometrics and Intelligent Laboratory Systems*, vol. 10, pp. 13–18, 1991.
- [164] M. Eckert, "Max von Laue and the discovery of X-ray diffraction in 1912," *Annalen der Physik*, vol. 524, no. 5, pp. 83–85, 2012.

- [165] C. Suryanarayana and M. G. Norton, *X-Ray Diffraction*, 1st ed. Boston, MA: Springer US, 1998.
- [166] B. E. Warren, "X-Ray Determination of the Structure of Glass," *Journal of the American Ceramic Society*, vol. 17, no. 1–12, pp. 249–254, Dec. 1934.
- [167] L. Liang, R. Rinaldi, and H. Schober, *Neutron Applications in Earth, Energy and Environmental Sciences*, 1st ed. Boston, MA: Springer US, 2009.
- [168] R. E. Dinnebier and S. J. L. Billinge, "Powder diffraction: Theory and practice," *Theory and practice*, p. 2, 2008.
- [169] R. M. Ibberson, W. I. F. David, and K. S. Knight, "The high resolution powder diffractometer (HRPD) at ISIS - a user guide," 1992.
- [170] H. M. Rietveld, "A Profile Refinement Method for Nuclear and Magnetic Structures," *Journal of Applied Crystallography*, vol. 2, no. 1, pp. 65–71, 1969.
- [171] A. C. Larson and R. B. Von Dreele, "General Structure Analysis System (GSAS)," Los Alamos National Laboratory Report LAUR 68-748, 2000.
- [172] B. H. Toby, "EXPGUI, a graphical user interface for GSAS," *Journal of Applied Crystallography*, vol. 34, no. 2, pp. 210–213, 2001.
- [173] B. Fultz and J. M. Howe, *Transmission Electron Microscopy and Diffractometry of Materials*, 3rd ed. Berlin, Heidelberg: Springer Berlin Heidelberg, 2008.
- [174] R. F. Egerton, *Physical Principles of Electron Microscopy*. Springer International Publishing, 2016.
- [175] D. J. Stokes, "Principles of SEM," in *Principles and Practice of Variable Pressure/Environmental Scanning Electron Microscopy (VP-ESEM)*, Chichester, UK: John Wiley & Sons, Ltd, 2008, pp. 17–62.
- [176] P. J. Goodhew, J. F. Humphreys, and R. Beanland, *Electron Microscopy and Analysis*, 3rd ed., vol. 54. Taylor & Francis, 2001.
- [177] G. E. Lloyd, "Atomic Number and Crystallographic Contrast Images with the SEM: A Review of Backscattered Electron Techniques," *Mineralogical Magazine*, vol. 51, no. 359, pp. 3–19, 1987.
- [178] H. Y. J. I. Goldstein, *Practical Scanning Electron Microscopy*. Boston, MA: Springer US, 1977.
- [179] M. E. Brown, *Introduction to Thermal Analysis: Techniques and Applications*, 2nd ed. Kluwer Academic Publishers, 2004.
- [180] M. Feist, "Thermal analysis: basics, applications, and benefit," *ChemTexts*, vol. 1, no. 1, p. 8, 2015.
- [181] P. Gabbot, *Principles and Applications of Thermal Analysis*. Blackwell Publishing, 2008.
- [182] J. Van Humbeeck, "Simultaneous Thermal Analysis," in *Handbook of Thermal Analysis and Calorimetry*, vol. 1, 1998, pp. 497–508.
- [183] Netzsch, "STA 449 F3 Jupiter," 2018. [Online]. Available: <https://www.netzsch->

- thermal-analysis.com/en/products-solutions/simultaneous-thermogravimetry-differential-scanning-calorimetry/sta-449-f3-jupiter/. [Accessed: 19-Feb-2018].
- [184] S. Lowell, J. E. Shields, M. A. Thomas, and M. Thommes, *Characterization of Porous Solids and Powders: Surface Area, Pore Size and Density*, vol. 16. Kluwer Academic Publishers, 2004.
- [185] J. Yano and V. K. Yachandra, “X-ray absorption spectroscopy,” *Photosynthesis Research*, vol. 102, no. 2, pp. 241–254, 2009.
- [186] G. N. Greaves, “X-Ray Absorption Spectroscopy,” in *Glass Science and Technology*, vol. 4B, Academic Press, 1990, pp. 1–76.
- [187] S. Calvin, *XAFS for Everyone*, 1st ed., no. 1. CRC Press, 2013.
- [188] J. A. V. A. N. Bokhoven and C. Lamberti, *X-Ray Absorption and X-Ray Emission Spectroscopy: Theory and Applications*, 1st ed. John Wiley & Sons, Ltd, 2016.
- [189] G. A. Meyer, “Still the Panacea for Trace Metals Analysis?,” *Analytical Chemistry*, vol. 59, no. 23, 1987.
- [190] J. W. Olesik, “Elemental analysis using ICP-OES and ICP/MS,” *Analytical Chemistry*, vol. 63, no. 1, pp. 12–21, Jan. 1991.
- [191] ASTM International, “Standard Test Methods for Determining Chemical Durability of Nuclear, Hazardous, and Mixed Waste Glasses and Multiphase Glass Ceramics : The Product Consistency Test (PCT),” 2008.
- [192] C. A. Utton, R. J. Hand, N. C. Hyatt, S. W. Swanton, and S. J. Williams, “Formation of alteration products during dissolution of vitrified ILW in a high-pH calcium-rich solution,” *Journal of Nuclear Materials*, vol. 442, no. 1–3, pp. 33–45, 2013.
- [193] N. C. Hyatt *et al.*, “Thermal treatment of simulant plutonium contaminated materials from the Sellafield site by vitrification in a blast-furnace slag,” *Journal of Nuclear Materials*, vol. 444, no. 1–3, pp. 186–199, 2014.
- [194] K. S. Matlack *et al.*, “Sellafield Thermal Treatment Trials Using Advanced Joule Heated Ceramic Melter Technology,” *WM2010 Conference*, 2010.
- [195] P. E. Raison and R. G. Haire, “Structural investigation of the pseudo-ternary system AmO₂–Cm₂O₃–ZrO₂ as potential materials for transmutation,” *Journal of Nuclear Materials*, vol. 320, no. 1–2, pp. 31–35, Jul. 2003.
- [196] H.-C. Yang, J.-H. Lee, J.-G. Kim, J.-H. Yoo, and J.-H. Kim, “Behavior of Radioactive Metal Surrogates Under Various Waste Combustion Conditions,” *Journal of the Korean Nuclear Society*, vol. 34, no. 1, pp. 80–89, 2002.
- [197] K. Witwer, S. Woosley, B. Campbell, M. Wong, and J. Hill, “GeoMelt ICV Treatment of Sellafield Pond Solids Waste,” in *Proceedings of the Waste Management Symposia*, 2013, pp. 1–11.
- [198] K. Witwer, E. Dysland, and J. Ave, “Thermal Treatment of UK Intermediate and Low Level Radioactive Waste : A Demonstration of the GeoMelt Process Towards Treatment of Sellafield Waste,” in *Proceedings of the Waste Management Symposia*, 2010, pp. 1–9.

- [199] Sellafield Ltd., “Technology Development and Delivery Summary 2010/11,” Seascale, Cumbria, 2011.
- [200] M. I. Ojovan and W. E. Lee, *An Introduction to Nuclear Waste Immobilisation*, 2nd ed. Oxford: Elsevier, 2014.
- [201] C. M. Jantzen, K. G. Brown, and J. B. Pickett, “Durable Glass for Thousands of Years,” *International Journal of Applied Glass Science*, vol. 1, no. 1, pp. 38–62, Mar. 2010.
- [202] S. T. Barlow, M. C. Stennett, R. J. Hand, S. P. Morgan, and N. C. Hyatt, “Thermal Treatment of UK Magnox Sludge,” in *Proceedings of the 2nd Petrus-OPERA PhD and Early Stage Researcher Conference 2016*, 2016, pp. 19–22.
- [203] S. Gražulis *et al.*, “Crystallography Open Database – an open-access collection of crystal structures,” *Journal of Applied Crystallography*, vol. 42, no. 4, pp. 726–729, Aug. 2009.
- [204] Y. Inagaki, T. Kikunaga, K. Idemitsu, and T. Arima, “Initial Dissolution Rate of the International Simple Glass as a Function of pH and Temperature Measured Using Microchannel Flow-Through Test Method,” *International Journal of Applied Glass Science*, vol. 4, no. 4, pp. 317–327, Dec. 2013.
- [205] D.-S. Kim *et al.*, “Development and Testing of ICV Glasses for Hanford LAW,” Richland, WA (United States), Aug. 2003.
- [206] J. S. McCloy, M. J. Schweiger, C. P. Rodriguez, and J. D. Vienna, “Nepheline Crystallization in Nuclear Waste Glasses: Progress Toward Acceptance of High-Alumina Formulations,” *International Journal of Applied Glass Science*, vol. 2, no. 3, pp. 201–214, Sep. 2011.
- [207] J. D. Vienna, A. Fluegel, D. S. Kim, and P. Hrma, “Glass Property Data and Models for Estimating High-Level Waste Glass Volume, PNNL-18501,” Pacific Northwest National Laboratory, Richland (WA), 2009.
- [208] H. Li, P. Hrma, J. D. Vienna, M. Qian, Y. Su, and D. E. Smith, “Effects of Al₂O₃, B₂O₃, Na₂O, and SiO₂ on nepheline formation in borosilicate glasses: chemical and physical correlations,” *Journal of Non-Crystalline Solids*, vol. 331, no. 1–3, pp. 202–216, Dec. 2003.
- [209] J. M. Schofield *et al.*, “Experimental studies of the chemical durability of UK HLW and ILW glasses,” Didcot, 2016.
- [210] R. K. Chinnam, P. C. M. Fossati, and W. E. Lee, “Degradation of partially immersed glass: A new perspective,” *Journal of Nuclear Materials*, vol. 503, pp. 56–65, 2018.
- [211] Nuclear Decommissioning Authority, “UK Radioactive Waste Inventory - 2D02/C Vitrified Magnox High Level Waste,” 2014.
- [212] Nuclear Decommissioning Authority, “Magnox Cladding and Miscellaneous Solid Waste,” *Waste Stream Data Sheet 2D22*, 2007.
- [213] ASTM International, “Standard Practice for Measurement of the Glass Dissolution Rate Using the Single-Pass Flow-Through Test Method,” 2017.
- [214] J. D. Vienna, “The Effects of Temperature and Composition on the Solubility of Chromium in Multi-Component Alkali-Borosilicate Glass Melts,” Thesis - Washington

State University, 2002.

- [215] N. Hyatt and M. J. Nuclear, “Thermal treatment of ILW,” *Nuclear Engineering International*, 2013. [Online]. Available: <https://www.neimagazine.com/features/featurethermal-treatment-of-ilw/>. [Accessed: 17-Apr-2019].
- [216] R. Short, “Phase separation and crystallisation in UK HLW vitrified products,” *Procedia Materials Science*, vol. 7, pp. 93–100, 2014.
- [217] P. A. Bingham, A. J. Connelly, N. C. Hyatt, and R. J. Hand, “Corrosion of glass contact refractories for the vitrification of radioactive wastes: a review,” *International Materials Reviews*, vol. 56, no. 4, pp. 226–242, Jul. 2011.
- [218] A. Hoch and M. Wilkes, “Modelling the Expansion and Cracking of Grouted Wasteforms Containing Mild Steel or Magnox,” Didcot, 2016.
- [219] A. Covill, N. C. Hyatt, J. Hill, and N. C. Collier, “Development of magnesium phosphate cements for encapsulation of radioactive waste,” *Advances in Applied Ceramics*, vol. 6753, no. 3, pp. 151–156, 2011.
- [220] D. J. Bailey and M. C. Stennett, “Synthesis and characterisation of brannerite compositions $(U_{0.9}Ce_{0.1})_{1-x}M_xTi_2O_6$ ($M = Gd^{3+}, Ca^{2+}$) for the immobilisation of MOX residues,” *RSC Advances*, vol. 8, pp. 2092–2099, 2018.
- [221] B. Ravel and M. Newville, “ATHENA, ARTEMIS, HEPHAESTUS: data analysis for X-ray absorption spectroscopy using IFEFFIT,” *Journal of Synchrotron Radiation*, vol. 12, pp. 537–541, 2005.
- [222] A. J. Connelly *et al.*, “The effect of uranium oxide additions on the structure of alkali borosilicate glasses,” *Journal of Non-Crystalline Solids*, vol. 378, no. 2013, pp. 282–289, 2013.
- [223] F. Farges, C. W. Ponader, G. Calas, and G. E. Brown, “Structural environments of incompatible elements in silicate glass/melt systems: II. UIV, UV, and UVI,” *Geochimica et Cosmochimica Acta*, vol. 56, no. 12, pp. 4205–4220, 1992.
- [224] C. Den Auwer, E. Simoni, S. Conradson, and C. Madic, “Investigating Actinyl Oxo Cations by X-ray Absorption Spectroscopy,” *European Journal of Inorganic Chemistry*, vol. 2003, no. 21, pp. 3843–3859, Nov. 2003.
- [225] C. Fillaux *et al.*, “Combining theoretical chemistry and XANES multi-edge experiments to probe actinide valence states,” *Comptes Rendus Chimie*, vol. 10, pp. 859–871, 2007.
- [226] B. Kosog, H. S. La Pierre, M. A. Denecke, F. W. Heinemann, and K. Meyer, “Oxidation State Delineation via U L III -Edge XANES in a Series of Isostructural Uranium Coordination Complexes,” *Inorganic Chemistry*, vol. 51, no. 14, pp. 7940–7944, Jul. 2012.
- [227] C. W. Stokes, R. Van Noort, and R. J. Hand, “Investigation of the chemical solubility of mixed-alkali fluorcanasite forming glasses,” *Journal of Non-Crystalline Solids*, vol. 352, no. 2, pp. 142–149, 2006.
- [228] C. M. Jantzen, K. G. Brown, and J. B. Pickett, “Impact of Phase Separation on Durability in Phosphate,” Aiken, 2001.

- [229] G. Sattonnay *et al.*, “Alpha-radiolysis effects on UO₂ alteration in water,” *Journal of Nuclear Materials*, vol. 288, no. 1, pp. 11–19, 2001.
- [230] P. C. Burns and K.-A. Hughes, “Studtite, [(UO₂)(O₂)(H₂O)₂](H₂O)₂: The first structure of a peroxide mineral,” *American Mineralogist*, vol. 88, no. 7, pp. 1165–1168, Jul. 2003.
- [231] F. Clarens, J. de Pablo, I. Díez-Pérez, I. Casas, J. Giménez, and M. Rovira, “Formation of Studtite during the Oxidative Dissolution of UO₂ by Hydrogen Peroxide: A SFM Study,” *Environmental Science & Technology*, vol. 38, no. 24, pp. 6656–6661, Dec. 2004.
- [232] B. E. Burakov, E. E. Strykanova, and E. B. Anderson, “Secondary Uranium Minerals on the Surface of Chernobyl ‘Lava,’” *MRS Proceedings*, vol. 465, p. 1309, Jan. 1996.
- [233] E. R. Weiner, *Applications of Environmental Aquatic Chemistry: A Practical Guide*, 3rd ed. CRC Press, 2013.
- [234] Department of Energy & Climate Change, “Waste Transfer Pricing Methodology for the disposal of higher activity waste from new nuclear power stations,” 2011.
- [235] G. T. Higgins, “Secondary recrystallisation in magnox AL 80,” *Journal of Nuclear Materials*, vol. 8, no. 2, pp. 153–159, Mar. 1963.
- [236] A. A. Chowdhury, M. G. Rasul, and M. M. K. Khan, “Thermodynamic processes and characterisation of dead burned magnesia: A review,” in *Recent Advances in Energy & Environment*, 2010, pp. 344–349.
- [237] R. J. Charles and F. E. Wagstaff, “Metastable Immiscibility in the B₂O₃-SiO₂ System,” *The American Ceramic Society*, vol. 51, no. 1, pp. 16–20, 1968.
- [238] S. T. Barlow, D. J. Bailey, A. J. Fisher, M. C. Stennett, C. L. Corkhill, and N. C. Hyatt, “Synthesis of simulatant ‘lava-like’ fuel containing materials (LFCM) from the Chernobyl reactor Unit 4 meltdown,” *MRS Advances*, vol. 2, no. 11, pp. 609–614, Dec. 2017.
- [239] A. S. Baev, Y. A. Teterin, K. E. Ivanov, A. Y. Teterin, and S. A. Bogatov, “X-ray photoelectron Study of the Samples of Fuel Containg Masses Formed as a Result of the Chernobyl Accident,” *Radiochemistry*, vol. 39, no. 2, pp. 169–174, 1997.
- [240] I. E. Kuz and V. V Tokarevskii, “Sources and mechanisms of aerosol formation in the Chernobyl ‘Sarcophagus,’” *Atomic Energy*, vol. 82, no. 2, pp. 130–136, 1997.
- [241] A. A. Borovoi, A. S. Lagunencko, and E. M. Pazukhin, “Radiochemical and Selected Physicochemical Characteristics of Lava and Concrete from Subreactor Room no. 304/3 of the Fourth Block of the Chernobyl Nuclear Power Plant and Their Connection with the Accident Scenario,” *Radiochemistry*, vol. 41, no. 2, pp. 197–202, 1999.
- [242] E. M. Pazukhin, A. S. Lagunencko, V. A. Krasnov, and V. V Bil, “Fuel at Upper Levels of the Destroyed Fourth Block of Chernobyl NPP . Refining the Formation Scenario of the Polychromatic Ceramics,” *Radiochemistry*, vol. 48, no. 5, pp. 522–534, 2006.
- [243] A. A. Borovoi, A. S. Lagunencko, and E. M. Pazukhin, “Estimating the amount of fuel in cellar building 305/2 at Chernobyl unit 4,” *Atomic Energy*, vol. 84, no. 4, pp. 295–299, 1998.

- [244] M. Trotabas, J.-Y. Blanc, B. E. Burakov, E. B. Anderson, and D. J., “Examination of Chernobyl samples. Impact on the accident scenario understanding. Report DMT/92/309, SETIC/LECR-92/36, Report IPSN/93/02, Report RI-1-63/92,” 1993.
- [245] E. B. Anderson, B. E. Burakov, and E. M. Pazukhin, “High-Uranium Zircon from ‘Chernobyl Lavas,’” *Radiochimica Acta*, vol. 60, no. 1993, pp. 149–151, 1993.
- [246] T. Geisler, B. E. Burakov, V. Zirlin, L. Nikloeave, and P. Poml, “A Raman spectroscopic study of high-uranium zircon from the Chernobyl ‘lava,’” *European Journal of Mineralogy*, vol. 17, no. 6, pp. 883–894, 2005.
- [247] P. Pöml *et al.*, “Micro-analytical uranium isotope and chemical investigations of zircon crystals from the Chernobyl ‘lava’ and their nuclear fuel inclusions,” *Journal of Nuclear Materials*, vol. 439, no. 1–3, pp. 51–56, 2013.
- [248] V. G. Savonenkov, “Radioactive technogenic novel formations from the ruins of the fourth block of the Chernobyl atomic energy station.pdf,” *Radiochemistry*, vol. 33, no. 4, pp. 140–149, 1991.
- [249] J. M. Rogozin, E. A. Smirnova, V. A. Savonenkov, V. G., Krivohatski, A. S., Avdeev, and E. J. Sagadaychenko, “Leaching of radionuclides from some neoformed products, excavated from the reactor area of the 4th block of the Chernobyl Nuclear power plant. (in Russian),” *Radiochemistry*, vol. 4, pp. 160 – 167, 1991.
- [250] A. N. Kiselev, A. Y. Nenaglyadov, A. I. Surin, and C. K. P., “Experimental study of lava-like fuel containing masses (FCM) at 4th Unit of ChNPP (based on results obtained in 1986 – 1991). (in Russian),” Moscow, 1992.
- [251] A. P. Krinitsyn, I. Y. Simanovskaya, and O. L. Strikhar, “Action of Water on the Construction and Fuel-containing Materials in the Facilities of the Chernobyl Sarcophagus,” *Radiochemistry*, vol. 40, no. 3. pp. 287–297, 1998.
- [252] A. A. Borovoy, B. Y. Galkin, A. P. Krinitsyn, V. M. Markushev, A. N. Pazukhin, E. M. Kheruvimov, and K. P. Checherov, “New products formed by reaction of fuel with construction materials in the 4th block of the Chernobyl NPP (in Russian),” *Radiochemistry*, vol. 32, pp. 659 – 667, 1990.
- [253] B. Y. Zubekhina and B. E. Burakov, “Leaching of actinides and other radionuclides from matrices of Chernobyl “ lava ” as analogues of vitrified HLW,” *The Journal of Chemical Thermodynamics*, vol. 114, pp. 25–29, 2017.
- [254] V. N. Bondarenko *et al.*, “Investigation of the elemental composition of surrogates of fuel-containing materials by nuclear microanalysis,” *Atomic Energy*, vol. 102, no. 4, pp. 304–309, 2007.
- [255] V. S. Krasnorutsky *et al.*, “Study of the interaction of nuclear fuel with core construction materials in the case of the above design accident (in Russian),” 2012.
- [256] V. S. Krasnorutsky *et al.*, “Microstructural analysis of lava-like fuel-contained masses (in Russian),” *Problems of atomic Science and Technology*, pp. 60–70, 2010.
- [257] A. P. Krinitsyn, O. L. Strikhar, and V. N. Shcherbin, “Management of Liquid Radioactive Waste from the Shelter,” *Radiochemistry*, vol. 45, no. 5, pp. 512–517, 2003.
- [258] V. Baryakhtar, V. Gonchar, A. Zhidkov, and A. Klutchnikov, “Dust productivity of

- damaged irradiated fuel and lava-like fuel containing materials of ‘Shelter’ object.,” 1997.
- [259] V. P. Badovskii, A. E. Melenevskii, Y. V. Morozov, I. A. Ushakov, and V. N. Shcherbin, “Generation of radioactive dust by lava-like fuel containing materials at the Shelter Object of Chernobyl NPP (In Russian),” *Radiochemistry*, vol. 56, pp. 311–318, 2014.
- [260] H. Koniship *et al.*, “Synchrotron radiation beamline to study radioactive Photon Factory materials at the,” *Nuclear Instruments and Methods in Physics Research Section A: Accelerators, Spectrometers, Detectors and Associated Equipment*, vol. 372, no. 1–2, pp. 322–332, 1996.
- [261] C. L. Corkhill, D. E. Crean, D. J. Bailey, D. Grolimund, and N. C. Hyatt, “Multi-scale investigation of uranium attenuation by arsenic at an abandoned uranium mine , South Terras,” *npj Materials Degradation*, vol. 1, pp. 1–7, 2017.
- [262] V. V. Gonchar and A. V. Zhidkov, “Dynamics of high-temperature interaction of damaged nuclear fuel with construction materials of RBMK (in Russian),” *Problems of Nuclear Power Plants Safety of Chernobyl*, vol. 9, pp. 25–33, 2002.
- [263] C. E. Curtis and H. G. Sowman, “Investigation of the thermal dissociation, re-association and synthesis of zircon.,” *Journal of the American Ceramic Society*, vol. 36, pp. 190–198, 1953.
- [264] W. C. Butterman and W. R. Foster, “Zircon stability and the ZrO₂-SiO₂ phase diagram.,” *American Mineralogist*, vol. 52, pp. 880–885, 1967.
- [265] B. E. Burakov, A. P. Smetannikov, and E. B. Anderson, “Investigation of natural and artificial Zr-silicate gels.,” *Materials Research Society Symposium Proceedings*, vol. 932, pp. 1017 – 1024, 2006.
- [266] P. Piluso, G. Trillon, and C. Journeau, “The UO₂-ZrO₂ system at high temperature (T > 2000 K): importance of the meta-stable phases under severe accident conditions.,” *Journal of Nuclear Materials*, vol. 344, pp. 259–264, 2005.
- [267] V. M. Oversby, “Uranium dioxide, SIMFUEL, and spent fuel dissolution rates – a review of published data. SKB Technical Report, TR-99-22,” 1999.
- [268] C. M. Jantzen and C. L. Trivelpiece, “Uranium dissolution and geochemical modelling in anoxic and oxic solutions.,” *MRS Advances*, vol. 2, pp. 705–710, 2017.
- [269] N. Liu, Z. Qin, J. J. Noel, and D. W. Shoesmith, “Modelling the radiolytic corrosion of α -doped UO₂ and spent nuclear fuel,” *Journal of Nuclear Materials*, vol. 494, pp. 87–94, 2017.
- [270] NASA, “Multi-Mission Radioisotope Thermoelectric Generator (MMRTG),” *NASA facts*, Oct-2013.
- [271] United States Department of Energy, “Start-up Plan for Plutonium-238 Production for Radioisotope Power Systems,” Washington, D.C, 2010.
- [272] T. P. Tinsley, M. Clough, C. Rhodes, M. J. Sarsfield, and K. Stephenson, “Design requirements for a plant to produce ²⁴¹Am suitable for use in an European RTG,” *Nuclear and Emerging Technologies for Space*, no. Paper #3029, pp. 2–3, 2012.

- [273] T. Tinsley, M. Sarsfield, and K. Stephenson, "Update on ^{241}Am production for use in Radioisotope Power Systems," *IEEE Aerospace conference*, pp. 1–8, 2017.
- [274] E. I. Grinberg *et al.*, "Estimate of Radiation Safety of Emergency Atmospheric Reentry of Radioisotope Thermal Generators Used for Space Applications," in *Proceedings of the First IAASS Conference*, 2005, no. 1, pp. 67–72.
- [275] T. D. Chikalla and L. Eyring, "Dissociation pressures and partial thermodynamic quantities for americium oxides," *Journal of Inorganic and Nuclear Chemistry*, vol. 29, no. 9, pp. 2281–2293, Sep. 1967.
- [276] P. A. Bingham, R. J. Hand, M. C. Stennett, N. C. Hyatt, and M. T. Harrison, "The Use of Surrogates in Waste Immobilization Studies: A Case Study of Plutonium," *MRS Proceedings*, vol. 1107, p. 421, Jan. 2008.
- [277] E. J. Watkinson, D. Chateigner, R. M. Ambrosi, S. Gascoin, H. R. Williams, and K. Stephenson, "Detailed X-ray diffraction analysis of $\text{Ce}_{1-x}\text{Nd}_x\text{O}_{2-(x/2)}$ as a surrogate for substoichiometric americium oxide," *Journal of Nuclear Materials*, vol. 507, pp. 158–163, Aug. 2018.
- [278] A. Mielewczyk-Gryń and A. Navrotsky, "Enthalpies of formation of rare earth niobates, RE_3NbO_7 ," *American Mineralogist*, vol. 100, pp. 1578–1583, 2015.
- [279] L. Cai, S. Denev, V. Gopalan, and J. C. Nino, "Phase transition in weberite-type Gd_3NbO_7 ," *Journal of the American Ceramic Society*, vol. 93, no. 3, pp. 875–880, 2010.
- [280] S. J. Skinner and Y. Kang, "X-ray diffraction studies and phase transformations of $\text{CeNbO}_{4+\delta}$ using in situ techniques," *Solid State Sciences*, vol. 5, no. 11–12, pp. 1475–1479, Nov. 2003.
- [281] J. G. Thompson, R. L. Withers, and F. J. Brink, "Modulated Structures in Oxidized Cerium Niobates," *Journal of Solid State Chemistry*, vol. 143, no. 1, pp. 122–131, Feb. 1999.
- [282] R. D. Bayliss *et al.*, "Fergusonite-type $\text{CeNbO}_{4+\delta}$: Single crystal growth, symmetry revision and conductivity," *Journal of Solid State Chemistry*, vol. 204, pp. 291–297, Aug. 2013.
- [283] F. Vullum and T. Grande, "Oxidation Driven Decomposition of CeNbO_4 in Pure Oxygen," *Chemistry of Materials*, vol. 20, no. 16, pp. 5434–5437, 2008.
- [284] N. E. Brese and M. O'Keeffe, "Bond-valence parameters for solids," *Acta Crystallographica Section B Structural Science*, vol. 47, no. 2, pp. 192–197, Apr. 1991.
- [285] I. D. Brown and D. Altermatt, "Bond-Valence Parameters Obtained from a Systematic Analysis of the Inorganic Crystal Structure Database," *Acta Crystallographica Section B Structural Science*, vol. 41, pp. 244–247, 1985.
- [286] M. C. Stennett, C. L. Freeman, A. S. Gandy, and N. C. Hyatt, "Crystal structure and non-stoichiometry of cerium brannerite: $\text{Ce}_{0.975}\text{Ti}_2\text{O}_{5.95}$," *Journal of Solid State Chemistry*, vol. 192, pp. 172–178, Aug. 2012.
- [287] A. Kahn-Harari, L. Mazerolles, D. Michel, and F. Robert, "Structural Description of La_3NbO_7 ," *Journal of Solid State Chemistry*, vol. 116, no. 1, pp. 103–106, 1995.

- [288] B. J. Campbell, H. T. Stokes, D. E. Tanner, and D. M. Hatch, "ISODISPLACE: A web-based tool for exploring structural distortions," *Journal of Applied Crystallography*, vol. 39, no. 4, pp. 607–614, 2006.
- [289] J. A. Small and S. J. Choquette, "Certificate of Analysis Standard Reference Material 674b," Gaithersburg, 2017.
- [290] M. Glerup, O. F. Nielsen, and F. W. Poulsen, "The Structural Transformation from the Pyrochlore Structure, $A_2B_2O_7$, to the Fluorite Structure, AO_2 , Studied by Raman Spectroscopy and Defect Chemistry Modeling," *Journal of Solid State Chemistry*, vol. 160, no. 1, pp. 25–32, Aug. 2001.
- [291] C. Kaliyaperumal, A. Sankarakumar, J. Palanisamy, and T. Paramasivam, "Fluorite to pyrochlore phase transformation in nanocrystalline $Nd_2Zr_2O_7$," *Materials Letters*, vol. 228, pp. 493–496, Oct. 2018.
- [292] A. Salamat *et al.*, "Structural Transformations and Disorder in Zirconolite ($CaZrTi_2O_7$) at High Pressure," *Inorganic Chemistry*, vol. 52, no. 3, pp. 1550–1558, Feb. 2013.
- [293] P. G. Lucuta, R. A. Verrall, H. Matzke, and B. J. Palmer, "Microstructural features of SIMFUEL - Simulated high-burnup UO_2 -based nuclear fuel," *Journal of Nuclear Materials*, vol. 178, pp. 48–60.
- [294] Z. Hiezl, D. I. Hambley, C. Padovani, and W. E. Lee, "Processing and microstructural characterisation of a UO_2 -based ceramic for disposal studies on spent AGR fuel," *Journal of Nuclear Materials*, vol. 456, no. 2015, pp. 74–84, Jan. 2015.